IRON AS AN INTEGRAL CONSTITUENT OF ANCIENT METABOLISM AND BIOCHEMISTRY

A Dissertation
Presented to
The Academic Faculty

by

Marcus Salvatore Bray

In Partial Fulfillment
of the Requirements for the Degree
Doctor of Philosophy in Biology

Georgia Institute of Technology
August 2019

IRON AS AN INTEGRAL CONSTITUENT OF ANCIENT METABOLISM AND BIOCHEMISTRY

Approved by:

Dr. Jennifer B. Glass, Advisor
School of Earth & Atmospheric Sciences
Georgia Institute of Technology

Dr. Loren Dean Williams, Co-Advisor
School of Chemistry & Biochemistry
Georgia Institute of Technology

Dr. Joel E. Kostka
School of Biological Sciences, School of Earth & Atmospheric Sciences
Georgia Institute of Technology

Dr. Kostas T. Konstantinidis
School of Civil & Environmental Engineering
Georgia Institute of Technology

Dr. Frank J. Stewart
School of Biological Sciences
Georgia Institute of Technology

Date Approved: April 25th, 2019

“Into the desert, with only a head and some crossing wires to trace. Here's the world - the one that kills our fathers, and that births our children. May we forever wind, crawl and stumble below the stars, barely living before we shed our mind to teach ourselves anew.”

-anonymous

ACKNOWLEDGEMENTS

I would first like to express my deep gratitude to both of my thesis advisors, Dr. Jennifer B. Glass and Dr. Loren Dean Williams for their continued guidance, support, and mentorship. I would also like to thank all the members of my thesis committee: Dr. Frank Stewart, Dr. Joel Kostka, and Dr. Kostas Konstantinidis for their service and support. I would like to thank members of both the Glass and Williams labs, with whom I had the pleasure of working closely during my time at Tech. I would especially like to thank Dr. Nadia Szeinbaum, and Jessica Bowman, for helpful discussion on experimental design and scientific theory. I would like to thank the amazing undergraduate students with whom I worked including Miles Mobley, Claudia Montllor Albalate, and Bianca Costa, for all their help with my research. I would also like to thank members from other labs, including the Kostka Lab, the Stewart Lab including Dr. Cory Padilla and Dr. Anthony Bertagnolli, the DiChristina lab including Ben Reed and Yael Toporek, and Lieberman lab, for helpful discussion and graciously allowing me access to their equipment. I would also like to thank Dr. Amit Reddi for helpful discussion and collaboration with Total Reflective X-ray Spectroscopy, as well as Dr. Roger Wartell for helpful discussion and troubleshooting of experiments. I would like to thank Sean Crowe from the University of British Columbia for helpful discussion and providing us with Lake Matano samples as well as members of his lab including Dr. Rachel Simister and Kate Thompson for help with experiments. I would also like to thank Dr. Corinna Tuckey from New England Biolabs for many helpful discussions. The research presented in this thesis was funded by NASA Exobiology grants NNX14AJ87G and NNX16AJ28G. Finally, I would like to sincerely thank my wife,

Kristina L. Leyva, and my parents, Jeffrey and Anna Bray for their love, support, and most importantly sacrifice, without which none of this would have been possible.

TABLE OF CONTENTS

LIST OF TABLES

LIST OF FIGURES

LIST OF SYMBOLS AND ABBREVIATIONS

BIFs	Banded Fe formations
CARD-FISH	Catalyzed reporter deposition fluorescence *in situ* hybridization
CH_4	Methane
ClO_4^-	Perchlorate
CPR	Candidate phyla radiation
DAPI	4′,6-diamidino-2-phenylindole
DIC	Dissolved inorganic carbon
DNA	Deoxyribonucleic acid
Fe	Fe
Fe^{2+}	Ferrous Fe ion
Fe^{3+}	Soluble ferric Fe ion
Fe(III)	Solid phase ferric Fe
Ga	Billion years ago
GOE	Great oxidation event
HPLC	High throughput liquid chromatography
HRP	Horse radish peroxidase
LC-MS/MS	Liquid chromatography tandem mass spectrometry
LSU	Large ribosomal subunit
M^{2+}	Divalent metal cation
MAG	Metagenome assembled genome
Mg^{2+}	Magnesium ion
Mn^{2+}	Manganese ion

mRNA	Messenger RNA
NO_x^-	Nitrogen oxides
O_2	Molecular oxygen
PAGE	Polyacrylamide gel electrophoresis
pre-GOE	Anoxic, high Fe^{2+} growth conditions
PTC	Peptidyl transferase center
RNA	Ribonucleic acid
rRNA	Ribosomal RNA
rProteins	Ribosomal proteins
SDS	Sodium dodecyl sulfate
SHAPE	Selective 2'-Hydroxyl Acylation analyzed by Primer Extension
SSU	Small ribosomal subunit
TCA	Tri carboxylic acid
tRNA	Transfer RNA

SUMMARY

Life on Earth evolved and proliferated for nearly 2 billion years in an environment devoid of O_2 and replete with Fe. Currently on Earth, Fe has widespread uses in the biochemistry and metabolism of extant organisms. It is therefore likely that this metal filled a larger role at life's inception and colonization across the planet. In this dissertation, I investigated the roles that Fe could have played for early lifeforms and early biochemistry. Specifically, I studied Fe(III) as an electron acceptor in bacterial respiration, as well as the ability of Fe^{2+} to substitute for Mg^{2+} in life's oldest macromolecular machine, the ribosome.

First, I examined the ability of Fe^{2+} to mediate the structure and function of the ribosome. The ribosome, which is responsible for the translation of RNA to protein, is the most highly conserved macromolecular structure in biology and can trace its roots to before the last universal common ancestor. Extant ribosomes are thought to associate extensively with Mg^{2+}, which is required to ensure the correct folding and operation of the ribosome. However, the Fe^{2+}-rich conditions under which the ribosome evolved, and the similar coordination chemistry of Fe^{2+} and Mg^{2+}, suggests that the former may have served as a cofactor for the ribosome during the origin and early evolution of life.

To test this hypothesis, I examined the ability of Fe^{2+} to mediate ribosomal structure and function by substituting Fe^{2+} for Mg^{2+}. *In vitro*, I showed that Fe^{2+} folds ribosomal RNA in a similar fashion to Mg^{2+} and that Fe^{2+}-bound ribosomes can catalyze the translation of active proteins. I also showed similar results substituting Mg^{2+} with Mn^{2+}, another metal ion that would have been prevalent on the early Earth. I then investigated the association of Fe^{2+} with ribosomes *in vivo* from cells grown under conditions that would

have been prevalent in the Archean before the GOE. By growing bacteria anaerobically in the presence of high levels of Fe^{2+}, I showed that the ribosomes purified from these cells contain significantly more Fe than those from bacteria grown either aerobically or in the absence of Fe^{2+}. I then showed that this Fe is associated mostly with the rRNA.

For the second half of this thesis, I investigated the role Fe played in microbial respiration in the early biosphere, by studying Fe(III)-reduction and the organisms responsible for it from Lake Matano, an Archean ocean analog. Fe(III)-reduction is thought to be one of the first metabolisms used by early life forms as both early biotic and abiotic processes would have led to oxidation of Fe^{2+} to Fe(III) in the environment. Ferric oxide minerals in Archean sediments were likely an abundant electron sink for early microorganisms, and it is likely that early lifeforms evolved to respire Fe(III).

I looked at the relationship between Fe(III)-reduction and another ancient metabolism, methanogenesis. Organisms capable of CH_4 production are significant sources of this greenhouse gas to the atmosphere. Like today, methanogens likely served as the main contributors of CH_4 to the Archean atmosphere, resulting in atmospheric greenhouse gas concentrations capable of maintaining planetary habitability under the reduced solar irradiance of the young Sun. Because Fe(III)-reducing organisms are known to inhibit methanogens, it is perplexing how methanogens living in Fe-rich sediments could have maintained early Earth habitability. I showed through long-term incubations that the form of Fe(III)-oxide mineral controls the relative activities of Fe(III)-reduction versus methanogenesis, and the relative abundances and location of these different minerals could have been a large control on habitability of the early planet.

I then investigated Fe(III)-reduction strategies employed by microorganisms in the environment. Certain organisms are able to use pili, long wire-like macromolecular structures made up of protein subunits, to directly contact and reduce solid Fe(III)-oxide minerals in their environment. Studies detailing the molecular mechanisms of the pilin proteins, the subunits of these electroactive pili (e-pili), have identified certain characteristics that seem to be required for granting these pili electroactive ability. Using these characteristics as search criteria, I identified pilins from a variety of microbial habitats, including Archean ocean analogs. These pilins belong to different bacterial taxa, some of which are not known to use e-pili or even reduce Fe(III).

The results of this work have expanded the potential role for Fe in the origin and propagation of life on this planet. By studying extant biological and ecological systems under conditions reminiscent to the ancient Earth, I have provided evidence that Fe was likely a major determinant in processes central to the evolution and proliferation of life. These studies not only inform life's past but also its current state and future trajectory. We can now consider Fe a major constituent in translation and nucleic acid based biochemical systems, and postulate what that may mean for biochemistry in extant microorganisms. In addition, we can consider other ways in which Fe could have modulated climate throughout earth history and possibly into the future. Finally, we have better a idea of the strategies organisms use to reduce Fe(III) in the environment, and the larger roles that this process may play in global element cycling.

CHAPTER 1. INTRODUCTION: IRON AND THE ANCIENT BIOSPHERE

Iron is abundant in the universe and within the rocky crust of Earth (1). In addition to its geological prevalence and immense importance in the history of our species, Fe serves widespread and universal roles in all biology. Iron's role in biology is particularly interesting given the great care that must be taken by organisms to both assimilate and sequester Fe in an environment that causes it to be both scarce and dangerously reactive. This paradox underscores a fundamental truth of biology: for many biological processes, Fe is an optimal and irreplaceable cofactor. Therefore, many cellular processes requiring Fe must have not only evolved around, but likely been catalyzed by its unique properties. In this thesis, I describe how the geochemical conditions in which life evolved led to iron's use in biology, and how the extant examples of this are in fact remnants of a time when Fe played even greater roles in life on Earth.

1.1 The Archean eon

The Archean eon (4-2.5 Ga) was the period of Earth's history when life first evolved. From a geochemical perspective, the Archean Earth was vastly different from our current planet, most notably with respect to O_2. The Archean atmosphere was devoid of O_2, allowing for the buildup of many reduced chemical species on the Earth's surface (2, 3). One of these compounds was Fe^{2+}. Even though oxygenic phototrophs evolved by the late Archean, atmospheric O_2 did not climb to appreciable levels until around 2.4 Ga, during the GOE (3, 4). The GOE marked a geochemical turning point in the history of our planet;

transitioning from a reducing environment and eventually leading to the highly oxidative environment of the current Earth. Below I will discuss certain characteristics of the Archean that would have made Fe a primary geological and biological player.

1.2 Sources and availability of iron in the Archean

There is general agreement that the Archean ocean was iron-rich or "ferruginous". The strongest evidence is multiple banded Fe formations deposited during the Archean that do not appear in the rock record after the Earth's deep ocean became fully oxic (5). Iron enters the world's oceans in three main processes: hydrothermal circulation from mid-ocean ridges, weathering of continental rocks, and atmospheric deposition of terrestrial Fe-containing dust (6, 7). Currently, it is weathering that constitutes the main flux of Fe to the oceans, leading to higher concentrations in coastal waters (8). Overall, Fe is extremely scarce in the world's oceans today, with concentrations in the majority of seawater never reaching above the low nanomolar range, limiting biological activity in many marine surface waters (8-12).

Extant Fe scarcity is the result of direct and indirect reactions of Fe and O_2. Molecular oxygen rapidly oxidizes soluble Fe^{2+} in aqueous solutions to Fe^{3+} which at circumneutral pH precipitates out of solution as Fe(III)-oxide minerals (13). In addition, atmospheric O_2 leads to oxidative weathering of sulfide minerals, supplying sulfate to the oceans (14). Through a combined effort of microorganisms and hydrothermal convection, seawater sulfate is reduced to sulfide, which precipitates Fe in the water column and vent fluids as FeS (15).

Molecular oxygen (O_2) is produced by oxygenic photosynthesis. In this process a water molecule is split into H^+ and O_2, and the O_2 molecule is released to the atmosphere. Currently cyanobacteria, algae, and land plants all perform this process, and so generate enough O_2 to keep the Earth's atmosphere sufficiently oxygenated. At the turn of the Archean (4 Ga) however there were likely no organisms capable of oxygenic photosynthesis, and so the Earth's atmosphere was devoid of O_2. Without an oxygenated atmosphere there would have been no oxidative weathering of continental materials and therefore much smaller inputs of sulfate into the ocean, making sulfur a trace constituent (14, 16). In contrast, the higher concentrations of atmospheric CO_2 could have led to increased silicate weathering, mobilizing nutrients such as Mg^{2+}, Ca^{2+} and Fe^{2+} into the oceans and terrestrial freshwater environments (17).

The main source of Fe to the Archean however was hydrothermal fluids. It is estimated that hydrothermal activity in the Archean was as much as 3 times that of the present Earth, meaning that vent fluid would have been a significant source of reduced species to the Archean ocean (18). Metal species such as Mn^{2+} and Fe^{2+} would have been constantly added to seawater from this enhanced hydrothermal activity. Without dissolved O_2 or sulfide in the water, this Fe^{2+} would stay soluble and over time could have built up to concentrations hundreds to thousands of times their current levels (19). In addition, certain chemical species, namely Mg^{2+}, would have been stripped from seawater during movement through hydrothermal systems, leading to lower Mg^{2+} concentrations in the Archean ocean than today (20, 21).

The factors described above would have resulted in an ocean high in dissolved Fe^{2+} on the anoxic Archean Earth (**Figure 1**). In addition to Fe^{2+}, abundant Fe(III) would have

also been present at this time, resulting from the oxidation of Fe^{2+} in surface waters from abiotic and then later also biotic processes. Solar UV radiation, able the penetrate the young atmosphere more easily than today has the capability to oxidize Fe^{2+} to Fe^{3+} in solution. Rates of this abiotic process alone could have accounted for much of the Fe(III) observed in the geological record from this time (22). Biological oxidation of Fe^{2+} would have been mediated by organisms resembling modern photoferrotrophs, as well as other anaerobic Fe^{2+} oxidizers. In addition, toward the latter half of the Archean, the emergence of oxygenic phototrophs would have resulted in oxygenated surface waters capable of oxidizing large amounts of Fe^{2+} (4). Together these processes would have led to ocean sediment replete with various forms of Fe(III)-oxide (23).

There is considerable debate in pinpointing the exact spatial and temporal location of life's origin, and it is entirely likely that the transition from abiotic chemical reactions to membrane bound biological reactions could have occurred over numerous environments either sequentially or at the same time. One parameter largely certain is that Fe was highly available to early biochemical systems as they formed the basis of cellular life, and that life lived in a high Fe environment for nearly 3.5 billions years before O_2 rose to modern levels. These unique geochemical conditions likely had profound impacts on the earliest biochemistries and respiratory processes.

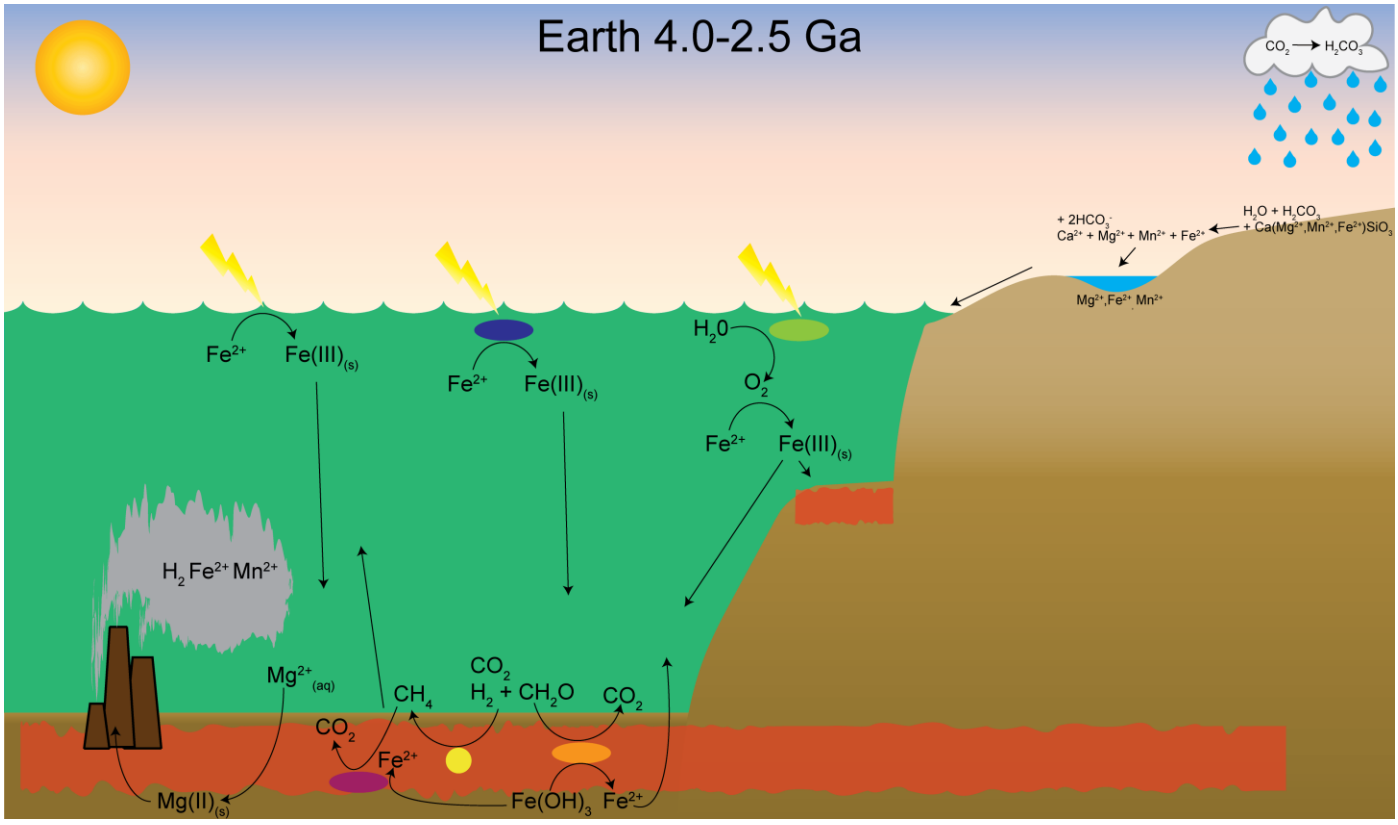

Figure 1. The Archean biosphere. The environment in which life proliferated what replete with Fe from largely hydrothermal, but also weathering sources adding dissolved Fe^{2+} to the oceans. Lifeforms capable of oxidizing Fe^{2+} would have inhabited the water column transforming Fe^{2+} to insoluble Fe^{3+} which precipitated as Fe(III)-minerals and fell to the sediments. Heterotrophic and Lithotrophic Fe(III) reduction in the sediment would had reduced this Fe(III) back to Fe^{2+}.

1.3 Iron in ancient biochemistry

Specific chemical and physical properties of Fe have rendered it an ideal biochemical cofactor for all life on Earth. As mentioned above, Fe is the most abundant transition metal in the Earth's crust. Iron is redox-active, existing as either reduced Fe^{2+} or oxidized Fe^{3+} and at widely different voltage potentials and electron spin states based on its ligand/coordinating environment (24-26). Organisms have taken advantage of these properties to use Fe as a redox reaction mediator stemming back to life's beginning. Iron's

roles in biochemistry include, electron transport, the TCA cycle, nitrogen fixation, photosynthesis, DNA synthesis, and carbon fixation, to name a few. While primarily serving redox purposes, Fe has some functions in the cell that do not depend on redox function (27).

While Fe is ubiquitously used by life (with rare exceptions), the modern oxygenated atmosphere makes Fe scare and hard to maintain for reasons discussed above. It is likely that Fe filled even more roles in biochemistry during the Archean, and what we observe in extant biology are remnants of iron's true biological potential. This would have been especially true at the origin of life, where simple biopolymers, still unable to assimilate, concentrate and compartmentalize, would have relied on whatever ions were plentiful in their environment. The abundant Fe surrounding them, coupled with its chemical properties would have rendered Fe very attractive to the natural selection of these molecules.

One of these expanded roles for Fe could have been mediating the structure as well as function of proteins and other biopolymers. Iron's current use by life is focused primarily as a cofactor for protein enzymes but it is possible Fe could have been an attractive cofactor for non-protein enzyme such as ribozymes which many believe would have been more important at the origin of life (28). In addition, Fe, specifically Fe^{2+}, could have served structural roles like we see for other M^{2+} such as Mg^{2+}. Nucleic acids in particular could have taken advantage of the abundant Fe^{2+} especially since the increased hydrothermal activity in the Archean would have depleted Mg^{2+} in seawater relative to today (21). Indeed, there is already evidence for Fe ability to serve both structural and functional positions in nucleic acids (29).

1.4 Iron in ancient metabolism

Some Bacteria and Archaea can use Fe^{2+} as a source of electrons and Fe(III) as a sink of electrons in respiration. The buildup of Fe in the Archean ocean from hydrothermal sources would have made it an attractive species for energy generation. Therefore, it is likely that early organisms evolved ways to utilize Fe in both its oxidation states.

Photoferrotrophy likely evolved early and represented a significant source of primary production in the Archean biosphere (30). Photoferrotrophy is a form of anoxygenic photosynthesis in which Fe^{2+} instead of H_2O is oxidized to replenish the electron pool for the photosystem. Although currently marginalized to the few habitats where abundant Fe^{2+} and sunlight coexist, the ferruginous upper water column in the Archean ocean would have been an optimal habitat for organisms capable of this process. The carbon fixed by photoferrotrophs would have provided a feed stock for heterotrophic organisms in much the same way cyanobacteria do on modern Earth. Other, non-photosynthetic organisms could also have used Fe^{2+} as an electron source. Organisms coupling the oxidation of Fe^{2+} to the reduction of other electron acceptors such as NO_x^- (31, 32). Towards the latter half of the Archean, the advent of oxygenic phototrophs could have also allowed for the evolution of microaerophilic Fe^{2+} oxidizers using O_2 as an electron acceptor.

The combination of these various Fe^{2+} oxidation metabolisms, plus the abiotic photo-oxidation of Fe^{2+} in the water column, would have seeded the Archean ocean with Fe(III)-oxide minerals as Fe^{3+} precipitated and deposited into the sediments (**Figure 1**). Heterotrophic and lithotrophic organisms capable of using these minerals as electron acceptors would have therefore likely been significant members of Archean sediment

communities. Autotrophs would have provided sources of organic carbon for heterotopic Fe(III)-reducers. This carbon would have come in many different molecular forms and so these organisms would have had to develop multiple pathways to ensure utilization of all available forms. Lithotrophic Fe(III)-reducers could have used inorganic compounds, such as H_2 or NH_4^+, as their source of electrons. These organisms would themselves be able to fix CO_2 to serve their organic carbon need and could have been more abundant than heterotrophic Fe(III)-reducers in the early part of the Archean before robust microbial food webs had been established. In addition the oxidation of CH_4 coupled to Fe(III)-reduction could have been prominent in the Archean.

The combined efforts of Fe^{2+} oxidizers and Fe(III)-reducers would have led to large scale cycling of Fe between Fe^{2+} in the water column and Fe(III)-oxides in the sediments. This Archean "ferrous wheel" would have not only controlled the movement of Fe through the Archean biosphere but also affected the biogeochemical cycling of other important elements for life.

CHAPTER 2. MULTIPLE PREBIOTIC METALS MEDIATE TRANSLATION

The work described in this chapter has been previously published in the journal *PNAS* (33). Experiments were performed either by myself or in collaboration with T.K. Lenz, C. Ito, and A.S. Petrov. I designed and performed all *in vitro* translation experiments described, as well as M^{2+}-ribosome association experiments. SHAPE experiments were performed by T.K. Lenz and C. Ito. Quantum mechanical calculations were made by A.S. Petrov. The manuscript was written with contributions from all coauthors.

2.1 Abstract

Today, Mg^{2+} is an essential cofactor with diverse structural and functional roles in life's oldest macromolecular machine, the translation system. We tested whether ancient Earth conditions (low O_2, high Fe^{2+}, high Mn^{2+}) can revert the ribosome to a functional ancestral state. First, SHAPE was used to compare the effect of Mg^{2+}, Fe^{2+}, and Mn^{2+} on the tertiary structure of rRNA. Then, we used *in vitro* translation reactions to test whether Fe^{2+} or Mn^{2+} could mediate protein production, and quantified ribosomal metal content. We found that: (i) Mg^{2+}, Fe^{2+}, and Mn^{2+} had strikingly similar effects on rRNA folding; (ii) Fe^{2+} and Mn^{2+} can replace Mg^{2+} as the dominant M^{2+} during translation of mRNA to functional protein; (iii) Fe and Mn associate extensively with the ribosome. Given that the translation system originated and matured when Fe^{2+} and Mn^{2+} were abundant, these findings suggest that Fe^{2+} and Mn^{2+} played a role in early ribosomal evolution.

2.2 Introduction

The translation system, which synthesizes all coded protein (34, 35), originated and matured during the Archean Eon (4-2.5 Ga) in low-O_2, high-Fe^{2+}, and high-Mn^{2+} conditions (36). The common core of the ribosome, and many other aspects of the translation system, have remained essentially frozen since the last universal common ancestor (37). In extant biochemistry, Mg^{2+} ions are essential for both structure and function of the ribosome (38) and other enzymes involved in translation (39). In ribosomes, Mg^{2+} ions engaged in a variety of structural roles (**Table 1**), including in Mg^{2+}-rRNA clamps (40, 41) (**Figure 2a**), in dinuclear microclusters that frame the PTC (41) (**Figure 2b**), and at the SSU-LSU interface (42) (**Figure 2c)**. Functional Mg^{2+} ions stabilize a critical bend in mRNA between the P-site and A-site codons (43) (**Figure 2d**), and mediate rRNA-tRNA and rRNA-mRNA interactions (44) (**Figure 2e, f**). Mg^{2+} ions also interact with some rProteins (45). Additionally, accessory enzymes needed for translation – aminoacyl tRNA synthetases, methionyl-tRNA transformylase, creatine kinase, myokinase, and nucleoside-diphosphate kinase – require Mg^{2+} ions as cofactors (**Table 1**).

Multiple types of cationic species can interact productively with RNAs in a variety of systems (46-48). Recent results support a model in which Fe^{2+} and Mn^{2+}, along with Mg^{2+}, were critical cofactors in ancient nucleic acid function (49, 50). As predicted by this model, functional Mg^{2+}-to-Fe^{2+} substitutions under anoxic conditions were experimentally verified to support RNA folding and catalysis by ribozymes (29, 51), a DNA polymerase, a DNA ligase, and an RNA polymerase (52). Functional Mg^{2+}-to-Mn^{2+} substitution has long been known for DNA polymerases (52-54). For at least some nucleic acid processing enzymes, optimal activity is observed at lower concentrations of Fe^{2+} than Mg^{2+} (29, 52).

In addition Fe^{2+} has shown to be important for the post transcriptional modification of rRNA (55). Based on these previous results, we hypothesized that Fe^{2+} and Mn^{2+} could partially or fully replace Mg^{2+} during translation. In this study, we relocated the translation system to the low-O_2, Fe^{2+}-rich, or Mn^{2+}-rich environment of its ancient roots, and compared its structure, function, and cation content under modern vs. ancient conditions.

Table 1. Structural and functional roles for select M^{2+} in the translation system. All biomolecules in the table have been shown to require Mg^{2+} and may also be active with Fe^{2+} or Mn^{2+}. "n.a." indicates that data are not available.

Translation system component(s)	**Location of M^{2+}**	**Role of M^{2+}**	**Optimal $[Mg^{2+}]$ (mM)**
Ribosome			
LSU/SSU	M^{2+}-rRNA clamps (40)	Mediates and maintains folding/structure of rRNAs	~10 (56)
LSU	Dinuclear microclusters (41)	Frames peptidyl transferase center (PTC)	~10 (56)
LSU/SSU	LSU/SSU interface (57)	Mediates docking of mRNA to SSU and association of SSU with LSU	~10 (56)
SSU/mRNA	Critical bend in mRNA between the P-site and A-site codons (44, 58)	Maintains correct reading frame mRNA	~10 (56)
A-site tRNA/ P-site tRNA	tRNA-tRNA interface (57)	Stabilize tRNAs in the PTC	~10 (56)
LSU/tRNA	rRNA-tRNA interface (57)	Stabilize rRNA-tRNA in the PTC	~10 (56)
Auxiliary			
EF-Tu	GTP binding site (59)	Stabilizes the transition state	5-15 (60)
EF-G	GTP binding site (61)	Stabilizes the transition state	n.a.
Aminoacyl-tRNA synthetases	ATP binding site (62)	Stabilizes the transition state	>1 (63)

Table 1. Structural and functional roles for select divalent cations in the translation system.

Methionyl-tRNA transformylase	ATP binding site (64)	Stabilizes the transition state	7 (64)
Creatine kinase	NTP binding site (65)	Stabilizes the transition state	~5 (65)
Myokinase	Acceptor NDP binding site (66)	Stabilizes the transition state	~3 (67)
Nucleoside-diphosphate kinase	NTP binding site (68)	Stabilizes the transition state	>1 (68)
Pyrophosphatase	Active site (69)	Stabilizes the transition state	>7 (70)

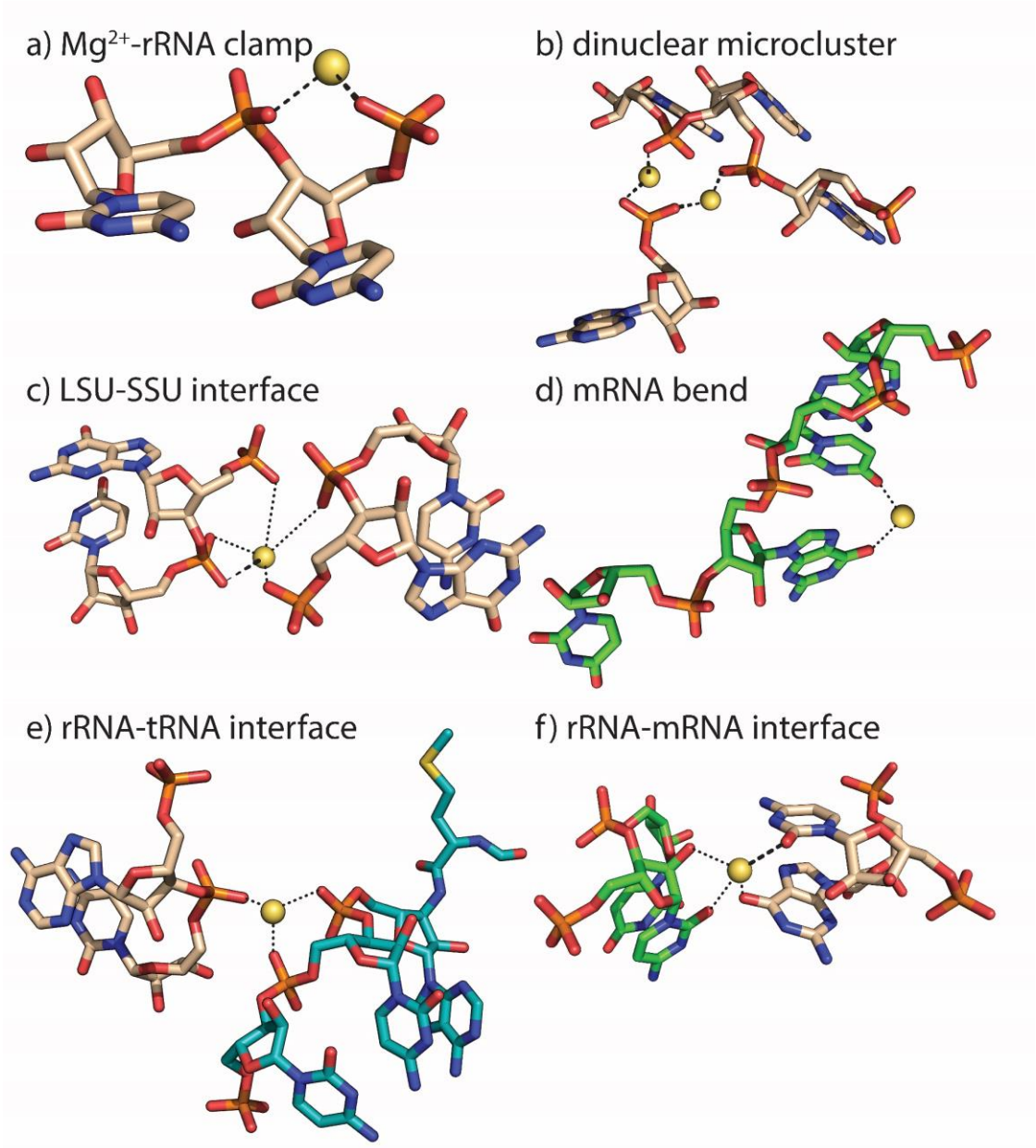

Figure 2. Divalent cations serve many structural and functional roles in the ribosome. Mg^{2+} ions: a) form bidentate clamps with adjacent phosphate groups of rRNA, b) form dinuclear microclusters that frame the rRNA of the PTC, c) stabilize the LSU-SSU interface, d) stabilize a functional kink in mRNA, e) stabilize association of tRNA (teal) with 23S rRNA (beige carbon atoms), and f) stabilize association of mRNA (green) with 16S rRNA (beige carbon atoms). Thick dashed lines are first shell RNA interactions of Mg^{2+}. Dotted lines indicate second shell interactions. Images are of the *Thermus thermophilus* ribosome (PDB ID: 1VY4). This figure was generated with the program RiboVision (71).

2.3 Experimental Methods

2.3.1 rRNA SHAPE reactions.

SHAPE (72-74) was conducted on the ~2900 nt *Thermus thermophilus* 23 rRNA (LSU) in 250 mM monovalent cation (Na^+ or K^+) to favor formation of secondary structure, and in 250 mM Na^+ or K^+ plus various M^{2+} (10 mM $MgCl_2$, 2.5 mM $FeCl_2$, or 2.5 mM $MnCl_2$) to favor tertiary interactions. These M^{2+} concentrations are sufficient to fold rRNA. To keep rRNA samples from O_2, solutions of rRNA alone or 200 mM NaOAc or KOAc plus 50 mM Na-HEPES (pH 8) or K-HEPES (pH 8) and M^{2+} were lyophilized and transferred into an anoxic chamber with a 98% Ar and 2% H_2 atmosphere. The rRNA solutions were rehydrated with nuclease-free, degassed water, and added to the dried salts to achieve the appropriate concentrations. After rRNA modification reactions, M^{2+} were removed by chelating beads. Samples were removed from the anoxic chamber before reverse transcription and analysis by capillary electrophoresis as in ref. (72). Essentially identical SHAPE profiles were observed with Na^+ or K^+ alone (**Figure 5**), as previously described (73, 75); and for monovalent cations in combination Mg^{2+}, Fe^{2+}, or Mn^{2+} (**Figure 5, 6**). Nucleotides were classified as exhibiting a significant change in SHAPE reactivity if the difference between the initial reactivity (in Na^+) and final reactivity (in Na^+/Mg^{2+}, Na^+/Fe^{2+}, or Na/Mn^{2+}) was >0.3 SHAPE units. To compare the Mg^{2+}-, Fe^{2+}-, and Mn^{2+}-responsiveness of specific nucleotides, we binned nucleotides into three categories (increased, decreased, or little/no change) based on their general SHAPE reactivity response to each M^{2+}.

2.3.2 In vitro translation.

Each 30 µL reaction contained 2 µM (4.5 µL of 13.3 µM stock) *E. coli* ribosomes in 10 mM Mg^{2+} (New England Biolabs, Ipswich MA, USA; catalog # P0763S), 3 µL factor mix (with RNA polymerase, and transcription/translation factors in 10 mM Mg^{2+}) from the PURExpress® Δ Ribosome Kit (New England Biolabs E3313S), 0.1 mM amino acid mix (Promega, Madison WI, USA; catalog # L4461), and 0.2 mM tRNAs from *E. coli* MRE 600 (Sigma-Aldrich, St. Louis MO, USA; product # TRNAMRE-RO). Thus, a total of 2.5 mM "background" Mg^{2+} was present in each reaction (**Figure 3a**). To remove the background Mg^{2+}, we exchanged the buffer of the ribosome and factor mix using centrifugal filter units. Thirty microliters of either ribosome solution or factor mix was added to an Amicon Ultra 0.5 mL centrifugal filter (Millipore-Sigma), followed by 450 µL of M^{2+}-free buffer (20 mM HEPES pH 7.6, 30 mM KCl, and 7 mM β-mercaptoethanol). Samples where spun at 14,000 x g at 4°C until the minimum sample volume (~15 µL) was reached. The samples were resuspended in 450 µL of M^{2+}-free buffer and centrifugation was repeated. The samples were then transferred to new tubes and 15 µL of M^{2+}-free buffer was added to bring the volume to 30 µL. This process decreased Mg^{2+} concentrations in the ribosome and factor mix from 10 mM to 10-30 µM Mg^{2+}, resulting in 4-6 µM Mg^{2+} in each reaction (**Figure 3b, 3c).**

2.3.3 Translation reaction buffer.

The reaction buffer was based on Shimizu et al. (76), with HEPES-OH instead of phosphate buffer to avoid precipitation of metal phosphates. We found that rates of translation were consistently lower with Tris-HCl than HEPES-OH, and therefore HEPES-OH was used as the buffer for all experiments. Buffer consisted of 20 mM HEPES-OH (pH

7.3), 95 mM potassium glutamate, 5 mM NH_4Cl, 0.5 mM $CaCl_2$, 1 mM spermidine, 8 mM putrescine, 1 mM dithiothreitol (DTT), 2 mM adenosine triphosphate (ATP), 2 mM guanosine triphosphate (GTP), 1 mM uridine triphosphate (UTP), 1 mM cytidine triphosphate (CTP), 10 mM creatine phosphate (CP), and 53 µM 10-formyltetrahydrofolate. The reaction buffer was lyophilized and stored at -80°C until resuspension in anoxic nuclease-free water immediately before experiments in an anoxic chamber.

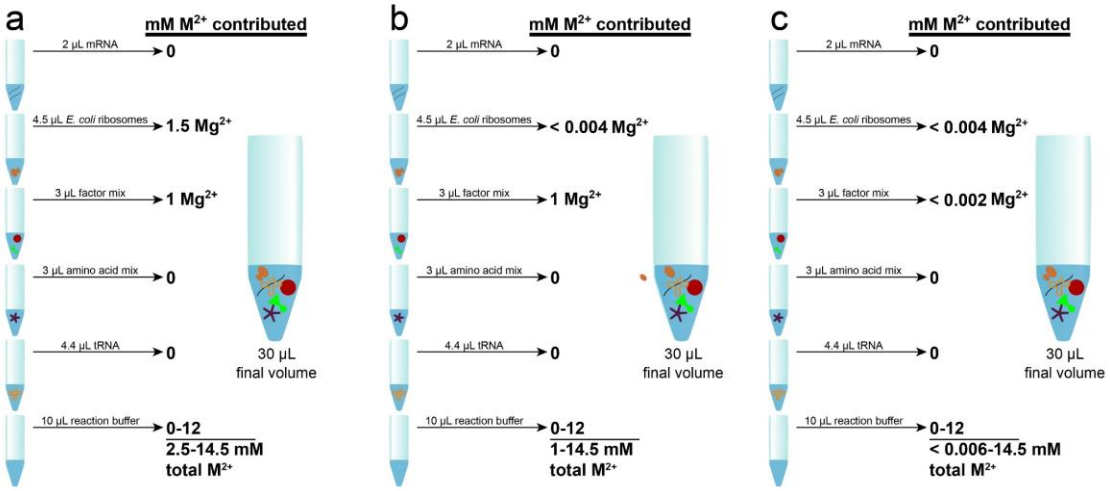

Figure 3. Anoxic translation reaction experimental design. Reactants are shown in the order they were added to the reaction (top to bottom). Divalent cation (M^{2+}) concentrations were varied in the 3x HEPES-OH reaction buffer (pH 7.3). Anoxic nuclease-free water was added to a final reaction volume of 30 µL. Three different reactions were performed: a) Standard reaction set up. *E. coli* ribosomes and factor mix contributed 1.5 and 1 mM Mg^{2+}, respectively, for a total background of 2.5 mM Mg^{2+}. Data presented in Figure 7, 8, and 9 are from reactions prepared this way; b) Reactions prepared using washed *E. coli* ribosomes, which reduced the background Mg^{2+} to 1 mM. Data presented in Figure 10a were from reactions prepared this way; c) Reactions prepared using washed ribosomes and washed factor mix, which reduced background Mg^{2+} to 4-6 µM range. Data presented in Figure 10b are from reactions prepared this way.

2.3.4 Translation experimental conditions.

All reactions (30 µL total volume) were assembled and incubated in an anoxic chamber. Divalent cation salts ($MgCl_2$, $FeCl_2$, $MnCl_2$, $Zn(OAc)_2$, $CoCl_2$, $CuSO_4$) were added to 7 mM final concentration, with the exception of $MgCl_2$ and $FeCl_2$, which were tested over a range of concentrations (1, 3, 4, 5, 6, 7, 8, 9, and 11 mM; **Figure 3**). Solutions were clear, with no indication of metal precipitate, suggesting that reduced M^{2+} were the primary chemical species. All experiments were assembled in the following order: dihydrofolate reductase (DHFR) mRNA (~5 µg per 30 µL reaction), factor mix, ribosomes, amino acids, tRNA, nuclease-free H_2O, reaction buffer. Changing the order of reactant addition did not affect translational activity. Reactions were run in triplicate on a 37°C heat block for up to 120 minutes. Reactions were quenched on ice and stored on ice until they were assayed for protein synthesis.

2.3.5 mRNA template.

A plasmid containing the gene encoding dihydrofolate reductase (DHFR) from *E. coli* was provided as a gift from New England Biolabs. The DHFR control plasmid was linearized using HindIII restriction enzyme, purified by phenol/chloroform extraction, precipitated in ethanol, and resuspended in nuclease-free water. Messenger RNA was generated using the HiScribe™ T7 High Yield RNA Synthesis Kit (New England Biolabs catalog # E2040S) and purified using the MEGAclear™ Transcription Clean-Up Kit (Thermo Fisher, Waltham MA, USA; catalog # AM1908).

2.3.6 Protein activity assay.

Protein synthesis was measured using a DHFR assay kit (Sigma-Aldrich product # CS0340), which measures the oxidation of NADPH (60 mM) to $NADP^+$ by dihydrofolic acid (51 μM). Assays were performed by adding 5 μL of protein synthesis reaction to 995 μL of 1x assay buffer. The NADPH absorbance peak at 340 nm (Abs_{340}) was measured in 15 s intervals over 2.5 min. The slope of the linear regression of Abs_{340} vs. time was used to determine protein activity (Abs_{340} min^{-1}). Different counter ions (Cl^-, CH_3COO^-, SO_4^{2-}) had no effect on protein synthesis from mRNA. To our knowledge, no dependence on, nor inhibitory effect of Mg^{2+} or Fe^{2+} exists for DHFR. We confirmed this by varying the metal concentrations in our assay reaction, which had no effect on DHFR activity.

2.3.7 Ribosome metal content.

In order to measure the Fe and Mn content of ribosomes, 300 μL reactions were prepared with *E. coli* ribosomes (New England Biolabs catalog # P0763S), 7 mM $FeCl_2$ or 7 mM $MnCl_2$, and reaction buffer. Blank samples without ribosomes were prepared with 7 mM $FeCl_2$ or 7 mM $MnCl_2$, and reaction buffer. All mixtures were incubated at 37°C for 2 hours. After incubation, samples were transferred to Vivaspin 500 centrifugal concentrators (Vivaproducts, Littleton, MA; catalog # VS0141) and spun at 15,000 x g until minimum retentate volume (~5 μL) was achieved. Retentate was transferred to a 1.5 mL microcentrifuge tube and suspended in 100-200 μL of 10 mM HEPES-OH (pH 7.3, 50 mM NaCl). Samples were spiked with 1 ppm Ga concentration standard, and 2 μL of each sample was dried onto siliconized quartz discs. Metal analysis was performed by total reflection x-ray fluorescence (TRXF) spectroscopy (S2 Picofox TRXF spectrometer; Bruker, Billerica, MA). Samples were run at 50 kV for 2000 s each. TRXF spectra were

used to calculate the concentration of Fe or Mn in mg L^{-1}. Blank values were subtracted from ribosome samples and these corrected concentrations were converted to mM. The final ribosomal concentration (3 μM) was based on our dilution of New England Biolabs ribosomes supplied at 13.3 μM using RNA absorbance at 260 nm ($1A_{260}$ = 60 μg mL^{-1}). Values were reported as moles of Fe or Mn per mole ribosome ± standard error of the mean of triplicate experiments.

2.3.8 Quantum mechanical calculations.

The atomic coordinates of a Mg^{2+}-rRNA clamp were initially extracted from the X-ray structure of the *Haloarcula marismortui* LSU (PDB 1JJ2) (77). The free 5′ and 3′ termini of the phosphate groups were capped with methyl groups in lieu of the remainder of the RNA polymer, and hydrogen atoms were added, where appropriate (**Figure 4**). The binding of hexahydrated metal ions (M^{2+}) to an rRNA clamp fragment ($rRNAcl^{2-}$) was described by the following reaction:

$$rRNAcl^{2-} + M^{2+}(H_2O)_6 \rightarrow rRNAcl^{2-}\text{-}M^{2+}\cdot(H_2O)_4 \text{ complex} + 2H_2O,$$

where M^{2+} = (Mg^{2+}, Fe^{2+}, Mn^{2+})

The reactants and products of this reaction were fully optimized using the density functional theory (DFT) with the hybrid B3LYP functional (78, 79), at the 6–311++G(d,p) basis set as implemented in Gaussian 09 (80). The Fe^{2+}-rRNA and Mn^{2+}-rRNA clamps as well as their water hexahydrates were optimized at the unrestricted UB3LYP/6–31G(d,p) level of theory with spin =2, multiplicity=5 for Fe and spin=2.5, multiplicity=6. Single point energies for these complexes were further obtained at the UB3LYP/6–311++G(d,p)

level of theory using SCF options DIIS, NOVARACC, VTL, MaxCyc=1000. Natural Bond Order (NBO) (81) and NBO charge calculations were performed on the optimized complexes at the (U)B3LYP/6–31G(d,p) level of theory using the GAMESS package (82) and NBO 5.0 routine.

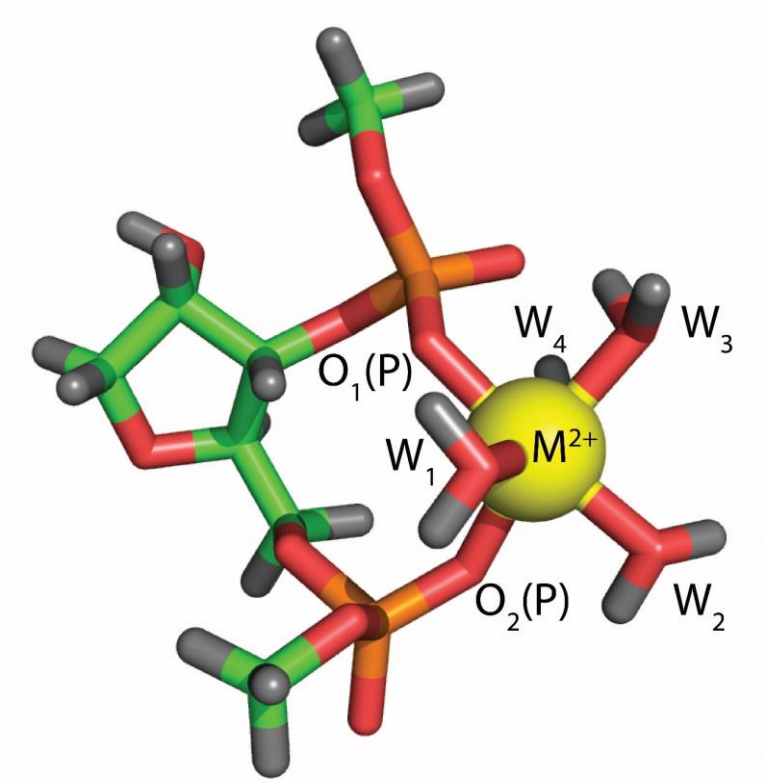

Figure 4. The $rRNA^{2-}$–M^{2+}•$(H_2O)_4$ complex ("M^{2+}-rRNA clamp") used for quantum mechanical calculations. The base has been replaced by a hydrogen atom and the chain is terminated with methyl groups. Abbreviations: M^{2+}: metal ion (Mg^{2+}, Fe^{2+}, or Mn^{2+}); W: water (H_2O); O1 and O2: oxygen atoms from phosphate; P: phosphate (PO_4^{3-}).

2.4 Results

2.4.1 Fe^{2+} and Mn^{2+} fold LSU rRNA to a near-native state.

To test whether Fe^{2+} or Mn^{2+} can substitute for Mg^{2+} in folding rRNA to a native-like state, we compared folding of LSU rRNA of the bacterial ribosome in the presence of Mg^{2+}, Fe^{2+}, or Mn^{2+} by SHAPE. SHAPE provides quantitative, nucleotide-resolution information about RNA flexibility, base pairing, and 3D structure, and has previously been used to monitor the influence of cations, small molecules, or proteins on RNA structure (57, 73, 74, 83-85). We previously used SHAPE to show that the LSU rRNA adopts a near-native state in the presence of Mg^{2+}, with the core inter-domain architecture of the assembled ribosome and residues positioned for interactions with rProteins (72). Here, SHAPE experiments were performed in an anoxic chamber to maintain the oxidation state of the metals and to prevent Fenton cleavage. The minimum concentration required to fully fold rRNA (10 mM Mg^{2+}, 2.5 mM Fe^{2+}, or 2.5 mM Mn^{2+}) was used for all SHAPE experiments.

Addition of Mg^{2+}, Fe^{2+}, or Mn^{2+} induced widespread structural changes in the LSU rRNA in the presence of Na^{+}, as reflected in SHAPE profiles (see **Experimental Methods**) and displayed as 'heat maps' on the LSU rRNA secondary structure (**Figure 5, 6**). Among the nucleotides forming the PTC, similar SHAPE profiles were obtained in the presence of Mg^{2+}, Fe^{2+}, or Mn^{2+} (**Figure 5**). The ΔFe^{2+} and ΔMg^{2+} heat maps obtained for the entire 23S rRNA are nearly identical in most regions (**Figure 6d**, **6e)**. As expected for conversion of secondary structure to fully folded tertiary structure, helices tended to be invariant,

whereas loops and bulges were impacted by addition of Mg^{2+}, Fe^{2+}, or Mn^{2+}. For the 23S rRNA, 86% of nucleotides (43/50) that exhibited a significant response (>0.3 SHAPE units) to Mg^{2+} also exhibited a similar trend with Fe^{2+}. The greatest discrepancy between Fe^{2+} and Mg^{2+} was observed in the L11 binding domain (**Figure 6d, 6e**).

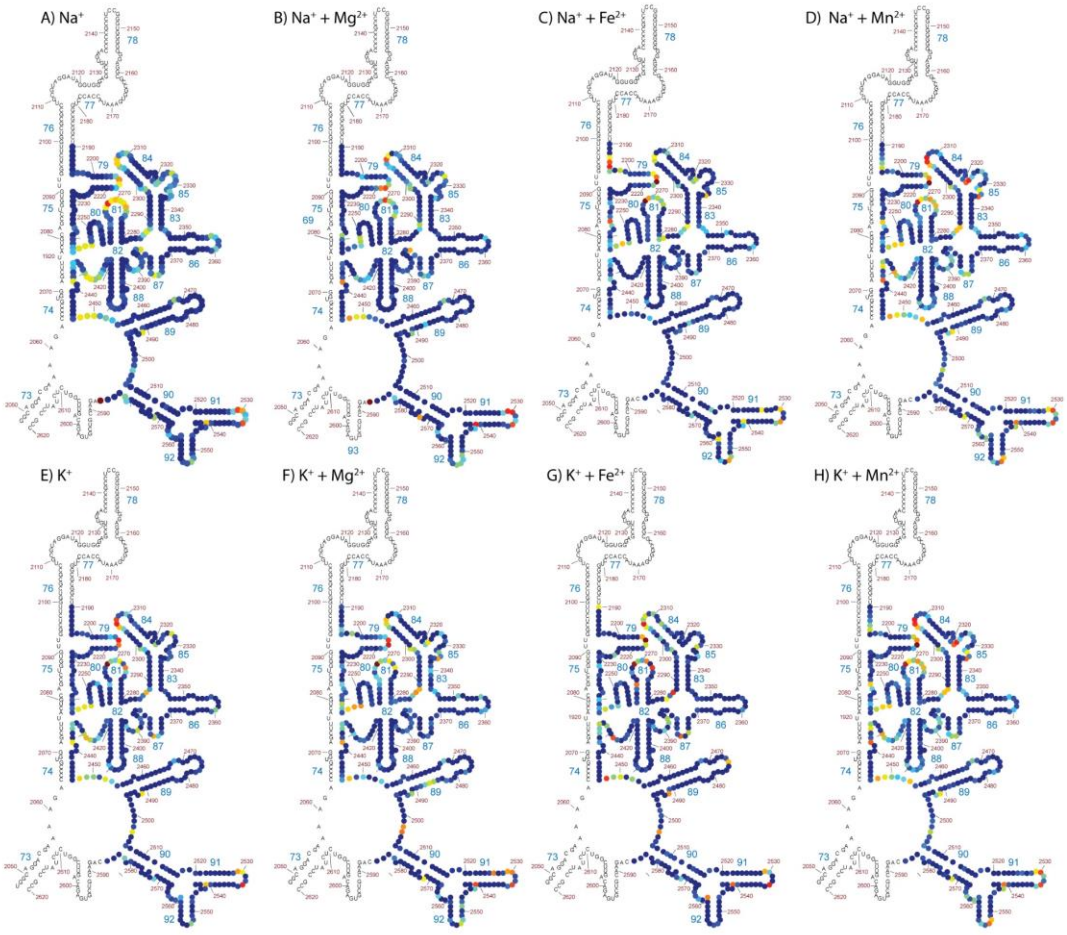

Figure 5. SHAPE data mapped onto the PTC region of the *T. thermophilus* ribosome, obtained in the presence of A) Na^+ alone, B) Na^+ plus Mg^{2+}, C) Na^+ plus Fe^{2+}, D) Na^+ plus Mn^{2+}, E) K^+ alone, F) K^+ plus Mg^{2+}, G) K^+ plus Fe^{2+}, H) K^+ plus Mn^{2+}. K^+ or Na^+ is 250 mM. Mg^{2+} is 10 mM. Fe^{2+} or Mn^{2+} is 2.5 mM. Red indicates high reactivity and blue indicates low reactivity as shown in Figure 6.

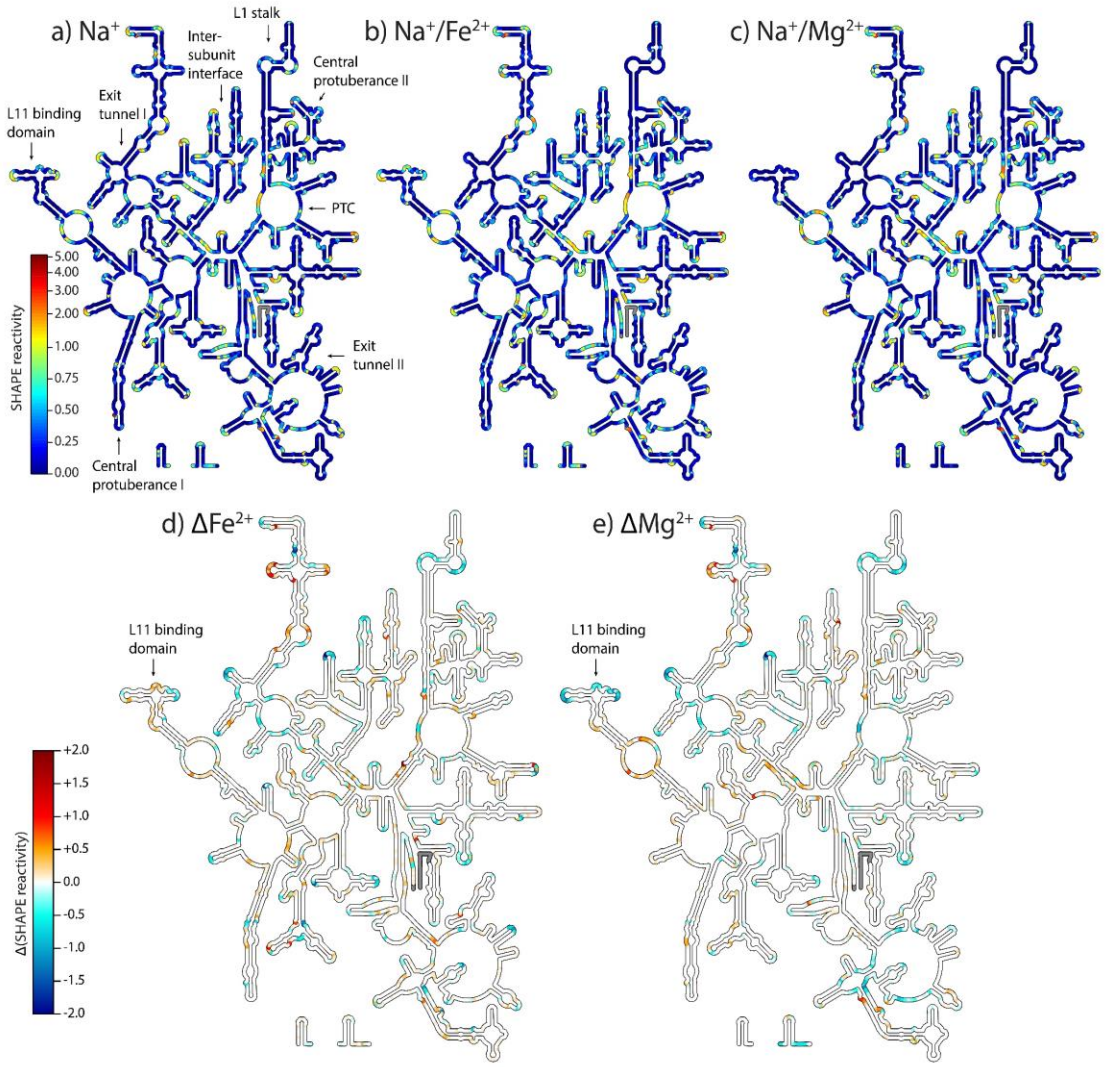

Figure 6. SHAPE reactivities mapped onto the *Thermus thermophilus* LSU rRNA secondary structure in a) Na^+, b) Na^+/Fe^{2+}, or c) Na^+/Mg^{2+}. Key functional elements are labeled in panel a, and the scale in panel (a) applies to panels b and c. d) Fe^{2+}-induced changes (ΔFe^{2+}) in SHAPE reactivity calculated by subtracting Na^+ data from Na^+/Fe^{2+} data for each nucleotide, and e) Mg^{2+}-induced changes (ΔMg^{2+}) in SHAPE reactivity calculated by subtracting Na^+ data from Na^+/Mg^{2+} data for each nucleotide. The scale shown for panel d also applies to panel e. Positive values indicate increased SHAPE reactivity in presence of the divalent cation, while negative values denote decreased reactivity. Regions where data are not available (5' and 3' ends) are grey. These figures were generated with the program RiboVision (71). The L11 binding region, where the greatest discrepancy between Fe^{2+} and Mg^{2+} is observed, is indicated with an arrow.

2.4.2 Fe^{2+} and Mn^{2+} mediate translation.

Translation reactions were performed in an anoxic chamber in the presence of various cations and cation concentrations. Production of the protein dihydrofolate reductase (DHFR) from its mRNA was used to monitor translational activity. Protein synthesis was assayed by measuring the rate of NADPH oxidation by DHFR. These reactions were conducted in a small background of 2.5 mM Mg^{2+} (**Figure 3**). This background is below the requirement to support translation, consistent with previous findings that a minimum of ~5 mM Mg^{2+} is needed for assembly of mRNA onto the SSU (56, 86). As a control, we recapitulated the previously established Mg^{2+} dependence of the translation system, and then repeated the assay with Fe^{2+}.

Activity of the translation system with variation in [Fe^{2+}] closely tracks activity with variation in [Mg^{2+}] (**Figure 7**). Below 7.5 mM, total M^{2+} concentration, minimal translation occurred with either Fe^{2+} or Mg^{2+}, as expected (87). Activity peaked at 9.5 mM for both cations and decreased modestly beyond the optimum. At a given M^{2+} concentration, Fe^{2+} supported around 50-80% of activity with Mg^{2+} (**Figure 7**). This result was observed with translation reactions run for 15, 30, 45, 60, 90 and 120 min at the optimal M^{2+} concentrations (**Figure 8**). Mn^{2+} also supported similar translation activity to Fe^{2+} at M^{2+} concentrations (**Figure 9**). Along with Mg^{2+}, Fe^{2+}, and Mn^{2+} we investigated whether other M^{2+} could support translation. No translation activity was detected with Co^{2+}, Cu^{2+}, or Zn^{2+} (**Figure 9**).

To test whether alternative M^{2+} could completely replace Mg^{2+} in translation, we decreased the background Mg^{2+} from 2.5 to 1 mM by thoroughly washing the ribosomes

prior to translation reactions with 7-11 mM Fe^{2+} or Mn^{2+} (**Figure 3b**). With 1 mM background Mg^{2+}, Fe^{2+} supported 12-23% of the activity with Mg^{2+} over the concentrations tested, while Mn^{2+} supported 43-50% activity relative to Mg^{2+} (**Figure 10a**). Washing the factor mix allowed us to decrease the background Mg^{2+} in translation reactions to ~4-6 µM (**Figure 3c**). At this level, minimal protein production was observed with Fe^{2+}, while Mn^{2+} supported 29-38% of the activity measured with Mg^{2+} (**Figure 10b**).

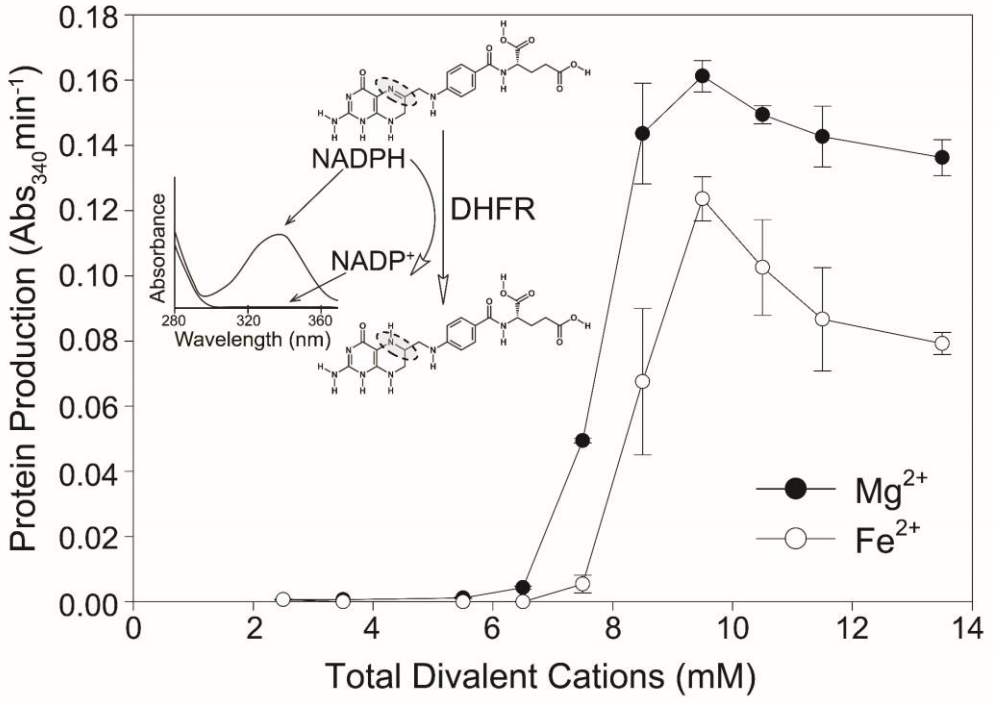

Figure 7. Mg^{2+} and Fe^{2+} stimulate translational activity over a range of concentrations. The activity of the translation product (dihydrofolate reductase, which catalyzes the oxidation of NADPH, with a maximum absorbance at 340 nm) was used as a proxy for protein production. Translation reactions were run for 120 minutes. All translation reactions contained 2.5 mM background Mg^{2+}, to which varying amounts of additional Mg^{2+} or Fe^{2+} were added. The error bars for triplicate experiments (n=3) are plotted as the standard error of the mean.

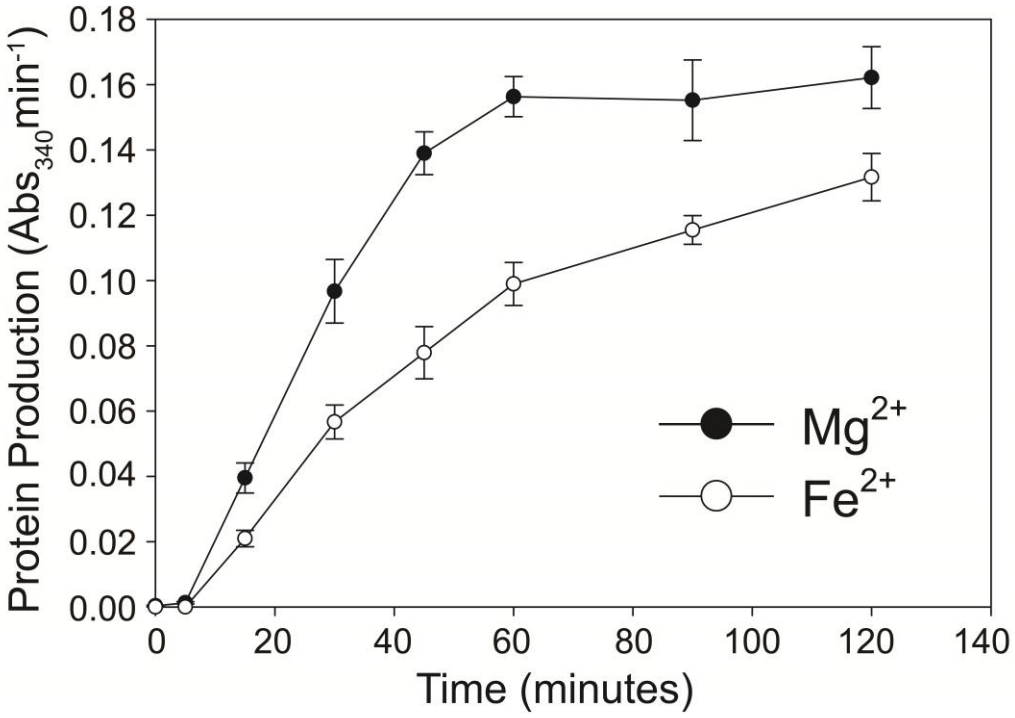

Figure 8. Fe^{2+} consistently supports 50-80% of the translational activity as Mg^{2+} when the translation experiments are run for 15-120 minutes. The activity of the translation product (dihydrofolate reductase, which catalyzes the oxidation of NADPH, with a maximum absorbance at 340 nm) was used as a proxy for protein production. All translation reactions contained 2.5 mM background Mg^{2+}, to which 7 mM additional Mg^{2+} or Fe^{2+} were added, totaling to 9.5 mM divalent cation. The error bars for triplicate experiments (n=3) are plotted as the standard error of the mean.

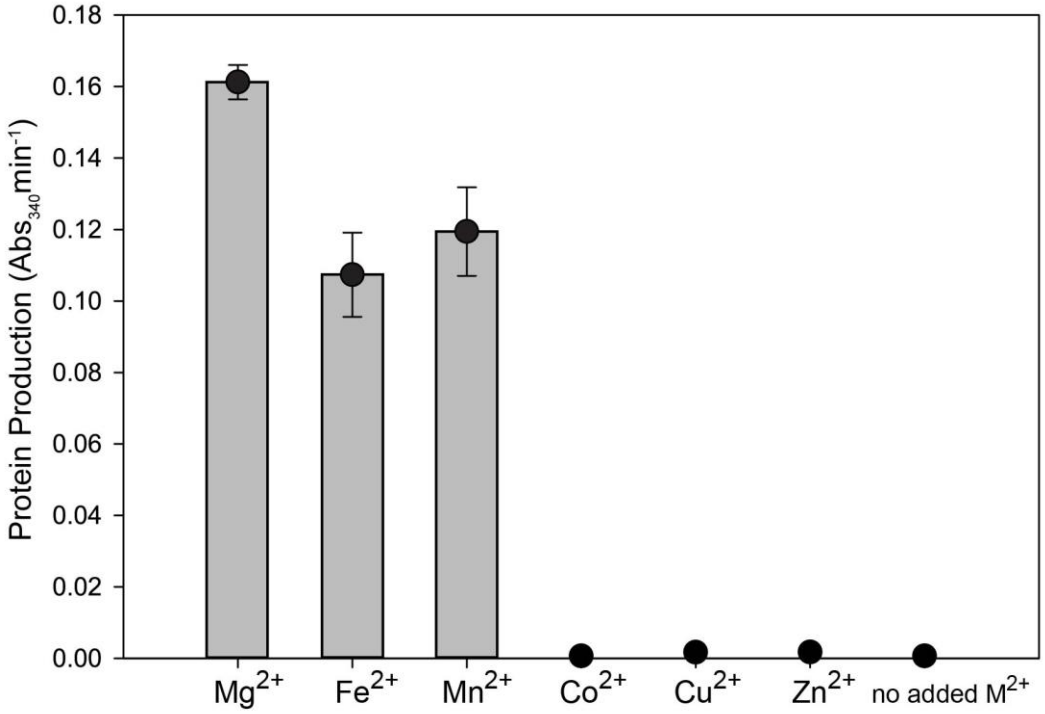

Figure 9. *In vitro* translation of active protein in the presence of different M^{2+}. The activity of the translation product (dihydrofolate reductase, which catalyzes the oxidation of NADPH, with a maximum absorbance at 340 nm) was used as a proxy for protein production. Reactions received 7 mM M^{2+}, in addition to 2.5 mM background Mg^{2+}, summing to 9.5 mM total M^{2+}. Translation reactions were run for 120 minutes. The error bars for triplicate experiments (n=3) are plotted as the standard error of the mean.

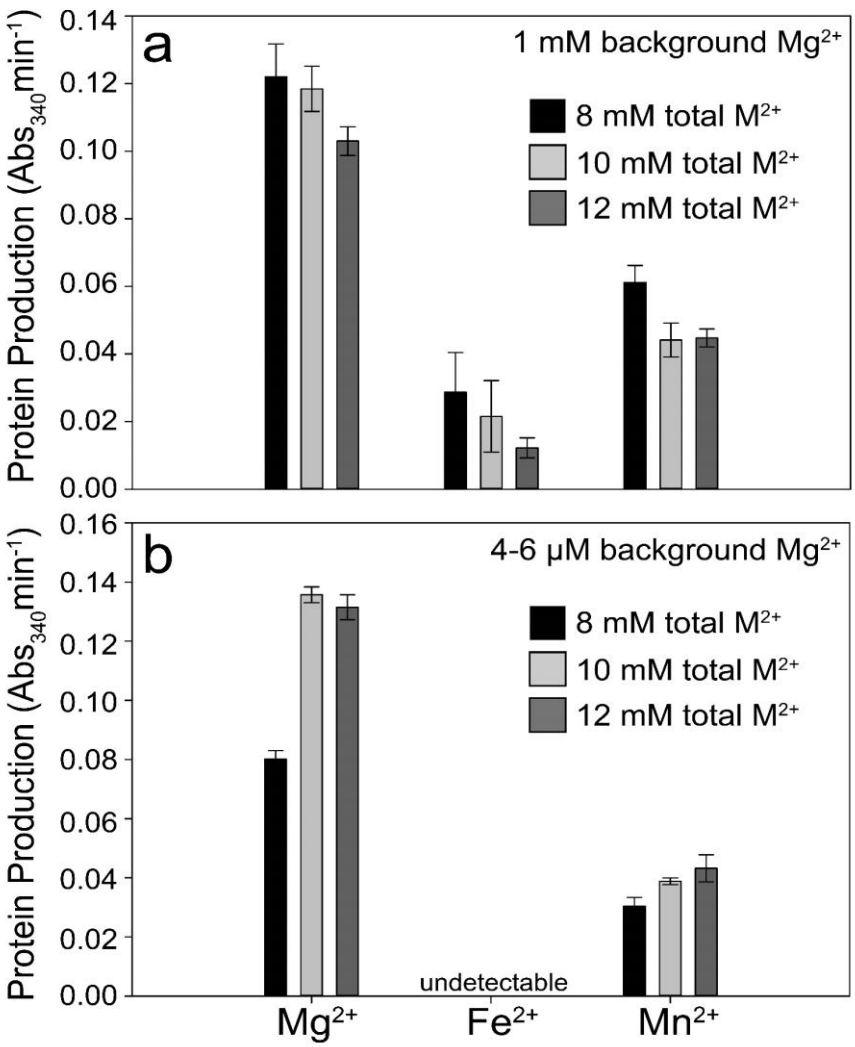

Figure 10. Mn^{2+} can support translation after removal of background Mg^{2+}. a) Reactions prepared with washed *E. coli* ribosomes, reducing the background Mg^{2+} to 1 mM, to which 7, 9, or 11 mM additional Mg^{2+}, Fe^{2+}, or Mn^{2+} were added, totaling 8, 10, or 12 mM M^{2+}. b) Reactions prepared using washed *E. coli* ribosomes and washed factor mix, which reduced the background Mg^{2+} to the low µM level, to which 8, 10, or 12 mM additional, Mg^{2+}, Fe^{2+}, or Mn^{2+} were added. The activity of the translation product (dihydrofolate reductase, which catalyzes the oxidation of NADPH, with a maximum absorbance at 340 nm) was used as a proxy for protein production. The error bars for triplicate experiments (n=3) are plotted as the standard error of the mean.

2.4.3 Iron and Mn associate extensively with the ribosome.

To experimentally confirm that Fe and Mn associate with the assembled ribosome, we analyzed the total Fe or Mn content of ribosomes after incubation in anoxic reaction buffer containing 7 mM Fe^{2+} or 7 mM Mn^{2+}. Under the conditions of our translation reactions, 584 ± 9 Fe atoms or 507 ± 28 Mn atoms associate with each ribosome.

Finally, we computationally investigated whether Mg^{2+}, Fe^{2+}, and Mn^{2+} might be interchangeable during translation using quantum mechanical characterization of M^{2+}-rRNA clamps (**Figure 2a and 4**) which are abundant in the ribosome (40, 41). The geometries of Mg^{2+}-rRNA, Fe^{2+}-rRNA and Mn^{2+}-rRNA clamps, are nearly identical (**Table 2-4**). However, due to the accessibility of their d-orbitals, more charge is transferred to Fe^{2+} or Mn^{2+} (**Table 3**) than to Mg^{2+} (**Table 3**). The effect of the modestly greater radius of Mn^{2+} (**Table 2**) is offset by d-orbital charge transfer **(Table 3**), leading to elevated stability of Fe^{2+}-rRNA clamp over the Mn^{2+}-rRNA clamp (**Table 4**)**.**

Table 2. M-O distance (Å) in diphosphate-sugar-hydrated metal complexes ("M^{2+}-rRNA clamps", shown in Figure 2a and Figure 4) obtained from calculations performed at the B3LYP/6-311g**(d,p)//B3LYP/6-311g**(d,p) level of theory. Abbreviations: M: metal ion (Mg^{2+}, Fe^{2+}, or Mn^{2+}); w: water (H_2O); O: oxygen; P: phosphate (PO_4^{3-}).

Complex	**M-O Distance, [Å]**					
	M-O1 (P)	M-O2 (P)	M-O3 (w1)	M-O4 (w2)	M-O3 (w3)	M-O4 (w4)
$rRNAcl^{2-}$-$Mg(H_2O)_4^{2+}$	2.0040	2.0046	2.1392	2.1613	2.1404	2.1819
$rRNAcl^{2-}$-$Mn(H_2O)_4^{2+}$	2.1369	2.0832	2.2524	2.3004	2.2644	2.3100
$rRNAcl^{2-}$-$Fe(H_2O)_4^{2+}$	2.0267	2.0771	2.0464	2.0274	2.2650	2.2458

Table 3. Natural Bond Order (NBO) charges calculated for diphosphate-sugar-hydrated metal complexes ("M^{2+}-rRNA clamps", shown in Figure 2a and Figure 4) at the HF/6-31d(d,p) level of theory.

Complex	NBO Charges		
	Backbone	Cation	Waters
$rRNAcl^{2-}$-$Mg(H_2O)_4^{2+}$	-1.82959	1.77630	0.05329
$rRNAcl^{2-}$-$Mn(H_2O)_4^{2+}$	-1.81532	1.76526	0.05006
$rRNAcl^{2-}$-$Fe(H_2O)_4^{2+}$	-1.77911	1.69864	0.08047

Table 4. Interaction energies for diphosphate-sugar-hydrated metal complexes ("M^{2+}-rRNA clamps", shown in Figure 2a and Figure 4) calculated in the gas phase and water calculated at the B3LYP/6-311g**(d,p)//B3LYP/6-311g**(d,p) and B3LYP/6-311g**(d,p)//B3LYP/6-311g**(d,p)[cpcm].

Complex	**Interaction energy^{gas}, kcal mol^{-1}**	**Interaction energy^{cpcm}, kcal mol^{-1}**
$rRNAcl^{2-}$-$Mg(H_2O)_4^{2+}$	-387.5	-31.9
$rRNAcl^{2-}$-$Mn(H_2O)_4^{2+}$	-385.1	-35.7
$rRNAcl^{2-}$-$Fe(H_2O)_4^{2+}$	-391.3	-43.7

2.5 Discussion

2.5.1 Fe^{2+} and Mn^{2+} can replace Mg^{2+} as the primary ribosomal cofactor.

In this study, we successfully replaced ribosomal Mg^{2+} with Fe^{2+} or Mn^{2+} under conditions mimicking the anoxic Archean Earth. Previously, the only M^{2+} known to mediate rRNA folding and function was Mg^{2+}. We found that isolated rRNA folds to essentially the same global state (88, 89) with Mg^{2+}, Fe^{2+}, or Mn^{2+} under anoxia. This study revealed that Fe^{2+} or Mn^{2+} can serve as the dominant M^{2+}during translation. Mg^{2+} at 2.5 mM was insufficient to mediate protein synthesis; 5 mM additional Mg^{2+}, Fe^{2+}, or Mn^{2+} restored translational activity. These findings suggest that functional substitutions of Mn^{2+} or Fe^{2+} for Mg^{2+} can occur in large ribozymes, similar to previous reports for protein enzymes and small ribozymes (52, 53, 90-92). Near-complete removal of Mg^{2+} prevented Fe^{2+}-mediated translation and partially inhibited Mn^{2+}-mediated translation, suggesting that Mg^{2+} is optimal for some specific roles in the translation system. Regardless, the general effectiveness of Mn^{2+} or Fe^{2+} for Mg^{2+} substitutions in the translation system is astounding considering the enormous number of M^{2+} associated with a given ribosome, and the broad scope of their structural and functional roles (38, 39) (**Table 1, Figure 2**).

The observation that >500 Fe or Mn ions can associate with a bacterial ribosome is consistent with the number of Mg^{2+} ions observed by X-ray diffraction (100-1000 Mg^{2+} per ribosome (93)), and supports a model in which Fe^{2+} or Mn^{2+} has replaced Mg^{2+} as the dominant M^{2+} in our experiments. The high capacity of ribosomes for Fe^{2+} and Mn^{2+} reflects all rRNA-associated M^{2+}, including condensed, glassy and chelated M^{2+} (94), and in addition, we presume that Fe^{2+} or Mn^{2+} can associate with a variety of rProteins,

including those previously shown to bind Zn^{2+} (e.g. S2, S15, S16, S17, L2, L13, L31, L36 in *E. coli*) (95).

The differences in protein production observed among the three M^{2+} likely arise from a variety of evolutionary and physiological factors. For instance, *E. coli* ribosomes may be evolutionarily adapted to Mg^{2+} instead of Fe^{2+} or Mn^{2+}. The difference in translational activity between Mn^{2+} and Fe^{2+}, particularly when background Mg^{2+} was removed, suggests that Mn^{2+} is more viable than Fe^{2+} upon full substitution. Mn^{2+}/Mg^{2+} interchangeability may depend on relative stabilities of Mn^{2+} and Mg^{2+} in M^{2+}-rRNA clamps (**Figure 4**). Besides the ribosome, our translation reactions utilize many accessory proteins such as elongation factors and aminoacyl-tRNA synthetases that also have M^{2+} requirements. Decreased activity of any of one these systems with Mn^{2+} and Fe^{2+} would cause a pinch point in an otherwise fully functional translation system. Indeed, the relative activity of myokinase and arginine t-RNA synthetase are both lower with Mn^{2+} or Fe^{2+} than with Mg^{2+} (67, 96).

2.5.2 Physiological relevance of these results.

While intracellular Mg^{2+} is around 10^{-3} M (97), specific physiological or environmental conditions can significantly elevate intracellular Fe^{2+} and Mn^{2+}. Under oxidative stress, some microbes accumulate excess Mn^{2+}. For example, radiation-tolerant *Deinococcus radiodurans* contains ~10 times higher Mn^{2+} than *E. coli* (~10^{-5} M Mn^{2+} (98, 99)). In the absence of O_2, *E. coli* contains ~10 times higher labile Fe^{2+} (~10^{-4} M) than in the presence of O_2 (~10^{-5} M (100)). Thus, it is possible that the absence of Fe^{2+} and Mn^{2+} in experimentally determined ribosomal structures is reflective of culturing, purification,

or crystallization conditions (high O_2, high Mg^{2+}, low Fe^{2+}, low Mn^{2+}), and that other cations may also be present under diverse physiological conditions.

2.6 Conclusions

We have shown that the translation system functions with mixtures of M^{2+}, which are variable during long-term evolutionary history and during short term changes in bioavailability and oxidative stress. When combined with previous results that DNA replication and transcription can be facilitated by Fe^{2+} and Mn^{2+} (29, 46-48, 51-53, 90-92), our findings that both Fe^{2+} and Mn^{2+} can mediate rRNA folding and translation of active protein has revealed that these "prebiotic" M^{2+} can facilitate the entire central dogma of molecular biology (DNA→RNA→protein). These findings raise important questions about evolutionary and physiological roles for Fe^{2+} and Mn^{2+} in ancient and extant biological systems. Were Mg^{2+}, Fe^{2+}, and Mn^{2+} collaborators as cofactors on the ancient Earth, when Fe^{2+} and Mn^{2+} were more abundant (19, 21, 101-103), and Mg^{2+} was less abundant (21), than today? What was the role of Fe^{2+} and Mn^{2+} in the origin and early evolution of the translational system? Finally, what are the implications for ribosome-bound Fe^{2+} in oxidative damage and disease (104, 105)?

CHAPTER 3. FUNCTIONAL IRON-CONTAINING RIBOSOMES UNDER LOW OXYGEN, HIGH IRON CONDITIONS

Work described in this chapter is currently in preparation for submission to a peer reviewed journal. I performed the majority of experiments. Mass spectrometry experimentation and data analysis was performed by S. Suttapitugsakul and R. Wu. The manuscript was written with contributions from all coauthors.

3.1 Abstract

The ribosome is the most ancient and evolutionarily conserved macromolecular assembly in biology. The core structure of the ribosome has not changed since the Archean, when O_2 was scarce and Fe^{2+} was plentiful. Previous characterizations of ribosome structure and function have commonly used bacteria grown with high O_2 and low Fe^{2+} like modern surface Earth conditions. These studies have implicated Mg^{2+} as the primary mediator of ribosomal structure and function. Yet many bacterial pathogens proliferate in anoxic ecosystems more reminiscent of the anoxic Archean. Here we show (i) ribosomes purified from cells grown under low O_2, high Fe^{2+} conditions contain significantly more Fe associated with them, and (ii) that this Fe is likely strongly associated with the ribosome and is likely bound to the rRNA in conserved, highly coordinated metal binding sites. These results suggest that modern bacteria retain the ability to use Fe in ribosomal structure and function when they are exposed to conditions reminiscent of the ancient Earth and highlight the importance of Fe^{2+} in ancestral biology. Our results may additionally inform drug design by optimizing antibiotic binding to ribosomes in modern anaerobic pathogens.

3.2 Introduction

The ribosome is responsible for the synthesis of all coded proteins in life on Earth. The central importance of the ribosome to biology is underscored by its conservation. The core structure of the ribosome is universal to all living systems and has been essentially invariant since the last universal common ancestor (106-108). Ribosomes can therefore be interrogated as molecular fossils (109). Life, and by extension the ribosome, originated and first proliferated on our planet when Fe^{2+} was abundant and soluble (110-114). Life evolved for over a billion years in anoxic and Fe^{2+}-rich conditions, until the GOE precipitated Fe and introduced Fe-mediated oxidative damage (3).

The structure and function of the ribosome is linked to the oxidative potential of the Earth via intimate relationships with M^{2+}. Divalent cations are essential for function of the ribosome and of many ancillary components of the translational machinery (94). In extant aerobic systems, Mg^{2+} ions act as the dominant counterion to the ribosome. Mg^{2+} ions mediate folding of rRNA (38, 41, 72, 94), aid in the association of the LSU and SSU ribosomal subunits(42), stabilize the mRNA and tRNA within the ribosome (44), maintain reading frame during translation (43), and link rProteins to rRNA (45).

We have proposed a model in which early ribosomal folding and catalysis were mediated by Fe^{2+} instead of, or alongside Mg^{2+}, and that Fe^{2+} was a critical player in the origins and early evolution of the translation system. We previously reported that Fe^{2+} and Mg^{2+} induce common rRNA tertiary structures and that Fe^{2+} can replace Mg^{2+} as the dominant M^{2+} during translation (33, 72). Based on these results, we hypothesize that ribosomes in extant systems can assemble and function *in vivo* with Fe^{2+} instead of Mg^{2+}

under pre-GOE conditions. Here we tested this prediction by determining if ribosomes associate with Fe in *E. coli* cells grown in anoxia and high Fe. We found each ribosome produced in these pre-GOE conditions contains ~10 tightly bound Fe atoms, that are not exchangeable with Mg^{2+} in solution over several days. It seems likely that these Fe atoms are buried within the ribosome. These results represent the first report of Fe association with ribosomes *in vivo* and extend our knowledge of the bioinorganic chemistry of life's origin. These findings may also offer possibilities for better understanding the physiology of pathogens or other organisms that encounter transient or permanent anaerobiosis.

3.3 Experimental Methods

3.3.1 Cell culture and harvesting.

Culturing media consisted of LB broth (10 g L^{-1} NaCl, 10 g L^{-1} tryptone, 5 g L^{-1} yeast extract) amended with 4 mM Tricine, 50 mM sodium fumarate, and 80 mM 3-(N-morpholino)propanesulfonic acid (MOPS; pH 7.8). Fifty-milliliter cultures containing all of these ingredients plus 0.25% glycerol were inoculated from glycerol stocks of *Escherichia coli* MRE600 cells and shaken overnight at 37ºC with or without O_2 and with either 1 mM $FeCl_2$ or ambient Fe^{2+} (6-9 μM, measured by ferrozine assay(115)). Two-mL of each overnight culture was used to inoculate 1 L cultures in the same conditions. These cultures were then orbitally shaken at 37ºC to OD_{600} 0.6-0.7. Aerobic cultures were grown in foil-covered Erlenmeyer flasks. Anaerobic, fumarate-respiring cultures were inoculated into stoppered glass bottles containing medium that had been degassed with N_2 for 1 hour to remove O_2. Cells were then harvested by centrifugation at 4,415 x g for 10 min, washed in 20 mL buffer containing 10 mM Tris pH 7.4, 30 mM NaCl, and 1 mM EDTA, and

pelleted at 10,000 x g for 10 min. Cell pellets were stored at -80°C until ribosome purification.

3.3.2 Ribosome purification.

The ribosome purification procedure was modified from Maguire et. al (116). All steps were performed in an anoxic chamber (97% Ar, 3% H_2 headspace) unless otherwise noted. Buffers varied in their metal cation content. Typical wash buffer contained 100 mM NH_4Cl, 0.5 mM EDTA, 3 mM β-mercaptoethanol, 20 mM Tris pH 7.5, 3 mM $MgCl_2$, and 22 mM NaCl. For "Fe purification" experiments, buffer was composed of 100 mM NH_4Cl, 0.5 mM EDTA, 3 mM β-mercaptoethanol, 20 mM Tris pH 7.5, 1 mM $FeCl_2$ and 28 mM NaCl. Sodium chloride concentrations were increased here to maintain ionic strength of buffer (.1315 M). Elution buffers contained the same composition as wash buffer except for NH_4Cl (300 mM). Frozen cell pellets were resuspended in ribosome wash buffer and lysed in a BeadBug microtube compact homogenizer using 0.5 mm diameter zirconium beads (Benchmark Scientific). Cell lysate was transferred into tightly sealed centrifuge bottles inside the anoxic chamber which were tightly sealed to prevent O_2 contamination. Cell debris was removed by centrifuging at 30,000 x g for 30 min at 4ºC; outside of the anoxic chamber. The soluble lysate was then transferred back into the chamber and loaded onto a column containing pre-equilibrated, cysteine-linked, SulfoLink™ Coupling Resin (Thermo Fisher Scientific). The resin was washed with 10 column volumes of wash buffer. Ribosomes were eluted into three 10 mL fraction with elution buffer. Eluted fractions were pooled into ultracentrifuge bottles inside the anoxic chamber which were tightly sealed to prevent O_2 contamination. Ribosomes were pelleted by centrifuging at 302,000 x g for 3 hr at 4ºC under vacuum in a Beckman Optima XPN-100 Ultracentrifuge using a Type 70

Ti rotor, outside of the anoxic chamber. Tubes containing ribosome pellets were brought back into the anoxic chamber and suspended in buffer containing 20 mM N-(2-hydroxyethyl)piperazine-N'-2-ethanesulfonic acid (HEPES; pH 7.6), 30 mM KCl, and 7 mM β-mercaptoethanol, heat sealed in mylar bags, and stored at -80ºC. Ribosome concentrations were calculated with a NanoDrop spectrophotometer assuming $1A_{260}$ = 60 µg ribosome mL^{-1} (conversion factor provided by New England Biolabs).

3.3.3 Ribosomal iron content.

Purified ribosomes were analyzed for Fe content by total reflection X-ray fluorescence spectroscopy (TRXF) as described in Bray and Lenz et al (33).

3.3.4 Ribosomal RNA purification and electrophoresis.

rRNA was isolated from purified ribosomes by phenol chloroform extraction. A one-tenth volume of sodium acetate pH 5.22 and an equal volume of 25:24:1 mixture of phenol:chloroform:isoamyl alcohol was added to purified ribosomes. The sample was vortexed and spun at 16,200 x g in a table top centrifuge for 5 min. The top aqueous layer was transferred to a new tube and extracted twice in pure chloroform using the same procedure. rRNA was then precipitated by adding 2 volumes of 100% ethanol, followed by incubation at -20ºC for 30 min. Precipitated rRNA was pelleted by centrifuging for 15 min. The pellet was washed with 70% ethanol and suspended in 0.1 mM EDTA. Ribosomal RNA concentrations were quantified with a NanoDrop spectrophotometer assuming $1A_{260}$ = 40 µg rRNA mL^{-1}. For rRNA electrophoresis, purified rRNA was normalized to 0.25 µg $µL^{-1}$ in Gel Loading Buffer II (Amicon), heated at 95ºC for 5 min, and then placed on ice

for 2 min. Samples were loaded onto a 1% Tris/borate/EDTA/agarose gel and run for 50 min at 120 V.

3.3.5 Ribosomal protein electrophoresis.

For SDS-PAGE, purified ribosomes were normalized to 3.33 mg mL^{-1} in 2X SDS-PAGE dye, heated at 95ºC for 5 min, and then incubated on ice for 2 min. Samples were loaded onto a 12% SDS acrylamide gel with a 4% stacking gel and run at 180 V for 60 minuntes.

3.3.6 In vitro translation.

Translation reactions were based on the methods of Bray and Lenz et al (33) with minor modifications. All 15 µL reactions contained 2.25 µL of purified ribosomes (9 µg µL-1) for a final concentration of 1.35 µg μL^{-1}, 0.1 mM amino acid mix, 0.2 mM tRNAs, ~0.2 µg μL^{-1} of dihydrofolate reductase mRNA, and 3 µL of factor mix (with RNA polymerase, and transcription/translation factors in 10 mM Mg^{2+}) from the PURExpress® Δ Ribosome Kit (New England Biolabs E3313S). The reaction buffer was based on Shimizu et al (76), with HEPES-OH instead of phosphate buffer to avoid precipitation of metal phosphates. Buffer consisted of 20 mM HEPES-OH (pH 7.3), 95 mM potassium glutamate, 5 mM NH_4Cl, 0.5 mM $CaCl_2$, 1 mM spermidine, 8 mM putrescine, 1 mM dithiothreitol (DTT), 2 mM adenosine triphosphate (ATP), 2 mM guanosine triphosphate (GTP), 1 mM uridine triphosphate (UTP), 1 mM cytidine triphosphate (CTP), 10 mM creatine phosphate (CP), and 53 µM 10-formyltetrahydrofolate. Divalent cation salts ($MgCl_2$ and $FeCl_2$) were added to 9 mM final

concentration. The reaction buffer was lyophilized and stored at -80°C until resuspension in anoxic nuclease-free water immediately before experiments in the anoxic chamber.

Reactions (15 µL) were assembled in the anoxic chamber and run at 37°C in a heat block for 120 min. Reactions were quenched on ice and stored on ice until they were assayed for extent of protein synthesis. Protein synthesis was measured using a DHFR assay kit (Sigma-Aldrich product # CS0340), which measures the oxidation of NADPH (60 mM) to $NADP^+$ by dihydrofolic acid (51 µM). Assays were performed by adding 5 µL of protein synthesis reaction to 995 µL of 1X assay buffer. The NADPH absorbance peak at 340 nm (Abs_{340}) was measured in 15 s intervals over 2.5 min. The slope of the linear regression of Abs_{340} vs. time was used to determine protein activity (Abs_{340} min^{-1}).

3.3.7 Protein identification by LC-MS/MS.

Proteins were reduced with β-mercaptoethanol, and then alkylated with 14 mM iodoacetamide for 30 minutes at room temperature in the dark. The alkylation was quenched with 5 mM dithiothreitol for 15 minutes at room temperature in the dark. The proteins were precipitated by the methanol/chloroform precipitation method. Dried protein pellets were digested with sequencing-grade modified trypsin in a buffer containing 5% acetonitrile, 1.6 M urea, and 50 mM HEPES at 37 ^oC with shaking overnight. The digestion was quenched with 1% formic acid. Peptides were purified by Stage-Tip and dried prior to LC-MS/MS analysis (117).

The peptides were dissolved in 5% acetonitrile and 4% formic acid solution, and loaded onto a C18-packed microcapillary column (Magic C18AQ, 3 µm, 200 Å, 75 µm x 16 cm, Michrom Bioresources) by a Dionex WPS-3000TPL RS autosampler

(Thermostatted Pulled Loop Rapid Separation Nano/Capillary Autosampler). Peptides were separated by a Dionex UltiMate 3000 UHPLC system (Thermo Scientific) using a 112-minute gradient of 4-17% acetonitrile containing 0.125% formic acid. The LC is coupled to an LTQ Orbitrap Elite Hybrid Mass Spectrometer (Thermo Scientific) with Xcalibur software (version 3.0.63). MS analysis was performed with a data-dependent Top15 method; for each cycle, a full MS scan with 60,000 resolution and 1 million automatic gain control (AGC) target in the Orbitrap was followed by up to 15 MS/MS scans in the Orbitrap for the most intense ions. Selected ions were excluded from further sequencing for 90 seconds. Ions with single or unassigned charge were not sequenced. Maximum ion accumulation time was 1,000 ms for each full MS scan, and 50 ms for each MS/MS scan.

Raw MS files were analyzed by MaxQuant (version 1.6.2.3) (118). MS spectra were searched against the *E. coli* database downloaded from UniProt containing common contaminants using the integrated Andromeda search engine (119). Due to the unavailability of the proteome database for *E. coli* strain MRE-600, the database for strain K12 was used. It has been shown that the two strains have nearly identical ribosomal proteins (120). All samples were searched separately and set as individual experiments. All default parameters in MaxQuant were used, except the maximum number of missed cleavages of 3. Label-free quantification was enabled with the LFQ minimum ratio count of 1. The match-between-runs option was also enabled. The false discovery rates (FDR) were kept at 0.01 at the peptide and protein levels.

The results were processed using the Perseus software (121). In the final dataset, the reverse hits and contaminants were removed. The LFQ intensity of each protein from the

proteinGroups table is extracted and reported. For the volcano plots showing differential regulation of proteins, the ratios used were from the LFQ intensities of samples from each of the three experiments. The cutoff for differential expression was set at 2-fold. The p-values were calculated using T-test with the threshold p-value of 0.05 for significant regulation.

3.4 Results

Ribosomes were purified from *E. coli* grown in four conditions: oxic or anoxic, with high (1 mM) or low (6-9 μM) Fe^{2+}. First, we purified ribosomes in 3 mM $MgCl_2$ to determine the tightly-bound Fe content. All purified ribosomes contained intact 23S, 16S, and 5S rRNAs (**Figure 11a**) and a protein banding pattern indicating of a full suite of rProteins (**Figure 12a**). Ribosomes from cells grown in pre-GOE (anoxic, high Fe^{2+}) conditions contained 9.1 ± 2.2 mol Fe mol^{-1} ribosome, compared to 1.6 ± 0.8 mol Fe mol^{-1} ribosome from cells grown in oxic conditions with 1 mM $FeCl_2$ (**Figure 13**). Ribosomes purified from cells grown without added $FeCl_2$ under anoxic and oxic conditions contained 1.6 ± 0.9 mol Fe mol^{-1} and 1.3 ± 0.3 mol Fe mol^{-1}, respectively.

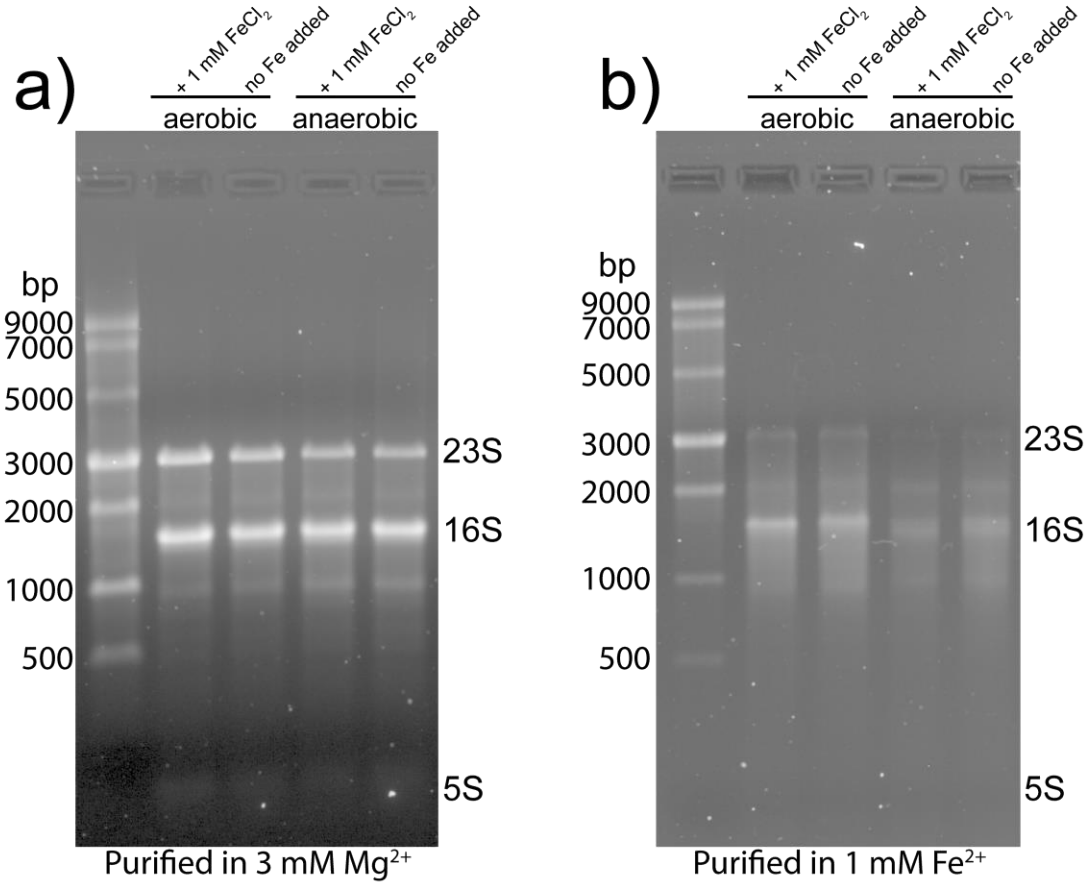

Figure 11. 1% Tris/borate/EDTA agarose gels showing RNA from ribosomes purified in (a) 3 mM $MgCl_2$ and (b) 1 mM Fe^{2+}. The banding pattern suggests that rRNA is relatively more intact in ribosomes purified with 3 mM $MgCl_2$ (a) and relatively more degraded in ribosomes purified with 1 mM $FeCl_2$ (b).

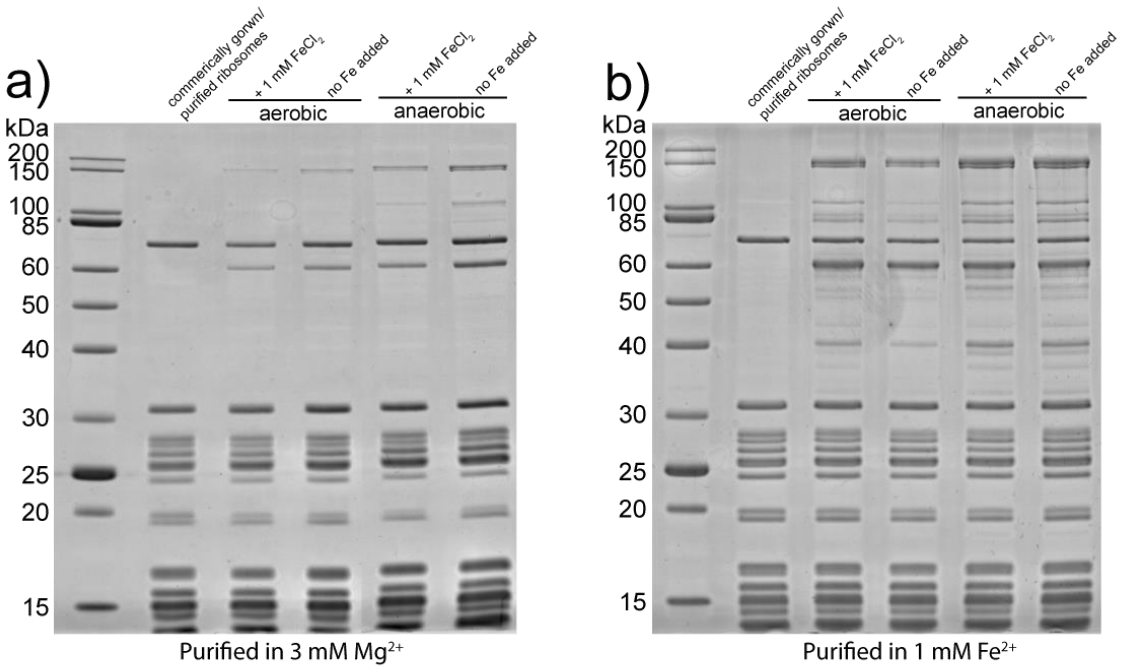

Figure 12. 12% SDS acrylamide gels for proteins in ribosomes purified in (a) 3 mM $MgCl_2$ and (b) 1 mM $FeCl_2$.

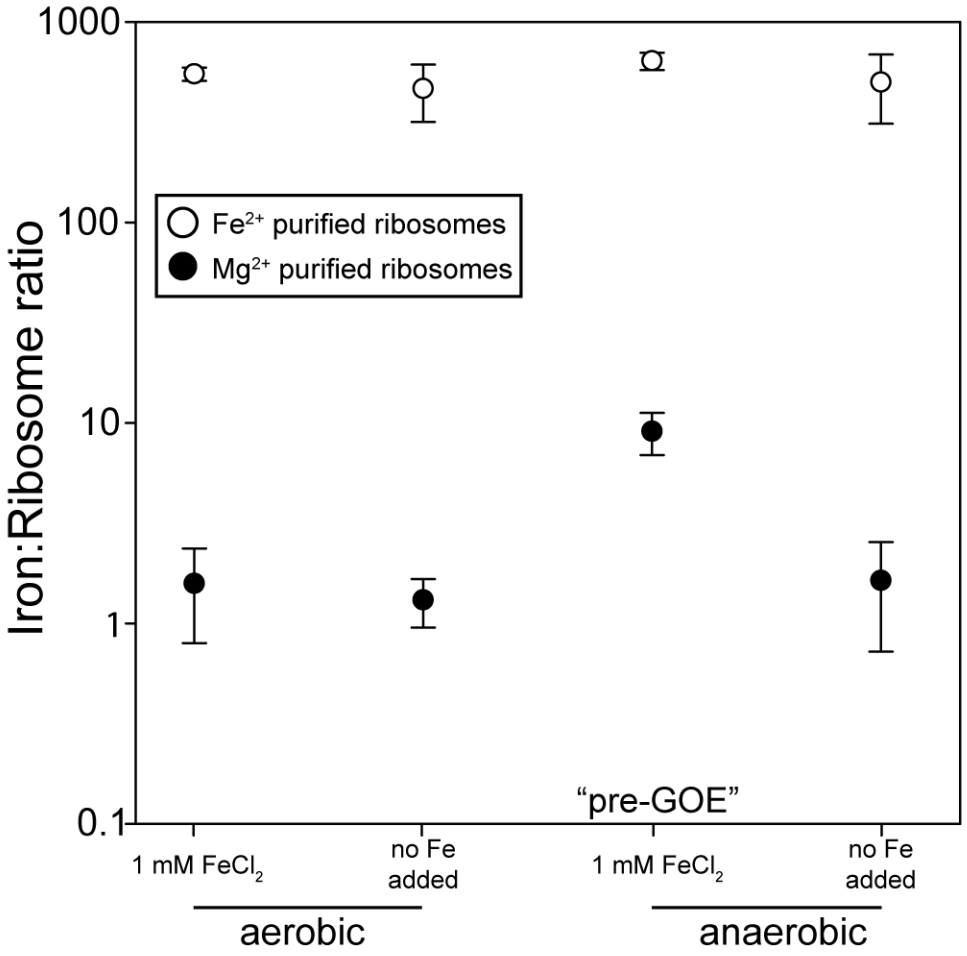

Figure 13. Fe content of purified ribosomes (mol Fe mol^{-1} ribosome) from *E. coli* MRE600 grown aerobically or anaerobically at 1 mM $FeCl_2$ or ambient Fe^{2+} (6-9 μM "no Fe added"), and purified in buffers containing either 3 mM $MgCl_2$ (black circles) or 1 mM $FeCl_2$ (white circles). Error bars represent standard error of the mean (n=3).

We also purified ribosomes using buffers with 1 mM $FeCl_2$ instead of 3 mM $MgCl_2$ to determine the effect of M^{2+} exchange during the purification process on the final ribosomal Fe content. While the protein banding pattern from ribosomes purified with 1 mM $FeCl_2$ was similar to that of ribosomes purified with 3 mM $MgCl_2$ (**Figure 12b**),

rRNAs from 1 mM $FeCl_2$-purified ribosomes were degraded (**Figure 11b**). All ribosomes purified in 1 mM $FeCl_2$ contained significantly higher Fe than those purified in 3 mM Mg^{2+} (**Figure 13**). While pre-GOE ribosomes contained the most Fe (640 ± 53 mol Fe mol^{-1} ribosome), it was not significantly higher than the Fe content in ribosomes from cells grown aerobically with 1 mM Fe^{2+} (551 ± 42 mol Fe mol^{-1} ribosome; p-value = 0.32), cells grown anaerobically without added Fe (501 ± 148 mol Fe mol^{-1} ribosome: p-value = 0.55), or aerobic cells without added Fe (466 ± 189 mol Fe mol^{-1} ribosome; p-value = 0.37).

Ribosomes from all growth conditions were able to translate active protein in 10 mM Mg^{2+} (**Table 5**). All ribosomes could also translate active protein in 8 mM Fe^{2+} and 2 mM Mg^{2+}, albeit at lower rates, consistent with our previous work (33). Ribosomes from anaerobic cells had lower translation activity than those from aerobic cells.

Table 5. *In vitro* translation activity of purified ribosomes. All ribosomes were normalized to 9 mg mL^{-1} before adding to translation reactions. Production of the protein dihydrofolate reductase (DHFR) from its mRNA was used to monitor translational activity. Protein synthesis was assayed by measuring the rate of NADPH oxidation by DHFR. Average values are reported ± standard error of the mean (n=4).

Growth conditions		**Divalent cation content of reaction**	
		10 mM Mg^{2+}	**8 mM Fe^{2+} + 2 mM Mg^{2+}**
aerobic	+ 1 mM $FeCl_2$	0.112 ± 0.004	0.027 ± 0.005
	No Fe added	0.100 ± 0.009	0.028 ± 0.004
anaerobic	+ 1 mM $FeCl_2$	0.074 ± 0.004	0.021 ± 0.004
	No Fe added	0.066 ± 0.013	0.013 ± 0.004

Mass spectrometry was used to characterize the proteins associated with ribosomes from the four growth conditions. All ribosomes contained a full repertoire of rProteins. All samples also contained additional proteins, ranging in function from translation to central metabolism. As expected, proteins from anaerobic pathways were generally more abundant in the anaerobic cells while those from aerobic pathways were more abundant in the aerobic cells (**Tables 6,7**). Proteins for synthesis of enterobactin, an Fe(III)-binding siderophore, were more abundant in ribosomes from aerobic cells and from those grown without added Fe, while the bacterial non-heme ferritin subunit was more abundant in ribosomes from anaerobic cells regardless of Fe content of media (**Table 7**). Several proteins were either more or less abundant in ribosomes from "pre-GOE' conditions (**Figure 14**). Notably, pre-GOE ribosomes had five times higher abundance of the LSU rRNA accumulation protein YceD than in ribosomes grown anaerobically without iron. Pre-GOE ribosomes had three times lower abundance of the ribosomal protein S12 methylthiotransferase protein RimO and ribosomal RNA large subunit methyltransferase K/L protein RlmL than those from aerobically grown cells with 1 mM Fe.

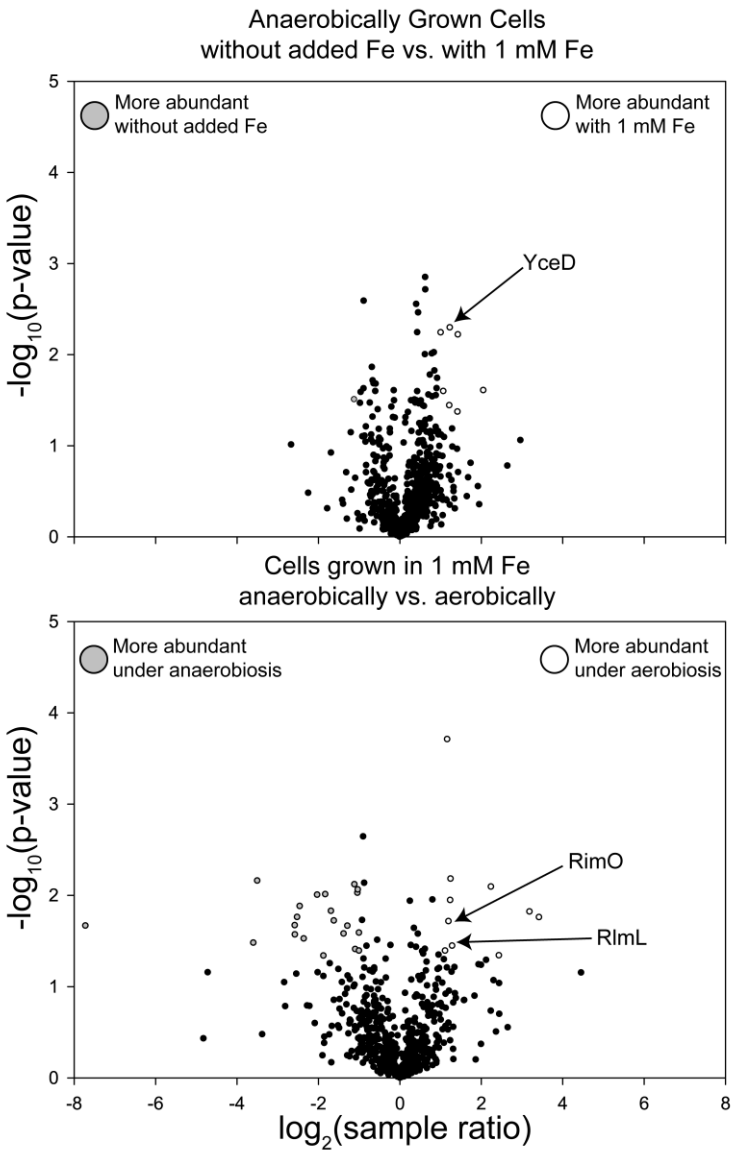

Figure 14. Differential protein abundance between ribosomes purified from cells grown under four growth conditions. Graphs display proteins found to be in higher abundance in ribosome samples between two growth conditions. Black circles represent proteins not significantly more abundant in either samples while gray and white circles represent protein significantly more abundant in one of the samples. Proteins with a 2-fold or greater abundance in one sample versus another and a p-value less than or equal to 0.05 (n=3), were classified as significantly more abundant.

3.5 Discussion

3.5.1 Iron in pre-GOE ribosomes.

We and others have shown that around 500-1000 M^{2+} associate with the *E. coli* ribosome (33, 93). The vast majority of these M^{2+} are readily exchangeable. When ribosomes are purified in either Fe^{2+} or Mg^{2+}, around 500-1000 ions from the purification solution associate with each ribosome, regardless of the dominant M^{2+} type during growth. Incubation in either M^{2+} (Mg^{2+} of Fe^{2+}) causes exchange of one M^{2+} for the other. Thus, the exchangeable mode of association appears to be conserved between Mg^{2+} and Fe^{2+}.

However, not all the M^{2+} associated with the ribosome are exchangeable. Around 10 Fe^{2+} ions associate with ribosomes *in vivo* during growth under pre-GOE conditions by a specific mode of interaction that resists exchange during purification in Mg^{2+}. Repeated washing of pre-GOE ribosomes with Mg^{2+} does not displace this subset of 10 Fe^{2+} ions. The number of non-exchangeable Fe^{2+} ions is smaller (~1 Fe^{2+} per ribosome) for cells grown with high O_2 and/or low Fe^{2+}. The resistance to exchange suggests that these Fe^{2+} ions are interacting directly with rRNA because as ions participate in more specific, first shell interaction with the backbone of RNA their ability to diffuse into the surrounding solvent decreases (94). Therefore it is likely that these iron ions are being directly chelated by one or more phosphate oxygens on the backbone of rRNA.

In addition to those tightly associated with the ribosome, it seems that Fe^{2+} can associate with rRNA *in vitro*. rRNA from ribosomes purified in 1 mM Fe^{2+} was degraded while rRNA from ribosomes purified with Mg^{2+} was not. More rRNA degradation in the presence of higher Fe^{2+} suggests that Fe^{2+} associating with the ribosome during purification

may be mediating the rRNA cleavage observed. While Fe^{2+} is known to react with O_2 to produce RNA-damaging reactive oxygen species such as hydroxyl radical (13, 122), our purification of ribosomes under strict anoxia should have eliminated that route of RNA degradation. It is possible that Fe^{2+} may be catalyzing accelerated in-line cleavage by interacting with the rRNA phosphate backbone in the same sites as Mg^{2+}. Indeed, rRNA degradation in ribosomes containing Fe^{2+} is consistent with previous finding that Fe^{2+} can induce rRNA in-line cleavage at much higher rates than Mg^{2+} (123). This would suggest that Fe^{2+} is associating with rRNA *in vitro* during purification of ribosomes in buffer containing 1 mM Fe^{2+}. Preliminary results performing in-line cleavage on our purified ribosome samples shows that the pre-GOE ribosomes which contain the most bound Fe succumb to this cleavage faster than ribosome from other growth conditions. This may further suggest that the iron in pre-GOE ribosomes is bound to the rRNA.

It seems unlikely that the rProtein content of our ribosomes is responsible for ribosomal Fe^{2+} content observed. To our knowledge, rProteins do not bind Fe^{2+}. In addition to rProteins however many other proteins were identified by mass spectrometry. Some of these are ribosome associated proteins involved in the assembly/function of the ribosome and it is likely that they were co purified due to their specific binding with the ribosome. Others were proteins not involved in translation and so their presence in our purified ribosome samples was perplexing. It is not clear whether these proteins nonspecifically bind the resin used for purification or have some yet unknown interaction with the ribosome. It is possible that some of these proteins were being translated at the time of cell harvesting and so were retained with the ribosome during purification.

Several of the non-ribosomal proteins identified with mass spectrometry use Fe as a cofactor. If these proteins were contributing to the non-exchangeable Fe^{2+} pool, their differential abundance between growth conditions would match the Fe:ribosome ratio pattern we observe between samples. This is not the case however, as all of these proteins, except aldehyde dehydrogenase, are more abundant in either the aerobic or anaerobic without added Fe ribosomes than they are in the pre-GOE samples. Therefore, it is unlikely that these proteins are significantly contributing to the Fe in our purified ribosomes.

Besides these proteins, the bacterial non-heme ferritin subunit protein was identified in all bacterial samples. Bacterial non-heme ferritin is an Fe storage protein that can hold as many as 3000 Fe(III) atoms as the mineral ferrihydrite (27). It is a 24-mer of identical subunits that self-assemble into the mature protein (124). To our knowledge there is no previous evidence of direct association between ferritin and the ribosome. There is some evidence for ferritin copurifying with ribosomes in sucrose gradients however the use of column chromatography in our study makes this unlikely (125). Non-heme ferritin is upregulated under high intracellular Fe so it is perhaps unsurprising that this protein is most abundant in ribosomes from pre-GOE conditions (126, 127). While we cannot be sure whether we are detecting subunits or assembled ferritin, and whether or not the ferritin is Fe loaded, we cannot discount the contribution of ferritin in elevated ribosomal Fe content. However, recent evidence suggests that ferritin bound Fe makes up a very small portion of the total Fe pool in exponentially growing *E. coli* (128).

3.5.2 Tightly-bound ribosomal iron likely occupies dinuclear microclusters.

It seems likely that the non-exchangeable 10 Fe^{2+} atoms are buried deep within the ribosome and are highly coordinated by the rRNA. We have previously parsed M^{2+} by rRNA coordination number (i.e., by number of first shell rRNA ligands) and detected a special subset of highly coordinated M^{2+}. Divalent cations with high rRNA coordination number are found in di-nuclear Mg^{2+} microclusters (μc's) (41). The Mg^{2+} ions in M^{2+}-μc's are directly chelated by multiple phosphate oxygens on the rRNA backbone and are substantially dehydrated due to numerous RNA interactions. Displacement of these M^{2+} would require large scale changes in ribosomal conformation. Microclusters within the LSU provide a framework for the ribosome's PTC, the site of protein synthesis in the ribosome, suggesting an essential and ancient role for M^{2+}-μc's in the ribosome. Overall there are four dinuclear M^{2+}-μc's in the LSU and one in the SSU (41). In sum there are ten M^{2+} per ribosome that are expected to exchange much more slowly than other M^{2+}. Based on the number and behavior of Fe^{2+} ions observed in pre-GOE ribosomes, we surmise that Fe^{2+} can inhabit M^{2+}-μc's. This prediction is supported by recent work showing that these μc's fold and catalyze electron transfer in the presence of Fe^{2+} *in vitro* (50). Although little is known about the incorporation of M^{2+} during ribosome assembly, the M^{2+}-μc's are likely incorporated early in the assembly process given their deeply buried location and their necessity for mediating long range rRNA tertiary interactions (41). It is possible that M^{2+}-μc synthesis and M^{2+} incorporation is mediated by dedicated cellular machinery.

3.5.3 Iron is most available for ribosomal association under pre-GOE conditions.

The difference in ribosomal Fe content in cells from different growth conditions is consistent with the availability and reactivity of Fe^{2+} and O_2. In oxic conditions, extracellular Fe exists as insoluble Fe(III), which is difficult for cells to assimilate (13,

129), and cells use siderophores like enterobactin for Fe(III) uptake (27, 100). Once in the cell, byproducts of aerobic metabolism, such as H_2O_2 and O_2^-, or O_2 diffusing in from the environment, can react with Fe^{2+} to form dangerous hydroxyl radicals (130). Thus, aerobic cells need to tightly regulate intracellular Fe to maintain low Fe^{2+} levels in the cytoplasm(131), which in turn may minimize Fe^{2+} available for ribosomal incorporation.

In anoxic conditions, Fe^{2+} is more bioavailable and is a lower risk to cellular systems because anaerobic growth generates fewer reactive oxygen species and there is no threat from O_2 diffusion into cells. Thus, anaerobic cells do not need to sequester Fe, and labile Fe^{2+} accumulates in the cytoplasm (100). Under pre-GOE conditions, Fe^{2+} is both abundant and bioavailable, allowing to cells to assimilate more of it (132). Notably, we only observed multiple tightly-bound Fe^{2+} ions in ribosomes from cells grown under pre-GOE conditions suggesting that only under pre-GOE conditions are intracellular Fe concentrations both high and labile enough for Fe to associate intimately with the ribosome. We hypothesize that *in vivo*, ribosomes in anaerobic cells likely contain Fe contents in between the upper and lower bounds measured here, depending on intracellular Fe^{2+} availability and lability.

3.5.4 Differential expression of ribosome associated proteins under pre-GOE conditions.

We used mass spectrometry to observe whether pre-GOE growth conditions had any significant effect on the ribosomal or ribosome-associated protein content of our samples. The only protein predicted to be involved in ribosome function or assembly that was significantly more abundant under pre-GOE conditions was the large ribosomal RNA

subunit accumulation protein YceD. YceD is a 173 amino acid protein with a single C-$X_{(2)}$-C cysteine motif suggesting a potential metal binding site. The function of YceD remains unclear. The *yceD* gene is co-transcribed with the rProtein L32 gene *rpmF* (133). *ΔyceD* mutants had decreased 23S rRNA content compared to the wild type, suggesting that YceD is involved in 23S rRNA synthesis and/or processing. The higher abundance of YceD associated with pre-GOE ribosomes suggests that YceD may play a role in incorporating Fe^{2+} into the ribosome *in vivo*. Proteins that were less abundant in pre-GOE ribosomes included the rProtein S12 methylthiotransferase, and the rRNA large subunit methyltransferase K/L. While the functions of these protein and rRNA modifications in the ribosome are not totally clear, some evidence points to structural roles (128). Whatever their utility, their reduced abundance in pre-GOE ribosomes suggests that the increased Fe association in these ribosomes may render the function of these proteins less important.

3.6 Conclusions

We have shown for the first time that bacteria grown in pre-GOE conditions contain functional ribosomes with tightly-bound Fe atoms. The ~10 ribosomal Fe ions in pre-GOE ribosomes are likely deeply buried and specifically bound to rRNA. Depending on intracellular Fe lability, ribosomes may have higher Fe content *in vivo* given the high capacity for the ribosome to substitute ~600 loosely-bound Mg^{2+} ions for Fe^{2+}. Our results support a model that alternate M^{2+} ions, namely Fe^{2+}, participated in the origin and early evolution of life: first in abiotic proto-biochemical systems, and then within early cellular life up until the GOE (49). Our study also expands the role of Fe^{2+} in modern biochemistry by showing that extant life retains the ability to incorporate Fe into ribosomes. We surmise that extant organisms under certain environmental and cellular states, such as pathogenic

organisms during infection of low O_2, high Fe^{2+} tissues, may use Fe^{2+} as a ribosomal cofactor. In addition, obligate anaerobic organisms that have spent the entirety of their evolutionary history in permanently anoxic environments may still use abundant Fe^{2+} in their ribosomes *in vivo*.

Table 6. Proteins differentially abundant in ribosome samples purified from cells with or without 1 mM added Fe. Proteins were defined as differentially abundant if they were ≥2-fold more abundant in one sample over another with a p-value < 0.05 (n=3). Proteins are involved in translation are indicated by one asterisk. Proteins involved in Fe homeostasis are indicated by two asterisks.

Condition	Protein more abundant in	Protein name	UniProt ID	Fold more abundant	p-value	metal cofactor
Anaerobic	1mM added Fe vs. Without added Fe	Transcriptional regulatory protein OmpR	P0AA16	2.0	0.01	N.A.
		UvrABC system protein B	P0A8F8	2.1	0.03	N.A.
		5'-methylthioadenosine/S-adenosylhomocysteine nucleosidase	P0AF12	2.3	0.04	N.A.
		Large ribosomal RNA subunit accumulation protein YceD*	P0AB28	2.3	0.01	N.A.
		ATP-dependent dethiobiotin synthetase BioD 2	P0A6E9	2.7	0.04	Mg^{2+}
		Phosphoribosylaminoimidazole-succinocarboxamide synthase	P0A7D7	2.7	0.01	N.A.
		Phosphoserine phosphatase	P0AGB0	4.1	0.02	Mg^{2+}
	Without added Fe vs. 1 mM Fe	4-alpha-glucanotransferase	P15977	2.2	0.03	N.A.
Aerobic	1mM added Fe vs. Without added Fe	Probable 4-deoxy-4-formamido-L-arabinose-phosphoundecaprenol deformylase ArnD	P76472	2.0	0.01	N.A.
		GDP-mannose pyrophosphatase NudK	P37128	2.0	0.03	Mg^{2+}
		Uncharacterized protein YfdQ	P76513	2.1	0.02	N.A.
		Uncharacterized protein YciO	P0AFR4	2.1	0.00	N.A.
		ABC transporter ATP-binding protein ModF	P31060	3.1	0.04	N.A.
	Without added Fe vs. 1 mM Fe	Enterobactin synthase component B**	P0ADI4	8.9	0.03	Mg^{2+}
		Fe(3+) dicitrate-binding periplasmic protein**	P15028	7.7	0.02	N.A.

Table 7. Proteins differentially abundant between ribosome samples purified from aerobic vs anaerobic cells. Proteins are defined as differentially abundant if they were ≥2-fold more abundant in one sample over another with a p-value < 0.05 (n=3). Proteins are involved in translation are indicated by one asterisk. Proteins involved in Fe homeostasis are indicated by two asterisks.

	Protein more abundant in	**Protein name**	**UniProt ID**	**Fold more abundant**	**p-value**	**Metal cofactor**
1 mM added Fe	Anaerobic vs. Aerobic	L-threonine dehydratase catabolic TdcB	P0AGF6	211.8	0.02	N.A.
		Hydrogenase maturation factor HypB	P0AAN3	12.1	0.03	N.A.
		Glycerol dehydrogenase	P0A9S5	11.4	0.01	Zn^{2+}
		Phosphoribosylaminoimidazole-succinocarboxamide synthase	P0A7D7	6.0	0.02	N.A.
		Aldehyde-alcohol dehydrogenase	P0A9Q7	6.0	0.03	Fe^{2+}
		Uncharacterized protein YjjI	P37342	5.8	0.02	N.A.
		Probable acrylyl-CoA reductase AcuI	P26646	5.5	0.01	N.A.
		Bacterial non-heme ferritin**	P0A998	5.1	0.03	N.A.
		Aspartate ammonia-lyase	P0AC38	4.1	0.01	N.A.
		Fumarate reductase flavoprotein subunit	P00363	3.7	0.05	N.A.
		UvrABC system protein B	P0A8F8	3.6	0.01	N.A.
		Formate acetyltransferase 1	P09373	3.2	0.01	N.A.
		UPF0227 protein YcfP	P0A8E1	3.1	0.02	N.A.
		Phosphoenolpyruvate-protein phosphotransferase	P08839	2.6	0.03	Mg^{2+}
		Ubiquinone/menaquinone biosynthesis C-methyltransferase UbiE	P0A887	2.4	0.02	N.A.
		Glycogen phosphorylase	P0AC86	2.2	0.01	N.A.
		Maltodextrin phosphorylase	P00490	2.1	0.04	N.A.
		Thymidine phosphorylase	P07650	2.1	0.01	N.A.
		Protein-export protein SecB	P0AG86	2.0	0.01	N.A.
		Integration host factor subunit beta	P0A6Y1	2.0	0.04	N.A.
		Cold shock-like protein CspE	P0A972	2.0	0.03	N.A.
		Fatty acid metabolism regulator protein	P0A8V6	1.9	0.02	N.A.
	Aerobic vs. Anaerobic	Lipoyl synthase	P60716	2.2	0.04	[4Fe-4S] cluster
		Translation initiation factor IF-3*	P0A707	2.2	0.00	N.A.
		Ribosomal protein S12 methylthiotransferase RimO*	P0AEI4	2.3	0.02	[4Fe-4S] cluster
		Dihydrolipoyllysine-residue acetyltransferase component of pyruvate dehydrogenase complex	P06959	2.4	0.01	N.A.
		Ribonucleotide monophosphatase NagD	P0AF24	2.4	0.01	Mg^{2+}
		Ribosomal RNA large subunit methyltransferase K/L*	P75864	2.4	0.04	N.A.
		2-oxoglutarate dehydrogenase E1 component	P0AFG3	4.7	0.01	N.A.
		Alkyl hydroperoxide reductase C	P0AE08	5.4	0.05	N.A.
		Pyruvate/proton symporter BtsT	P39396	9.1	0.02	N.A.
		Bifunctional protein PutA	P09546	10.7	0.02	N.A.

Table 7. Proteins differentially abundant between ribosome samples purified from aerobic vs anaerobic cells.

Without added Fe	Anaerobic vs. Aerobic	L-threonine dehydratase catabolic TdcB	P0AGF6	137.5	0.00	N.A.
		Uncharacterized protein YfdQ	P76513	38.0	0.02	N.A.
		Hydrogenase-2 large chain	P0ACE0	31.5	0.01	Ni^{2+}
		Fumarate reductase Fe-sulfur subunit	P0AC47	17.5	0.01	[2Fe-2S], [3Fe-4S], and [4Fe-4S] clusters
		Glycerol dehydrogenase	P0A9S5	16.9	0.01	Zn^{2+}
		Bacterial non-heme ferritin**	P0A998	14.9	0.00	N.A.
		Hydrogenase maturation factor HypB	P0AAN3	11.6	0.02	N.A.
		PFL-like enzyme TdcE	P42632	8.6	0.01	N.A.
		Aldehyde-alcohol dehydrogenase	P0A9Q7	7.2	0.01	Fe^{2+}
		Anaerobic ribonucleoside-triphosphate reductase	P28903	5.8	0.04	N.A.
		Aspartate ammonia-lyase	P0AC38	4.5	0.01	N.A.
		Uncharacterized protein YjjI	P37342	4.3	0.03	N.A.
		SCP2 domain-containing protein YhbT	P64599	4.1	0.01	N.A.
		2,3-bisphosphoglycerate-independent phosphoglycerate mutase	P37689	3.9	0.00	Mn^{2+}
		2-octaprenylphenol hydroxylase	P25535	3.7	0.05	N.A.
		Fructose-1,6-bisphosphatase 1 class 2	P0A9C9	3.3	0.03	Mn^{2+}
		Stationary-phase-induced ribosome-associated protein*	P68191	3.3	0.00	N.A.
		Evolved beta-galactosidase subunit alpha	P06864	3.2	0.04	N.A.
		Ribonuclease T	P30014	2.8	0.03	Mg^{2+}
		UPF0227 protein YcfP	P0A8E1	2.5	0.03	
		UPF0313 protein YgiQ	Q46861	2.4	0.01	[4Fe-4S] cluster
		Methionine--tRNA ligase	P00959	2.4	0.02	Zn^{2+}
		Polyphosphate kinase	P0A7B1	2.4	0.03	Mg^{2+}
		RecBCD enzyme subunit RecC	P07648	2.3	0.02	N.A.
		ADP-heptose--LPS heptosyltransferase 2	P37692	2.2	0.03	N.A.
	Aerobic vs. Anaerobic	RNA-binding protein YhbY	P0AGK4	2.2	0.01	N.A.
		Chaperone protein HscA	P0A6Z1	2.3	0.00	N.A.
		Cytochrome bd-I ubiquinol oxidase subunit 2	P0ABK2	2.3	0.03	heme
		5'-methylthioadenosine/S-adenosylhomocysteine nucleosidase	P0AF12	2.3	0.02	N.A.
		Ribosomal silencing factor RsfS*	P0AAT6	2.4	0.00	N.A.
		DNA topoisomerase 4 subunit B	P20083	2.7	0.01	Mg^{2+}
		Lipoyl synthase	P60716	3.0	0.01	[4Fe-4S] cluster
		Transcriptional regulatory protein GlrR	P0AFU4	3.2	0.00	N.A.
		Modulator of FtsH protease HflC	P0ABC3	3.5	0.01	N.A.
		Ribosomal RNA small subunit methyltransferase A*	P06992	3.7	0.01	N.A.
		Pyruvate/proton symporter BtsT	P39396	5.8	0.04	N.A.
		Enterobactin synthase component B**	P0ADI4	8.0	0.01	Mg^{2+}
		Respiratory nitrate reductase 1 alpha chain	P09152	37.3	0.01	[4Fe-4S] cluster

Table 7. Proteins differentially abundant between ribosome samples purified from aerobic vs anaerobic cells.

						Mo-bis-MGD

CHAPTER 4. MICROBIAL IRON AND METHANE DYNAMICS AND THEIR EFFECT ON EARLY EARTH HABITABILITY

The work described in this chapter has been previously published in the journal *Geobiology* (134). I performed the majority of the experiments. Sediment samples used to inoculate cultures were provided by S. A. Crowe. I performed DNA amplicon sequencing with help from J. Wu and R.L. Simister. The manuscript was written with contributions from all coauthors.

4.1 Abstract

Reactive Fe(III) minerals can influence CH_4 emissions by inhibiting microbial methanogenesis or by stimulating anaerobic CH_4 oxidation. The balance between Fe(III) reduction, methanogenesis, and CH_4 oxidation in ferruginous Archean and Paleoproterozoic oceans would have controlled CH_4 fluxes to the atmosphere, thereby regulating the capacity for CH_4 to warm the early Earth under the Faint Young Sun. We studied CH_4 and Fe cycling in anoxic incubations of ferruginous sediment from the ancient ocean analogue Lake Matano, Indonesia over three successive transfers (500 days total). Iron reduction, methanogenesis, CH_4 oxidation, and microbial taxonomy were monitored in treatments amended with ferrihydrite or goethite. After three dilutions, Fe(III) reduction persisted only in bottles with ferrihydrite. Enhanced CH_4 production was observed in the presence of goethite, highlighting the potential for reactive Fe(III)-oxides to inhibit methanogenesis. Supplementing the media with hydrogen, nickel and selenium did not stimulate methanogenesis. There was limited evidence for Fe(III)-dependent CH_4

oxidation, although some incubations displayed CH_4-stimulated Fe(III)-reduction. 16S rRNA profiles continuously changed over the course of enrichment, with ultimate dominance of unclassified members of the order *Desulfuromonadales* in all treatments. Microbial diversity decreased markedly over the course of incubation, with subtle differences between ferrihydrite and goethite amendments. These results suggest that Fe(III)-oxide mineralogy and availability of electron donors could have led to spatial separation of Fe(III)-reducing and methanogenic microbial communities in ferruginous marine sediments, potentially explaining the persistence of CH_4 as a greenhouse gas throughout the first half of Earth history.

4.2 Introduction

Elevated atmospheric CH_4 (100-1000 ppmv vs. ~2 ppmv in the modern atmosphere) likely played an important role in the first half of Earth history by helping warm Earth's surface temperature enough to sustain liquid water under considerably lower solar radiation (135-138). During this time, the main source of CH_4 was likely hydrogenotrophic methanogenesis [$CO_2 + 4\ H_2 \rightarrow CH_4 + 2H_2O$; (139, 140]) from anoxic oceans, which were ferruginous for most of the Archean and Paleoproterozoic eons (102). In these seas, a "ferrous wheel" would have cycled Fe from dissolved Fe^{2+} to Fe(III) oxides via microbial photoferrotrophy and/or abiotic photo-oxidation,(141, 142) and then back to Fe^{2+} via microbial Fe(III) respiration (143-146).

Ferruginous oceans could have influenced CH_4 cycling by several mechanisms. It is well established that Fe(III)-reducing bacteria have higher affinity for H_2 than hydrogenotrophic methanogens, and will therefore outcompete them in the presence of

poorly crystalline Fe(III) oxides, e.g. ferrihydrite,(147-149) [note that Fe(III)-reducing bacteria also outcompete acetoclastic methanogens (150), but acetoclastic methanogenesis likely evolved much later in Earth history (151)]. In addition, evidence Fe(III) oxides can mediate or stimulate microbial CH_4 oxidation, either as the direct oxidant (152, 153), or indirectly by regenerating sulfate by oxidization of reduced sulfur compounds (154).

The putative microbial metabolism of CH_4 oxidation coupled to Fe(III) reduction is thermodynamically favorable with ferrihydrite ($CH_4 + 8\ Fe(OH)_3 + 15H^+ \rightarrow HCO_3^- + 8Fe^{2+} + 21H_2O$; $\Delta G_r^0 = -571$ kJ mol^{-1} CH_4) and goethite ($CH_4 + 8\ FeOOH + 15H^+ \rightarrow HCO_3^- + 8Fe^{2+} + 13H_2O$; $\Delta G_r^0 = -355$ kJ mol^{-1} CH_4) as terminal electron acceptors (155, 156). Based on the chemical equations and free energy yields above, we would expect to observe a stoichiometric ratio of 1 CH_4 oxidized per 8 Fe(III) reduced and preferential use of ferrihydrite over goethite as the electron acceptor. Evidence for microbial CH_4 oxidation coupled to, or stimulated by, Fe(III) reduction is widespread across modern anoxic ecosystems and anaerobic digester communities (154, 156-167). Recent studies have reported simultaneous CH_4 oxidation and ferrihydrite reduction and have identified archaea closely related to the methanogens as the organisms likely responsible for this process (152, 168).

Despite the possible importance of coupled Fe(III) and CH_4 cycling in the Archean and Paleoproterozoic eons, long-term studies of Fe(III) reduction under low organic carbon and high CH_4 conditions remain sparse. Lake Matano, Indonesia is one of the only modern analogues for the ferruginous Archean ocean (142). Despite the abundance of Fe(III) oxides that might be expected to suppress methanogenesis, CH_4 accumulates to 1.4 mM in anoxic deep waters (142, 163, 169-171). Methanotrophy is a key carbon fixation process

in Lake Matano's oxic-anoxic transition zone, and the dearth of other oxidants (<100 nM nitrate and sulfate) suggests that Fe(III) might be the terminal electron acceptor in methanotrophy (163, 164). In this study, we examined the influence of CH_4 and Fe(III) mineral speciation on rates of Fe(III) reduction, methanogenesis, and CH_4 oxidation, and microbial community composition, over three successive dilutions (500 total days of incubation) of anoxic Lake Matano sediments.

4.3 Experimental Methods

4.3.1 Sample collection and storage.

A 15-cm sediment core from 200 m water depth in Lake Matano, Sulawesi Island, Indonesia (2°26′S, 121°15′E; *in situ* sediment temperature ~27°C) was sampled in November 2010 and sub-sampled at 5 cm increments. Sediments from 0-5 and 5-10 cm depth were fluffy and black, and 10-15 cm was dark gray. Sediments were sealed in gas-tight bags with no headspace (172) and stored at 4°C until incubations began in March 2015.

4.3.2 Enrichment medium and substrate synthesis.

A modified artificial freshwater medium lacking nitrate and sulfate was developed based on the pore water composition of Lake Matano sediments (S.A. Crowe and D.A. Fowle, unpublished work). The medium contained 825 μM $MgCl_2$, 550 μM $CaCO_3$, 3 mM $NaHCO_3$, 3.5 μM K_2HPO_4, 5 μM Na_2HPO_4, 225 μM NH_4Cl, 1 μM $CuCl_2$, 1.5 μM Na_2MoO_4, 2.5 μM $CoCl_2$, 23 μM $MnCl_2$, 4 μM $ZnCl_2$, 9.4 μM $FeCl_3$ and 3 mM Na_2NTA, 0.07 μM vitamin B_{12}, 0.4 μM biotin, and 68.5 μM thiamine. Filter-sterilized vitamin

solutions were added after autoclaving. Ferrihydrite ($Fe(OH)_3$) and goethite (FeOOH) were synthesized as described in (173)and added to enrichments to 10 mM as described below.

4.3.3 Inoculation of enrichments and amendments.

The sediment was pre-treated for 36 days at 30°C in 100% N_2 headspace to deplete endogenous organic carbon, electron donors, and reactive electron acceptors. After pre-treatment, sediment from the 0-5 cm depth layer was inoculated in a ratio of sediment to medium of 1:5 (v/v) in an anoxic chamber (97% N_2 and 3% H_2; Coy Laboratory Products, Grass Lake, MI, USA). Sediment slurry (35 mL) was aliquoted into 70 mL sterile serum bottles, stoppered with sterile butyl stoppers (Geo-Microbial Technologies, Ochelata, OK, USA; pre-boiled in 0.1 N NaOH), and crimped with aluminum seals. Ferric Fe was added either as ferrihydrite or goethite to 10 mM. Bottles were purged with 99.99% N_2 for 1 hr, and CH_4 amendments were injected with 10 mL 99.99% CH_4 and 5 mL 99% $^{13}CH_4$ (Cambridge Isotope Laboratories, Tewksbury, MA, USA). Controls were autoclaved at 121°C for 1 hr on day 0 and again on day 6 of the 1° enrichment. All treatments were duplicated, and bottles were incubated in the dark at 30°C with shaking at 200 rpm.

After 50 days, the volume of all cultures was reduced to 5 mL, and 30 mL of fresh media was added to each bottle, constituting a 6-fold dilution. These 2° enrichments were amended with approximately 10 mM of either ferrihydrite or goethite. All bottles were purged with 99.99% N_2 for 1 hr, and all bottles except N_2 controls were injected with 8 mL 99.99% CH_4 and 2 mL 99% $^{13}CH_4$. Controls were autoclaved again at 121°C for 1 hr. DL-Methionine (10 μM) was added as a sulfur source. After 303 days, cultures were diluted 10-fold with fresh media into new serum bottles (3° enrichment) with the same substrate

and headspace composition as the 2° enrichment. A schematic of the incubation and dilutions is shown at the top of **Figures 15** and **16**.

After an additional 220 days, goethite-amended N_2 cultures were diluted 25-fold with fresh anoxic media into new serum bottles. Cultures received either 10 mM goethite or no Fe(III). A subset of cultures received 5 mL of 99.99% H_2 (20% headspace) while all others had 100% N_2 headspace. Controls were autoclaved at 121°C. After 48 days, an anoxic solution of nickel (Ni) and selenium (Se) was added to all bottles, yielding final concentrations of 1 µM Ni and 1 µM Se. For more information on these cultures, refer to **Tables 22, 23**, and **24** in **Appendix D**.

4.3.4 HCl extractable Fe^{2+} and Fe^{3+} and soluble Fe^{2+}.

Samples were taken from each bottle in the anoxic chamber using a 21-gauge needle (BD PrecisionGlide™) and plastic syringe. Plasticware was stored in the anoxic chamber for at least 24 hr to minimize O_2 sample contamination. For HCl-extractable Fe^{2+} analyses, 100 µL of sediment slurry was extracted with 400 µL 0.5 N HCl in the dark for 1 hr, followed by centrifugation at 10,000 x g for 1 min, injection of 10 µL of supernatant into 990 µL of 10 mM FerroZine reagent in 46 mM HEPES (pH 8.3), and measurement of absorbance at 562 nm (174). For HCl-extractable Fe^{3+}, 100 µL of sediment slurry was incubated overnight in 0.5 N HCl and 0.25 M NH_2OH-HCl in the dark, followed by centrifugation and measurement as above, and subtraction of HCl-extractable Fe^{2+} as in Kostka & Luther (175).

4.3.5 Methane oxidation.

Samples were collected for δ^{13}C-DIC analysis by 0.2 µm membrane filtration of medium into crimp top autosampler vials (Thermo Scientific National Target LoVial) and analysis as described in Brandes (176). Rates of $^{13}CH_4$ oxidation to ^{13}C-DIC were calculated over the linear period of δ^{13}C-DIC increase based on the method in Scheller et al. (177). First, the δ^{13}C-DIC values were converted into fractional abundances ($^{13}F = (^{13}C/^{12}C+^{13}C)$), and then DIC production from CH_4 oxidation was calculated using the following formula:

$$\Delta[DIC] = (([DIC]_n(^{13}F_n)) - ([DIC]_0(13F_0))/^{13}F_{CH4})$$

Where $[DIC]_n$ and $^{13}F_n$ are equal to the total DIC concentration (mM) and fractional abundance of ^{13}C in the DIC at time n respectively. $[DIC]_0$ and $^{13}F_0$ are the total DIC concentration (mM) and fractional abundance of DIC at time 0 respectively, and $^{13}F_{CH4}$ is the fractional abundance of ^{13}C in the CH_4.

4.3.6 Headspace methane.

Headspace (50 µL) was sampled using a gastight syringe and injected into a gas chromatograph (SRI Instruments 8610C, Torrance, CA, USA) with a HayeSep N column and flame ionization detector to measure headspace CH_4 concentrations. A CH_4 standard (1000 ppm, Airgas, USA) was used for calibration.

4.3.7 Inductively coupled plasma mass spectrometry.

Total dissolved Ni and Se concentrations were measured using inductively coupled plasma mass spectrometry (ICP-MS). In order to determine the amounts of Ni and Se supplied by the media and Fe(III) oxides, aliquots of media were dispensed in serum

bottles, purged with 99.99% N_2, and amended with 10 mM goethite or ferrihydrite in the same manner as enrichments. Stoppers were penetrated multiple times with 21 gauge stainless steel needles (BD PrecisionGlide^{TM}) to mimic the effect of sampling on enrichment cultures. All samples for ICP-MS were filtered through 0.2 µm pore polypropylene syringe filters and diluted in 2% trace metal grade HNO_3 (Fisher Scientific, Inc.) containing scandium and yttrium as internal standards to account for instrument drift. Calibration standards were prepared from certified stock solutions of Ni (CertiPREP) and Se (BDH), and a blank and calibration standard were measured periodically as quality controls. The measurement detection limits, calculated as 3 times the standard deviation of the blank (n=8), were 7 and 128 nM for Ni and Se, respectively.

4.3.8 16S rRNA gene amplicon sequencing.

Samples (2 mL) of sediment used for inoculating incubations (hereafter, "sediment inoculum") were taken in February 2015 (prior to pre-treatment) and after incubation for 15 days (1° enrichment), 72 days (2° enrichment) and 469 days (3° enrichment). Nucleic acid was extracted and purified using a MO BIO PowerSoil Isolation Kit following the manufacturer's protocol and MO BIO UltraClean® 15 Purification Kit. 16S rRNA gene amplicons were synthesized from extracted DNA with V4 region-specific barcoded primers F515 and R806 (178) appended with Illumina-specific adapters according to Kozich et al. (2013) using a Bio-Rad C1000 Touch Thermocycler and QIAGEN Taq PCR Master Mix. Thermal cycling conditions were as follows: initial denaturing at 94°C (5 min), 35 cycles of denaturing at 94°C (40 sec), primer annealing at 55°C (40 sec), and primer extension at 68°C (30 sec). Amplicons were checked for correct

size (~400 bp) on a 1% agarose gel and purified using Diffinity RapidTips. Amplicon concentrations were determined on a Qubit™ (ThermoFisher) fluorometer. Amplicons were pooled at equimolar concentrations (4 nmol) and sequenced on an Illumina MiSeq running MiSeq Control software v.2.4.0.4 using a 500 cycle MiSeq reagent kit v2 with a 5% PhiX genomic library control, as described by Kozich et al. (2013). Sequences were deposited as NCBI accession numbers SAMN04532568-04532641 and SAMN05915184-05915222.

4.4 Results

4.4.1 Iron reduction.

1° enrichment. Over the first 10 days of incubation, HCl-extractable Fe^{2+} increased from 10 to 25 mM in ferrihydrite treatments **(Figure 15a**) and from 10 to 20 mM in goethite treatments (1-2 mM d^{-1}; **Figure 15b**). From day 6 to 10, HCl-extractable Fe^{3+} (7 and 12 mM in ferrihydrite and goethite treatments, respectively) was completely consumed in all bottles except autoclaved controls with ferrihydrite (data not shown). Fe reduction rates were identical with and without CH_4 (**Figure 15a, b**). Initial autoclaving did not suppress Fe(III) reduction. A second round of autoclaving on day 6 slightly suppressed further activity. From day 10-28, HCl-extractable Fe^{2+} fluctuated in ferrihydrite treatments (Figure 1a) and declined slightly in goethite treatments (**Figure 15b**). Soluble Fe^{2+} was consistently <1% of HCl-extractable Fe^{2+}, and sediment-free controls did not reduce Fe(III) (data not shown).

2° enrichment. After 1:6 dilution and 10 mM ferrihydrite addition on day 50, HCl-extractable Fe^{2+} increased from 3 to 4 mM over two days, and then remained constant

through the final time point (day 497) in bottles with and without added CH_4 (**Figure 15a**). After 10 mM goethite addition on day 50, HCl-extractable Fe^{2+} increased from 2 to 3 mM after a two-day lag period. Thereafter, HCl-extractable Fe^{2+} rose to 4 mM by day 497 in goethite treatments with added CH_4; without CH_4, HCl-extractable Fe^{2+} dropped back to 2 mM (**Figure 15b**). Autoclaved controls had no activity. Black magnetic minerals formed in all ferrihydrite treatments except autoclaved controls (Fig 1a). No magnetic minerals formed in goethite treatments (**Figure 15b**).

3° enrichment. After 1:10 dilution and addition of 10 mM ferrihydrite on day 352, HCl-extractable Fe^{2+} doubled in the first week in N_2 treatments and bottle CH_4-1 (**Figure 15a**). Bottle CH_4-2 displayed similar activity after a two-week lag period. Over an additional 100 days (day 466), HCl-extractable Fe^{2+} increased to 2 mM. Goethite treatments and autoclaved controls had minimal activity (**Figure 15b**). As in the 2° enrichment, magnetic minerals formed in the presence of ferrihydrite (**Figure 15a**), but not goethite (**Figure 15b**).

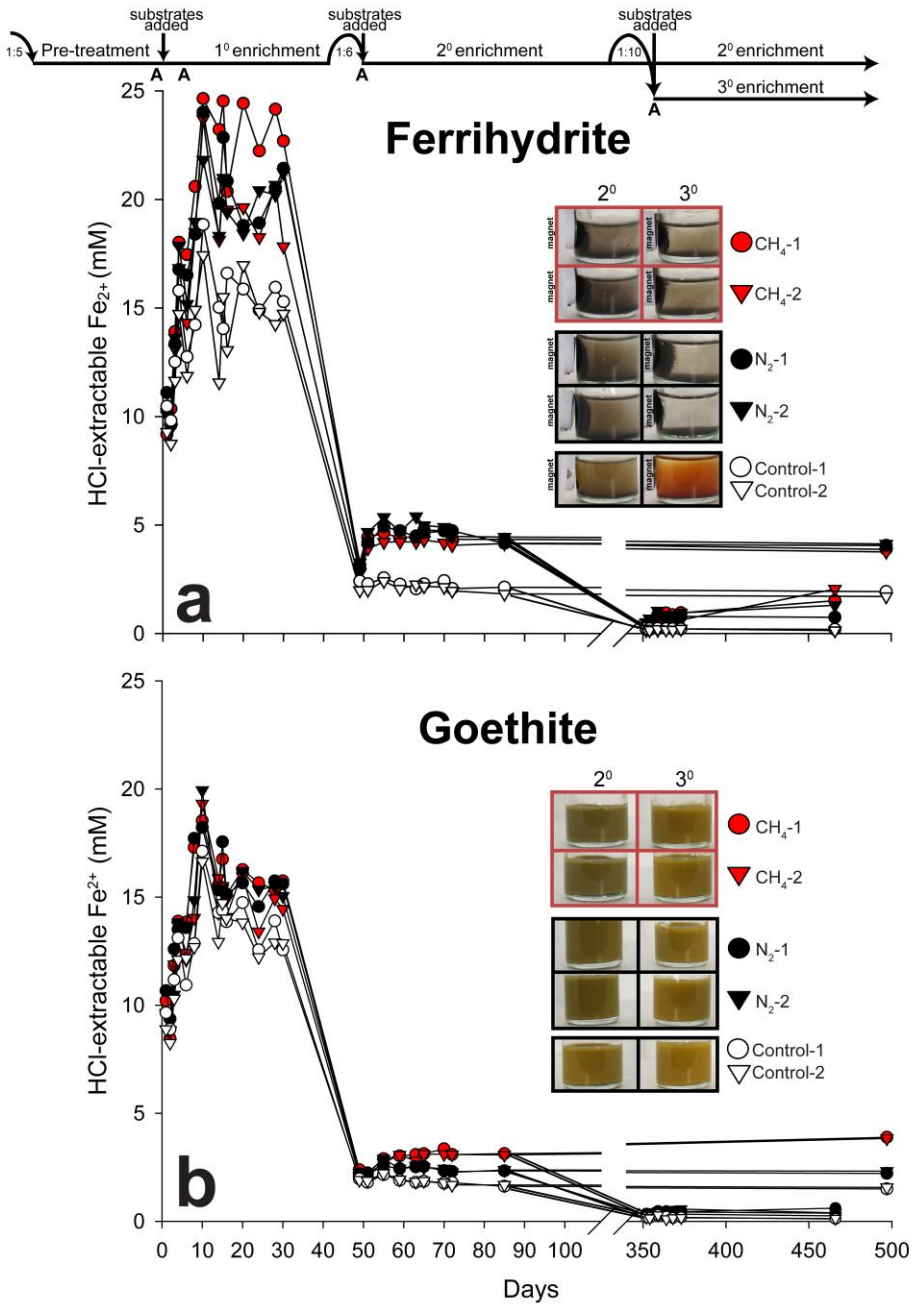

Figure 15. HCl-extractable Fe^{2+} for sediment enrichments with (a) ferrihydrite and (b) goethite over 497 days. Timeline at top shows transfer dates and dilution ratios. "A" represents days that controls were autoclaved. Red and black symbols represent treatments with and without CH_4, respectively. White symbols represent autoclaved controls. All treatments were run in duplicate (circle and triangle symbols). Photos depict 2° and 3° enrichment bottles on day 497 with evidence for magnetic mineral formation in live treatments amended with ferrihydrite.

4.4.2 Trace metal concentrations.

Total dissolved Ni averaged 41 ± 20 nM in fresh basal growth media, and was neither affected by Fe(III) oxide additions nor by puncturing of stainless steel needles through stoppers into culture liquid (**Table 8**). Dissolution of ferrihydrite in HNO_3 liberated significant Ni (2.5 μM; **Table 8**. Nickel was higher in enrichment cultures than in basal media: 96-286 and 54-134 nM with ferrihydrite and goethite, respectively; **Table 9**). Selenium was consistently below the detection limit (<128 nM) in growth media and enrichments culture.

Table 8. Total dissolved Ni (nM) in basal media with and without Fe(III) oxides. Samples were prepared in the same manner as enrichment cultures. A subset of samples was acidified in HNO_3^- prior to filtering and measurement. Error is reported as the standard deviation of triplicate measurements. "n.d." indicates not detectable.

Number of needle exposures	Medium	Medium +10 mM ferrihydrite	Medium +10 mM goethite	Medium +10 mM ferrihydrite + HNO_3	Medium +10 mM goethite + HNO_3
1	41 ± 20	32 ± 1	50 ± 36	2365	65*
2	44 ± 13	33 ± 11	52 ± 31	n.d.	n.d.
4	39 ± 9	30 ± 17	33 ± 10	n.d.	n.d.
6	41 ± 18	22 ± 19	33 ± 15	2385	605
8	41 ± 12	40 ± 19	42 ± 23	n.d.	n.d.
10	46 ± 16	38 ± 27	35 ± 4	n.d.	n.d.

Table 9. Total dissolved Ni (nM) in 2° and 3° enrichment cultures.

Treatment		Enrichment	
		2°	3°
Ferrihydrite	CH_4-1	130	241
	CH_4-2	150	118
	N_2-1	202	96
	N_2-2	286	254
Goethite	CH_4-1	104	101
	CH_4-2	56	117
	N_2-1	53	134
	N_2-2	54	90

4.4.3 Methane production.

Goethite treatments consistently displayed higher CH_4 production than those with ferrihydrite (**Figure 16**). In the 1° goethite enrichment, methanogenesis (13-19 µM CH_4 d^{-1}) coincided with the period of Fe(III) reduction, and stopped after HCl-extractable Fe^{3+} was completely consumed on day 10. Methanogenesis persisted throughout the 3° goethite enrichment (3 µM CH_4 d^{-1}). Negligible CH_4 was produced in the presence of ferrihydrite, except for the final timepoint for bottle N_2-2 in the 3° enrichment.

In an additional 4° enrichment (day 571-663), we tested the effect of H_2, Ni, and Se amendments, as well as no Fe(III) controls, on CH_4 production in goethite treatments (**Figure 17**). As in previous enrichments, bottle 1 consistently produced more CH_4 (17 µM CH_4 d^{-1}) than Bottle 2. There were no significant differences in CH_4 production with and without 20% H_2 headspace and 10 mM goethite. Like in previous enrichments with

goethite, minimal Fe(III) reduction was observed (data not shown). No CH_4 was produced in any of the treatments between day 619, when 1 μM Ni and Se were added, and day 663.

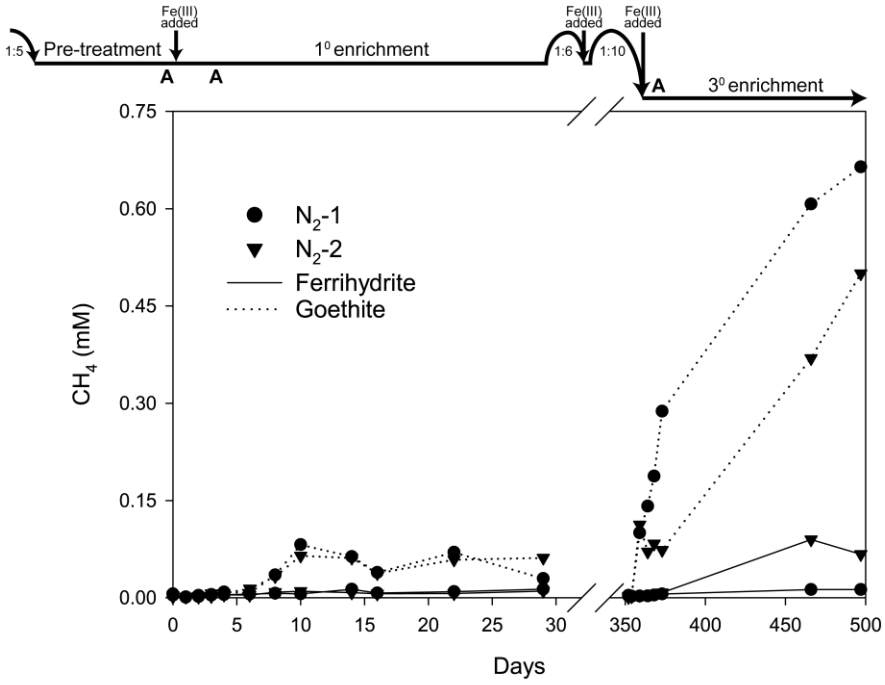

Figure 16. Accumulation of CH_4 in the headspace of sediment enrichments. Timeline at top shows transfer dates and dilution ratios. Solid and dotted lines represent ferrihydrite and goethite treatments, respectively. All treatments were run in duplicate (circle and triangle symbols). Original headspace was 100% N_2.

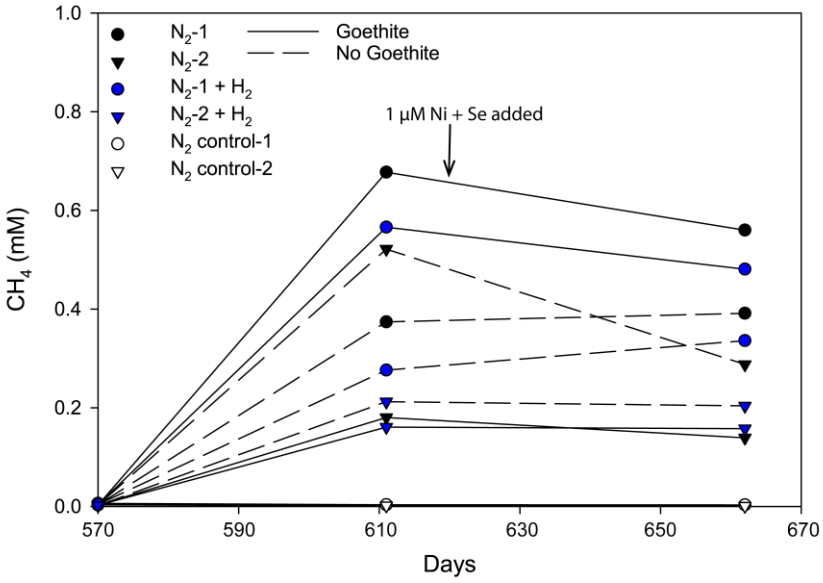

Figure 17. Accumulation of CH_4 in the headspace during the 4° enrichment (days 571-663). All treatments were run in duplicate (circle and triangle symbols). The arrow represents addition of 1 µM Ni and Se on day 619. Original headspace was 100% N_2 (black symbols) or 80 N_2 / 20% H_2 (blue symbols). White symbols represent autoclaved controls. Solid and dashed lines represent goethite and no Fe(III) treatments, respectively.

4.4.4 Methane oxidation.

1° enrichment. ^{13}C incorporation into DIC began on day 6 in both ferrihydrite and goethite treatments and continued for the remainder of the sampling period (**Figure 18a,b**). Ferrihydrite treatments showed lower ^{13}C-DIC enrichment but higher total DIC production (totaling to 1-2 µM CH_4 oxidized d^{-1}) than goethite treatments, which had greatest $\delta^{13}C$ enrichment but decreasing DIC concentrations, making calculation of CH_4 oxidation rates impossible. Autoclaved controls showed neither ^{13}C incorporation nor DIC production.

2° enrichment. Both ferrihydrite treatments displayed ^{13}C enrichment (**Figure 18a**), but declining DIC, precluding calculation of CH_4 oxidation rates. Initial pH of 8 declined to 7.6, 6.7 and 6 in the autoclaved, N_2 and CH_4 treatments, respectively. DIC in goethite treatments with CH_4 dropped to undetectable values within three weeks, suggesting sampling or analytical error, which precluded accurate isotopic measurement at these time points. These data are thus not considered further. Autoclaved and N_2 controls did not show pH changes.

3° enrichment. Bottle CH_4-2 with ferrihydrite was the only treatment with significant ^{13}C incorporation into DIC over the first 15 days (**Figure 18a**). Over the same interval, DIC increased in both ferrihydrite-amended bottles (yielding CH_4 oxidation rates of 32 and 7 $\mu M\ d^{-1}$ in bottle 1 and 2, respectively) and pH dropped from 8.2 to 7.1 and 7.9 in bottles 1 and 2, respectively. By day 470, ^{13}C enrichment and DIC concentrations in both ferrihydrite-amended bottles had returned to a level similar to that at the start of the 3° enrichment. Autoclaved controls did not exhibit any change in DIC and pH. Goethite treatments had initial DIC concentrations (3-5 mM) higher than those in previous enrichments. In the goethite-amended autoclaved controls and bottle CH_4-1, DIC concentrations dropped over the 3° enrichment. Only goethite-amended bottle CH_4-2 increased in DIC, without concurrent ^{13}C enrichment. Large DIC variability implies that reported rates may be underestimates if declining pH led to outgassing of ^{13}C-DIC into the headspace CO_2 pool.

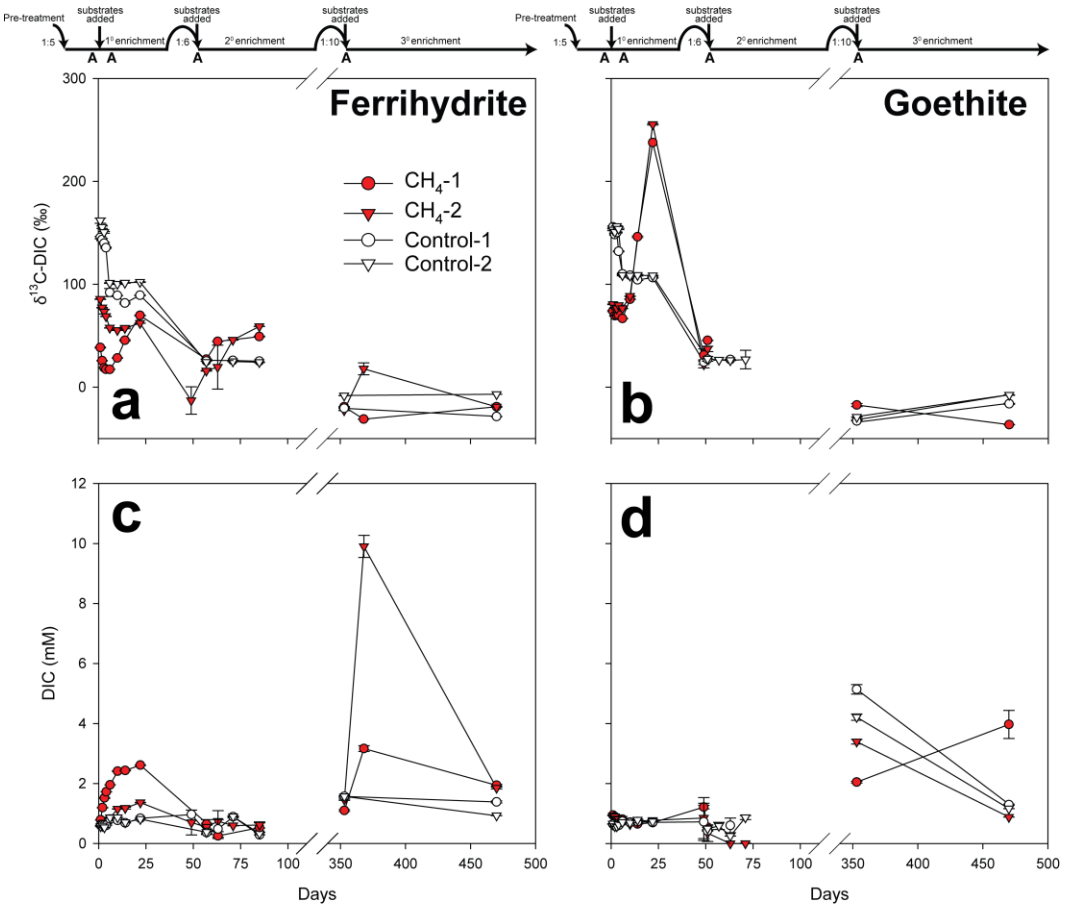

Figure 18. Dissolved inorganic carbon (DIC) isotopic composition and concentration for sediment enrichments amended with $^{13}CH_4$ and either (a,c) ferrihydrite or (b,d) goethite. Timeline at top shows transfer dates and dilution ratios. "A" represents days that controls were autoclaved. Red and white symbols represent live treatments and autoclaved controls, respectively. Errors bars represent standard deviation of triplicate measurements. Calculated CH_4 oxidation rates for the 1° enrichment were 1.7 and 1.1 □M CH_4 d^{-1} ferrihydrite bottles 1 and 2, respectively and 0.2 and 0.8 □M CH_4 d^{-1} for goethite bottles 1 and 2, respectively. Isotopic data are not plotted for DIC concentrations 0.5 mM. Rate calculations were not possible for the 2° enrichment due to low/variable DIC.

4.4.5 Microbial taxonomy.

Inoculum. 16S rRNA gene amplicons from the sediment inoculum were dominated by *Bathyarchaeota* (25%), formerly Miscellaneous Crenarchaeotal Group (MCG) and unclassified Archaea (11%; **Figure 19**).

1° enrichment. Species richness, evenness and phylogenetic diversity decreased relative to the inoculum in all treatments (**Figure 19**). *Geobacteraceae* (*Deltaproteobacteria*) became dominant (22-36%) in all ferrihydrite treatments (**Figure 19a**); the dominant OTU had 97% similarity to *Geothermobacter* sp. Ferrihydrite-amended bottle CH_4-1 was enriched in the *Betaproteobacteria*, specifically *Comamonaceadeae* (17%) and *Rhodocyclaceae* (9%; **Figure 19a**). *Bathyarchaeota* persisted in goethite treatments (11-25%; **Figure 19b**).

2° enrichment. All treatments declined further in species richness, evenness, and phylogenetic diversity. Unclassified *Desulfuromondales* dominated both ferrihydrite and goethite enrichments (34-68%). The dominant OTU had 98% similarity to *Geobacter hephaestius/Geobacter lovleyi. Geobacteraceae* declined in ferrihydrite enrichments (2-18%; **Figure 19a**). *Campylobacteraceae* (*Epsilonproteobacteria*), a trace constituent of the inoculum and 1° enrichment, were enriched in goethite treatments with CH_4 (23-40%); the dominant OTU had 98% similarity to *Sulfurospirillum barnesii* (**Figure 19b**). The most abundant methanogenic *Euryarchaeota* family, *Methanobacteriaceae*, comprised 1-2% and 6-7% of sequences in ferrihydrite and goethite treatments, respectively; the dominant

OTU had 100% similarity to *Methanobacterium flexile*. *Bathyarchaeota* were depleted compared to the 1° enrichment (**Figure 19**).

3° enrichment. Species richness, evenness, and phylogenetic diversity continued to decline (**Figure 19a,b**). Unclassified *Desulfuromondales* dominated goethite treatments (32-76%; **Figure 19b**) and were less abundant in ferrihydrite treatments (18-38%); as in the 2° enrichment, the dominant OTU had 98% identity to *Geobacter hephaestius/Geobacter lovleyi*. *Rhodocyclaceae* were more abundant in ferrihydrite treatments with CH_4 (14-15%) than with N_2 (2-4%; **Figure 19a**); the dominant OTU had 100% similarity to *Azospira oryzae/Dechlorosoma suillum*. *Peptococcaceae* (*Firmicutes*) were most abundant in bottle CH_4-2 with ferrihydrite (30%); the dominant OTU had 96% similarity to uncultured members of the genus *Thermincola*. *Syntrophaceae* (*Deltaproteobacteria*) were enriched in all ferrihydrite treatments (11-16%) and goethite treatments with N_2 (8-15%); the dominant OTU had 97% similarity to *Smithella propionica*. *Methanobacteriaceae* comprised 1-4% of sequences in goethite treatments and were absent from ferrihydrite treatments; as in the 2° enrichment, the dominant OTU had 100% identity to *Methanobacterium flexile*.

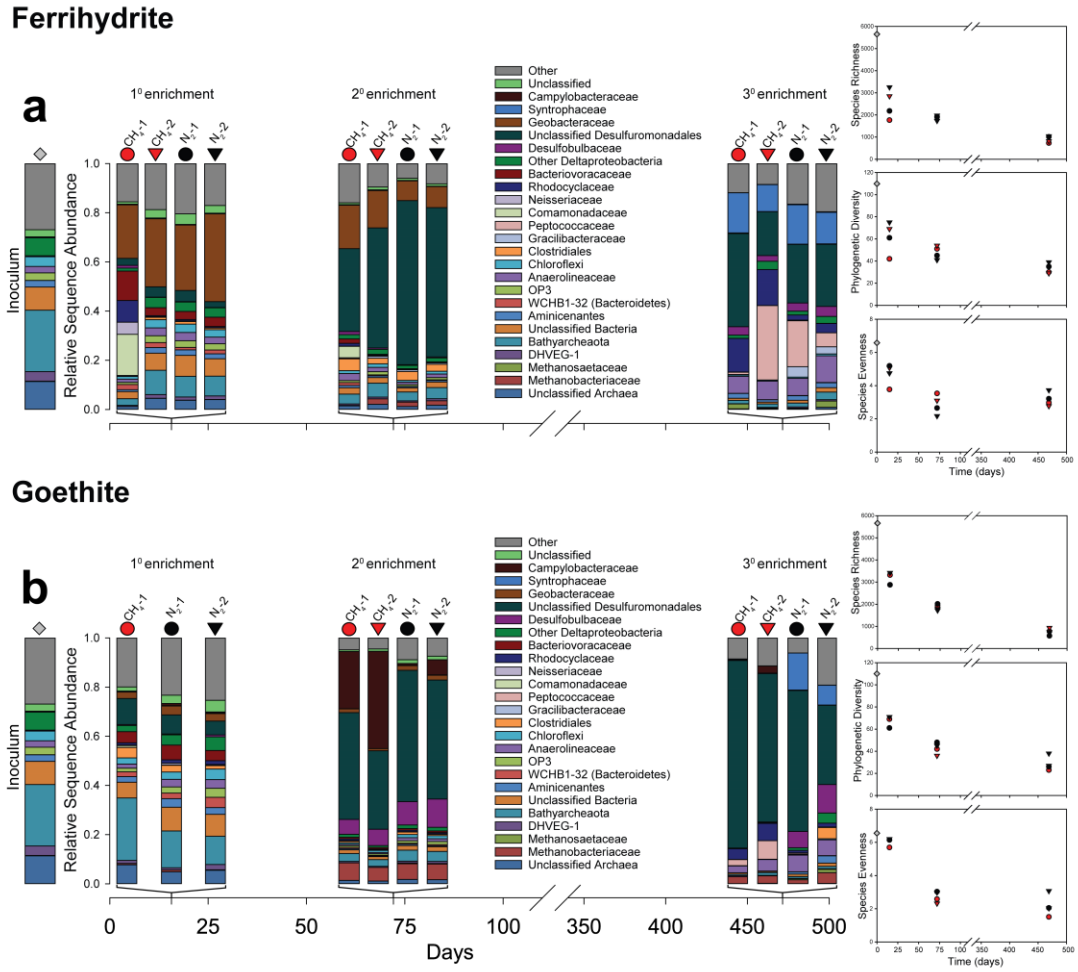

Figure 19. 16S rRNA gene diversity and phylogenetic diversity for inoculum and sediment enrichments amended with (a) ferrihydrite and (b) goethite. Samples were taken on day 15 (1° enrichment), 72 (2° enrichment) and 469 (3° enrichment). Red and black symbols represent treatments with and without CH_4, respectively. Gray diamonds represent inoculum samples. All treatments were run in duplicate (circle and triangle symbols). Species richness, phylogenetic diversity, and species evenness for the sediment inoculum and enrichments normalized to 4000 sequences per sample are shown to the right of bar charts.

4.5 Discussion

4.5.1 Fe(III) reduction rates in long-term ferruginous sediment incubations.

Initial rates of HCl-extractable Fe^{2+} production (1-2 mM d^{-1}) in the 1° enrichment were similar to those from freshwater wetlands with organic carbon as the electron donor (180-182). Despite replenishment of Fe(III) substrates, activity declined with each successive transfer, likely reflecting organic carbon limitation. The next most thermodynamically favorable electron donor, H_2, could have been supplied by fermenters (such as *Syntrophaceae* in the 3° enrichment), but would ultimately still require a source of organic carbon. Some of our incubations display evidence for CH_4, the next most thermodynamically favorable electron donor, as a source of electrons for Fe(III) reduction (e.g. higher Fe^{2+} yields with CH_4 addition with ferrihydrite in 1° and 3° enrichments, and with goethite in the 2° enrichment; see further discussion below).

Higher Fe(III) reduction rates were maintained on ferrihydrite than goethite, consistent with its higher energetic yield and (typically) greater surface area. Magnetic mineral formation was likely due to adsorption of Fe^{2+} onto ferrihydrite followed by solid-state conversion of ferrihydrite to magnetite (183). Since the HCl-extraction method does not dissolve magnetite and magnetite-adsorbed Fe^{2+} (184), it is possible that our Fe(III) reduction rates based on HCl-extractable Fe(II) production were underestimates of the total Fe(III) reduction.

4.5.2 Fe(III) oxide mineralogy controls methane production and methanogen taxonomy.

Our observation of higher rates of methanogenesis in goethite vs. ferrihydrite amendments is consistent with prior results showing that bacteria that reduce ferrihydrite better outcompete methanogenic archaea for H_2 and acetate than those that reduce more crystalline Fe(III) oxides, including goethite (147-149, 185, 186). This out competition is also broadly supported by taxonomic shifts in our enrichment cultures. In particular, anaerobic heterotrophs such as *Geothermobacter sp.* (187) were enriched in ferrihydrite treatments by day 15 and may have outcompeted other microbes for organic carbon sources.

Higher abundances of *Methanobacteriaceae* (0.1-1% and 1-4% on days 15 and 469, respectively) in goethite than ferrihydrite treatments (≤0.1%) suggest that CH_4 in goethite treatments came from the substrates used by *Methanobacteriaceae* (H_2/CO_2, formate, or CO). Addition of H_2 did not stimulate additional methanogenesis in the 4° amendment, implying another limiting substrate or growth condition. The ferrihydrite treatment (bottle 2) that produced CH_4 by day 469 contained 3% *Methanosaetaceae*; the most dominant OTU had 98% similarity to *Methanosaeta concilii,* in agreement with observations from the Lake Matano water column (163). *Methanosaeta* spp. produce CH_4 from acetate, or from H_2/CO_2 via direct interspecies electron transfer with *Geobacter* (188).

4.5.3 Fe(III)-dependent CH_4 oxidation.

Enrichments were established under conditions thought to be favorable for Fe(III)-dependent CH_4 oxidation, with Fe(III) oxides and CH_4 as the most abundant electron acceptors and donors, respectively. In the 1° enrichment, incorporation of $^{13}CH_4$ into DIC overlapped with the second phase of Fe(III) reduction (days 6-10), but calculating the

stoichiometry of CH_4 oxidized to Fe(III) reduced posed a challenge due to similar rates of Fe(III) reduction with and without added CH_4 and in autoclaved controls. ^{13}C-DIC enrichment from the back reaction of hydrogenotrophic methanogenesis (189) was ruled out because CH_4 oxidation continued after Fe(III) reduction and methanogenesis stopped at day 10. Therefore, CH_4 was likely oxidized by an electron acceptor other than Fe(III) (e.g. O_2, Mn(IV), NO_x^-, SO_4^{2-}) in the 1° enrichment, likely supplied by residual sediment or inadvertent introduction of air.

During the first 15 days of the 3° enrichment, rates of CH_4 oxidation and HCl-extractable Fe^{2+} production were similar (~10-20 μM d^{-1}) and roughly consistent with the low rates presented in K. F. Ettwig et al. (152) that yielded a 1:8 ratio, but lower than the rates from C. Cai et al. (168). However, the lack of multiple time points for the interval of simultaneous Fe(III) reduction and CH_4 oxidation, as well as similar initial rates of Fe(III) reduction with and without CH_4 throughout this interval, prevent us from attributing this activity to Fe(III)-dependent CH_4 oxidation with high confidence.

It is notable that the two incubations with the highest rates of CH_4 oxidation (ferrihydrite bottle 1 in 1° and 3° enrichments) were also the only treatments with very different microbial community compositions relative to other bottles in the same enrichment. In the 1° enrichment, ferrihydrite bottle-1 was enriched in Betaproteobacteria (*Comamonadaceae* and *Rhodocyclaceae*). In the 3° enrichment, the CH_4-1 sample had less *Peptococcaceae* than other ferrihydrite incubations. By day 469, the betaproteobacterium *Azospira oryzae/Dechlorosoma suillum*, a member of the *Rhodocyclaceae* family, was more abundant in both of the CH_4 vs. N_2 treatments. The potential role of this microbe in CH_4 cycling remains unclear, as laboratory cultures of this species are not known to oxidize

CH_4. Notably, related members of the *Betaproteobacteria*, including the genera *Azospira* and *Comamonas* found here, are typically facultative anaerobes that can use alternative electron acceptors like NO_3^-, NO_2^-, or perchlorate (190, 191). As such, these *Betaproteobacteria* are poised to respond to enhanced electron acceptor supply that accompanies pulse of O_2. Anecdotally, *Betaproteobacteria* are frequently associated with environments that are characterized by fluctuating redox conditions and periodic exposure to O_2 (192). Thus, their growth in our incubations may be a response to trace O_2 introduction. It is also possible that the growth of novel organisms capable of high rates of Fe(III)-dependent CH_4 oxidation was inhibited by other unidentified factors, potentially related to the batch-style incubations, the use of butyl rubber stoppers (193), or the lack of a critical substrate in the enrichment medium.

4.5.4 Effect of Fe(III) oxide and carbon substrates on microbial community diversity.

The microbial community underwent multiple shifts over the 500-day incubation, with an overall decrease in species richness, evenness, and phylogenetic diversity, likely in response to declining organic carbon. By the 3° enrichment, species evenness was consistently lower in each goethite-amended treatment than in the respective ferrihydrite-amended treatment. Higher species evenness could mean that the greater energetic yield of ferrihydrite reduction fosters higher diversity, or that the higher reactivity of ferrihydrite allowed it to be utilized by more organisms than goethite.

All of the most enriched taxa in our enrichments comprised ≤0.1% of the inoculum community and have relatives that reduce Fe(III) in laboratory cultures. Within those taxa, the most abundant OTUs were closely related to organisms capable of Fe(III) reduction

(*Geothermobacter sp.*, *Geobacter hephaestius/Geobacter lovleyi*, *Thermincola sp.*, and *Sulfurospirillum barnesii*) (187, 194, 195). *Desulfuromonadales* was the only metal-reducing taxon that was continuously present in all enrichments (3-11%, 34-53%, and 18-76% in the, 1°, 2°, and 3° enrichment respectively). Other taxa differed significantly in their abundance over the course of incubation. *Geobacteraceae* was enriched at day 15 with ferrihydrite (22-36%) but had declined in abundance by day 72 (8-18%). Still other taxa, including *Rhodocyclaceae* and *Peptococcaceae*, were enriched in the presence of ferrihydrite at day 469. In goethite treatments, *Campylobacteraceae* (23-40%) were enriched at day 72, but were minimal at day 469. The succession of different metal-reducing taxa may be due to the changing availability of electron donors (e.g. H_2 and organic C). Enrichment of *Syntrophaceae*, known for their synthrophic fermentative interactions, suggests the establishment of syntrophy in the 3° enrichment in response to depletion of electron donors.

4.5.5 Nickel sources.

Enrichment cultures contained ~2-10x more total dissolved Ni than the basal growth medium. The inoculum, ~60 nM in Lake Matano deep water, (169) would not have significantly contributed to the Ni pool past the 1° enrichment, and repeated needle exposure had no effect on Ni concentrations. The Ni source to enrichment cultures was likely partial ferrihydrite dissolution, since ferrihydrite readily scavenges Ni from solution (196), while its dissolution liberates Ni (Table 9; 197). Slow Ni leaching from silicate glass during extended contact between microbes and the serum bottles could have contributed another source of Ni in microbial enrichments vs. abiotic controls (198).

4.5.6 Geobiological implications.

Our results point to a mineralogical control on Fe(III) reduction, methanogenesis, and microbial community composition and diversity, under conditions of severe organic carbon limitation. These conditions likely existed in Archean and Paleoproterozoic oceans with relatively low amounts of primary production (4, 199). We posit that the relative abundance and distribution of Fe(III) phases in marine sediments would have impacted methanogenesis rates in the Archean and Paleoproterozoic. Sediments below shallow water columns were likely fed by abundant amorphous Fe(III) from photoferrotrophic activity, resulting in rapid sedimentation of amorphous Fe(III) phases (e.g. ferrihydrite). These Fe(III) oxides could have supported diverse Fe(III)-reducing communities that outcompeted other taxa such as methanogens for limited carbon and nutrients.

Conversely, slow deposition and aging of ferrihydrite to goethite could have limited both the abundance and diversity of Fe(III)-reducing microbes in sediments, allowing for more organic carbon remineralization via methanogenesis than Fe(III) reduction, as recently calculated for Lake Matano (163, 171). In the open ocean, organic carbon and Fe(III) would likely have been consumed before reaching sediments, leaving behind more crystalline Fe(III) phases. Importantly, the role of Fe(III)-driven CH_4 oxidation appears limited given our experimental results, although we cannot rule out this pathway given that some of our data suggest it may operate at low rates.

Availability of trace metal nutrients is another important consideration in potential controls on ancient CH_4 and Fe cycling. Measurements of Ni/Fe ratios in ancient marine sediments indicate that total dissolved Ni decreased from ~400 nM before 2.7 Ga to 200

nM between 2.7-2.5 Ga, to modern levels of 2-11 nM at ~0.5 Ga, assuming that the Fe(III) minerals in Archean sediments were of biological origin (200-202). It is likely that abundant Ni would have been bound and sequestered in Fe(III)-oxide rich sediments. Rapid and widespread Archean redox cycling of Fe(III) could have served as constant source of Ni for methanogenic communities. The influence of changing availability of Se (203) and other trace nutrients on methanogenesis rates through time remains open for further exploration.

4.6 Conclusions

Overall, our results support a model for a sustained CH_4 greenhouse in the Archean and Paleoproterozoic due to emissions from ferruginous oceans with spatially segregated habitats of bacterial reduction of reactive Fe(III) oxides and methanogenesis in the presence of less reactive Fe(III) phases. Rates of Fe(III) deposition, aging, and recrystallization may thus have played an important role in regulating the preservation of sedimentary Fe(III), the production of CH_4, and the ecology and diversity of the biosphere during the first half of Earth history. By the mid-Proterozoic, rising seawater sulfate likely stimulated anaerobic CH_4 oxidation, thereby minimizing marine CH_4 emissions and the CH_4 greenhouse (204).

CHAPTER 5. PHYLOGENETICALLY AND STRUCTURALLY DIVERSE ELECTROACTIVE PILI FROM ANOXIC ECOSYSTEMS

The work described in this chapter is currently in preparation for submission to a peer reviewed journal. I performed the majority of experimentation and data analyses. C. C. Padilla aided in the metagenomic sequencing and assembly. R.L. Simister and K. Thompson aided in BLAST searches and provided metagenomes. N. Szeinbaum provided sequences from Mn(IV) enrichments. The manuscript was written by J.B. Glass and myself.

5.1 Abstract

Electroactive type IV pili, or e-pili, are used by some microbial species for extracellular electron transport. Recent studies suggest that e-pili may be more phylogenetically and structurally diverse than previously assumed. All e-pilins studied to date contain a high percentage (≥9.8%) of aromatic amino acids and have no gaps > 35 aa between aromatic residues. Here, we investigated e-pilin genes in metagenomes from long term enrichment of Lake Matano sediment and diverse ecosystems including those in which metal reduction is likely important. We found that laboratory enrichments selected for e-pilins that were phylogenetically and structurally different than those in Lake Matano sediments. We also recovered genomes containing putative e-pilin genes from our laboratory incubations and used structural modelling to predict their electroactive capabilities. The putative e-pilins we recovered from environmental metagenomes were

diverse in phylogeny and protein length. We found that the majority of e-pilins in the environment may be “full-length” pilins and could be used by diverse bacterial taxa including members of the candidate phyla radiation. Our results expand upon the structural and phylogenetic diversity of e-pilins.

5.2 Introduction

Electroactive bacteria transport electrons through cell membranes into the extracellular environment (205). These organisms play important roles in biogeochemical cycles in soils and sediments, bioremediation of toxic metals, and energy generation in microbial fuel cells (206-209). Electroactive *Deltaproteobacteria* in the genus *Geobacter* transport electrons through conductive pili, also known as e-pili or geopili, composed of e-pilin subunits (210). *Geobacter* use e-pili for Fe(III) respiration, direct interspecies electron transfer (DIET), and growth on anodes (211-213).

E-pili are members of the ancient type IV pili proteins (214). Type IV pili have evolved to perform diverse cellular functions, including twitching motility, attachment, and genetic competence. Type IV pili are composed of pilin monomer proteins that assemble into the pili structure. Most bacteria also encode pseudopilins with distinct phylogeny (211) that share a similar structure to type IV pilins but assemble into type II secretion systems instead of pili (215-217).

Aromatic amino acid density seems to be essential for efficient electron transport in e-pili (218). The most conductive e-pilus measured to date is that of *Geobacter metallireducens*, which contains pilins with 15.3% aromatics, 59-aa mature length (after signal peptide sequence removal at the prepilin cleavage site), and no aromatic-free gaps

larger than 22 aa. The *G. metallireducens* e-pilus is 5000 times more conductive than the *Geobacter sulfurreducens* e-pilus, which has pilins with 9.8% aromatics, 61-aa mature length and the same aromatic spacing (219). These pilin proteins are truncated versions of canonical type IV pilins. The *G. sulfurreducens* e-pilus is 100 times more conductive than the *Geobacter uraniireducens* pilus, which is made up of a full length pilins at 193-aa and has 9.1% aromatics and a 53-aa aromatic-free gap (220). Longer, non-electroactive type IV pilins (120-160 aa), such as those from *G. uraniireducens*, and *Neisseria gonorrhoeae* are thought to be incapable of electroactivity due to insufficient aromatic residue packing (221-223).

Recently, the phylogenetic and structural diversity of e-pili has been expanded with the discovery of strongly conductive pili made of much longer e-pilins from organisms outside *Geobacter* (224). Like *Geobacter* e-pili, e-pilins from *Desulfurivibrio alkaliphilus* and *Calditerrivibrio nitroreducens* have high aromatic percentage (11 and 13%, respectively) and small aromatic-free gaps (22-aa and 27-aa, respectively). But *D. alkaliphilus* and *C. nitroreducens* have significantly longer sequences (119- and 182-aa, respectively) than *Geobacter* spp. (224). In addition, the archaellum of the methanogenic archaeon *Methanospirillum hungatei*, with pilins proteins containing 11% aromatics and a 35-aa aromatic free gap has also been shown to be conductive (225). Non-conductive pili from *Desulfofervidus auxilii*, *Shewanella oneidensis*, and *Pseudomonas aeruginosa* have pilins with 5.6-6.8% aromatics, 126-206-aa and 42-52-aa aromatic gaps (211, 224, 226). Therefore, it seems that the key factor for identifying e-pilins based on primary sequence is aromatic density, defined here as percentage of aromatic amino acids and spacing of aromatic residues in the pili sequence.

The phylogenetic and structural diversity of environmental e-pilins is largely unknown. Recently, pili were discovered in uncultivated microbes belonging to the candidate phyla radiation (CPR) from deep subsurface samples. These bacteria have type IV pilin genes and pili-like structures (227-229). The CPR is an enigmatic group of bacteria with unusually small genomes that comprise a significant fraction of the bacterial domain (230, 231), but the function of their type IV pili remains unknown.

In this study, we used aromatic density to predict e-pilins in metagenomes from anoxic, metal-rich, and oxic environments. Our results suggest that organisms from diverse phyla may use e-pili, and longer e-pilins may be more prevalent than truncated e-pilins in nature. We also found that Fe(III)-reducing sediment enrichments select for shorter e-pilins from *Desulfuromonadales* compared to native sediment.

5.3 Experimental Methods

5.3.1 Sampling and enrichment of Lake Matano sediment.

Two sediment cores were obtained from 590 and 200 m water depth in Lake Matano, Sulawesi Island, Indonesia in May 2010 and November 2014 respectively (2°28′S, 121°20′E, *in situ* sediment temperature ~27°C) and stored under anoxic conditions. The 590m sediments were mixed with anoxic freshwater media in a 1:5 ratio in an anoxic chamber and dispensed in stoppered serum bottles. Cultures were amended first with goethite and later with ferrihydrite. They were incubated for 490 days at 30ºC, with multiple transfers, each time diluting the original sediment with freshwater media. Sediment had been diluted over 600 times by the time DNA was extracted for sequencing. Details on 200 m sediment sampling methods and enrichment are found in Bray et al. (134).

Briefly, sediment was mixed in a 1:1 ratio with a minimal freshwater media and dispensed into 70 mL stoppered serum bottles under anoxic conditions. Cultures were amended with ferrihydrite and CH_4 before incubation at 30°C. Details on metagenomes from 395-day anoxic enrichments of Lake Matano sediment incubated with Mn^{3+} pyrophosphate are reported in a separate publication (Szeinbaum et al., in prep).

5.3.2 DNA extraction and metagenome sequencing, assembly, binning and annotation.

Community DNA was extracted from 2 g samples and purified using a PowerSoil Isolation Kit and UltraClean® 15 Purification Kit (formerly MO BIO Laboratories, now Qiagen, Carlsbad, CA, USA) following the manufacturer's protocol. Indexed libraries were created from purified community DNA using the NexteraXT DNA Sample Prep kit (Illumina, San Diego, CA, USA) following manufacturer instructions. Libraries were pooled and sequenced on two runs of an Illumina MiSeq using a 500 cycle (paired end 250 x 250 bp) kit. Illumina reads were quality trimmed using Trim Galore! (http://www.bioinformatics.babraham.ac.uk/projects/trim_galore/) with a quality score and minimum length cutoff of Q25 and 100 bp, respectively, and merged with FLASH with the shortest overlap of 25 bp. Barcoded sequences were de-multiplexed, trimmed (length cutoff 100 bp), and filtered to remove low quality reads (average Phred score <25) using Trim Galore!. Forward and reverse reads were assembled using SPAdes (232) with the 'meta' option. The number of contigs, contig length, GC content, N50, and L50 assembly statistics were calculated with metaQUAST (233). Contigs ≥ 500 nt were organized into genome bins based on tetranucleotide frequency and sequence coverage using MaxBin 2.0 (234). Bin completeness and contamination levels were estimated based on the representation of lineage-specific marker gene sets using CheckM (235). Marker

gene sets generated by CheckM were used to assess phylogeny of binned genomes. Binned genomes were annotated using RAST (236, 237). Raw sequence reads, and all genomic bins were deposited in NCBI under the accession number PRJNA505658.

5.3.3 Pilin identification from microbial metagenomes.

Environmental metagenomes and MAGs were downloaded from IMG JGI and NCBI (see **Table 13** for taxon object IDs). For all metagenomes, Prodigal (237) was used to predict genes from contig files and write them to amino acid fasta files. Predicted protein files were then used as databases for protein BLAST, using the *G. sulfurreducens* PilA protein as query. Hits with a bit score greater than 55 were pulled from the databases. These recovered sequences were then further verified as type IV pili using Pilfind (http://signalfind.org/pilfind.html), a web tool that identifies type IV pilin signal sequences (238). Pilin amino acid sequences were then run through a python script that calculated the mature pilin length, percent aromatic amino acids, and aromatic free gaps (https://github.com/GlassLabGT/Python-scripts). Partial genes were retained if truncated on the N-terminus before the signal peptide and removed if truncated on the C-terminus.

5.3.4 Pilin sequence and phylogenetic analysis.

Identified pilin sequences were aligned using ClustalW and a maximum likelihood tree was constructed using MEGA. Duplicate sequences were removed before tree construction. The evolutionary history among sequences was inferred by using the Maximum Likelihood method based on the JTT matrix-based model (239). The tree with the highest log likelihood is shown. Initial tree(s) for the heuristic search were obtained automatically by applying Neighbor-Join and BioNJ algorithms to a matrix of pairwise

distances estimated using a JTT model, and then selecting the topology with superior log likelihood value. The tree is drawn to scale, with branch lengths measured in the number of substitutions per site. The analysis involved 182 amino acid sequences. All positions with less than 95% site coverage were eliminated. That is, fewer than 5% alignment gaps, missing data, and ambiguous bases were allowed at any position. There were a total of 53 positions in the final dataset. Evolutionary analyses were conducted in MEGA7 (240). Relative conductivities of characterized e-pilin genes were calculated conductance values from D. J. F. Walker et al. (224), Y. Tan et al. (219) and D. J. F. Walker et al. (225).

5.3.5 Phylogenetic tree construction.

Phylogeny of MAGs was assessed by constructing a phylogenetic tree from a concatenated marker gene alignment generated from CheckM (235). Whole genome average amino acid and average nucleotide identity (AAI/ANI) values were generated using the AAI/ANI matrix tool available at http://enve-omics.ce.gatech.edu/ (241). Alignments and trees were constructed in MEGA (240) using maximum likelihood and each node was bootstrapped 100 times.

5.3.6 Pilus modelling.

Structural modelling of PilA amino acid sequences was conducted using the Iterative Threading ASSEmbly Refinement tool (I-TASSER) (242). The resulting .pdb files were visualized in pymol (https://pymol.org/2/). Pilus models were constructed by fitting PilA amino acid sequences onto the structure of the *N. gonorrhoeae* pilus (PDB entry 2HIL) using the ChimeraX program (243), except for the *G. sulfurreducens* pilin

NMR structure was used (PDB entry 2M7G; (244)). Inter-aromatic distances were calculated using the "Measurement" tool in pymol.

5.4 Results

5.4.1 Aromatic density distinguishes e-pilins from other type IV pilins.

We retrieved sequences for 7 biochemically confirmed e-pilins (**Table 10**)**,** 10 predicted e-pilins (**Table 11**; 245), and 36 functionally verified attachment/motility/competence pilins (26 type IV pilins and 10 pseudopilins; **Table 12**). All strongly conductive and predicted e-pilins had >9.8% aromatics and an aromatic-free gap of ≤35-aa, although most had a gap ≤22-aa. All but two of the 36 pilins implicated in functions other than electroactivity had <9.8% aromatic percentage and >22-aa aromatic-free gaps. The two aromatically-dense pilins were OxpG, an atypical pseudopilin involved in metal reduction in *G. sulfurreducens* (246), and PilA from *Dichelobacter nodosus* (247). The low aromatic density of 34/36 of the pilins implicated in functions other than electroactivity supports our hypothesis that high aromatic density is indicative of e-pilins. Therefore, we used ≥9.8% aromatics and <22-aa aromatic-free gap as a conservative threshold for recovering putative e-pilins from metagenomes.

Table 10. Characteristics of biochemically characterized e-pilin genes in order of increasing aromatic density, with conductivity relative to *G. sulfurreducens* calculated from D. J. F. Walker et al. (224), Y. Tan et al. (219), and D. J. F. Walker et al. (225).

Pili Type	Protein name	GenBank Accession	Organism	Function	Reference	% aro m-atics	Aromatic-free gap (aa)	Mature length	Relative conductivity (%)
Type IV	PilA	Gura_2677	*Geobacter uraniireducens*	Weakly conductive e-pilin (confirmed)	(219)	9.1	53	193	0.01
Type IV	PilA	GSU1496	*Geobacter sulfurreducens*	Strongly conductive e-pilin	**(211)**	9.8	22	61	1.0
Type IV	PilA	ADH86948.1	*Desulfurivibrio alkaliphilus*	(confirmed)	(224)	11.0	27	182	1.0
Type IV	PilA	Flexsi_2288	*Flexistipes sinusarabici*		(224)	13.3	22	60	1.5
Type IV	PilA	WP_013450279.1	*Calditerrivibrio nitroreducens*		(224)	13.4	22	119	2.2
Type IV	PilA	Gmet_1399	*Geobacter metallireducens*		(219)	15.3	22	59	5771
Archaellin	FlaA	WP_011450070.1	*Methanospirillum hungatei*		(225)	11.0	35	164	3.8

Table 11. Characteristics of predicted type IV e-pilin (PilA) proteins from D. E. Holmes et al. (245) in order of increasing aromatic density.

GenBank Accession	Organism	% aromatics	Aromatic-free gap (aa)	Mature length
Glov_2096	*Geobacter lovleyi*	10.0	22	60
WP_039645155	*Geobacter soli*	10.8	22	65
Ppro_1656	*Pelobacter propionicus*	10.9	22	64
WP_041974243	*Geobacter* sp. OR-1	12.5	22	64
Gbem_2590	*Geobacter bemidjiensis*	13.6	22	66
Hipma_0737	*Hippea maritima*	13.6	22	59
DEFDS_1270	*Deferribacter desulfuricans*	13.6	22	59
TOL2_21350	*Desulfobacula toluolica*	13.8	22	58
HRM2_27700	*Desulfobacterium autotrophicum*	15.3	22	59
WP_040199521	*Geoalkalibacter subterraneus*	15.5	22	66

Table 12. Functionally verified pseudopilins and attachment/motility/competence type IV pilins.

Pili Type	Protein name	GenBank Accession	Organism	Function	Reference	% arom-atics	Aromatic-free gap (aa)	Mature length
Type IV	PilA	WP_004090380.1	*Xylella fastidiosa*	Motility	(248)	3.5	75	142
Type IV	PilA	WP_011912242.1	*Pseudomonas stutzeri*	Competence	(249)	4.9	66	162
Type IV	PilA	WP_011767078.1	*Azoarcus sp.* BH72	Motility	(250)	5.0	33	60
Type IV	PilA	CAD14088.1	*Ralstonia solanacearum*	Competence Attachment Motility	(251)	5.2	37	154
Type IV	TfpQ	P07640.1	*Moraxella bovis*	Attachment	(252)	5.3	41	151
Type IV	PilA	CAH34774.1	*Burkholderia pseudomallei*	Attachment	(253)	5.4	42	167
Type IV	PilA	WP_003112842.1	*Pseudomonas aeruginosa*	Attachment Motility	(254, 255)	5.6	45	143
Type IV	PilA	WP_011070777.1	*Shewanella oneidensis*	Motility Attachment	(256)	5.6	42	126
Type IV	PilA	WP_019390097.1	*Kingella kingae*	Attachment	(257)	6.0	41	149
Type IV	PilA	CAC94922.1	*Ruminococcus albus*	Attachment	(258)	6.4	45	157
Pseudopilin	XpsG	WP_011035902.1	*Xanthomonas campestris*	Protein secretion	(259)	7.1	49	126
Type IV	PilA	WP_005694367.1	*Haemophilus influenzae*	Competence Motility	(260, 261)	7.3	24	137
Type IV	PilE	NP_273084.1	*Neisseria meningitidis*	Attachment	(262)	7.4	31	163
Type IV	PilA	AAA25310.1	*Moraxella nonliquefaciens*	Attachment	(263)	7.4	40	148
Type IV	PilA	AAL32049.1	*Vibrio vulnificus*	Attachment	(264)	7.4	32	135
Type IV	ComGC	AFQ58422.1	*Bacillus subtilis*	Competence	I. Chen et al. (265)	7.5	23	93
Type IV	ComGC	WP_000738626.1	*Streptococcus pneumoniae*	Competence	(266)	7.5	29	93
Type IV	HofG	WP_010872381.1	*Synechocystis sp.* PCC 6803	Motility	(267)	7.5	48	147
Type IV	PilA	AAC28468.1	*Eikenella corrodens*	Competence, Motility	(268)	7.6	25	145
Pseudopilin	Yts1G	CAC83032.1	*Yersinia enterocolitica*	Protein secretion	(269)	7.9	48	139
Type IV	PilE	5VXX_A	*Neisseria gonorrhoeae*	Competence Attachment	(270)	8.2	31	122
Pseudopilin	PulG	EUC91830.1	*Klebsiella oxytoca*	Protein secretion	(271)	8.2	48	134
Type IV	PilA	WP_005741096.1	*Pasteurella multocida*	Attachment	(252)	8.3	23	132
Type IV	PilA	AAM55486.1	*Thermus thermophilus*	Competence Motility	(272)	8.8	37	125
Pseudopilin	EspG	WP_000738789.1	*Vibrio cholerae*	Protein secretion	(273)	8.8	30	137
Pseudopilin	GspG	NP_417787.1	*Escherichia coli* str. K12	Protein secretion	(274)	8.8	48	136
Type IV	ApfA	ABN73976.1	*Actinobacillus pleuropneumoniae*	Attachment	(275)	8.9	25	135
Pseudopilin	ExeG	WP_011704371.1	*Aeromonas hydrophila*	Protein secretion	(276)	8.9	25	202
Pseudopilin	XcpT	WP_003103532.1	*Pseudomonas aeruginosa*	Protein secretion	(277)	9.0	48	134
Pseudopilin	LsdG	AAK58496.1	*Gluconacetobacter diazotrophicus*	Protein secretion	(278)	9.2	35	130

Table 12. Functionally verified pseudopilins and attachment/motility/competence type IV pilins.

Type IV	PilA	CAE79186.1	*Bdellovibrio bacteriovorus*	Attachment	(279)	9.5	35	179
Pseudopilin	LspG	AAD43220.1	*Legionella pneumophila*	Protein secretion	(280)	9.7	48	134
Type IV	PilA	WP_012031206.1	*Dichelobacter nodosus*	Competence	(247)	9.8	22	143
Type IV	PilA	AAC38305.1	*Legionella pneumophila*	Attachment	(281)	9.9	40	132
Type IV	PilA	WP_011555734.1	*Myxococcus xanthus*	Motility	(282)	10.1	31	208
Pseudopilin	OxpG	WP_010942420.1	*Geobacter sulfurreducens*	Protein secretion	(246)	11.0	22	127

5.4.2 Putative e-pilins can be a significant portion of type IV pilins in natural environments and are longer and more aromatically dense than characterized e-pilins.

We used the *G. sulfurreducens* e-pilin to query metagenomes and 16 MAGs from environments chosen based on where we predicted anaerobic respiration of metals to be an important microbial metabolism **(Table 13**). Environments included ferruginous sediments and lake water, lake and river sediments, lake water, deep anoxic groundwater, temperate forest soils, and crustal aquifer fluids. We then screened the retrieved sequences for type IV pilins using Pilfind (238).

Our search recovered 2,433 type IV pilins, which were then screened using the aromatic density threshold established above (≥9.8% aromatic amino acids and <22-aa aromatic gaps). After partial sequences were removed, the search resulted in 183 putative e-pilins of varying length (58-219 aa) and aromatic density (9.8-17.8%). Putative e-pilins

comprised up to one-third of the total type IV pilins recovered from a single environmental metagenome (**Table 13**). Less than one-fifth (28 sequences) of them were truncated (<70 aa). Seventy nine percent of truncated e-pilins clustered with *Deltaproteobacteria* sequences. Most putative e-pilins were long (133 were >100 aa). Most had 10-15% aromatics (144) and 22-aa aromatic-free gaps (162). Eight had ≥15% aromatics and three had >17% aromatics, including one with 17.8% aromatics from *Falkowbacteria*. Twenty-one had <22 aa maximum gap sizes (minimum: 15 aa), including a putative e-pilin from *Falkowbacteria* with 17.8% aromatics (16-aa gap).

Table 13. Putative e-pilin genes identified from 16 environments analyzed in this study. Putative e-pilins are defined as containing ≥9.8% aromatics and no >22-aa aromatic gaps. See Figure 20 for details about each putative e-pilin.

Environment	Sample	IMG ID/ GenBank BioProject	Protein-coding genes	Putative e-pilins / type 4 pilins	Mature length (aa)
Lake Matano, Indonesia	Ferruginous sediment	PRJNA521166	1,157,873	7/93	90-184
Lake Towuti, Indonesia		3300010328, 3300010324	10,203,152	16/113	58-131
Kabuno Bay, Lake Kivu, Democratic Republic of Congo	Ferruginous water column	3300014720, 3300013122, 3300013123, 3300013125, 3300013126, 3300013131, 3300013132, 3300013136, 3300013137	24,761,074	88/ 1,118	57-220
Prairie Pothole Lake, North Dakota, USA	Sediment	3300027975	1,493,055	8/24	60-119
Lake Baikal, Russia		3300025843	1,180,048	4/32	67-174
Broad Kill River, Delaware, USA		3300019765	669,074	0/1	N/A
Aspo, Sweden	Groundwater	3300014656	3,495,273	7/140	60-185
Crystal Geyser, Utah, USA		PRJNA297582, PRJNA362739	1,537,765	29/413	56-214
Rifle, Colorado, USA		PRJNA273161	633,116	11/389	106-158

Table 13. Putative e-pilin genes identified from 16 environments analyzed in this study.

Horonobe, Japan		PRJNA321556	557,865	7/37	64-146
Lake Tanganyika, Africa	Water column	3300020183, 3300021092	4,124,017	1/13	58
Georgia, USA		3300021437	464,898	0/5	129
Indiana, USA	Forest Soil	3300024317	530,797	1/12	67
Norway		3300028037	161,101	0/0	N/A
Czech Republic		3300023019	80,325	0/0	N/A
North Pond, Mid-Atlantic Ridge	Crustal aquifer	PRJNA391950	494,807	4/43	131-146
			Total	**183/ 2,433**	**56-220**

5.4.3 Sediment incubations enrich for different e-pilins than those present in the environment.

Next, we compared putative e-pilins sequences in metagenomes of native ferruginous sediment from Lake Matano, Indonesia and year-long laboratory incubations inoculated with Lake Matano sediment. Putative e-pilins in the native sediment had closest similarity to *Deltaproteobacteria*, *Aminicenantes* (OP8), *Planctomycetes*, and *Zixibacteria* (47-86% identity; **Table 14**). After incubation in the presence of metal oxides, thirteen putative e-pilin sequences were identified in metagenomes (**Table 15**). Twelve had closest BLAST hits (61-86% identity) to *Deltaproteobacteria*, and one to *Actinobacteria* (53% identity). Truncated e-pilins were present in long-term enrichments (length range: 59-128 aa). We did not identify truncated e-pilins in the native sediment, where e-pilin length ranged from 98-135 aa. Aromatic densities (10.0-15.3%) were similar between native and incubated sediments. Putative e-pilins comprised a higher fraction of total type IV pilins in incubations (38-100%) compared to native sediment (8%).

Table 14. Top BLAST hits of putative e-pilins from Lake Matano sediment environmental metagenome (NCBI PRJNA521166).

Sequence Identifier	Highest BLAST hit	% identity	GenBank Accession
Mat2015_MH110217_1821307_5	*Candidatus* Aminicenantes bacterium 4484_214	67	OQX53064.1
Mat2015_MH110217_1047526_0	Candidate division *Zixibacteria* bacterium SM23_73_3	73	KPL00836.1
Mat2015_MH110217_1012563_1	*Candidatus* Aminicenantes bacterium 4484_214	86	OQX53064.1
Mat2015_MH110217_793719_1	*Candidatus* Aminicenantes bacterium 4484_214	63	OQX53064.1
Mat2015_MH110217_2342034_1	*Deltaproteobacteria* bacterium SM23_61	66	KPK92234.1
Mat2015_MH110217_201312_0	*Deltaproteobacteria* bacterium SM23_61	66	KPK92234.1
Mat2015_MH110217_178736_0	*Blastopirellula marina*	50	WP_081444895.1

Table 15. Highest BLAST hits of putative e-pilin sequences recovered from metagenomes of Lake Matano sediment enrichments. For identical sequences in multiple samples, all samples and sequence IDs are reported.

Enrichment condition(s)	Sequence Identifier	Highest BLAST hit	% identity	GenBank Accession
490-d Fe/CH_4 (311FMe)	NODE_14350_length_528_cov_2.926_ID_1352499_1	*Actinobacteria* bacterium HGW-Actinobacteria-1	53	PKQ38888.1
490-d Fe/CH_4 (311FMe)	NODE_66_length_43557_cov_17.4325_ID_1134761_24,	*Geobacteraceae* bacterium GWB2_52_12	78	OGT98677.1
490-d Fe/N_2 (311FN)	NODE_20_length_106690_cov_51.9889_ID_2925246_25	*Geobacteraceae* bacterium GWB2_52_12	78	OGT98677.1
490-d Fe/N_2 (311FN)	NODE_9312_length_1309_cov_2.84609_ID_3097345_2	*Geobacteraceae* bacterium GWC2_55_20	81	OGU08484.1
490-d Fe/N_2 (311FN)	NODE_1878_length_3699_cov_4.42563_ID_2976734_6	*Geobacter metallireducens* GS-15	86	ABB32086.1
490-d Fe/N_2 (311FN)	NODE_378_length_15370_cov_9.81312_ID_2943955_10	*Geobacteraceae* bacterium GWC2_55_20	71	OGU08484.1
490-d Fe/N_2 (311FN)	NODE_412_length_14811_cov_10.6042_ID_3649004_13	*Deltaproteobacteria* bacterium HGW-Deltaproteobacteria-1	62	PKN88777.1
490-d Fe/N_2 (311FN)	NODE_124993_length_391_cov_1.22619_ID_3689834_1	*Deltaproteobacteria* bacterium HGW-Deltaproteobacteria-6	61	PKN20377.1
395-d Mn/N_2 (s9)	NODE_49_length_49434_cov_49.5395_ID_406942_28	*Geobacteraceae* bacterium GWB2_52_12	84	RNC67631.1
395-d Mn/N_2 (s11)	NODE_93_length_31945_cov_19.3338_ID_476675_17	*Geobacteraceae* bacterium GWB2_52_12	84	RNC67631.1
395-d Mn/N_2 (s9)	NODE_34_length_82392_cov_49.8953_ID_405241_34	*Geobacter pickeringii*	72	RNC68730.1
395-d Mn/N_2 (s11)	NODE_26_length_82413_cov_20.5335_ID_472006_33	*Geobacter pickeringii*	72	RNC68730.1

5.4.4 Putative e-pilins are phylogenetically diverse.

To determine the phylogenetic diversity of pilins, we aligned all of the pilins described above and constructed a maximum likelihood tree (**Figure 20**). The phylogeny shows that the majority of our environmental putative e-pilins are distinct from

pseudopilins and other type IV pilins. A third of environmental putative e-pilins, including most of the truncated (<70-aa) sequences, clustered with *Deltaproteobacteria*. Twelve sequences were identified in MAGs of CPR bacteria from deep subsurface samples, and nine sequences from ferruginous water from Kabuno Bay clustered with these CPR pilins. Putative e-pilins were also found in groundwater MAGs from members of the *Flavobacteriaceae*, *Dependentiae* (formerly TM6), *Nitrospinae*, *Acidobacteria*, *Elusimicrobia, Alteromonas, Ectothiorhodospiraceae,* and *Betaproteobacteria*.

Nine out of ten pseudopilins, as well as two putative e-pilins from Kabuno Bay, formed a distinct cluster from other type IV pilins. More than half non electroactive type IV pilins formed a distinct cluster; the others were dispersed throughout the tree. The *G. sulfurreducens* OxpG protein did not cluster with the other pseudopilins. Eleven putative e-pilins from anoxic groundwater and anoxic and ferruginous sediment clustered with the *G. sulfurreducens* OxpG sequence. The two competence pilins from Firmicutes, the only sequences from gram positive organisms, were divergent from most other sequences in the analysis.

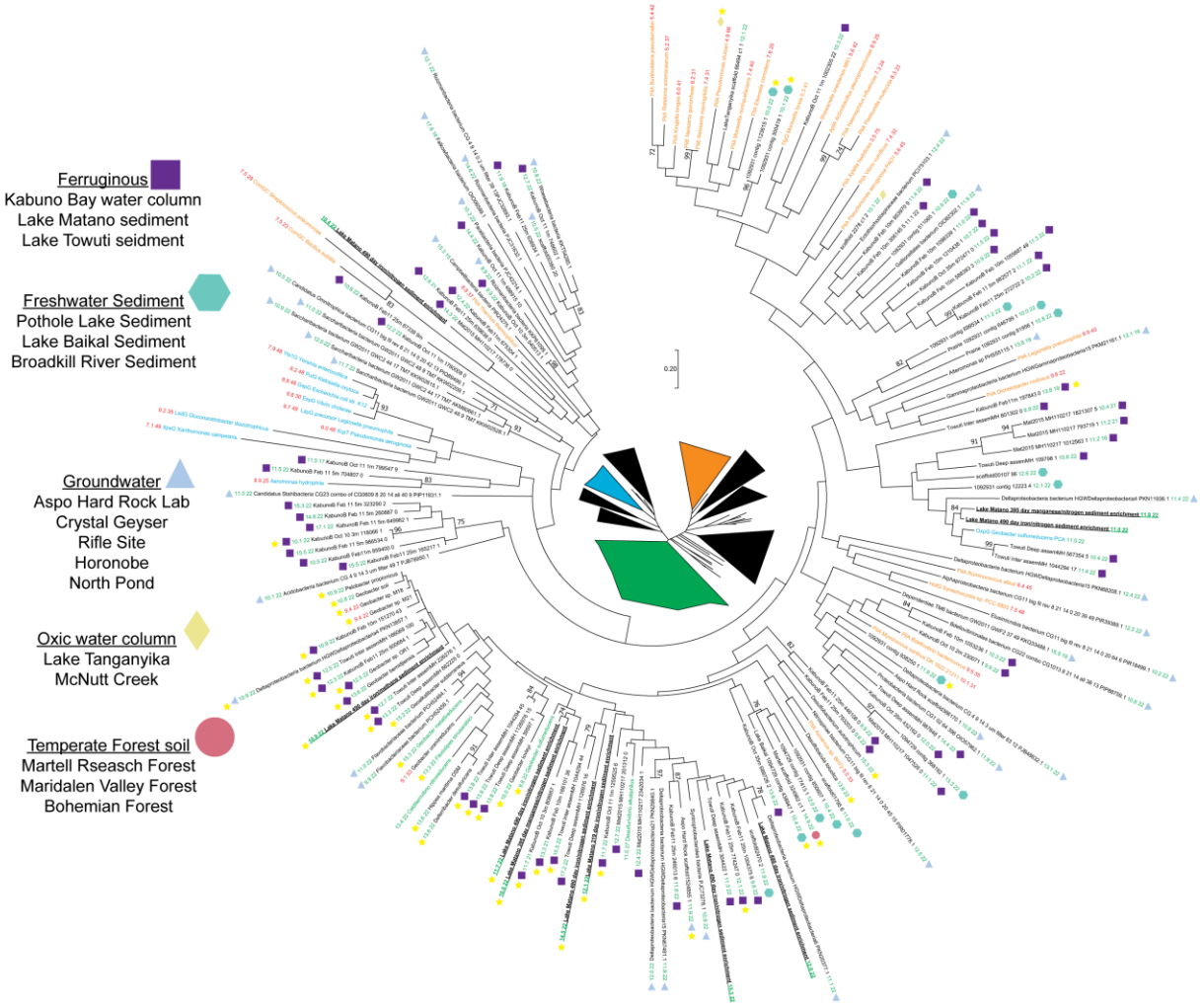

Figure 20. Maximum likelihood phylogenetic tree of pilin genes. Functionally verified pseudopilins are shown in blue while Type IV pilin implicated in functions other than electroactivity are shown in orange. Characterized e-pilins are shown in green. Putative e-pilins from Lake Matano sediment enrichments are bolded and underlined. Putative e-pilins from environmental genomes have symbols beside them denoting the type of environment they were recovered from. All sequences have aromatic percentage and smallest aromatic free gap besides their name. Red numbers refer to low aromatic density with green ones refer to high aromatic density. Starred sequences are <70aa long. The small radiation tree in the middle highlights the major clusters on the larger tree.

5.4.5 Identification of pilins from Lake Matano sediment enrichment MAGs.

Metagenomes were sequenced from two enrichments (D1FMe1 and 311FN) of Lake Matano sediment after anoxic incubations with CH_4 and ferrihydrite for 12 and 319 days, respectively. (The enrichment activity is described in a previous publication (134).) Both metagenomes yielded nearly complete MAGs (D1FMe1.001 and 311FN.001, respectively) classified to the Deltaproteobacteria order *Desulfuromonadales* (**Figure 21**). 311FN.001 had 77% average nucleotide identity (ANI) to *Geobacter uraniireducens.* D1FMe1.001 had 77% ANI to *Desulfuromonas soudanensis*. Both MAGs contained homologs to the major type IV structural pilin subunit (*pilA*) and pili biosynthesis genes (**Figure 22**). Compared to verified e-pilins, PilA from 311FN.001 (NCBI BioSamlpe accession SAMN10431265) was most closely related to the 61-aa PilA from *Geobacter sulfurreducens* (79% AAI), hereafter GsPilA. PilA from D1FMe1.001 (NCBI BioSample accession SAMN1043199) was most closely related to the 182-aa PilA of *Desulfovibrio alkaliphilus* (42% amino acid identity, or AAI). The synteny of pilin biosynthesis genes in 311FN.001 and D1FMe1.001 was similar to that of *G. sulfurreducens*. PilA from 311FN.001 had a mature length of 64 aa after signal peptide sequence removal at the prepilin cleavage site, and contained 10.9% aromatics, with a 22-aa aromatic-free gap from position 1-23; this PilA is hereafter referred to as “64-aa PilA”. PilA from D1FMe1.001 had a mature length of 186 aa and contained 9.7% aromatics, with a 63-aa aromatic-free gap from position 58-120; this PilA is hereafter referred to as “186-aa PilA”.

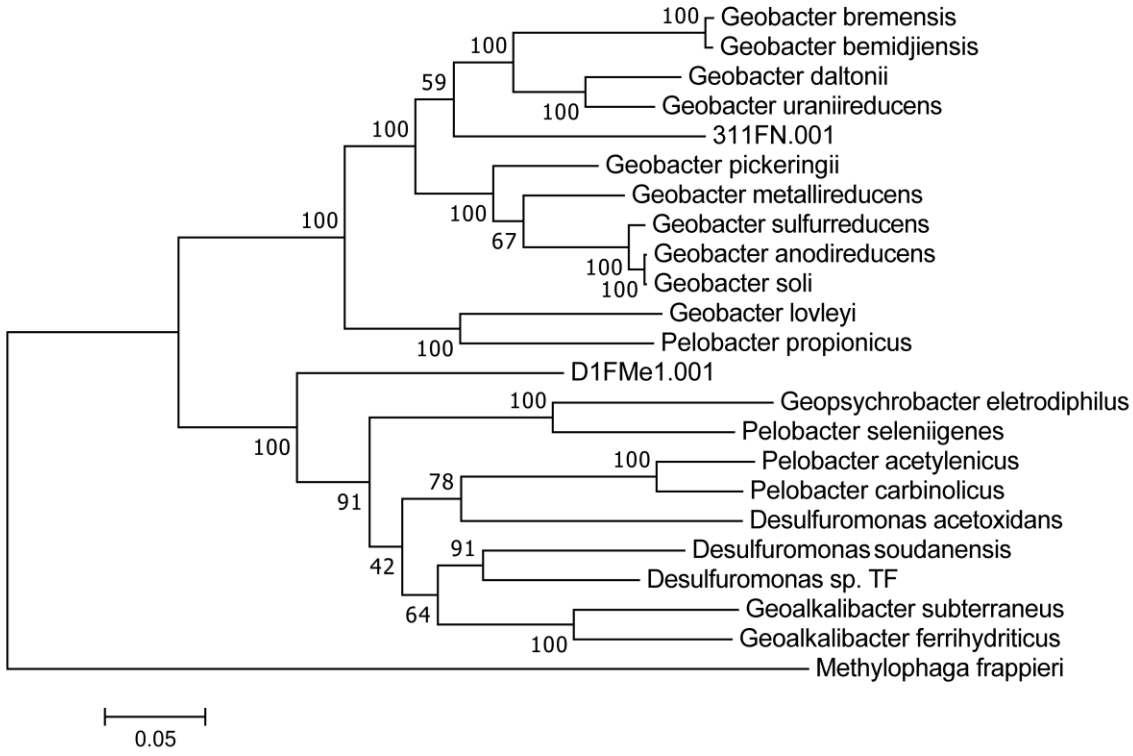

Figure 21. Maximum-likelihood phylogeny based on concatenated alignment of single copy marker genes for two MAGs 311FN.001 (SBEG00000000.1) and D1FMe1.001 (SRXA00000000) from anoxic Fe(III)-reducing enrichments of Lake Matano sediments. 311FN.001 had 77% ANI to *Geobacter uraniireducens*. D1FMe1.001 had 77% ANI to *Desulfuromonas soudanensis*. The alignment was generated with CheckM (235). 100 bootstrap values are reported at tree nodes.

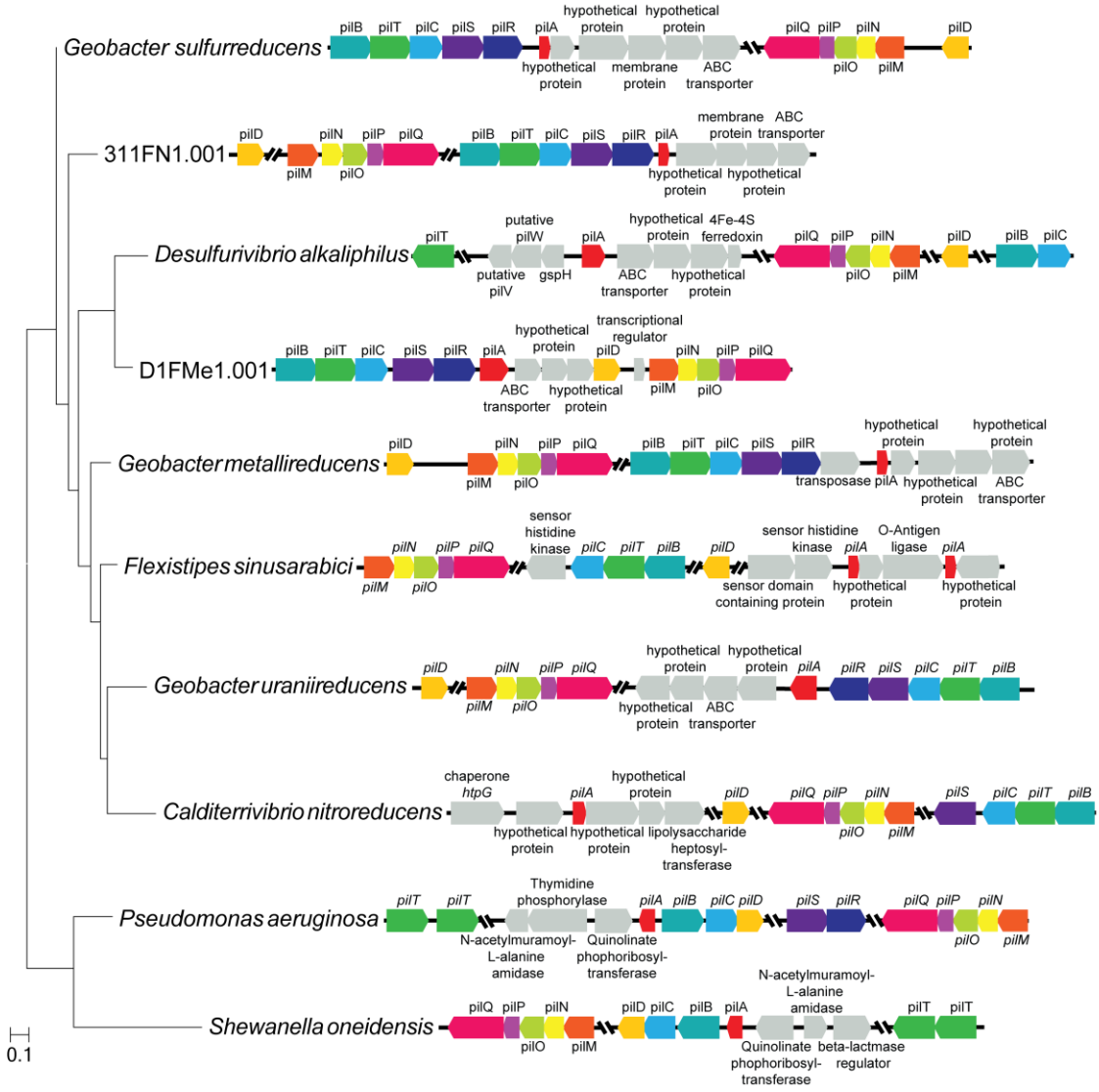

Figure 22. Gene organization of putative pili compared to pili tested for conductivity. Maximum likelihood phylogenetic tree of the two mature pilin genes identified from the Lake Matano metagenome and the eight pilins tested for conductivity in D. J. F. Walker et al. (224). Also shown is the synteny of major pilin biosynthesis genes. Tree was constructed in MEGA using the first 60 amino acids of each sequence and bootstrapped 500 times for verification.

5.4.6 Structural modelling of predicted e-pili.

Homology-based structural modelling predicted that the 64-aa PilA contained a single α-helix, similar to the truncated e-pilin NMR structure from *G. sulfurreducens* (PDB entry 2M7G; 244), but without the mid-helix kink found in most PilA structures (214) (**Figure 23a)**. The 186-aa PilA model was more structurally similar to longer type IV pilins with C-terminal globular domains, such as PilA from *Neisseria gonorrhoeae* (PDB entry 2IH2; 283), which has not been tested for conductivity, but contains only 5.6% aromatics and a 31-aa aromatic-free gap. We also modeled PilA from *G. uraniireducens* (hereafter GuPilA) due to its similar length (198-aa) and aromatic density (9.1%) to the 186-aa PilA. Like the 186-aa PilA model, the GuPilA model consisted of an N-terminal α-helix with a globular C-terminal domain containing antiparallel beta sheets.

To measure inter-aromatic distances, we modeled the full pilus assembly of 64-aa PilA, 186-aa PilA, GsPilA, and GuPilA monomers by fitting each protein over the NMR structure of the 12.5 Å crystal/cryo-EM structure of the *N. gonorrhoeae* type IV pilus (Figure. 23b, PDB entry 2HIL; 283). We also modeled the structure of the weakly conductive pilus from *P. aeruginosa* (284). All pilus models had aromatic residues dotting their outer surface. The modeled 311FN.001 pilus (made of 64-aa PilA) was less tightly packed than the modeled *G. sulfurreducens* pilus. Like the individual PilA models, D1FMe1.001 and *G. uraniireducens* pilus models were similar, with a left-handed helix of aromatics spiraling up their lengths. Further inspection revealed electron paths between aromatics through all four pilus models, with inter-aromatic distances of 7.0-11.8 Å in 311FN.001, 3.3-9.1 Å in D1FMe1.001, 4.4-10.4 Å in *G. sulfurreducens*, and 3.6-11.9 Å in *G. uraniireducens* (compared to 3.3-11.4 Å in *N. gonorrhoeae*). Due to the large distance

between aromatics, and their positioning on opposite sides of the pilins, we were unable to trace a complete electron path between aromatic residues in the *P. aeruginosa* pili (Data not shown).

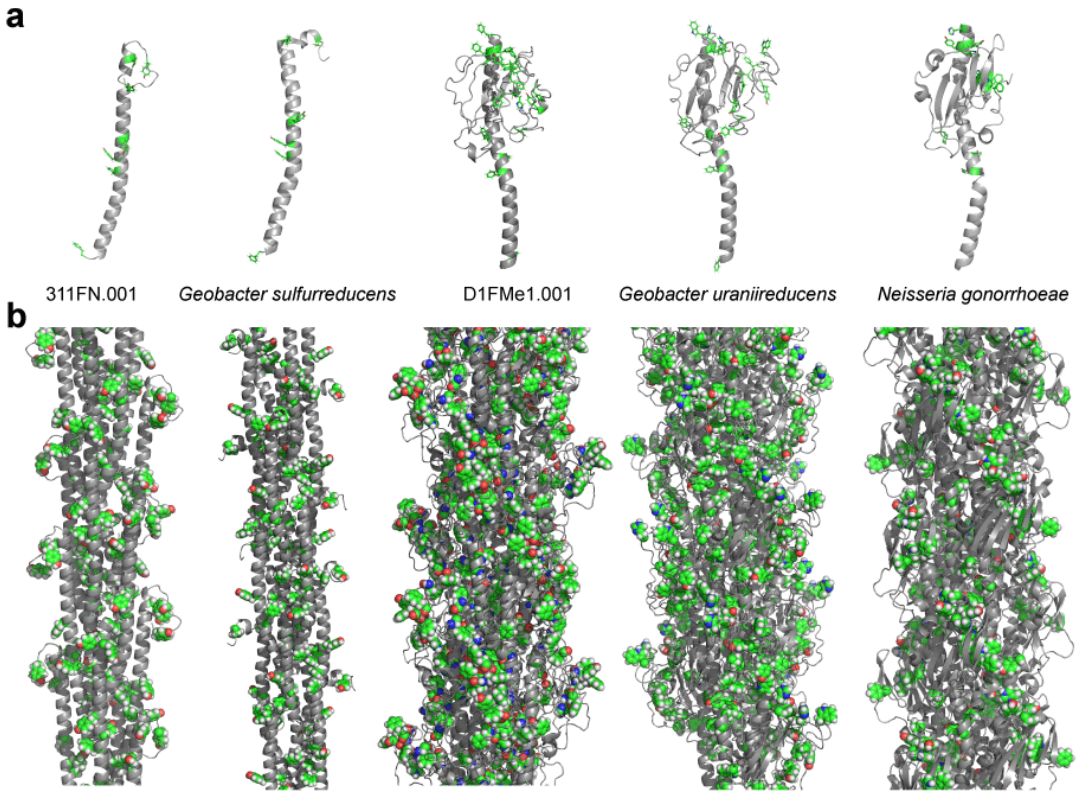

Figure 23. Modeled structures of PilA (a) and pili (b) for Lake Matano MAGs and *G. uraniireducens* compared to PilA crystal structures from *G. sulfurreducens* (PDB entry 2M7G) (244) and *N. gonorrhoeae* (PDB entry 2HI2) (283), and *N. gonorrheae* pilus crystal structure (PDB entry 2HIL). PilA models were generated using iTASSER webtool (285). Pilus models were constructed by fitting the PilA models or PDB structures onto the structure of the *N. gonorrhoeae* pilus (PDB entry 2HIL) using ChimeraX (286). Pymol was used for visualization and measurement of inter-aromatic distances.

5.5 Discussion

5.5.1 Expanding the phylogenetic diversity of e-pili.

Our identification of putative e-pilins in many bacterial taxa outside of *Deltaproteobacteria* suggests that a wide diversity of organism may use e-pili for electroactivity. Perhaps the most interesting among these are the CPR. Not much is known about the biogeochemical contribution of these organisms despite them making up >15% of the bacterial domain (230). While pilin genes have been identified in the genomes of these organisms, their function has not been identified. Although other genes involved in metal reduction have not been identified in CPR, our result suggests that some members of the CPR may use e-pili for some electroactive purpose. Images of what appear to be CPR cells using pili to attach to other larger cells have been reported, suggestive of DIET by these organisms (231). Due to their small genome size, many CPR organisms lack the genes necessary for full respiration pathways so DIET mediated by e-pili may allow these organisms to perform electron transfer (230).

We identified e-pilins in taxa known or predicted to perform metal reduction including *Alteromonas, Acidobacteria*, and *Zixibacteria*. Not only do cultured isolates of *Alteromonas* reduce Fe(III), but members of this genus can form electroactive biofilms (287). The presence of e-pilins is also consistent with the predicted capability of *Zixibacteria* for Fe(III) reduction (288). We also identified e-pilins in many clades that have not been implicated in metal reduction or extracellular electron transport including *Planctomycetes*, *Elusimicrobia*, *Nitrospinae*, *Aminicenantes*, *Ectothiorhodospiraceae*, *Dependentiae* (formerly TM6), and *Flavobacteriacea*. Although multiheme cytochromes

and MtrH homologs have been identified in *Planctomycetes* and *Elusimicrobia* (289, 290), none of these taxa have predicted capability for Fe(III) reduction. E-pilin proteins in *Ectothiorhodospiraceae* are interesting given that members of this clade are capable of iron oxidation and photoferrotrophy, suggesting a possible role for e-pilins in this process (291, 292). In addition to putative e-pilins, several sequences identified in this study clustered with OxpG from *G. sulfurreducens*, which suggests that some recovered sequences may not be type IV pilins but atypical pseudopilins that form metal-reducing type II secretion systems.

5.5.2 The diversity of pilin structure and characteristics is larger than previously thought.

Our results suggest that truncation may be rare among e-pilins, and a feature most common to *Deltaproteobacteria*. We found pilins of many different sizes to be aromatically dense, suggesting that length may not be a determinant for e-pili. Three environmental e-pilins were more aromatically dense than previously characterized e-pilin (>15.5%). Not only did some pilins have high percentage of aromatic residues, they also had aromatic residues that were evenly spaced leading to small aromatic-free gaps.

5.5.3 Laboratory incubations enrich for truncated Deltaproteobacterial e-pilins.

Long term incubations of ferruginous lake sediments under Fe(III)-reducing conditions enriched for organisms that utilize e-pilin proteins. Nearly all type IV pilins identified from sediment enrichments were putative e-pilins, whereas a smaller percentage of pilins in the native sediment were aromatically dense. In addition, enrichment under metal-reducing conditions yielded pilin proteins totally different from those found in the

native sediment. While pilins identified in native sediments were more phylogenetically diverse and longer, laboratory incubation seemed to select for shorter pilins belonging to the *Deltaproteobacteria*. This discrepancy is likely due to the fact that many environmental organisms do not grow well under laboratory conditions (293, 294). Furthermore e-pilins in the natural environments may not only be used for metal reduction, but instead DIET or some other unknown function, and so will not be selected for under metal-reducing conditions.

5.5.4 PilA proteins in enrichment metagenomes.

Based on the handful of e-pili biochemically characterized to date, the lowest aromatic percentage reported for a strongly conductive e-pilin is 9.8% (GsPilA), and the highest aromatic percentage reported for a weakly conductive e-pilin unable to support growth on Fe(III)-oxides is 9.1% (224). The percentage of aromatics in both PilA proteins identified from MAGs in this study suggest that they may form conductive structures. In addition to aromatic percentage, all of the characterized e-pilins have no aromatic-free sequence gaps >27 aa. While the 64-aa PilA meets both this criterion, the 186-aa does not as it has a gap of 63 aa. These findings suggest that the 64-aa PilA can likely form e-pili, while the 186-aa PilA is less likely to form for pili conductive enough to support electron transfer.

5.5.5 Modelling for pilus structural and functional prediction.

Overall, the pilin/pili model from 311FN.001 most resembled the *G. sulfurreducens* pilin structure/pili model, while the pilin/pili model from D1FMe1.001 resembled the *G. uraniireducens* model and the *N. gonorrhoeae* crystal structure. The 311FN.001 pilus

model is markedly less dense than the *G. sulfurreducens* pilus, despite similarities in pilin structure. Likely this discrepancy is caused by the lack of the S-shaped kink in the model structure of the 64-aa PilA that is seen in the structures of *G. sulfurreducens* and other type IV pilins (214). The lack of this kink in our model is perplexing and may indicate a limitation in the modelling software used, given that the sequence of 64-aa PilA contains the proline at site 22 that is thought to be responsible for this kink (295). Both the 186-aa PilA and GuPilA produced thicker pili like *N. gonorrhoeae*, but with more aromatic residues dotting the outer surface. The higher density of surface aromatic residues was most apparent for the D1FMe1.001 pilus. The pili from D1FMe1.001, *G. uraniireducens*, and *N. gonorrhoeae* had aromatics arranged in a left-handed helix, mostly due to the arrangement of pilin monomers in the pilus structure in a left-handed helix.

All of the pili modelled in this study, with the exception of *P. aeruginosa*, contained inter-aromatic distances in close enough proximity to facilitate electron transfer reactions (<12 Å). This observation was particularly interesting for the *N. gonorrhoeae* pilus crystal/cryo-EM hybrid structure. Based on the aromatic density of its pilins, this pilus should not be conductive enough to support electron transfer to solid surfaces. Yet the position of aromatics in the model suggest they are close enough to move electrons between them efficiently. To our knowledge there is no account of *N. gonorrhoeae* nor any member of *Neisseria* able to perform respiratory Fe(III)-reduction. Still it may be warranted to determine if these pili can restore solid Fe(III)-reduction activity in PilA-deficient strains of *Geobacter* as has been shown for pili from other organisms (224). In addition, the D1FMe1.001 pilus modelled structure showed discrepancy with its determined pilin

aromatic density. The results suggest limitations structural modeling analysis and highlight the need for additional measures in assigning function.

5.5.6 Possible functions for aromatically dense pilins besides electroactivity.

Out of the 36 non-electroactive pilin and pseudopilin proteins we analyzed, only two pilins were sufficiently aromatically dense to form e-pili based on the thresholds we established. The OxpG pseudopilin from *G. sulfurreducens*, is involved in metal reduction, possibly explaining its high aromatic density. Overall, this suggests that pilins dedicated to functions other than extracellular electron transport have low aromatic density. Low aromatic density is not surprising given that the highly conserved N-terminal region of the protein would be resistant to mutations needed to incorporate more aromatic amino acids. In addition, high amounts of aromatics in pilins could make pili more susceptible to oxidative damage (296). Hence, it is unlikely for pilin proteins to contain a high percentage of evenly spaced aromatic residues if not for some specific purpose.

While we infer that the aromatically dense pilins in this study form e-pili, we cannot be certain that they are not being used for some other function. It is unlikely that many of the sequences could be pseudopilins, given the functionally verified pseudopilin proteins clustered by themselves on the tree with only a couple of putative e-pilin sequences. Still without biochemical and genetic characterization of these proteins and the organisms they belong to, we cannot assign this function for certain. Other uses for aromatic amino acids included protein stability and DNA binding. Aromatic residues may help to hold pilin structure together under harsh environmental conditions (297, 298). However, none of the environments used in this study have extreme conditions that would necessitate increased

protein stability. In addition, the competence pilins analyzed in this study contained very low aromatic density, suggesting that either aromatic residues are not the method of DNA binding in these pilins or that only a few specific residues are needed. In addition, we cannot rule out the possibility that aromatically dense pilins are used for some other yet unknown function.

5.6 Conclusions

This study identified putative e-pilins in the environment using aromatic density and gaps as the predictive tool. The sequences we recovered suggest that e-pilins are both phylogenetically and structurally diverse. We conclude that e-pili may be composed of pilin monomers of a variety of lengths and aromatic densities, and that a variety of organisms may use e-pili for electron transfer or possibly other unknown functions. Still, without biochemical verification of conductivity and/or identification of other genes involved in pili biogenesis and Fe(III)-reduction we cannot for certain predict these protein's function in extracellular electron transport. While alternate uses for aromatic amino acid residues exist (protein stability, nucleic acid binding), these seem unlikely explanations given the environments from which e-pilins were recovered and the low aromatic density of known competence pilins. Overall, this study suggests there is variety of electroactive potential from diverse and understudied organisms and environments.

CHAPTER 6. IRON IN THE PAST, PRESENT, AND FUTURE OF LIFE ON EARTH

6.1 Expanding the role of Fe in biochemistry

This dissertation has shown that Fe^{2+} can play roles in biochemistry once thought exclusive to Mg^{2+}, shedding light on novel roles of this metal in extant biology while at the same time reaffirming its importance as a fixture in ancient biology. We infer from our results that because Fe^{2+} was abundant and soluble at the time of life's origin, it was the obvious choice as a cofactor for fledgling biochemical systems. More specifically, Fe^{2+} aided the form and function of molecules that would eventually perform protein synthesis, revolutionizing chemistry in what was possibly the most important single step on the way to cellular life. One can compare the advent of protein synthesis in biochemistry, with that of tool use in our early ancestor, *Homo habilis*. As soon as the first tool was carved from rock, no longer were early humans bound by the limitations of their physical forms, now they could perform new novel functions never before possible in the initial blueprint of the human body. While it was our ancestors' amazing and unique intelligence that allowed a useful tool to be born out of an otherwise banal piece of stone, it was M^{2+} such as Fe^{2+} that allowed early nucleic acids to fold and realize totally new, transformative functions. Given its geochemical important in the Archean, the biochemical roles we recognize Fe to fill in life on Earth today are merely a snapshot, a muted signal of its true importance to initializing and maintaining life on this planet.

What do these results say about extant translation and other similarly central and ancient biochemical systems still used by life? It is likely that the ribosome is not the only structure or system assimilating Fe when cells encounter environmental conditions reminiscent of the early Earth. Possibly other nucleic acid and nucleic acid processing systems behave in a similar fashion to the ribosome. One can imagine a cell in which DNA and multiple RNAs all have significant bound Fe^{2+}. Indeed, there is already *in vitro* evidence for this in the two other main reactions making up the central dogma of molecular biology (52). Furthermore, our knowledge of Fe in biochemistry comes almost exclusively from aerobes and facultative anaerobes, organisms that encounter oxygen on a regular basis, and so must very stringent with their Fe use. But what of obligate anaerobic organisms, those who have not been exposed to oxygen for nearly their entirely evolutionary history? What can we expect their bioinorganic chemistry to look like when they never had to cope with Fe scarcity or reactivity? In addition, are there transient states in bacteria and even higher organisms that could allow Fe to assume more roles in the cell? And what effect does that have on cellular homeostasis? Just like how the true influence of Fe on ancient biochemistry is still not fully realized, I believe that the true impact of Fe on extant biology has yet to be fully appreciated as well.

6.2 Iron influenced planetary habitability in the Archean

We know from the studies of current microbial ecosystems that microorganisms cohabitating the same environment can have significant effects on each other's growth and activity. We know too that the activity of microorganisms have serious, systemic effects on the cycling of elements through the Earth and on large scale planetary processes (299). These types of relationships and their effect on planetary cycles are harder to predict in the

ancient biosphere. By studying environments analogous to the ancient Earth, I have shown how the competing interests of Fe(III)-reducing microorganisms with methanogens in sediments could have had a significant effect on a major, long-term planetary process: habitability. The action of Fe(III)-reducing organisms had implications for all lifeforms in the early biosphere, and Fe's dynamic ability to interconvert between different mineral phases are likely what allowed CH_4 to increase greenhouse warming in the Archean.

The long-term habitability of our planet was and is essential to life. It is not enough that conditions on Earth were adequately favourable to give rise to lifeforms, conditions on our planet had to remain stable through evolutionary time for organisms to persist, multiply, spread, and adapt. Iron's role in this process may have been relevant throughout Earth history and could still be relevant today as humanity grapples with a rapidly changing climate. Understanding how Fe may positively or negatively affect greenhouse gas emission may crucial for mankind to predict and mitigate climate change. A better understanding of how different Fe mineral phases have different impacts on microbial activity is crucial to realizing its utility in maintaining planetary habitability in the past, present, and future.

6.3 Electroactive pili may be a diverse and important Fe reduction strategy

I sought to expand knowledge on how microorganisms are able to use solid chemical species such as Fe(III)-oxides as electron acceptors in the environment. Nearly all biochemistry occurs in an aqueous solution between soluble molecules and macromolecules, so the interaction of life with insoluble material presents unique challenges that life answered in unique ways. Of the mechanisms microorganisms use to

reduce Fe(III), electroactive pili are the only ones in which the cells make direct, yet long-distance contact with Fe(III) particles in their surrounding environment. The work presented in this thesis shows that this mechanism represents an important Fe(III)-reduction strategy that may be used by a wide range of microorganisms. The presence of these proteins in a wide range of bacteria phyla, some of them deeply branching, suggests this strategy may be older than previously considered and its use in the ferruginous environment of the Archean ocean can be postulated. We know that organisms would have evolved mechanisms to reduce the abundant Fe(III)-oxide minerals present in Archean sediment, and it may be that e-pili or perhaps a simpler version of them were one of the strategies used. Accurate quantifications of e-pili to Fe reduction in the environment will allow scientists to more confidently and accurately predict the movement of Fe through ecosystems over temporal and spatial gradients and as ecosystems respond to environmental changes.

Identifying more examples of e-pili may also lead to beneficial technological advancements. Microorganisms are objectively the greatest chemists in the known universe. They can catalyze molecular transformations at environmental parameters of which scientists can only dream. It is no wonder that scientists have time and time again looked to nature to solve challenging engineering and technological problems. Among these impressive chemistries that microorganisms employ is the reduction of solid species in the environment using e-pili. The aqueous-to-solid electron bridge that e-pili represent has resulted in organisms capable of reducing artificial surfaces such as those of electrical anodes. Electroactive organisms utilizing e-pili have become prime candidates for energy generation in microbial fuel cells, suggesting that bacteria may be a very real alternative

energy source. Our identification of more organisms with e-pili suggests that there may still be organisms in the environment that are very attractive candidates for current generation in microbial fuel cells. Further studies to enrich, isolate, and characterize diverse organisms carrying diverse e-pili have the potential to revolutionize microbial energy generation and be of great service to human civilization.

APPENDIX A. ENRICHMENT AND ISOLATION OF PERCHLORATE REDUCING ORGANISMS FROM LAKE MATANO

The work described in this appendix was not performed as part of my main thesis studies. This work represents a side project and is unpublished.

A.1 Introduction

Microbial perchlorate reduction is a fascinating process for a number of reasons. Despite ClO_4^- being principally an anthropogenic contaminant, microorganisms from a wide range of environments and taxa have been identified that are able to mediate the reduction of ClO_4^- into chloride anions. In addition, ClO_4^- has a higher redox potential than O_2, meaning organisms can extract more energy from this compound than they would growing aerobically. One of the steps of ClO_4^- reduction is the dismutation of chlorite (ClO_2^-) into Cl^- and O_2, making this metabolism one of only a handful on Earth with the terraforming potential of O_2 production. Finally, ClO_4^- has been recognized as an abundant constituent of other planetary bodies in our solar system, namely Mars (300). It is no wonder that ClO_4^- reduction is of great interest to diverse scientific fields spanning from bioremediation to astrobiology.

We previously performed sediment enrichments from Lake Matano Indonesia, a ferruginous tropical lake, under Fe(III)- and CH_4-rich conditions. Over the course of incubations, we consistently saw the presence of bacterial taxa that have been shown to contain members capable of ClO_4^- reduction. This signal was consistent between different

incubations and seemed to correlate with the presence of CH_4 in the headspace of our enrichments, leading me to speculate that the microbial community in these sediments could link the ClO_4^- and CH_4 cycles. Perchlorate coupled CH_4 oxidation is thermodynamically favorable based on the reaction below:

$$CH_4 + ClO_4^- \rightarrow HCO_3^- + Cl^- + H_2O + H^+$$

$$\Delta G_r^{0'} = -935.9 \text{ kJ mol}^{-1} CH_4$$

Based on previous publications reporting CH_4 linked ClO_4^- reduction (301, 302), we surmised that CH_4 oxidation could be linked to ClO_4^- reduction by two mechanisms. The first mechanism is that a single organism possessing the machinery for CH_4 oxidation and ClO_4^- reduction was mediating this process. This could be done either by performing reverse methanogenesis, or by using the O_2 produced by ClO_4^- reduction to activate CH_4 via the aerobic CH_4 oxidation pathway similar to the NC10 bacteria (303). Alternatively, a CH_4 oxidizer living in a consortium with a ClO_4^- reducer could mediate this process. In this mechanism, heterotrophic perchlorate reducers could produce O_2 for aerobic methanotrophs to use in the oxidation of CH_4 resulting in "cryptic" oxygen cycling under anoxic conditions. To investigate any links between CH_4 oxidation and ClO_4^- reduction in Lake Matano, we set up and monitored sediment enrichments containing both ClO_4^- and CH_4. We then attempted to isolate the microorganisms involved in ClO_4^- reduction.

A.2 Experimental Methods

A.2.1 Samples collection and storage.

Information on the collection and storage of sediment used in this study can be found in reference (134).

A.2.2 Enrichment medium.

A modified artificial freshwater medium lacking nitrate and sulfate was developed based on the pore water composition of Lake Matano sediments (S.A. Crowe and D.A. Fowle, unpublished work). The medium contained 825 μM $MgCl_2$, 550 μM $CaCO_3$, 3 mM $NaHCO_3$, 3.5 μM K_2HPO_4, 5 μM Na_2HPO_4, 225 μM NH_4Cl, 4.8 μM $MnCl_2$, 17 μM NaCl, 0.7 μM $FeSO_4$, 0.4 μM $CoCl_2$, 1 μM $CaCl_2$, 0.4 μM $ZnSO_4$, 0.04 μM $CuSO_4$, 0.02 μM $AlK(SO_4)_2$, 0.03 μM H_3BO_3, 0.04 μM Na_2MoO_4, 0.03 μM $LaCl_3$, 0.03 μM $CeCl_3$, 0.04 $NiCl_2$, 0.08 $NaSeO_4$, .1 μM biotin, 0.04 μM, 0.6 μM pyridoxine hydrochloride, 0.2 μM thiamine, 0.1 μM riboflavin, 0.4 μM nicotinic acid, 0.1 μM panthotenate, 0.7 μM cobalamin, 0.4 μM p-aminobenzoic acid, 0.2 μM thiotic acid. The vitamins were filter-sterilized and added separately after autoclaving.

A.2.3 Inoculation and incubation of sediments.

One hundred millilitres of enrichment media were dispensed into glass serum vials and sparged for 10 min with 10% CO_2 in N_2. Lake Matano sediment from 10-15 cm below the sediment water interface was mixed with enrichment media in a 1:1 ratio and 2 mL of this slurry was added to each serum bottle. Bottles were stoppered and headspace was then sparged with 100% N_2 for an additional ten minutes. Heat killed control bottles were then autoclaved for 30 min at 120º C. Sodium perchlorate and sodium acetate were added to cultures from stock solutions to a final concentration of 5 mM and 2 mM respectively. Five millilitres of ^{13}C labelled CH_4 was added to corresponding cultures using a gas tight

syringe. Cultures were left on bench top for several days for gaseous species to equilibrate before beginning incubation at 30º C in the dark. Culture treatments were as follows: Methane with acetate and perchlorate (CH_4 + Ac + ClO_4), Methane with perchlorate (CH_4 + ClO_4), No methane (100% N_2 headspace) with acetate and perchlorate (N_2 + Ac + ClO_4), and methane only (CH_4, no ClO_4). Heat killed controls were also incubated that contained methane acetate and perchlorate. All treatments were run in duplicate. For more information on these cultures, refer to **Table 26** in **Appendix D**.

A.2.4 δ^{13}C-DIC analysis.

Sampling for analysis of the ^{13}C content of the dissolved inorganic carbon in our cultures (^{13}C-DIC) was done by injecting 1 mL of culture into helium flushed 12 mL Exetainers (Labco Ltd, High Wycombe, UK) containing 1 mL 85% phosphoric acid. The solution was gently mixed and Exetainers were stored upside down until being sent for ^{13}C-DIC analysis at the UC Davis Stable Isotope Facility.

A.2.5 Acetate analysis.

Samples for acetate concentrations were measured by HPLC. Porewater samples were taken from enrichment cultures and filtered through 0.2 µm pore filters into 1 mL glass HPLC vials. Filtered samples were run on loaded onto an Agilent 1100 series HPLC system and run through a SUPELCOGEL C-610H column.

A.2.6 Isolation procedure.

In an anoxic chamber, agar slants were inoculated for isolation of perchlorate reducing organisms. The CH_4 with acetate and perchlorate culture (CH_4 + Ac + ClO_4) was

unstopped and a sterile inoculating loop was submerged into the culture. The loop was then spread over 2 agar slant that were then stoppered. Agar was made with enrichment media plus 5 mM sodium perchlorate and 5 mM sodium acetate. Both slants had headspace exchanged with 10% CO_2 in N_2. One culture also had 7 mL of 100% CH_4 injected into the headspace. Slants were place in 30º C incubator. Colonies from both slants were picked and used to inoculate 2 liquid cultures containing 50 mL of enrichment media with 5 mM sodium perchlorate and 5 mM sodium acetate. Colonies picked from CH_4 headspace slant also received 10 mL of 100% CH_4 in the headspace. Cultures were placed in 30º C incubator. A week after inoculation, and additional 5 mM sodium perchlorate and sodium acetate were added to both cultures and 3 mL CH_4 was added to CH_4 headspace culture.

A.3 Results

A.3.1 Perchlorate stimulates acetate production.

All cultures to which perchlorate was added produced significant acetate from days 1 to 4 (**Figure 24**). Autoclaved controls and cultures that received no perchlorate produced no acetate. Most acetate (~6 mM) was produced in cultures that received CH_4 perchlorate and acetate. This was significantly more than that produced in bottles that received just perchlorate and acetate (~4 mM), suggesting CH_4 was contributing to acetate production.

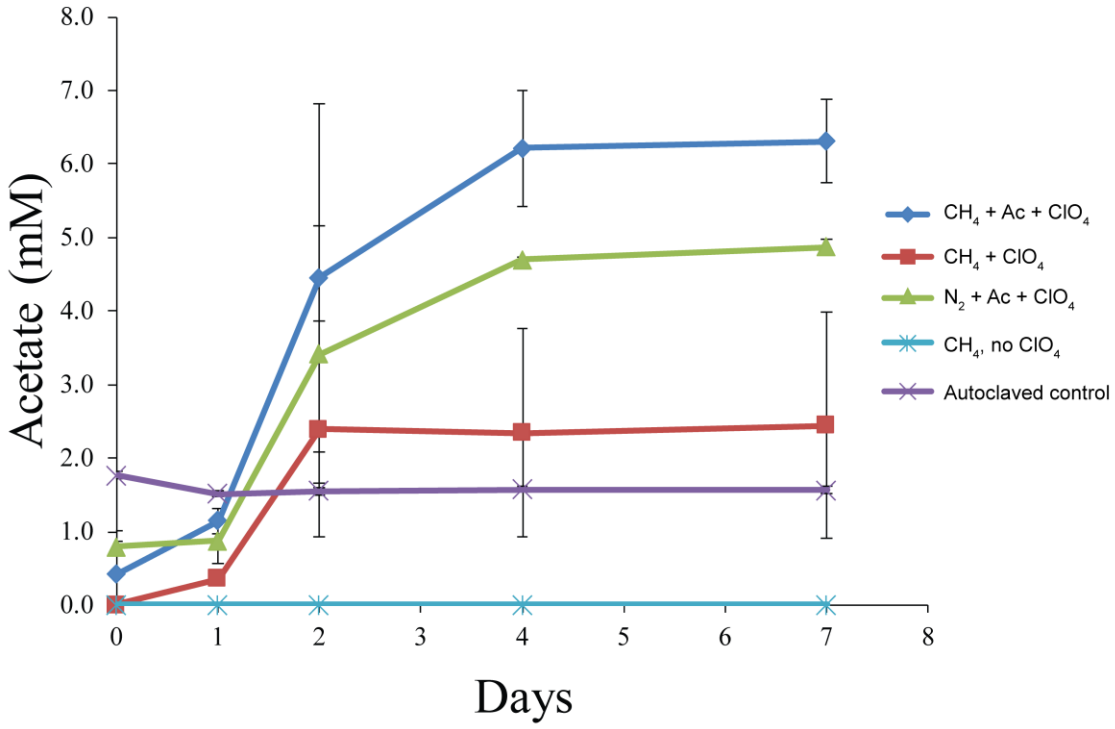

Figure 24. Acetate production in sediment incubations. Error bars represent standard deviation between duplicate incubation treatments. Ac: acetate.

A.3.2 Isotopic enrichment of ^{13}C-DIC.

Cultures containing perchlorate also showed significant ^{13}C-DIC enrichment (**Figure 25**). Enrichment occurred over days 1 to 4, coinciding with acetate production. Isotopic enrichment was also observed in no CH_4 cultures. Enrichment in cultures containing perchlorate, acetate, and no CH_4 (12.7‰ ± 1.7‰) was nearly as high as those observed in CH_4, acetate, perchlorate cultures (13.6‰ ± 1.2‰) and higher than CH_4, perchlorate cultures (7.2‰ ± 3.1‰). No enrichment was observed in heat killed controls

or cultures containing CH_4 but no perchlorate. Isotopic enrichment coincided with a reduction in the DIC concentration in all cultures (**Figure 26**).

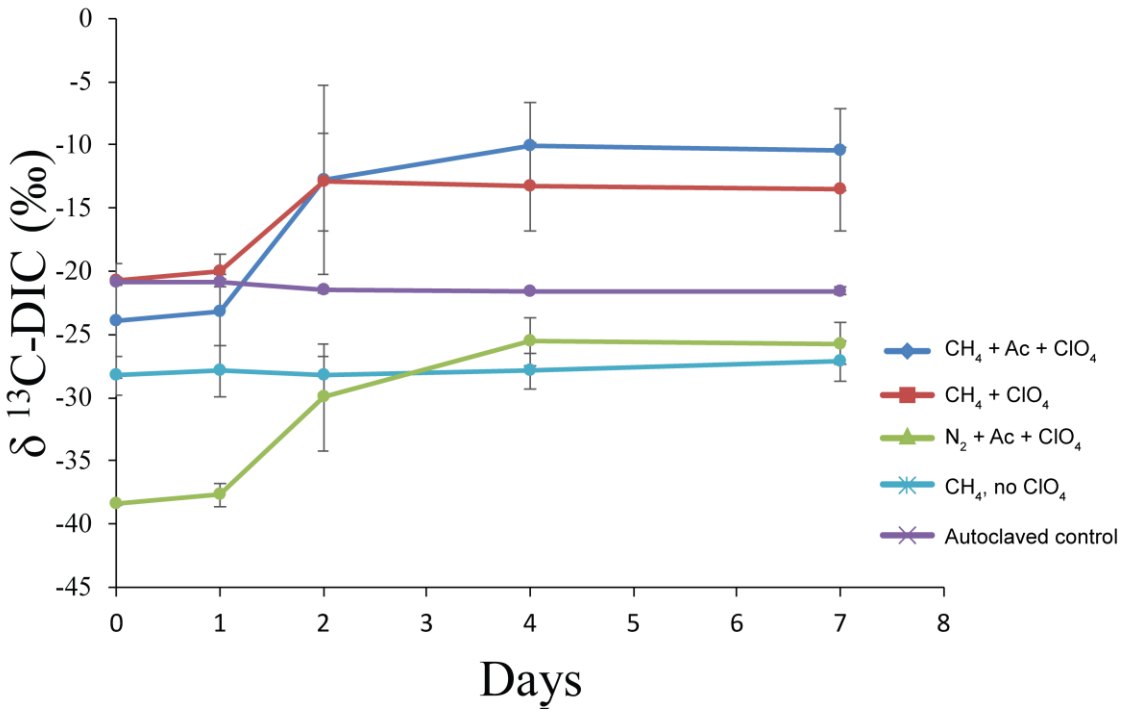

Figure 25. ^{13}C enrichment of the dissolved inorganic carbon (DIC) pool in sediment incubations. Isotopic enrichment is reported as $\delta^{13}C_{VPDB}$. Errors represent standard deviation between duplicate incubation treatments. Ac: acetate.

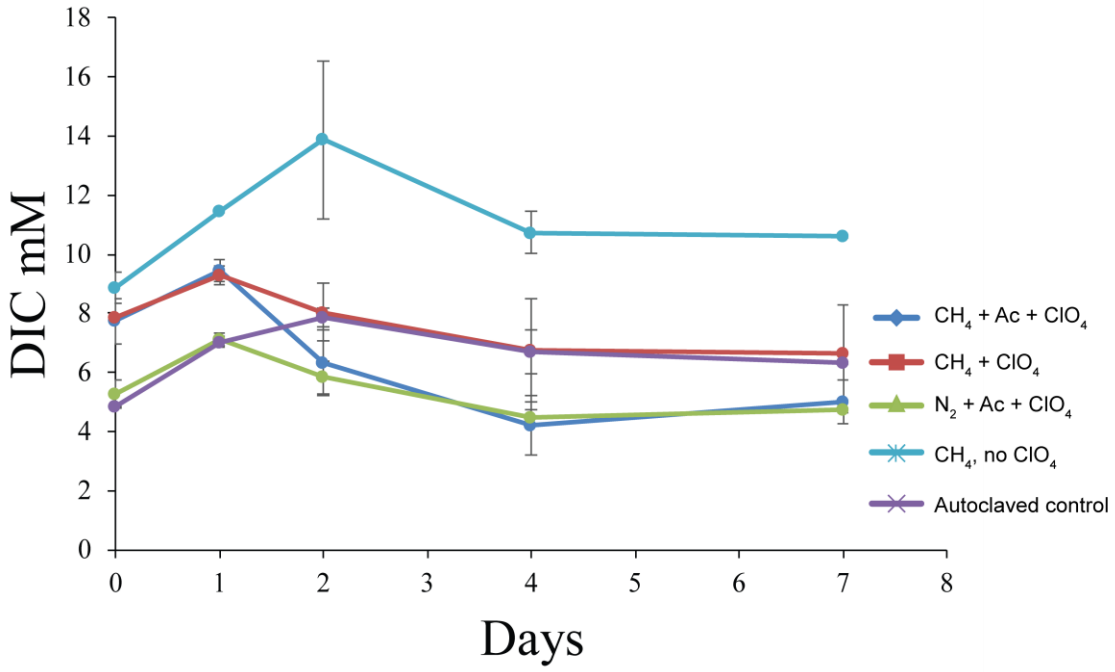

Figure 26. DIC concentration during sediment incubation. Error bars represent standard deviation of duplicate incubation treatments. Ac: acetate.

A.3.3 Isolation of perchlorate-reducing organisms.

Five hundred and sixty days after inoculation of sediment incubations, the CH_4 with acetate and perchlorate culture (CH_4 + Ac + ClO_4) was used to inoculate agar slant cultures for isolation of single colonies. This culture was chosen because it exhibited the most acetate production as well as the highest ^{13}C-DIC enrichment. Agar slants were made with enrichment media plus 5 mM perchlorate and acetate. Some slants also contained CH_4 in their headspace in addition to the 10% CO_2 in N_2 that all received.

Eight days after incubation at 30º C, small, colourless colonies appeared on agar slants with and without CH_4 headspace. Colonies were picked and used to inoculate 50 mL cultures containing 5 mM perchlorate and acetate. Colonies picked from slants with CH_4 headspace were inoculated into liquid cultures containing CH_4 headspace. Twenty-six days after inoculation, cultures both with and without CH_4 headspace were visibly turbid. Cultures with CH_4 headspace appeared to be the most turbid.

A.4 Discussion

We have shown that perchlorate stimulates microbial activity in sediment from Lake Matano. This activity is biological and dependent on perchlorate as neither heat killed controls, nor live cultures lacking perchlorate, displayed any acetate production nor change in ^{13}C-DIC. It is interesting how cultures that started with 2 mM acetate were able to produce more acetate than cultures that did not start with any. This suggests that some initial feeding of the microbial community could have stimulated the organisms responsible for acetate production.

The mode of acetate production in our incubations is not clear. We may be seeing acetate production from the either intra or extracellular breakdown of large carbon compounds. This may be mediated by the production of O_2 from perchlorate reduction and its subsequent use in monooxygenases to activate alkane/long chain carbon compounds, or possibly even the reaction of O_2 with endogenous Fe^{2+} to produce hydroxyl radical that has previously been shown to degrade lignin molecules (304). Alternatively, acetate production could be due to acetogenesis, or the reduction of CO_2 to acetate. Indeed, the ability for acetogenic bacteria to perform perchlorate reduction has been shown previously (305). The

processes did not seem to be coupled in this organism, however. In addition, the possible electron donor for acetate production in our cultures is unknown.

The effect of CH_4 on our incubations is more challenging to elucidate. The ^{13}C-DIC of sediment incubations containing ^{13}C labelled CH_4 did increase during incubation, which would suggest CH_4 oxidation. However, the ^{13}C-DIC enrichment of no CH_4 cultures suggest that this cannot be attributed to CH_4 oxidation. Microbial acetogenesis preferentially reduces isotopically light CO_2 into acetate which would result in isotopically heavy DIC (306). Indeed, the isotopic enrichment observed coincides with acetate production and an overall reduction in DIC concentration, strongly suggesting that most of the ^{13}C-DIC enrichment observed in this study is actually perchlorate stimulated acetogenesis. Still, given that highest acetate production and highest isotopic enrichment were both observed in CH_4 containing cultures, we cannot discount some small effect of CH_4 on our results.

We attempted to isolate the organism(s) responsible for perchlorate reduction in our sediment incubation and have successfully obtained a pure culture growing on perchlorate and acetate. Cultures containing CH_4 in the headspace appeared more turbid suggesting CH_4 was stimulating growth. More work must be done to understand the roles of CH_4, acetate, and perchlorate in these sediment incubations and to characterize the microorganism(s) responsible for these processes.

APPENDIX B ENRICHMENT OF ORGANISMS MEDIATING IRON OXIDATION AND NITROUS OXIDE REDUCTION

The work described in this appendix was not performed as part of my main thesis studies. This work represents a side project and is unpublished.

B.1 Introduction

Despite being thermodynamically favorable by the proposed mechanism, organisms capable of coupling the oxidation of Fe^{2+} to the reduction of N_2O have not been isolated.

$$2Fe^{2+} + N_2O + H^+ \rightarrow 2Fe^{3+} + N_2 + H_2O$$

$$\Delta G_r^{0\prime} = -227.22 \text{ kJ mol}^{-1} N_2O$$

In this study, I attempted to enrich for organisms mediating Fe^{2+} oxidation coupled to N_2O reduction from ferruginous Lake Matano sediments.

B.2 Experimental Methods

B.2.1 Sampling and incubation of inoculum sediments.

Two sediment cores were obtained from 590 and 200 m water depth in Lake Matano, Sulawesi Island, Indonesia in May 2010 and November 2014 respectively (2°28′S, 121°20′E, *in situ* sediment temperature ~27°C) and stored under anoxic conditions. The 590 m sediments were mixed with anoxic freshwater media in a 1:5 ratio in an anoxic chamber (3% H_2, 97% N_2) and dispensed in stoppered serum bottles. Cultures were

amended first with goethite and later with ferrihydrite. They were incubated for 1278 days at 30ºC, with multiple transfers, each time diluting the original sediment with freshwater media. Sediment had been diluted over 1000 times by the time it was used as inoculum for Fe^{2+}/ N_2O cultures. Details on 200 m sediment sampling methods and enrichment are found in Bray et al. (134). Briefly, sediment was mixed in a 1:1 ratio with a minimal freshwater media and dispensed into 70 mL stoppered serum bottles under anoxic conditions. Cultures were amended with ferrihydrite and either CH_4 or N_2 headspace before incubation at 30ºC. After 50 days, the volume of all cultures was reduced to 5 mL, and 30 mL of fresh media was added to each bottle, constituting a 6-fold dilution. These 2° enrichments were amended with approximately 10 mM of either ferrihydrite or goethite and incubated for 764 days before being used as inoculum for Fe^{2+}/N_2O cultures.

B.2.2 Enrichment medium.

For details on enrichment media used in these studies please refer to the **Experimental Methods** section of **Appendix A**.

B.2.3 Inoculation and incubation of enrichment cultures.

All treatments were run in duplicate. Long-term incubations of Lake Matano sediment from 590 m or 200 m water depth were used to inoculate enrichment cultures for Fe^{2+} oxidation coupled to N_2O reduction. Cultures inoculated with 590 m sediment enrichments received 1 mL of inoculum culture and 100 mL of anoxic enrichment media into stoppered serum bottles. Ten millimolar $FeCl_2$ and 2 mM $NaNO_3^-$ were added to all cultures. Some cultures also received 0.1 mM sodium acetate. Bottles were sparged for 10

minutes with 10% CO_2 in N_2. These cultures were incubated at 30º C for one month before 5 mL of 100% N_2O was added to the headspace of all bottles.

Cultures inoculated from 200 m sediment enrichments received 2 mL of inoculum from either CH_4 or N_2 headspace cultures and 100 ml of anoxic enrichment media into stoppered serum bottles. Ten millimolar $FeCl_2$ and 5 mL of 100% N_2O was added to all bottles. Some cultures also received 0.1 mM sodium acetate. All cultures were incubated at 30º C. For more information on these cultures refer to **Table 25** in **Appendix D**.

B.2.4 Ferrous iron measurements.

For detailed information on Fe^{2+} measurements, refer to the **Experimental Methods** of **Chapter 4**. Briefly, 100 µL of culture was incubated with 400 µL of 0.5 M HCl for 1 hr followed by centrifugation at 10,000 x g for 1 min, injection of 10 µL of supernatant into 990 µL of 10 mM FerroZine reagent in 46 mM HEPES (pH 8.3), and measurement of absorbance at 562 nm (174).

B.2.5 Headspace N_2O

Headspace (50 µL) was sampled using a gastight syringe and injected into a gas chromatograph (SRI Instruments 8610C, Torrance, CA, USA) with a HayeSep N column and electron capture detector to measure headspace N_2O concentrations. A N_2O standard (1 ppm, Airgas, USA) was used for calibration.

B.3 Results and Discussion

B.3.1 Iron oxidation.

We tracked Fe^{2+} oxidation in our enrichment cultures by measuring the decrease in Fe^{2+} concentrations. The only significant decrease in Fe^{2+} that was observed between day 35 and 55 in the enrichments containing NO_3^-, N_2O, and no acetate inoculated from 590 m sediment cultures (**Figure 28a**). Over this time period, Fe^{2+} concentrations decreased from 9.8 ± 0.1 mM to 8.6 ± 0.1 mM. No other decreases in Fe^{2+} concentration were observed in any other culture, suggesting that little to no Fe^{2+} oxidation occurred during incubation of these cultures.

B.3.2 Nitrous oxide reduction.

N_2O decreased in the headspace of multiple enrichments. In enrichments containing N_2O and N_2O + acetate that had been inoculated from 200 m CH_4 cultures, headspace N_2O was completely consumed over the first 8 days (**Figure 27b**). When the N_2O and N_2O + acetate enrichments were spiked with additional N_2O on day 15, it was again completely consumed by day 19 in the N_2O + acetate enrichment, while only moderately decreasing in the N_2O culture. Other enrichments inoculated from the 200 m sediment cultures also showed decreases in their headspace N_2O. Enrichments inoculated with 200 m N_2 headspace cultures had headspace N_2O decreasing from day 5 to day 20 at variable rates. From the enrichments inoculated from 590 m sediment cultures, only one of the NO_3^- + N_2O + Ac replicates showed a significant decrease in headspace N_2O (**Figure 28b**).

For both the 200 m and 590 m sediment inoculated enrichments, controls lacking any added Fe^{2+} showed complete depletion of N_2O in their headspace. This result combined with the minimal Fe^{2+} oxidation observed suggests that N_2O reduction was not coupled to Fe^{2+} oxidation in these enrichments.

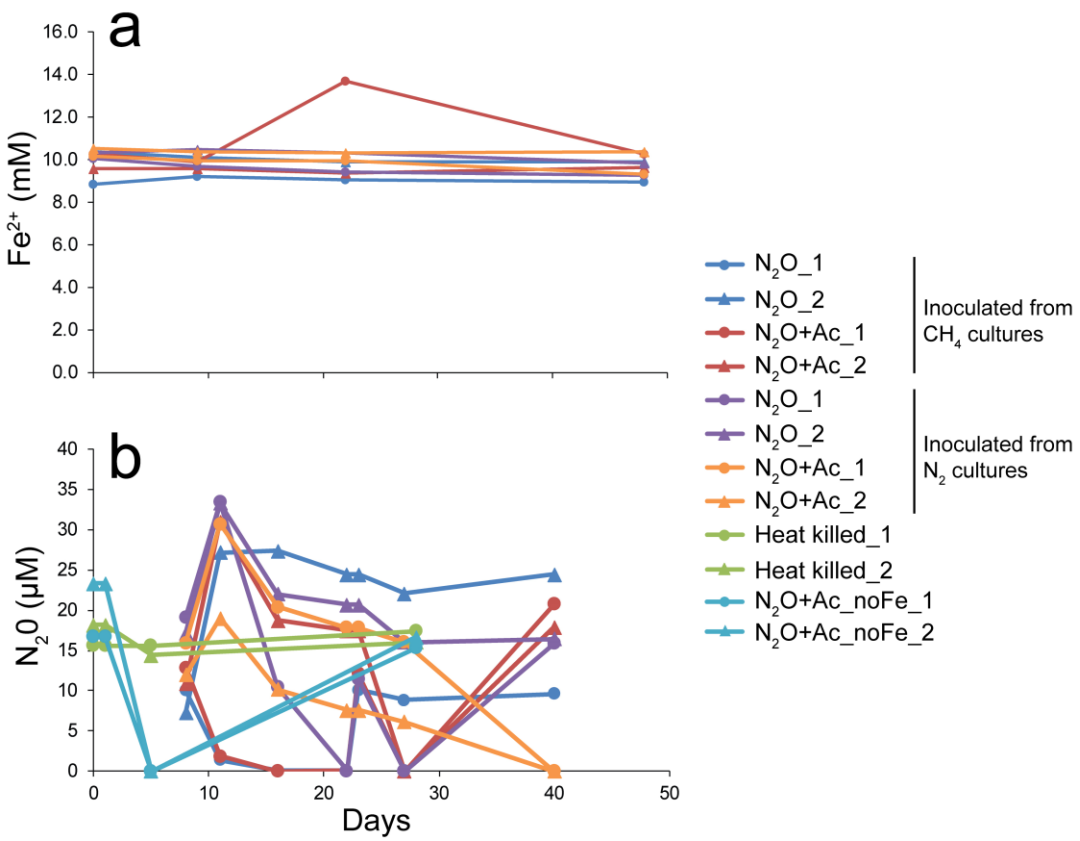

Figure 27. Activity of N_2O-Fe^{2+} enrichments inoculated from long term incubations of Lake Matano sediment from 200-meter water depth. (a) Ferrous iron measurements. (b) Headspace N_2O measurements. Enrichments were inoculated from sediment incubated with either CH_4 or N_2 headspace. On day 23 of enrichment, 0.25 mL of 100% N_2O was added to the "N_2O_2" and "N_2O+Ac_1" from CH_4 sediment and the "N_2O_1" from N_2 sediment bottles. On day 40 of enrichment, 0.25 mL of 100% N_2O was added to the "N_2O+Ac_1" and "N_2O+Ac_2" from CH_4 sediments, the "N_2O_1" from N_2 sediments, and the "no Fe" control" bottles. Duplicate treatment cultures are plotted separately. Ac: acetate.

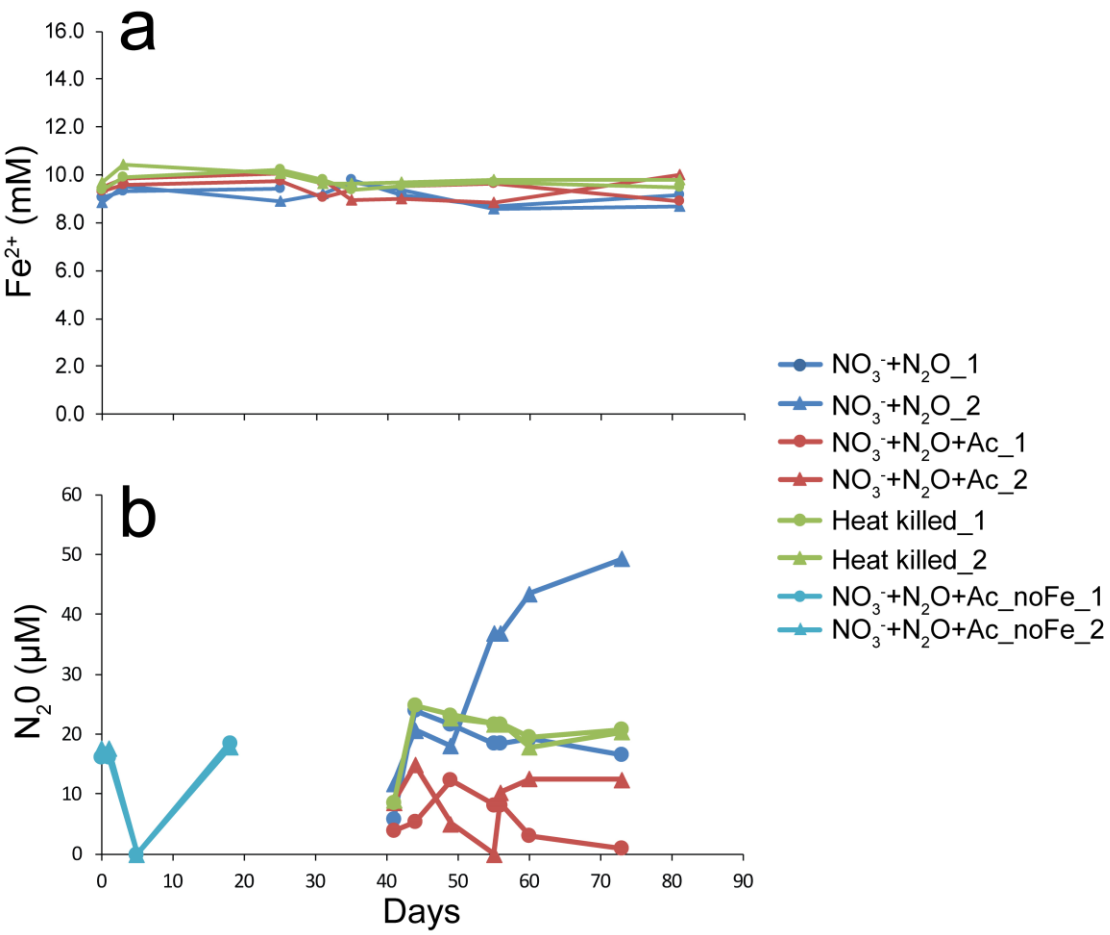

Figure 28. Activity of N_2O-Fe^{2+} enrichments inoculated from long term incubations of Lake Matano sediment from 590-meter water depth. (a) Ferrous iron measurements. (b) Headspace N_2O measurements. On day 56 of enrichment, 0.25 mL of 100% N_2O was added to the "NO_3^-+N_2O+Ac_2" bottle. On day 73 of enrichment, 0.25 mL of 100% N_2O was added to both "noFe" control bottles. Duplicate treatment cultures are plotted separately. Ac: acetate.

B.3.3 Turbidity and colour change of cultures

Over the course of enrichment, the turbidity of cultures increased and the colour changes from brown/red at inoculation, to white and/or black (**Figure 29**). In the cultures inoculated with 200 m sediment cultures, bottles that received acetate ended up as opaque white, while those with only N_2O were black.

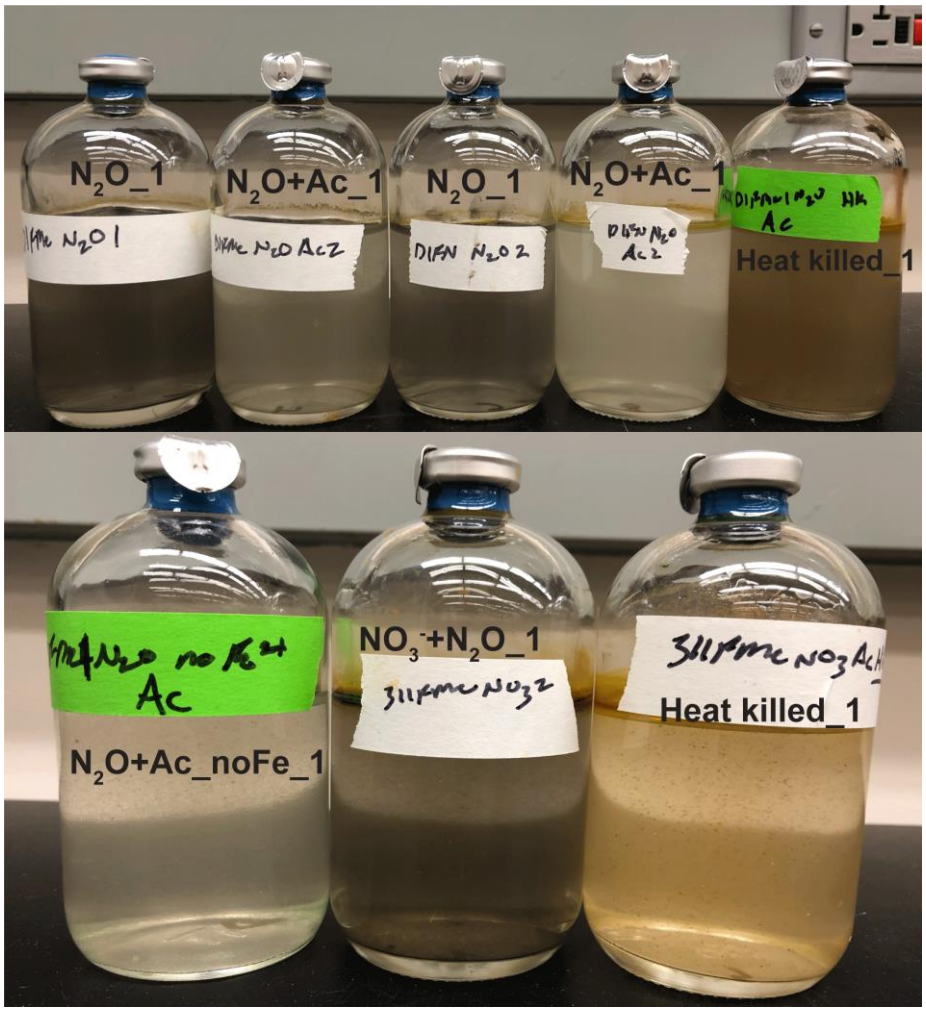

Figure 29. Turbidity and color of enrichments inoculated from 200 m (top) and 590 m (bottom) long-term sediments incubations following incubation with N_2O and Fe^{2+}.

APPENDIX C IMAGING CELLS IN LAKE MATANO SEDIMENT ENRICHMENTS USING FLUORESCENCE *IN SITU* HYBRIDIZATION

C.1 Introduction

This appendix details the use of catalyzed reporter deposition fluorescence *in situ* hybridization (CARD-FISH) to visualize bacterial cells from Lake Matano sediment enrichment cultures.

C.2 Experimental Methods

C.2.1 Fixing of samples.

All buffers and reagents were made with ddiH_2O and filtered sterilized through 0.2 µm pore filters before use. Five hundred microliters of sediment enrichment were taken and fixed in 4% paraformaldehyde for 1 hour at room temperature. Fixed samples were pelleted by centrifuging at 10,000x g for 5 minutes before resuspension in 1 mL PBS and centrifugation at 10,000x g for 5 min. This was repeated 3 times before fixed samples were stored at -20°C in 50% ethanol and 50% PBS. Ten to one hundred microliters of fixed sample were then diluted in 1 mL PBS and this solution was immobilized on 0.2 µm pore polycarbonate membrane filters. Filters containing fixed cells were then embedded in 0.2% low melting agarose by dipping filter into agarose solution and dried at 45º C mounted a parafilm wrapped glass slide. Filters were then sectioned with a razor blade and stored at -20º C.

C.2.2 Nonselective DNA staining.

The fluorescent DNA stains DAPI and acridine orange. For staining, filter sections were retrieved from the freezer and a 25 ng uL^{-1} solution of either dye was pipetted on top. Filters were incubated for 5 minutes under aluminium foil. Filters were then washed for 10 minutes in H_2O and briefly in 100% ethanol before being air dried in the dark under a tent of aluminum foil. The dry filter was mounted onto a glass microscope slide with Citifluor antifade mounting media (Electron Microscopy Sciences) and covered with a glass cover slip. CARD-FISH samples were stored at -20º C in the dark before viewing with a fluorescence microscope.

C.2.3 CARD-FISH.

For CARD-FISH, filters were retrieved from the freezer and incubated with 10 mg mL^{-1} lysozyme for 30-60 minutes at 37º C in a Binder laboratory oven. Filters were then washed by submerging in H_2O in a petri dish for one minute three times and then incubated in 0.1 M HCl for 15 minutes at room temperature. Filters were then washed for 1 min 3x in H_2O. Hybridization of horse radish peroxidase (HRP) labelled DNA oligo probes to samples was performed in a humidity chamber composed of a 50 mL falcon tube containing Kim wipes soaked in the appropriate water/formamide mixture (see **Table 16** for a list of probes used). HRP-probes were added to hybridization buffer to a final concentration of 0.17 ng μL^{-1} and this solution was pipetted directly on top of the filter. The filter was placed in a parafilm covered glass slide and into the humidity chamber. The probe was allowed to hybridize with the sample for 3 hours at 46ºC. The hybridized filter

was then removed from the humidity chamber and incubated in pre-warmed washing buffer for 30 minutes at 48º C.

For signal amplification, filters were removed from washing buffer and briefly dipped in H_2O before being washed in PBS for 1 minute at room temperature. Tyramide conjugated dye was added to amplification buffer in a 1:1000 ratio. H_2O_2 was added to 0.0015%. Filters were removed from PBS, dabbed lightly on a Kim wipe, dipped in amplification buffer, and placed on a parafilm wrapped glass slide. The remainder of amplification buffer was pipetted on top of the filter and the slide was placed in a humidity chamber containing sterile water-soaked Kim wipes. Signal was allowed to amplify at 46º C for one hour. After this step, the filter was light sensitive. After signal amplification, filters were briefly submerged in PBS and washed in PBS, then H_2O for 10 minutes at room temperature covered in aluminum foil.

For hybridizing additional probes to the same sample, filters would first be re-incubated in 0.1 M HCl for 15 minutes at room temperature and washed thrice in H_2O. Hybridization and amplification were then performed again as described above the desired HRP-probe/tyramide conjugated dye.

Once all hybridization and amplification steps were performed, counter staining was performed by adding a 25 ng μL^{-1} solution of DAPI to the filter and incubating at room temperature for 5 minutes in the dark. Filters were then washed for 10 minutes in H_2O and briefly in 100% ethanol before being air dried in the dark under a tent of aluminum foil. The dry filter was mounted onto a glass microscope slide with Citifluor antifade mounting

media (Electron Microscopy Sciences) and covered with a glass cover slip. CARD-FISH samples were stored at -20º C in the dark before viewing with a fluorescence microscope.

Table 16. HRP-linked probes used in this study.

Probe name	Target	Formamide concentration	Reference
EUB338	Most bacteria	0-50%	(307)
nonEUB338*	Competitor for EUB338	0-50%	(308)
Bet42a	Most *Betaproteobacteria*	35%	(309)
Gam42a*	Most *Gammaproteobacteria* Competitor for Bet42a	35%	(309)
Delta495a	Most *Deltaproteobacteria*	35%	(310)
Geo3-A	*Geobacter*	20-35%	(311)
Geo3-B	*Geobacter*	20-35%	(311)
Geo-C	*Geobacter*	20-35%	(311)

*Competitor probes were not labelled with HRP

C.2.4 Microscopy

Samples were imaged on a Zeiss fluorescence microscope with an AxioCam Mrc5 digital camera attachment. First the microscope and lamp were switched on at the power boxes located to the left of the microscope. The AxioVision software was opened on the adjacent computer. The correct light filter (DAPI, GFP, AF 568, TL) and objective (10X, 20X, 40X, 100X) were selected using the touchscreen located on the right side of the microscope. The DAPI filter and 10X objective were always selected first. The sample stage was moved to the load position using the touchpad and the prepared slide was place on the stage before moving it back to the work position. The samples were focused at 10X using the coarse adjustment knob. The stage was then again lowered, and immersion oil

was added on top of the slide before switching to the 100X objective. From here the fine adjustment knob was used to focus the sample and the stage movement knobs were used to visualized different portions of the sample. The “snap” function in the AxioVision software was used to take images and the “show properties” tools were used to improve image quality. Scale bars were added manually using the scale bar function and the image was exported as a .tiff. Images are stored in the DropBox directory \Fe-AOM metagenome paper\Microscopy\.

C.3 Results

CARD-FISH images were obtained for the following enrichment cultures: 311FMe, 321FMe, 3º 321FMe -S, 3º 321FN -S, D1FMe1 (secondary enrichment). For more information on these cultures see **Appendix D**.

C.3.1 311FMe.

Samples from this culture were hybridized with the Bet42a probe that detects most *Betaproteobacteria* (**Figure 30**). Cells hybridized with the Beta42a probes appeared as curved rods.

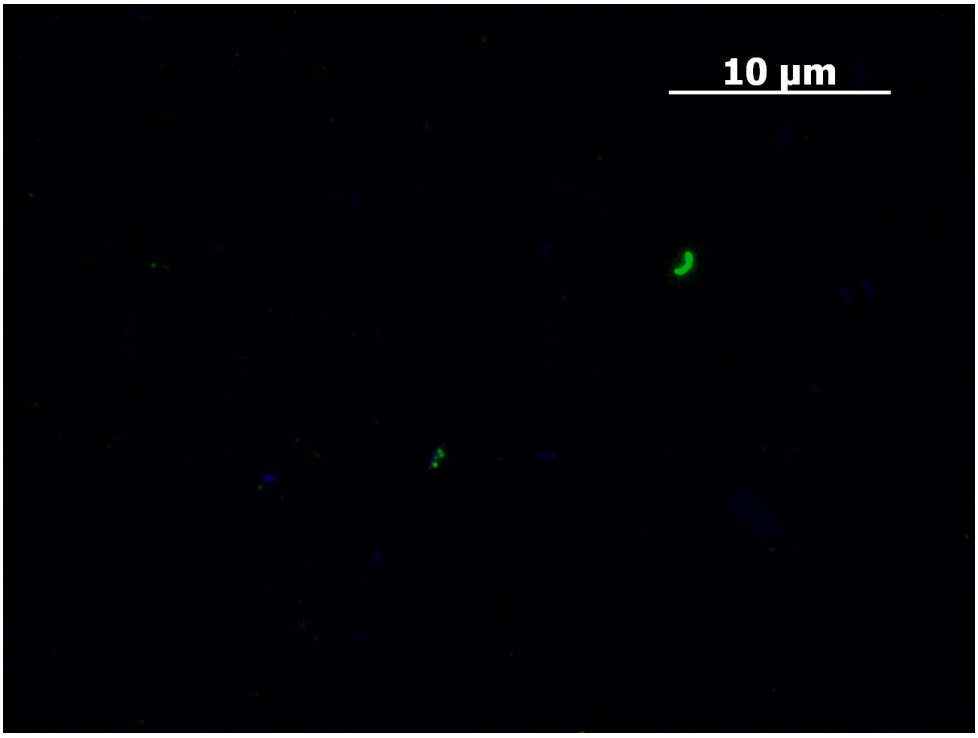

Figure 30. CARD-FISH image from sample of 311FMe hybridized with Bet42a (green). Sample was counterstained with DAPI.

C.3.2 321FMe.

Samples from this culture were stained with Bet42a and Delta495a as well as Geo3-A, Geo3-B, and Geo3-C (**Figure 31**). Cells that hybridized to the Delta495a and Geo3-B appeared as short rods while cells which hybridized to the Bet42a probe were curved rods like those seen in 311FMe.

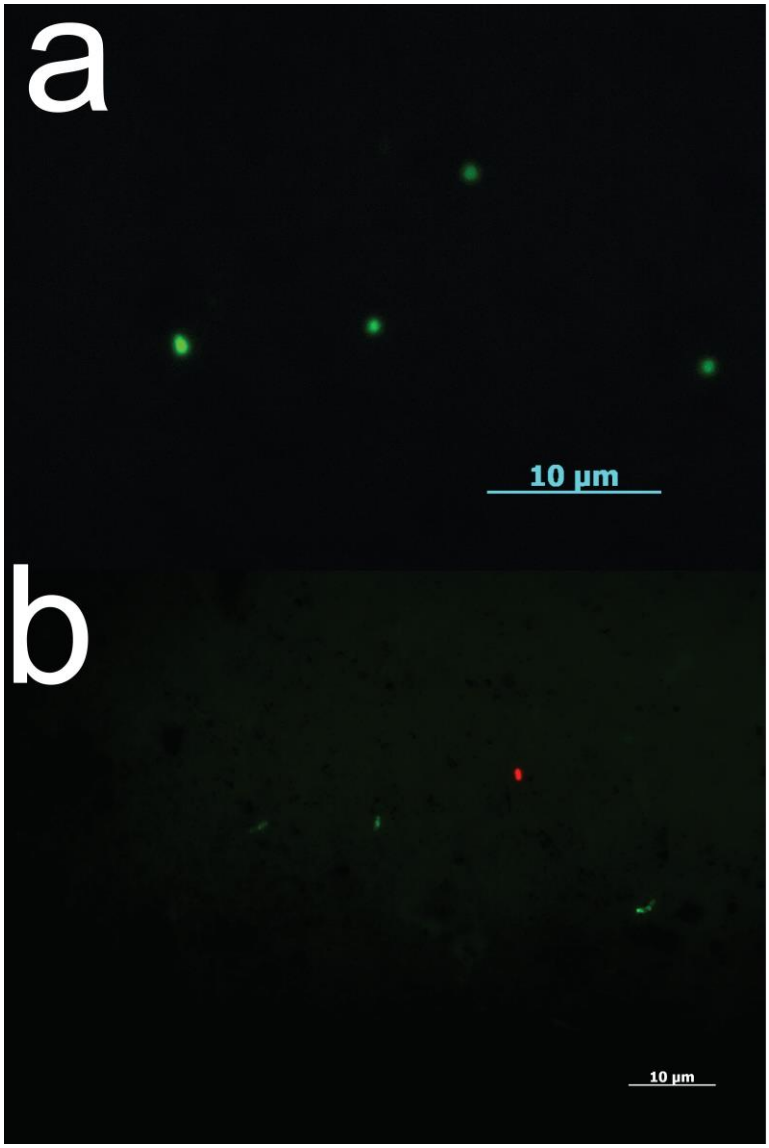

Figure 31. CARD-FISH images from sample of 321FMe hybridized with (a) Delta495a (green) or (b) Bet42a (green) and Geo3-B (red). Samples were counterstained with DAPI.

C.3.3 3º 321FMe -S and 3º 321FN -S.

Samples from these cultures were hybridized with Delt495a. No cells appeared to hybridize with the Delta495a probes. When cells from these samples were stained with acridine orange, cells of various rod shape as well as filamentous morphology were visualized (**Figure 32**). Cells existed both planktonically as well as in aggregates and many appeared to associate with Fe(III)-oxide particles.

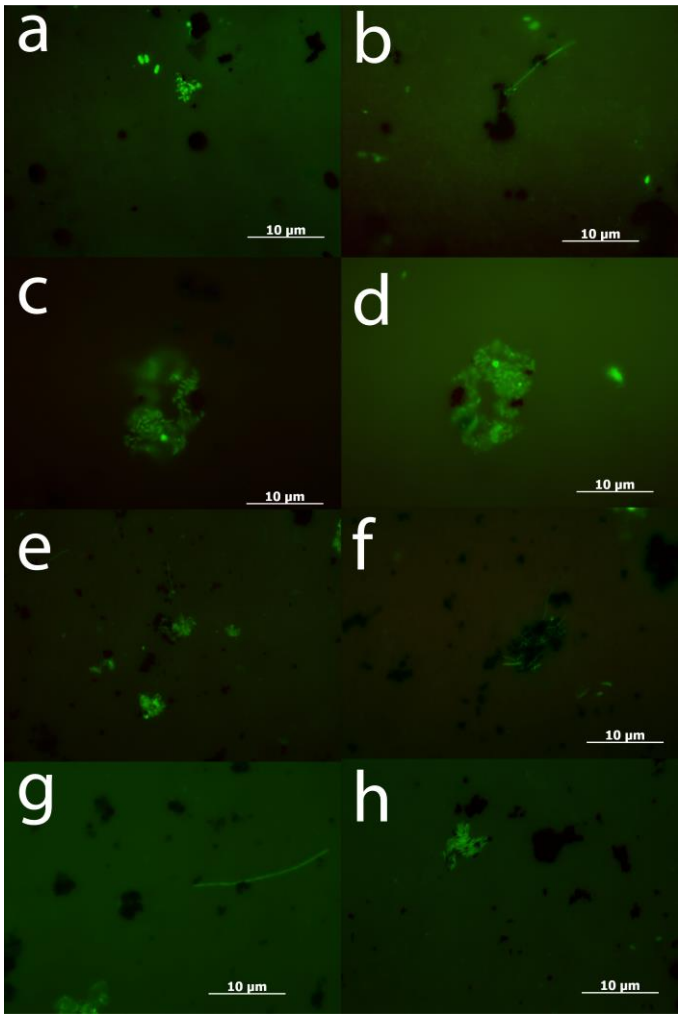

Figure 32. Acridine orange images from sample of 3º 321FMe -S (a-d) and 3º 321FN -S (e-h).

C.3.4 D1FMe1 secondary enrichment.

Samples from the secondary enrichment of D1FMe1 were hybridized with Eub338, Bet42a, and Geo3-B. Cells hybridized to both probes were detected and appeared as short rods (**Figure 33**).

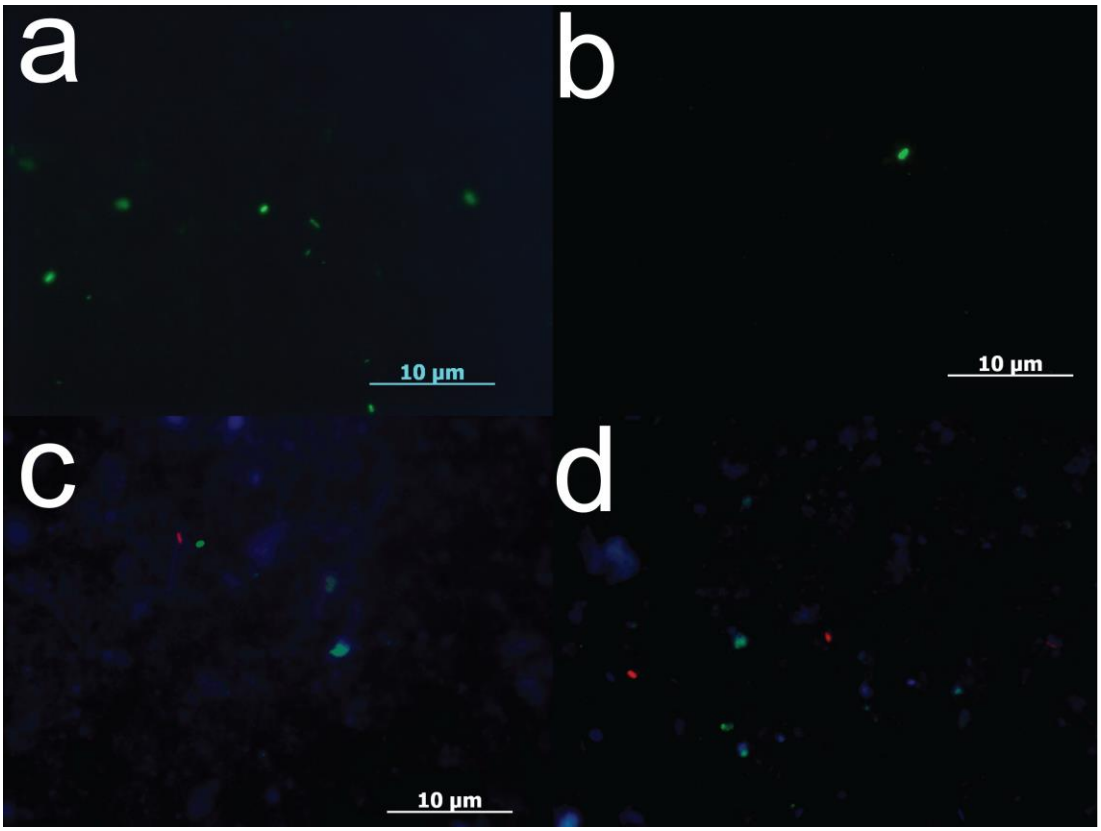

Figure 33. CARD-FISH images from the secondary enrichment of D1FMe1 hybridized with (a) Eub338 (green), (b) Bet42 (green), and (c and d) Bet42a (green) and Geo3-B (red).

APPENDIX D LAKE MATANO SEDIMENT CULTURE INVENTORY

Table 17. Lake Matano 590-meter water depth sediment primary Fe-AOM enrichment inventory. Enrichment cultures were started by Ben C. Reed on 11-18-13 using fresh Lake Matano sediment. For information describing enrichment media and basic incubation methods, see Chapter 4. For more specific information on inoculation and incubation of this enrichment, see "Fe/Mn AOM, Ben Reed, Nov '13-Sep '14" red laboratory notebook located in the Glass Lab.

Culture name	Treatment	Inoculum	Storage location	Comment
110F0	Goethite + CH_4	None	30º C incubator, bottom shelf	Abiotic Control
120F0	Goethite + CH_4	None	30º C incubator, bottom shelf	Abiotic Control
110FA	Goethite + CH_4 + AQDS	None	30º C incubator, bottom shelf	Abiotic Control
120FA	Goethite + CH_4 + AQDS	None	30º C incubator, bottom shelf	Abiotic Control
110FC	Goethite + CH_4 + Cysteine	None	30º C incubator, bottom shelf	Abiotic Control
120FC	Goethite + CH_4 + Cysteine	None	30º C incubator, bottom shelf	Abiotic Control
110M0	Birnessite + CH_4	None	30º C incubator, bottom shelf	Abiotic Control
120M0	Birnessite + CH_4	None	30º C incubator, bottom shelf	Abiotic Control
110MA	Birnessite + CH_4 + AQDS	None	30º C incubator, bottom shelf	Abiotic Control
120MA	Birnessite + CH_4 + AQDS	None	30º C incubator, bottom shelf	Abiotic Control
110MC	Birnessite + CH_4 + Cysteine	None	30º C incubator, bottom shelf	Abiotic Control
120MC	Birnessite + CH_4 + Cysteine	None	30º C incubator, bottom shelf	Abiotic Control
111FCH	Goethite + CH_4 + Cysteine Autoclaved control	590 m water depth sediment, 0-5 cm	30º C incubator, bottom shelf	
11100	CH_4	590 m water depth sediment, 0-5 cm	30º C incubator, bottom shelf	
12100	CH_4	590 m water depth sediment, 0-5 cm	30º C incubator, bottom shelf	
1110A	AQDS + CH_4	590 m water depth sediment, 0-5 cm	30º C incubator, bottom shelf	
1210A	AQDS + CH_4	590 m water depth sediment, 0-5 cm	30º C incubator, bottom shelf	
1110C	Cysteine + CH_4	590 m water depth sediment, 0-5 cm	30º C incubator, bottom shelf	
1210C	Cysteine + CH_4	590 m water depth sediment, 0-5 cm	30º C incubator, bottom shelf	
111F00M	Goethite, no CH_4	590 m water depth sediment, 0-5 cm	30º C incubator, bottom shelf	

Table 17. Lake Matano 590-meter water depth sediment primary Fe-AOM enrichment inventory.

121F00M	Goethite, no CH_4	590 m water depth sediment, 0-5 cm	30º C incubator, bottom shelf	
111FA0M	Goethite + AQDS, no CH_4	590 m water depth sediment, 0-5 cm	30º C incubator, bottom shelf	
121FA0M	Goethite + AQDS, no CH_4	590 m water depth sediment, 0-5 cm	30º C incubator, bottom shelf	
111FC0M	Goethite + Cysteine, no CH_4	590 m water depth sediment, 0-5 cm	30º C incubator, bottom shelf	
121FC0M	Goethite + Cysteine, no CH_4	590 m water depth sediment, 0-5 cm	30º C incubator, bottom shelf	
111M00M	Birnessite, no CH_4	590 m water depth sediment, 0-5 cm	30º C incubator, bottom shelf	
121M00M	Birnessite, no CH_4	590 m water depth sediment, 0-5 cm	30º C incubator, bottom shelf	
111MA0M	Birnessite + AQDS, no CH_4	590 m water depth sediment, 0-5 cm	30º C incubator, bottom shelf	
121MA0M	Birnessite + AQDS, no CH_4	590 m water depth sediment, 0-5 cm	30º C incubator, bottom shelf	
111MC0M	Birnessite + Cysteine, no CH_4	590 m water depth sediment, 0-5 cm	30º C incubator, bottom shelf	
121MC0M	Birnessite + Cysteine, no CH_4	590 m water depth sediment, 0-5 cm	30º C incubator, bottom shelf	
111F0	Goethite + CH_4	590 m water depth sediment, 0-5 cm	30º C incubator, bottom shelf	
121F0	Goethite + CH_4	590 m water depth sediment, 0-5 cm	30º C incubator, bottom shelf	
111FA	Goethite + CH_4 + AQDS	590 m water depth sediment, 0-5 cm	30º C incubator, bottom shelf	
121FA	Goethite + CH_4 + AQDS	590 m water depth sediment, 0-5 cm	30º C incubator, bottom shelf	
111FC	Goethite + CH_4 + Cysteine	590 m water depth sediment, 0-5 cm	30º C incubator, bottom shelf	
121FC	Goethite + CH_4 + Cysteine	590 m water depth sediment, 0-5 cm	30º C incubator, bottom shelf	
111M0	Birnessite + CH_4	590 m water depth sediment, 0-5 cm	30º C incubator, bottom shelf	
121M0	Birnessite + CH_4	590 m water depth sediment, 0-5 cm	30º C incubator, bottom shelf	
111MA	Birnessite + CH_4 + AQDS	590 m water depth sediment, 0-5 cm	30º C incubator, bottom shelf	
121MA	Birnessite + CH_4 + AQDS	590 m water depth sediment, 0-5 cm	30º C incubator, bottom shelf	
111MC	Birnessite + CH_4 + Cysteine	590 m water depth sediment, 0-5 cm	30º C incubator, bottom shelf	
121MC	Birnessite + CH_4 + Cysteine	590 m water depth sediment, 0-5 cm	30º C incubator, bottom shelf	
112FCH	Goethite + CH_4 + Cysteine Autoclaved control	590 m water depth sediment, 5-10 cm	30º C incubator, bottom shelf	
11200	CH_4	590 m water depth sediment, 5-10 cm	30º C incubator, bottom shelf	
12200	CH_4	590 m water depth sediment, 5-10 cm	30º C incubator, bottom shelf	
1120A	AQDS + CH_4	590 m water depth sediment, 5-10 cm	30º C incubator, bottom shelf	
1220A	AQDS + CH_4	590 m water depth sediment, 5-10 cm	30º C incubator, bottom shelf	
1120C	Cysteine + CH_4	590 m water depth sediment, 5-10 cm	30º C incubator, bottom shelf	
1220C	Cysteine + CH_4	590 m water depth sediment, 5-10 cm	30º C incubator, bottom shelf	

Table 17. Lake Matano 590-meter water depth sediment primary Fe-AOM enrichment inventory.

112F00M	Goethite, no CH_4	590 m water depth sediment, 5-10 cm	30º C incubator, bottom shelf	
122F00M	Goethite, no CH_4	590 m water depth sediment, 5-10 cm	30º C incubator, bottom shelf	
112FA0M	Goethite + AQDS, no CH_4	590 m water depth sediment, 5-10 cm	30º C incubator, bottom shelf	
122FA0M	Goethite + AQDS, no CH_4	590 m water depth sediment, 5-10 cm	30º C incubator, bottom shelf	
112FC0M	Goethite + Cysteine, no CH_4	590 m water depth sediment, 5-10 cm	30º C incubator, bottom shelf	
122FC0M	Goethite + Cysteine, no CH_4	590 m water depth sediment, 5-10 cm	30º C incubator, bottom shelf	
112M00M	Birnessite, no CH_4	590 m water depth sediment, 5-10 cm	30º C incubator, bottom shelf	
122M00M	Birnessite, no CH_4	590 m water depth sediment, 5-10 cm	30º C incubator, bottom shelf	
112MA0M	Birnessite + AQDS, no CH_4	590 m water depth sediment, 5-10 cm	30º C incubator, bottom shelf	
122MA0M	Birnessite + AQDS, no CH_4	590 m water depth sediment, 5-10 cm	30º C incubator, bottom shelf	
112MC0M	Birnessite + Cysteine, no CH_4	590 m water depth sediment, 5-10 cm	30º C incubator, bottom shelf	
122MC0M	Birnessite + Cysteine, no CH_4	590 m water depth sediment, 5-10 cm	30º C incubator, bottom shelf	
112F0	Goethite + CH_4	590 m water depth sediment, 5-10 cm	30º C incubator, bottom shelf	
122F0	Goethite + CH_4	590 m water depth sediment, 5-10 cm	30º C incubator, bottom shelf	
112FA	Goethite + CH_4 + AQDS	590 m water depth sediment, 5-10 cm	30º C incubator, bottom shelf	
122FA	Goethite + CH_4 + AQDS	590 m water depth sediment, 5-10 cm	30º C incubator, bottom shelf	
112FC	Goethite + CH_4 + Cysteine	590 m water depth sediment, 5-10 cm	30º C incubator, bottom shelf	
122FC	Goethite + CH_4 + Cysteine	590 m water depth sediment, 5-10 cm	30º C incubator, bottom shelf	
112M0	Birnessite + CH_4	590 m water depth sediment, 5-10 cm	30º C incubator, bottom shelf	
122M0	Birnessite + CH_4	590 m water depth sediment, 5-10 cm	30º C incubator, bottom shelf	
112MA	Birnessite + CH_4 + AQDS	590 m water depth sediment, 5-10 cm	30º C incubator, bottom shelf	
122MA	Birnessite + CH_4 + AQDS	590 m water depth sediment, 5-10 cm	30º C incubator, bottom shelf	
112MC	Birnessite + CH_4 + Cysteine	590 m water depth sediment, 5-10 cm	30º C incubator, bottom shelf	
122MC	Birnessite + CH_4 + Cysteine	590 m water depth sediment, 5-10 cm	30º C incubator, bottom shelf	
113FCH	Goethite + CH_4 + Cysteine Autoclaved control	590 m water depth sediment, 10-15 cm	30º C incubator, bottom shelf	
11300	CH_4	590 m water depth sediment, 10-15 cm	30º C incubator, bottom shelf	
12300	CH_4	590 m water depth sediment, 10-15 cm	30º C incubator, bottom shelf	
1130A	AQDS + CH_4	590 m water depth sediment, 10-15 cm	30º C incubator, bottom shelf	
1230A	AQDS + CH_4	590 m water depth sediment, 10-15 cm	30º C incubator, bottom shelf	
1130C	Cysteine + CH_4	590 m water depth sediment, 10-15 cm	30º C incubator, bottom shelf	

Table 17. Lake Matano 590-meter water depth sediment primary Fe-AOM enrichment inventory.

1230C	Cysteine + CH_4	590 m water depth sediment, 10-15 cm	30º C incubator, bottom shelf	
113F00M	Goethite, no CH_4	590 m water depth sediment, 10-15 cm	30º C incubator, bottom shelf	
123F00M	Goethite, no CH_4	590 m water depth sediment, 10-15 cm	30º C incubator, bottom shelf	
113FA0M	Goethite + AQDS, no CH_4	590 m water depth sediment, 10-15 cm	30º C incubator, bottom shelf	
123FA0M	Goethite + AQDS, no CH_4	590 m water depth sediment, 10-15 cm	30º C incubator, bottom shelf	
113FC0M	Goethite + Cysteine, no CH_4	590 m water depth sediment, 10-15 cm	30º C incubator, bottom shelf	
123FC0M	Goethite + Cysteine, no CH_4	590 m water depth sediment, 10-15 cm	30º C incubator, bottom shelf	
113M00M	Birnessite, no CH_4	590 m water depth sediment, 10-15 cm	30º C incubator, bottom shelf	
123M00M	Birnessite, no CH_4	590 m water depth sediment, 10-15 cm	30º C incubator, bottom shelf	
113MA0M	Birnessite + AQDS, no CH_4	590 m water depth sediment, 10-15 cm	30º C incubator, bottom shelf	
123MA0M	Birnessite + AQDS, no CH_4	590 m water depth sediment, 10-15 cm	30º C incubator, bottom shelf	
113MC0M	Birnessite + Cysteine, no CH_4	590 m water depth sediment, 10-15 cm	30º C incubator, bottom shelf	
123MC0M	Birnessite + Cysteine, no CH_4	590 m water depth sediment, 10-15 cm	30º C incubator, bottom shelf	
113F0	Goethite + CH_4	590 m water depth sediment, 10-15 cm	30º C incubator, bottom shelf	
123F0	Goethite + CH_4	590 m water depth sediment, 10-15 cm	30º C incubator, bottom shelf	
113FA	Goethite + CH_4 + AQDS	590 m water depth sediment, 10-15 cm	30º C incubator, bottom shelf	
123FA	Goethite + CH_4 + AQDS	590 m water depth sediment, 10-15 cm	30º C incubator, bottom shelf	
113FC	Goethite + CH_4 + Cysteine	590 m water depth sediment, 10-15 cm	30º C incubator, bottom shelf	
123FC	Goethite + CH_4 + Cysteine	590 m water depth sediment, 10-15 cm	30º C incubator, bottom shelf	
113M0	Birnessite + CH_4	590 m water depth sediment, 10-15 cm	30º C incubator, bottom shelf	
123M0	Birnessite + CH_4	590 m water depth sediment, 10-15 cm	30º C incubator, bottom shelf	
113MA	Birnessite + CH_4 + AQDS	590 m water depth sediment, 10-15 cm	30º C incubator, bottom shelf	
123MA	Birnessite + CH_4 + AQDS	590 m water depth sediment, 10-15 cm	30º C incubator, bottom shelf	
113MC	Birnessite + CH_4 + Cysteine	590 m water depth sediment, 10-15 cm	30º C incubator, bottom shelf	
123MC	Birnessite + CH_4 + Cysteine	590 m water depth sediment, 10-15 cm	30º C incubator, bottom shelf	

Table 18. Lake Matano 590-meter water depth sediment secondary Fe-AOM enrichment inventory. Enrichment cultures were started by Ben C. Reed on 3-25-14 by transferring aliquots of primary enrichments to new bottles along with fresh media and substrates. For information describing enrichment media and basic incubation methods, see Chapter 4. For more specific information on inoculation and incubation of this enrichment, see "Fe/Mn AOM, Ben Reed, Nov '13-Sep '14" red laboratory notebook located in the Glass Lab.

Culture name	Treatment	Inoculum	Storage location	Comments
211F0	Goethite + CH_4	111F0	30º C incubator, bottom shelf	
221F0	Goethite + CH_4	121F0	30º C incubator, bottom shelf	
211FA	Goethite + CH_4 + AQDS	111FA	30º C incubator, bottom shelf	
221FA	Goethite + CH_4 + AQDS	121FA	30º C incubator, bottom shelf	
211FC	Goethite + CH_4 + Cysteine	111FC	30º C incubator, bottom shelf	
221FC	Goethite + CH_4 + Cysteine	121FC	30º C incubator, bottom shelf	
211F00S	Ferrihydrite + CH_4	111F0	30º C incubator, bottom shelf	
221F00S	Ferrihydrite + CH_4	121F0	30º C incubator, bottom shelf	
211FA0S	Ferrihydrite + CH_4 + AQDS	111FA	30º C incubator, bottom shelf	
221FA0S	Ferrihydrite + CH_4 + AQDS	121FA	30º C incubator, bottom shelf	
211FC0S	Ferrihydrite + CH_4 + Cysteine	111FC	30º C incubator, bottom shelf	
221FC0S	Ferrihydrite + CH_4 + Cysteine	121FC	30º C incubator, bottom shelf	
211P00S	Fe(III)-citrate + CH_4	111F0	30º C incubator, bottom shelf	
221P00S	Fe(III)-citrate + CH_4	121F0	30º C incubator, bottom shelf	
211M0	Birnessite + CH_4	111M0	30º C incubator, bottom shelf	
221M0	Birnessite + CH_4	121M0	30º C incubator, bottom shelf	
211MA	Birnessite + CH_4 + AQDS	111MA	30º C incubator, bottom shelf	
221MA	Birnessite + CH_4 + AQDS	121MA	30º C incubator, bottom shelf	
211MC	Birnessite + CH_4 + Cysteine	111MC	30º C incubator, bottom shelf	
221MC	Birnessite + CH_4 + Cysteine	121MC	30º C incubator, bottom shelf	
211M00S	CH_4	11100	30º C incubator, bottom shelf	No metal substrate
221M00S	CH_4	12100	30º C incubator, bottom shelf	No metal substrate
211MA0S	CH_4 + AQDS	1110A	30º C incubator, bottom shelf	No metal substrate
221MA0S	CH_4 + AQDS	1210A	30º C incubator, bottom shelf	No metal substrate

Table 18. Lake Matano 590-meter water depth sediment secondary Fe-AOM enrichment inventory.

211MC0S	CH_4 + Cysteine	1110C	30º C incubator, bottom shelf	No metal substrate
221MC0S	CH_4 + Cysteine	1210C	30º C incubator, bottom shelf	No metal substrate
211P0	Mn(III) + CH_4	111M0	30º C incubator, bottom shelf	
221P0	Mn(III) + CH_4	121M0	30º C incubator, bottom shelf	
211F00M	Goethite, no CH_4	111F00M	30º C incubator, bottom shelf	
221F00M	Goethite, no CH_4	121F00M	30º C incubator, bottom shelf	
211FA0M	Goethite + AQDS, no CH_4	111FA0M	30º C incubator, bottom shelf	
221FA0M	Goethite + AQDS, no CH_4	121FA0M	30º C incubator, bottom shelf	
211FC0M	Goethite + Cysteine, no CH_4	111FC0M	30º C incubator, bottom shelf	
221FC0M	Goethite + Cysteine, no CH_4	121FC0M	30º C incubator, bottom shelf	
211F00S0M	Ferrihydrite, no CH_4	111F00M	30º C incubator, bottom shelf	
221F00S0M	Ferrihydrite, no CH_4	121F00M	30º C incubator, bottom shelf	
211FA0S0M	Ferrihydrite + AQDS, no CH_4	111FA0M	30º C incubator, bottom shelf	
221FA0S0M	Ferrihydrite + AQDS, no CH_4	121FA0M	30º C incubator, bottom shelf	
211FC0S0M	Ferrihydrite + Cysteine, no CH_4	111FC0M	30º C incubator, bottom shelf	
221FC0S0M	Ferrihydrite + Cysteine, no CH_4	121FC0M	30º C incubator, bottom shelf	
211P00S0M	Fe(III)-citrate, no CH_4	111F00M	30º C incubator, bottom shelf	
221P00S0M	Fe(III)-citrate, no CH_4	121F00M	30º C incubator, bottom shelf	
211M00M	Birnessite, no CH_4	110M0	30º C incubator, bottom shelf	
221M00M	Birnessite, no CH_4	120M0	30º C incubator, bottom shelf	
211MA0M	Birnessite + AQDS, no CH_4	110MA	30º C incubator, bottom shelf	
221MA0M	Birnessite + AQDS, no CH_4	120MA	30º C incubator, bottom shelf	
211MC0M	Birnessite + Cysteine, no CH_4	110MC	30º C incubator, bottom shelf	
221MC0M	Birnessite + Cysteine, no CH_4	120MC	30º C incubator, bottom shelf	
211M00S0M	No substrates	11100	30º C incubator, bottom shelf	No metal substrate
221M00S0M	No substrates	12100	30º C incubator, bottom shelf	No metal substrate
211MA0S0M	AQDS	1110A	30º C incubator, bottom shelf	No metal substrate
221MA0S0M	AQDS	1210A	30º C incubator, bottom shelf	No metal substrate
211MC0S0M	Cysteine	1110C	30º C incubator, bottom shelf	No metal substrate
221MC0S0M	Cysteine	1210C	30º C incubator, bottom shelf	No metal substrate

Table 18. Lake Matano 590-meter water depth sediment secondary Fe-AOM enrichment inventory.

211P00M	Mn(III), no CH_4	110M0	30º C incubator, bottom shelf	
221P00M	Mn(III), no CH_4	120M0	30º C incubator, bottom shelf	
212F0	Goethite + CH_4	112F0	30º C incubator, bottom shelf	
222F0	Goethite + CH_4	122F0	30º C incubator, bottom shelf	
212FA	Goethite + CH_4 + AQDS	112FA	30º C incubator, bottom shelf	
222FA	Goethite + CH_4 + AQDS	122FA	30º C incubator, bottom shelf	
212FC	Goethite + CH_4 + Cysteine	112FC	30º C incubator, bottom shelf	
222FC	Goethite + CH_4 + Cysteine	122FC	30º C incubator, bottom shelf	
212F00S	Ferrihydrite + CH_4	112F0	30º C incubator, bottom shelf	
222F00S	Ferrihydrite + CH_4	122F0	30º C incubator, bottom shelf	
212FA0S	Ferrihydrite + CH_4 + AQDS	112FA	30º C incubator, bottom shelf	
222FA0S	Ferrihydrite + CH_4 + AQDS	122FA	30º C incubator, bottom shelf	
212FC0S	Ferrihydrite + CH_4 + Cysteine	112FC	30º C incubator, bottom shelf	
222FC0S	Ferrihydrite + CH_4 + Cysteine	122FC	30º C incubator, bottom shelf	
212P00S	Fe(III)-citrate + CH_4	112F0	30º C incubator, bottom shelf	
222P00S	Fe(III)-citrate + CH_4	122F0	30º C incubator, bottom shelf	
212M0	Birnessite + CH_4	112M0	30º C incubator, bottom shelf	
222M0	Birnessite + CH_4	122M0	30º C incubator, bottom shelf	
212MA	Birnessite + CH_4 + AQDS	112MA	30º C incubator, bottom shelf	
222MA	Birnessite + CH_4 + AQDS	122MA	30º C incubator, bottom shelf	
212MC	Birnessite + CH_4 + Cysteine	112MC	30º C incubator, bottom shelf	
222MC	Birnessite + CH_4 + Cysteine	122MC	30º C incubator, bottom shelf	
212M00S	CH_4	11200	30º C incubator, bottom shelf	No metal substrate
222M00S	CH_4	12200	30º C incubator, bottom shelf	No metal substrate
212MA0S	CH_4 + AQDS	1120A	30º C incubator, bottom shelf	No metal substrate
222MA0S	CH_4 + AQDS	1220A	30º C incubator, bottom shelf	No metal substrate
212MC0S	CH_4 + Cysteine	1120C	30º C incubator, bottom shelf	No metal substrate
222MC0S	CH_4 + Cysteine	1220C	30º C incubator, bottom shelf	No metal substrate
212P0	Mn(III) + CH_4	112M0	30º C incubator, bottom shelf	
222P0	Mn(III) + CH_4	122M0	30º C incubator, bottom shelf	

Table 18. Lake Matano 590-meter water depth sediment secondary Fe-AOM enrichment inventory.

212F00M	Goethite, no CH_4	112F00M	30º C incubator, bottom shelf	
222F00M	Goethite, no CH_4	122F00M	30º C incubator, bottom shelf	
212FA0M	Goethite + AQDS, no CH_4	112FA0M	30º C incubator, bottom shelf	
222FA0M	Goethite + AQDS, no CH_4	122FA0M	30º C incubator, bottom shelf	
212FC0M	Goethite + Cysteine, no CH_4	112FC0M	30º C incubator, bottom shelf	
222FC0M	Goethite + Cysteine, no CH_4	122FC0M	30º C incubator, bottom shelf	
212F00S0M	Ferrihydrite, no CH_4	112F00M	30º C incubator, bottom shelf	
222F00S0M	Ferrihydrite, no CH_4	122F00M	30º C incubator, bottom shelf	
212FA0S0M	Ferrihydrite + AQDS, no CH_4	112FA0M	30º C incubator, bottom shelf	
222FA0S0M	Ferrihydrite + AQDS, no CH_4	122FA0M	30º C incubator, bottom shelf	
212FC0S0M	Ferrihydrite + Cysteine, no CH_4	112FC0M	30º C incubator, bottom shelf	
222FC0S0M	Ferrihydrite + Cysteine, no CH_4	122FC0M	30º C incubator, bottom shelf	
212P00S0M	Fe(III)-citrate, no CH_4	112F00M	30º C incubator, bottom shelf	
222P00S0M	Fe(III)-citrate, no CH_4	122F00M	30º C incubator, bottom shelf	
212M00M	Birnessite, no CH_4	112M00M	30º C incubator, bottom shelf	
222M00M	Birnessite, no CH_4	122M00M	30º C incubator, bottom shelf	
212MA0M	Birnessite + AQDS, no CH_4	112MA0M	30º C incubator, bottom shelf	
222MA0M	Birnessite + AQDS, no CH_4	122MA0M	30º C incubator, bottom shelf	
212MC0M	Birnessite + Cysteine, no CH_4	112MC0M	30º C incubator, bottom shelf	
222MC0M	Birnessite + Cysteine, no CH_4	122MC0M	30º C incubator, bottom shelf	
212M00S0M	No substrates	11200	30º C incubator, bottom shelf	No metal substrate
222M00S0M	No substrates	12200	30º C incubator, bottom shelf	No metal substrate
212MA0S0M	AQDS	1120A	30º C incubator, bottom shelf	No metal substrate
222MA0S0M	AQDS	1220A	30º C incubator, bottom shelf	No metal substrate
212MC0S0M	Cysteine	1120C	30º C incubator, bottom shelf	No metal substrate
222MC0S0M	Cysteine	1220C	30º C incubator, bottom shelf	No metal substrate
212P00M	Mn(III), no CH_4	112M00M	30º C incubator, bottom shelf	
222P00M	Mn(III), no CH_4	122M00M	30º C incubator, bottom shelf	
213F0	Goethite + CH_4	113F0	30º C incubator, bottom shelf	
223F0	Goethite + CH_4	123F0	30º C incubator, bottom shelf	

Table 18. Lake Matano 590-meter water depth sediment secondary Fe-AOM enrichment inventory.

213FA	Goethite + CH_4 + AQDS	113FA	30º C incubator, bottom shelf	
223FA	Goethite + CH_4 + AQDS	123FA	30º C incubator, bottom shelf	
213FC	Goethite + CH_4 + Cysteine	113FC	30º C incubator, bottom shelf	
223FC	Goethite + CH_4 + Cysteine	123FC	30º C incubator, bottom shelf	
213F00S	Ferrihydrite + CH_4	113F0	30º C incubator, bottom shelf	
223F00S	Ferrihydrite + CH_4	123F0	30º C incubator, bottom shelf	
213FA0S	Ferrihydrite + CH_4 + AQDS	113FA	30º C incubator, bottom shelf	
223FA0S	Ferrihydrite + CH_4 + AQDS	123FA	30º C incubator, bottom shelf	
213FC0S	Ferrihydrite + CH_4 + Cysteine	113FC	30º C incubator, bottom shelf	
223FC0S	Ferrihydrite + CH_4 + Cysteine	123FC	30º C incubator, bottom shelf	
213P00S	Fe(III)-citrate + CH_4	123F0	30º C incubator, bottom shelf	
223P00S	Fe(III)-citrate + CH_4	113FA	30º C incubator, bottom shelf	
213M0	Birnessite + CH_4	113M0	30º C incubator, bottom shelf	
223M0	Birnessite + CH_4	123M0	30º C incubator, bottom shelf	
213MA	Birnessite + CH_4 + AQDS	113MA	30º C incubator, bottom shelf	
223MA	Birnessite + CH_4 + AQDS	123MA	30º C incubator, bottom shelf	
213MC	Birnessite + CH_4 + Cysteine	113MC	30º C incubator, bottom shelf	
223MC	Birnessite + CH_4 + Cysteine	123MC	30º C incubator, bottom shelf	
213M00S	CH_4	11300	30º C incubator, bottom shelf	No metal substrate
223M00S	CH_4	12300	30º C incubator, bottom shelf	No metal substrate
213MA0S	CH_4 + AQDS	1130A	30º C incubator, bottom shelf	No metal substrate
223MA0S	CH_4 + AQDS	1230A	30º C incubator, bottom shelf	No metal substrate
213MC0S	CH_4 + Cysteine	1130C	30º C incubator, bottom shelf	No metal substrate
223MC0S	CH_4 + Cysteine	1230C	30º C incubator, bottom shelf	No metal substrate
213P0	Mn(III) + CH_4	113M0	30º C incubator, bottom shelf	
223P0	Mn(III) + CH_4	123M0	30º C incubator, bottom shelf	
213F00M	Goethite, no CH_4	113F00M	30º C incubator, bottom shelf	
223F00M	Goethite, no CH_4	123F00M	30º C incubator, bottom shelf	
213FA0M	Goethite + AQDS, no CH_4	113FA0M	30º C incubator, bottom shelf	
223FA0M	Goethite + AQDS, no CH_4	123FA0M	30º C incubator, bottom shelf	

Table 18. Lake Matano 590-meter water depth sediment secondary Fe-AOM enrichment inventory.

213FC0M	Goethite + Cysteine, no CH_4	113FC0M	30º C incubator, bottom shelf	
223FC0M	Goethite + Cysteine, no CH_4	123FC0M	30º C incubator, bottom shelf	
213F00S0M	Ferrihydrite, no CH_4	113F00M	30º C incubator, bottom shelf	
223F00S0M	Ferrihydrite, no CH_4	123F00M	30º C incubator, bottom shelf	
213FA0S0M	Ferrihydrite + AQDS, no CH_4	113FA0M	30º C incubator, bottom shelf	
223FA0S0M	Ferrihydrite + AQDS, no CH_4	123FA0M	30º C incubator, bottom shelf	
213FC0S0M	Ferrihydrite + Cysteine, no CH_4	113FC0M	30º C incubator, bottom shelf	
223FC0S0M	Ferrihydrite + Cysteine, no CH_4	123FC0M	30º C incubator, bottom shelf	
213P00S0M	Fe(III)-citrate, no CH_4	113F00M	30º C incubator, bottom shelf	
223P00S0M	Fe(III)-citrate, no CH_4	123F00M	30º C incubator, bottom shelf	
213M00M	Birnessite, no CH_4	113M00M	30º C incubator, bottom shelf	
223M00M	Birnessite, no CH_4	123M00M	30º C incubator, bottom shelf	
213MA0M	Birnessite + AQDS, no CH_4	113MA0M	30º C incubator, bottom shelf	
223MA0M	Birnessite + AQDS, no CH_4	123MA0M	30º C incubator, bottom shelf	
213MC0M	Birnessite + Cysteine, no CH_4	113MC0M	30º C incubator, bottom shelf	
223MC0M	Birnessite + Cysteine, no CH_4	123MC0M	30º C incubator, bottom shelf	
213M00S0M	No substrates	11300	30º C incubator, bottom shelf	No metal substrate
223M00S0M	No substrates	12300	30º C incubator, bottom shelf	No metal substrate
213MA0S0M	AQDS	1130A	30º C incubator, bottom shelf	No metal substrate
223MA0S0M	AQDS	1230A	30º C incubator, bottom shelf	No metal substrate
213MC0S0M	Cysteine	1130C	30º C incubator, bottom shelf	No metal substrate
223MC0S0M	Cysteine	1230C	30º C incubator, bottom shelf	No metal substrate
213P00M	Mn(III), no CH_4	113M00M	30º C incubator, bottom shelf	
223P00M	Mn(III), no CH_4	123M00M	30º C incubator, bottom shelf	

Table 19. Matano 590-meter water depth sediment tertiary Fe-AOM enrichment inventory. Enrichment cultures were started 9-1-14 by adding fresh media and substrates to previous enrichments. The heat killed controls were inoculated by transferring aliquots of previous enrichments to new bottles. For information describing enrichment media and inoculation/incubation methods, see Chapter 4 and the "AOM-Fe, Aug 2014-May 2015" red laboratory notebook located in the Glass Lab.

Culture name	Treatment	Inoculum	Storage location	Comments	NCBI accession
311FMe	Ferrihydrite + CH_4	111F0	30º C incubator, bottom shelf	SAMN11586853-6 (metagenomic bins)	Metagenomic Bins: SAMN11586853-6 Reads: SAMN10492640
321FMe	Ferrihydrite + CH_4	121F0	30º C incubator, bottom shelf		
311FN	Ferrihydrite, no CH_4	111F00M	30º C incubator, bottom shelf	SAMN10431265-78 (metagenomic bins)	Metagenomic Bins: SAMN10431265-78 Reads: SAMN10411764
321FN	Ferrihydrite, no CH_4	12100M	30º C incubator, bottom shelf		
311MnMe	Birnessite + CH_4	211M0	30º C incubator, bottom shelf		
321MnMe	Birnessite + CH_4	221M0	30º C incubator, bottom shelf		
311MnN	Birnessite, no CH_4	211M00M	30º C incubator, bottom shelf		
321MnN	Birnessite, no CH_4	221M00M	30º C incubator, bottom shelf		
312FMe	Ferrihydrite + CH_4	112F0	30º C incubator, bottom shelf		
322FMe	Ferrihydrite + CH_4	122F0	30º C incubator, bottom shelf		
312FN	Ferrihydrite, no CH_4	112F00M	30º C incubator, bottom shelf		
322FN	Ferrihydrite, no CH_4	122F00M	30º C incubator, bottom shelf		
312MnMe	Birnessite + CH_4	212M0	30º C incubator, bottom shelf		
322MnMe	Birnessite + CH_4	222M0	30º C incubator, bottom shelf		
312MnN	Birnessite, no CH_4	212M00M	30º C incubator, bottom shelf		
322MnN	Birnessite, no CH_4	222M00M	30º C incubator, bottom shelf		
313FMe	Ferrihydrite + CH_4	113F0	30º C incubator, bottom shelf		
323FMe	Ferrihydrite + CH_4	123F0	30º C incubator, bottom shelf		
313FN	Ferrihydrite, no CH_4	113F00M	30º C incubator, bottom shelf		
323FN	Ferrihydrite, no CH_4	123F00M	30º C incubator, bottom shelf		
313MnMe	Birnessite + CH_4	213M0	30º C incubator, bottom shelf		
323MnMe	Birnessite + CH_4	223M0	30º C incubator, bottom shelf		
313MnN	Birnessite, no CH_4	213M00M	30º C incubator, bottom shelf		
323MnN	Birnessite, no CH_4	223M00M	30º C incubator, bottom shelf		
311FMeH	Ferrihydrite + CH_4 Autoclaved control	111F0	30º C incubator, bottom shelf		
321FMeH	Ferrihydrite + CH_4	121F0	30º C incubator, bottom shelf		

Table 19. Lake Matano 590-meter water depth sediment tertiary Fe-AOM enrichment inventory.

	Autoclaved control				
311MnMeH	Birnessite + CH_4 Autoclaved control	211M0	30º C incubator, bottom shelf		
321MnMeH	Birnessite + CH_4 Autoclaved control	221M0	30º C incubator, bottom shelf		
312FMeH	Ferrihydrite + CH_4 Autoclaved control	112F0	30º C incubator, bottom shelf		
322FMeH	Ferrihydrite + CH_4 Autoclaved control	122F0	30º C incubator, bottom shelf		
312MnMeH	Birnessite + CH_4 Autoclaved control	212M0	30º C incubator, bottom shelf		
322MnMeH	Birnessite + CH_4 Autoclaved control	222M0	30º C incubator, bottom shelf		
313FMeH	Ferrihydrite + CH_4 Autoclaved control	113F0	30º C incubator, bottom shelf		
323FMeH	Ferrihydrite + CH_4 Autoclaved control	123F0	30º C incubator, bottom shelf		
313MnMeH	Birnessite + CH_4 Autoclaved control	213M0	30º C incubator, bottom shelf		
323MnMeH	Birnessite + CH_4 Autoclaved control	223M0	30º C incubator, bottom shelf		

Table 20. Matano 590-meter water depth sediment quaternary Fe-AOM enrichment inventory. Enrichment cultures were started 11-24-15 by transferring aliquots of tertiary enrichments to new bottles. For information describing enrichment media and inoculation/incubation methods, see Chapter 4 and the "Fe-AOM, May 2015-June 2016" red laboratory notebook located in the Glass Lab.

Culture name	Treatment	Inoculum	Storage location	Comment
2º 311FMe + FeS	Ferrihydrite + CH_4 + FeS	311FMe	30º C incubator, bottom shelf	
2º 311FMe + SO_4^{2-}	Ferrihydrite + CH_4 + SO_4^{2-}	311FMe	30º C incubator, bottom shelf	
2º 311FMe - S	Ferrihydrite + CH_4	311FMe	30º C incubator, bottom shelf	
2º 321FMe + FeS	Ferrihydrite + CH_4 + FeS	321FMe	30º C incubator, bottom shelf	
2º 321FMe + SO_4^{2-}	Ferrihydrite + CH_4 + SO_4^{2-}	321FMe	30º C incubator, bottom shelf	
2º 321FMe - S	Ferrihydrite + CH_4	321FMe	30º C incubator, bottom shelf	
2º 311FN + FeS	Ferrihydrite, no CH_4 + FeS	311FN	30º C incubator, bottom shelf	
2º 311FN + SO_4^{2-}	Ferrihydrite, no CH_4 + SO_4^{2-}	311FN	30º C incubator, bottom shelf	
2º 311FN - S	Ferrihydrite, no CH_4	311FN	30º C incubator, bottom shelf	
2º 321FN + FeS	Ferrihydrite, no CH_4 + FeS	321FN	30º C incubator, bottom shelf	
2º 321FN + SO_4^{2-}	Ferrihydrite, no CH_4 + SO_4^{2-}	321FN	30º C incubator, bottom shelf	
2º 321FN - S	Ferrihydrite, no CH_4	321FN	30º C incubator, bottom shelf	
2º 311FMeH + FeS	Ferrihydrite + CH_4 + FeS Autoclaved control	311FMe	30º C incubator, bottom shelf	
2º 311FMeH + SO_4^{2-}	Ferrihydrite + CH_4 + SO_4^{2-}	311FMe	30º C incubator, bottom shelf	
2º 311FMeH - S	Ferrihydrite + CH_4 Autoclaved control	311FMe	30º C incubator, bottom shelf	
2º 321FMeH + FeS	Ferrihydrite + CH_4 + FeS Autoclaved control	321FMe	30º C incubator, bottom shelf	
2º 321FMeH + SO_4^{2-}	Ferrihydrite + CH_4 + SO_4^{2-} Autoclaved control	321FMe	30º C incubator, bottom shelf	
2º 321FMeH - S	Ferrihydrite + CH_4 Autoclaved control	321FMe	30º C incubator, bottom shelf	

Table 21. Matano 590-meter water depth sediment quinary Fe-AOM enrichment inventory. Enrichment cultures were started 5-20-16 by transferring aliquots of quaternary enrichments to new bottles. For information describing enrichment media and inoculation/incubation methods, see Chapter 4 and the "Fe-AOM, May 2015-June 2016" red laboratory notebook located in the Glass Lab.

Culture name	Treatment	Inoculum	Storage location	Comment
3º 311FMe Fes	Ferrihydrite + CH_4 + FeS	2º 311FMe + FeS	30º C incubator, bottom shelf	
3º 311FMe -S	Ferrihydrite + CH_4	2º 311FMe - S	30º C incubator, bottom shelf	
3º 321FMe Fes	Ferrihydrite + CH_4 + FeS	2º 321FMe + FeS	30º C incubator, bottom shelf	
3º 321FMe -S	Ferrihydrite + CH_4	2º 321FMe - S	30º C incubator, bottom shelf	
3º 311FN Fes	Ferrihydrite, no CH_4 + FeS	2º 311FN + FeS	30º C incubator, bottom shelf	
3º 311FN -S	Ferrihydrite, no CH_4	2º 311FN - S	30º C incubator, bottom shelf	
3º 321FN Fes	Ferrihydrite, no CH_4 + FeS	2º 321FN + FeS	30º C incubator, bottom shelf	
3º 321FN -S	Ferrihydrite, no CH_4	2º 321FN - S	30º C incubator, bottom shelf	
3º 311FMeH Fes	Ferrihydrite + CH_4 + FeS Autoclaved control	2º 311FMeH + FeS	30º C incubator, bottom shelf	
3º 311FMeH -S	Ferrihydrite + CH_4 Autoclaved control	2º 311FMeH - S	30º C incubator, bottom shelf	
3º 321FMeH Fes	Ferrihydrite + CH_4 + FeS Autoclaved control	.	30º C incubator, bottom shelf	
3º 321FMeH -S	Ferrihydrite + CH_4 Autoclaved control	2º 321FMeH - S	30º C incubator, bottom shelf	

Table 22. Matano 200-meter water depth sediment primary and secondary Fe-AOM enrichment inventory. Enrichment cultures were started on 3-31-15 (0-5 cm) or 4-7-19 (5-15 cm) using fresh Lake Matano sediment. Secondary enrichments were initialized by adding fresh media and substrates to the primary enrichment bottles on 5-19-15 (0-5 cm), 5-26-15 (5-10 cm), or 6-3-15 (10-15cm). For information describing enrichment media and inoculation/incubation methods, see Chapter 4 and the "Fe-AOM, May 2015-June 2016" red laboratory notebook located in the Glass Lab.

Culture name	Treatment	Inoculum	Storage location	Comment	NCBI accession
D1FMe1	Ferrihydrite + CH_4	200 m water depth sediment, 0-5 cm	30º C incubator, bottom shelf		SAMN4532580-3 (16S amplicon) SAMN10431999-2011 (metagenomic bins) SAMN10411531 (metagenomic reads)
D1FMe2	Ferrihydrite + CH_4	200 m water depth sediment, 0-5 cm	30º C incubator, bottom shelf		SAMN4532584-5 (16S amplicon)
D1FN1	Ferrihydrite, no CH_4	200 m water depth sediment, 0-5 cm	30º C incubator, bottom shelf		SAMN4532586 (16S amplicon) SAMN11586698-700 (metagenomic bins) SAMN10495303 (metagenomic reads)
D1FN2	Ferrihydrite, no CH_4	200 m water depth sediment, 0-5 cm	30º C incubator, bottom shelf		SAMN4532587-8 (16S amplicon)
D1HFMe1	Ferrihydrite + CH_4, Autoclaved control	200 m water depth sediment, 0-5 cm	30º C incubator, bottom shelf		
D1HFMe2	Ferrihydrite + CH_4, Autoclaved control	200 m water depth sediment, 0-5 cm	30º C incubator, bottom shelf		
D1GMe1	Goethite + CH_4	200 m water depth sediment, 0-5 cm	30º C incubator, bottom shelf		SAMN4532589-91 (16S amplicon)
D1GMe2	Goethite + CH_4	200 m water depth sediment, 0-5 cm	30º C incubator, bottom shelf		
D1GN1	Goethite, no CH_4	200 m water depth sediment, 0-5 cm	30º C incubator, bottom shelf		SAMN4532592-3 (16S amplicon)
D1GN2	Goethite, no CH_4	200 m water depth sediment, 0-5 cm	30º C incubator, bottom shelf		SAMN4532594-7 (16S amplicon)
D1HGMe1	Goethite + CH_4 Autoclaved controls	200 m water depth sediment, 0-5 cm	30º C incubator, bottom shelf		SAMN4532590 (16S amplicon)
D1HGMe2	Goethite + CH_4 Autoclaved controls	200 m water depth sediment, 0-5 cm	30º C incubator, bottom shelf		SAMN4532591 (16S amplicon)
D1XMe1	CH_4	200 m water depth sediment, 0-5 cm	30º C incubator, bottom shelf	No metal substrate	SAMN4532598-01 (16S amplicon)
D1XMe2	CH_4	200 m water depth sediment, 0-5 cm	30º C incubator, bottom shelf	No metal substrate	
D2FMe1	Ferrihydrite + CH_4	200 m water depth sediment, 5-10 cm	30º C incubator, bottom shelf		SAMN4532501-3 (16S amplicon)
D2FMe2	Ferrihydrite + CH_4	200 m water depth sediment, 5-10 cm	30º C incubator, bottom shelf		SAMN4532504-5 (16S amplicon)
D2FN1	Ferrihydrite, no CH_4	200 m water depth sediment, 5-10 cm	30º C incubator, bottom shelf		SAMN4532506-7 (16S amplicon)
D2FN2	Ferrihydrite, no CH_4	200 m water depth sediment, 5-10 cm	30º C incubator, bottom shelf		SAMN4532508-9 (16S amplicon)
D2HFMe1	Ferrihydrite + CH_4, Autoclaved control	200 m water depth sediment, 5-10 cm	30º C incubator, bottom shelf		
D2HFMe2	Ferrihydrite + CH_4, Autoclaved control	200 m water depth sediment, 5-10 cm	30º C incubator, bottom shelf		
D2GMe1	Goethite + CH_4	200 m water depth sediment, 5-10 cm	30º C incubator, bottom shelf		SAMN4532510-1 (16S amplicon)
D2GMe2	Goethite + CH_4	200 m water depth sediment, 5-10 cm	30º C incubator, bottom shelf		SAMN4532512-3 (16S amplicon)

Table 22. Matano 200-meter water depth sediment primary and secondary Fe-AOM enrichment inventory.

D2GN1	Goethite, no CH_4	200 m water depth sediment, 5-10 cm	30º C incubator, bottom shelf		SAMN4532514-5 (16S amplicon)
D2GN2	Goethite, no CH_4	200 m water depth sediment, 5-10 cm	30º C incubator, bottom shelf		SAMN4532515-7 (16S amplicon)
D2HGMe1	Goethite + CH_4 Autoclaved controls	200 m water depth sediment, 5-10 cm	30º C incubator, bottom shelf		
D2HGMe2	Goethite + CH_4 Autoclaved controls	200 m water depth sediment, 5-10 cm	30º C incubator, bottom shelf		
D2XMe1	CH_4	200 m water depth sediment, 5-10 cm	30º C incubator, bottom shelf	No metal substrate	SAMN4532518-9 (16S amplicon)
D2XMe2	CH_4	200 m water depth sediment, 5-10 cm	30º C incubator, bottom shelf	No metal substrate	SAMN4532520-1 (16S amplicon)
D3FMe1	Ferrihydrite + CH_4	200 m water depth sediment, 10-15 cm	30º C incubator, bottom shelf		SAMN4532522-3 (16S amplicon)
D3FMe2	Ferrihydrite + CH_4	200 m water depth sediment, 10-15 cm	30º C incubator, bottom shelf		SAMN4532524-3 (16S amplicon)
D3FN1	Ferrihydrite, no CH_4	200 m water depth sediment, 10-15 cm	30º C incubator, bottom shelf		SAMN4532526-7 (16S amplicon)
D3FN2	Ferrihydrite, no CH_4	200 m water depth sediment, 10-15 cm	30º C incubator, bottom shelf		SAMN4532528-9 (16S amplicon)
D3HFMe1	Ferrihydrite + CH_4, Autoclaved control	200 m water depth sediment, 10-15 cm	30º C incubator, bottom shelf		
D3HFMe2	Ferrihydrite + CH_4, Autoclaved control	200 m water depth sediment, 10-15 cm	30º C incubator, bottom shelf		
D3GMe1	Goethite + CH_4	200 m water depth sediment, 10-15 cm	30º C incubator, bottom shelf		SAMN4532530-1 (16S amplicon)
D3GMe2	Goethite + CH_4	200 m water depth sediment, 10-15 cm	30º C incubator, bottom shelf		SAMN4532532-3 (16S amplicon)
D3GN1	Goethite, no CH_4	200 m water depth sediment, 10-15 cm	30º C incubator, bottom shelf		SAMN4532534-5 (16S amplicon)
D3GN2	Goethite, no CH_4	200 m water depth sediment, 10-15 cm	30º C incubator, bottom shelf		SAMN4532536-7 (16S amplicon)
D3HGMe1	Goethite + CH_4 Autoclaved controls	200 m water depth sediment, 10-15 cm	30º C incubator, bottom shelf		
D3GHMe2	Goethite + CH_4 Autoclaved controls	200 m water depth sediment, 10-15 cm	30º C incubator, bottom shelf		
D2XMe1	CH_4	200 m water depth sediment, 10-15 cm	30º C incubator, bottom shelf	No metal substrate	SAMN4532538-9 (16S amplicon)
D2XMe2	CH_4	200 m water depth sediment, 10-15 cm	30º C incubator, bottom shelf	No metal substrate	SAMN4532540-1 (16S amplicon)

Table 23. Matano 200-meter water depth sediment tertiary Fe-AOM enrichment inventory. Enrichment cultures were started on 3-15-16 by transferring aliquots of secondary enrichments into new bottles. For information describing enrichment media and inoculation/incubation methods, see Chapter 4 and the "Fe-AOM, May 2015-June 2016" red laboratory notebook located in the Glass Lab.

Culture name	Treatment	Inoculum	Storage Location	Comment
2º D1FMe1	Ferrihydrite + CH_4	D1Fme1	30º C incubator, bottom shelf	
2º D1FMe2	Ferrihydrite + CH_4	D1Fme2	30º C incubator, bottom shelf	
2º D1FN1	Ferrihydrite, no CH_4	D1FN1	30º C incubator, bottom shelf	
2º D1FN2	Ferrihydrite, no CH_4	D1FN2	30º C incubator, bottom shelf	
2º D1HFMe1	Ferrihydrite + CH_4, Autoclaved control	D1HFMe1	30º C incubator, bottom shelf	
2º D1HFMe2	Ferrihydrite + CH_4, Autoclaved control	D1HFMe2	30º C incubator, bottom shelf	
2º D1XMe1	CH_4	D1Xme1	30º C incubator, bottom shelf	No metal substrates
2º D1XMe2	CH_4	D1Xme2	30º C incubator, bottom shelf	No metal substrates
2º D1GMe1	Goethite + CH_4	D1Gme1	30º C incubator, bottom shelf	
2º D1GMe2	Goethite + CH_4	D1Gme2	30º C incubator, bottom shelf	
2º D1GN1	Goethite, no CH_4	D1GN1	30º C incubator, bottom shelf	
2º D1GN2	Goethite, no CH_4	D1GN2	30º C incubator, bottom shelf	
2º D1HGMe1	Goethite + CH_4 Autoclaved controls	D1HGMe1	30º C incubator, bottom shelf	
2º D1HGMe2	Goethite + CH_4 Autoclaved controls	D1HGMe2	30º C incubator, bottom shelf	
2º D1AMe1	Ferrihydrite + CH_4	Nome	30º C incubator, bottom shelf	Abiotic control Became contaminated
2º D1AGMe1	Goethite + CH_4	None	30º C incubator, bottom shelf	Abiotic control
2º D3GN1	Goethite, no CH_4	D3GN1	30º C incubator, bottom shelf	
2º D3GN2	Goethite, no CH_4	D3GN2	30º C incubator, bottom shelf	

Table 24. Matano 200-meter water depth sediment quaternary Fe-AOM enrichment inventory. Enrichment cultures were started on 10-21-16 (Goethite cultures) and 12-20-16 (Ferrihydrite cultures) by transferring aliquots of secondary enrichments into new bottles. For information describing enrichment media and inoculation/incubation methods, see Chapter 4 and the "Marcus Fe-AOM June 2016-June 2019" blue laboratory notebook located in the Glass Lab.

Culture name	Treatment	Inoculum	Storage Location	Comment
3º D1GN1	Goethite, no CH_4	2º D1GN1	30º C incubator, bottom shelf	
3º D1GN2	Goethite, no CH_4	2º D1GN2	30º C incubator, bottom shelf	
3º D1GN1 H2	Goethite + H_2, no CH_4	2º D1GN1	30º C incubator, bottom shelf	
3º D1GN2 H2	Goethite + H_2, no CH_4	2º D1GN2	30º C incubator, bottom shelf	
3º D1N1	No substrates	2º D1GN1	30º C incubator, bottom shelf	
3º D1N2	No substrates	2º D1GN2	30º C incubator, bottom shelf	
3º D1N1 H2	H_2	2º D1GN1	30º C incubator, bottom shelf	
3º D1N2 H2	H_2	2º D1GN2	30º C incubator, bottom shelf	
3º D1GN1K	Goethite, no CH_4 Autoclaved controls	2º D1GN1	30º C incubator, bottom shelf	
3º D1GN2K	Goethite, no CH_4 Autoclaved controls	2º D1GN2	30º C incubator, bottom shelf	
3º D1GN1K H2	Goethite + H_2, no CH_4 Autoclaved controls	2º D1GN1	30º C incubator, bottom shelf	
3º D1GN1K H2	Goethite + H_2, no CH_4 Autoclaved controls	2º D1GN2	30º C incubator, bottom shelf	
3º D1FMe1	Ferrihydrite + CH_4	2º D1FMe1	30º C incubator, bottom shelf	
3º D1FMe2	Ferrihydrite + CH_4	2º D1FMe2	30º C incubator, bottom shelf	
3º D1FN1	Ferrihydrite, no CH_4	2º D1FMe1	30º C incubator, bottom shelf	
3º D1FN2	Ferrihydrite, no CH_4	2º D1FMe2	30º C incubator, bottom shelf	
3º D1HFMe1	Ferrihydrite + CH_4, Autoclaved control	2º D1HFMe1	30º C incubator, bottom shelf	
3º D1HFMe2	Ferrihydrite + CH_4, Autoclaved control	2º D1HFMe2	30º C incubator, bottom shelf	
3º D1XMe1	CH_4	2º D1XMe1	30º C incubator, bottom shelf	
3º D1XMe2	CH_4	2º D1XMe2	30º C incubator, bottom shelf	
3º D1AFMe1	Ferrihydrite + CH_4	2º D1Ame1	30º C incubator, bottom shelf	Inculcated with contaminated abiotic control
3º D1ADMe2	Ferrihydrite + CH_4	2º D1Ame1	30º C incubator, bottom shelf	Inculcated with contaminated abiotic control

Table 25. Matano sediment Fe^{2+}-N_2O enrichment inventory. Enrichments were started on 5-19-17 or 6-21-17 by transferring and aliquot of either 590-meter or 200-meter Fe-AOM enrichments into new bottles with fresh media. For information describing enrichment media and inoculation/incubation methods, see Appendix B and the "Marcus Fe-AOM June 2016-June 2019" blue laboratory notebook located in the Glass Lab.

Culture name	Treatment	Inoculum	Storage Location	Comment
311FMe NO_3 1	Fe^{2+} + NO_3 + N_2O	3º 311FMe FeS	30º C incubator, middle shelf	N_2O was added after first month of incubation
311FMe NO_3 2	Fe^{2+} + NO_3 + N_2O	3º 311FMe FeS	30º C incubator, middle shelf	N_2O was added after first month of incubation
311FMe NO_3 Ac 1	Fe^{2+} + NO_3 + N_2O + acetate	3º 311FMe FeS	30º C incubator, middle shelf	N_2O was added after first month of incubation
311FMe NO_3 Ac 2	Fe^{2+} + NO_3 + N_2O + acetate	3º 311FMe FeS	30º C incubator, middle shelf	N_2O was added after first month of incubation
311FMe NO_3 Ac HK1	Fe^{2+} + NO_3 + N_2O + acetate Autoclaved control	3º 311FMe FeS	30º C incubator, middle shelf	N_2O was added after first month of incubation
311FMe NO_3 Ac HK2	Fe^{2+} + NO_3 + N_2O + acetate Autoclaved control	3º 311FMe FeS	30º C incubator, middle shelf	N_2O was added after first month of incubation
311FMe N_2O Ac no Fe^{2+}	NO_3 + N_2O + acetate, no Fe^{2+}	3º 311FMe FeS	30º C incubator, middle shelf	N_2O was added after first month of incubation
311FMe N_2O Ac no Fe^{2+}	NO_3 + N_2O + acetate, no Fe^{2+}	3º 311FMe FeS	30º C incubator, middle shelf	N_2O was added after first month of incubation
D1FMe N_2O 1	Fe^{2+} + N_2O	D1FMe1	30º C incubator, middle shelf	
D1FMe N_2O 2	Fe^{2+} + N_2O	D1FMe2	30º C incubator, middle shelf	
D1FMe N_2O Ac 1	Fe^{2+} + N_2O + acetate	D1FMe	30º C incubator, middle shelf	
D1FMe N_2O Ac 2	Fe^{2+} + N_2O + acetate	D1FMe2	30º C incubator, middle shelf	
D1FN N_2O 1	Fe^{2+} + N_2O	D1FN1	30º C incubator, middle shelf	
D1FN N_2O 2	Fe^{2+} + N_2O	D1FN2	30º C incubator, middle shelf	
D1FN N_2O Ac 1	Fe^{2+} + N_2O + acetate	D1FN1	30º C incubator, middle shelf	
D1FN N_2O Ac 2	Fe^{2+} + N_2O + acetate	D1FN2	30º C incubator, middle shelf	
D1FMe1 N_2O Ac no Fe^{2+}	N_2O + acetate, no Fe^{2+}	D1FMe1	30º C incubator, middle shelf	
D1FMe2 N_2O Ac no Fe^{2+}	N_2O + acetate, no Fe^{2+}	D1FMe2	30º C incubator, middle shelf	
D1FMe1 N_2O Ac HK	Fe^{2+} + N_2O + acetate Autoclaved control	D1FMe1	30º C incubator, middle shelf	
D1FMe1 N_2O Ac HK	Fe^{2+} + N_2O + acetate Autoclaved control	D1FMe2	30º C incubator, middle shelf	

Table 26. Matano sediment ClO_4^-AOM primary and secondary enrichment inventory. Enrichments were started on 4-7-17 (primary) and 10-15-18 (secondary) using fresh Lake Matano sediment. For information describing enrichment media and inoculation/incubation methods, see Appendix A and the "Marcus Fe-AOM June 2016-June 2019" blue laboratory notebook located in the Glass Lab.

Culture name	Treatment	Inoculum	Storage Location	Comment
CH4 Ac ClO4 1	CH_4 + acetate + ClO_4^-	200 m water depth sediment, 10-15 cm	30º C incubator, middle shelf	
CH4 Ac ClO4 2	CH_4 + acetate + ClO_4^-	200 m water depth sediment, 10-15 cm	30º C incubator, middle shelf	
CH4 ClO4 1	CH_4 + ClO_4^-	200 m water depth sediment, 10-15 cm	30º C incubator, middle shelf	
CH4 ClO4 2	CH_4 + ClO_4^-	200 m water depth sediment, 10-15 cm	30º C incubator, middle shelf	
N2 Ac ClO4 1	Acetate + ClO_4^-, no CH_4	200 m water depth sediment, 10-15 cm	30º C incubator, middle shelf	
N2 Ac ClO4 2	Acetate + ClO_4^-, no CH_4	200 m water depth sediment, 10-15 cm	30º C incubator, middle shelf	
CH4 Ac ClO4 H 1	CH_4 + acetate + ClO_4^- Autoclaved control	200 m water depth sediment, 10-15 cm	30º C incubator, middle shelf	
CH4 Ac ClO4 H 2	CH_4 + acetate + ClO_4^- Autoclaved control	200 m water depth sediment, 10-15 cm	30º C incubator, middle shelf	
CH4 1	CH_4	200 m water depth sediment, 10-15 cm	30º C incubator, middle shelf	
CH4 2	CH_4	200 m water depth sediment, 10-15 cm	30º C incubator, middle shelf	
$^2CH_4AcClO_4^-$	CH_4 + acetate + ClO_4^-	CH4 Ac ClO4 2	30º C incubator, middle shelf	
$^2CH_4ClO_4^-$	CH_4 + ClO_4^-	CH4 Ac ClO4 2	30º C incubator, middle shelf	
$^2CH_4Ac$	Acetate + ClO_4^-, no CH_4	CH4 Ac ClO4 2	30º C incubator, middle shelf	
$^2N_2AcClO_4^-$	ClO_4^- + acetate, no CH_4	CH4 Ac ClO4 2	30º C incubator, middle shelf	
$^2N_2ClO_4^-$	ClO_4^-, no CH_4	CH4 Ac ClO4 2	30º C incubator, middle shelf	
From slants CH_4 headspace ClO_4	CH_4 + acetate + ClO_4^-	Colony picked from agar slant inoculated by CH4 Ac ClO4 2	30º C incubator, middle shelf	Pure culture
From slants N_2 headspace ClO_4	ClO_4^- + acetate, no CH_4	Colony picked from agar slant inoculated by CH4 Ac ClO4 2	30º C incubator, middle shelf	Pure culture
11-27-18 CH_4 headspace and ClO_4^- and acetate	CH_4 + acetate + ClO_4^-	From slants CH_4 headspace ClO_4	30º C incubator, middle shelf	Pure culture
11-27-18 CH_4 headspace and ClO_4^-	CH_4 + ClO_4^-	From slants CH_4 headspace ClO_4	30º C incubator, middle shelf	Pure culture
11-27-18 N_2 headspace and ClO_4^- acetate	Acetate + ClO_4^-, no CH_4	From slants CH_4 headspace ClO_4	30º C incubator, middle shelf	Pure culture
CH_4 ClO_4^- acetate culture for DNA cell mass	CH_4 + acetate + ClO_4^-	From slants CH_4 headspace ClO_4	30º C incubator, middle shelf	Pure culture

REFERENCES

1. Taylor S. 1964. Abundance of chemical elements in the continental crust: a new table. Geochimica et Cosmochimica Acta 28:1273-1285.

2. Pavlov A, Kasting J. 2002. Mass-independent fractionation of sulfur isotopes in Archean sediments: strong evidence for an anoxic Archean atmosphere. Astrobiology 2:27-41.

3. Canfield DE. 2005. The early history of atmospheric oxygen: Homage to Robert M. Garrels. Annual Review of Earth and Planetary Sciences 33:1-36.

4. Farquhar J, Zerkle AL, Bekker A. 2011. Geological constraints on the origin of oxygenic photosynthesis. Photosynthesis Research 107:11-36.

5. Cloud P. 1973. Paleoecological significance of the banded iron-formation. Economic Geology 68:1135-1143.

6. Jickells TD, An ZS, Andersen KK, Baker AR, Bergametti G, Brooks N, Cao JJ, Boyd PW, Duce RA, Hunter KA, Kawahata H, Kubilay N, laRoche J, Liss PS, Mahowald N, Prospero JM, Ridgwell AJ, Tegen I, Torres R. 2005. Global iron connections between desert dust, ccean biogeochemistry, and climate. Science 308:67-71.

7. Poulton S, Raiswell R. 2002. The low-temperature geochemical cycle of iron: from continental fluxes to marine sediment deposition. American Journal of Science 302:774-805.

8. Johnson KS, Gordon RM, Coale KH. 1997. What controls dissolved iron concentrations in the world ocean? Marine Chemistry 57:137-161.

9. Tortell PD, Maldonado MT, Granger J, Price NM. 1999. Marine bacteria and biogeochemical cycling of iron in the oceans. FEMS Microbiology Ecology 29:1-11.

10. Brand LE, Sunda WG, Guillard RR. 1983. Limitation of marine phytoplankton reproductive rates by zinc, manganese, and iron. Limnology and Oceanography 28:1182-1198.

11. Greene RM, Geider RJ, Falkowski PG. 1991. Effect of iron limitation on photosynthesis in a marine diatom. Limnology and Oceanography 36:1772-1782.

12. Coale KH, Johnson KS, Fitzwater SE, Gordon RM, Tanner S, Chavez FP, Ferioli L, Sakamoto C, Rogers P, Millero F. 1996. A massive phytoplankton bloom induced by an ecosystem-scale iron fertilization experiment in the equatorial Pacific Ocean. Nature 383:495.

13. Morgan B, Lahav O. 2007. The effect of pH on the kinetics of spontaneous Fe(II) oxidation by O2 in aqueous solution – basic principles and a simple heuristic description. Chemosphere 68:2080-2084.

14. Canfield DE, Habicht KS, Thamdrup B. 2000. The Archean sulfur cycle and the early history of atmospheric oxygen. Science 288:658-661.

15. Von Damm K. 1995. Controls on the chemistry and temporal variability of seafloor hydrothermal fluids. Seafloor Hydrothermal Systems: Physical, Chemical, Biological, and Geological Interactions 91:222-247.

16. Crowe SA, Paris G, Katsev S, Jones C, Kim S-T, Zerkle AL, Nomosatryo S, Fowle DA, Adkins JF, Sessions AL, Farquhar J, Canfield DE. 2014. Sulfate was a trace constituent of Archean seawater. Science 346:735-739.

17. Kasting JF. 1993. Earth's early atmosphere. Science 259:920-926.

18. Isley AE. 1995. Hydrothermal plumes and the delivery of iron to banded iron formation. The Journal of Geology 103:169-185.

19. Holland HD. 1984. The Chemical Evolution of the Atmosphere and Oceans. Princeton University Press, Princeton, N.J.

20. Butterfield D, Jonasson I, Massoth G, Feely R, Roe K, Embley R, Holden J, McDuff R, Lilley M, Delaney J. 1997. Seafloor eruptions and evolution of hydrothermal fluid chemistry. Philosophical Transactions of the Royal Society of London Series A: Mathematical, Physical and Engineering Sciences 355:369-386.

21. Jones C, Nomosatryo S, Crowe SA, Bjerrum CJ, Canfield DE. 2015. Iron oxides, divalent cations, silica, and the early earth phosphorus crisis. Geology 43:135-138.

22. Anbar AD, Holland HD. 1992. The photochemistry of manganese and the origin of banded iron formations. Geochimica et Cosmochimica Acta 56:2595-2603.

23. Konhauser KO, Hamade T, Raiswell R, Morris RC, Ferris FG, Southam G, Canfield DE. 2002. Could bacteria have formed the Precambrian banded iron formations? Geology 30:1079-1082.

24. Cammack R, Patil DS, Fernandez VM. 1985. Electron-spin-resonance/electron-paramagnetic-resonance spectroscopy of iron-sulphur enzymes. Biochemical Society Transactions 13:572-578.

25. Twilfer H, Bernhardt FH, Gersonde K. 1985. Dioxygen-activating iron center in putidamonooxin: Electron spin resonance investigation of the nitrosylated putidamonooxin. European Journal of Biochemistry 147:171-176.

26. Andrews SC. 1998. Iron storage in bacteria, p 281-351, Advances in Microbial Physiology, vol 40. Elsevier.

27. Andrews S, Norton I, Salunkhe AS, Goodluck H, Aly WSM, Mourad-Agha H, Cornelis P. 2013. Control of Iron Metabolism in Bacteria, p 203-239. *In* Banci L (ed), Metallomics and the Cell doi:10.1007/978-94-007-5561-1_7. Springer Netherlands.

28. Leslie E O. 2004. Prebiotic chemistry and the origin of the RNA world. Critical Reviews in Biochemistry and Molecular Biology 39:99-123.

29. Athavale SS, Petrov AS, Hsiao C, Watkins D, Prickett CD, Gossett JJ, Lie L, Bowman JC, O'Neill E, Bernier CR, Williams LD. 2012. RNA folding and catalysis mediated by iron (II). PLoS One 7:e38024.

30. Camacho A, Walter XA, Picazo A, Zopfi J. 2017. Photoferrotrophy: Remains of an ancient photosynthesis in modern environments. Frontiers in Microbiology 8:323-323.

31. Weber KA, Pollock J, Cole KA, O'Connor SM, Achenbach LA, Coates JD. 2006. Anaerobic nitrate-dependent iron (II) bio-oxidation by a novel lithoautotrophic betaproteobacterium, strain 2002. Applied and Environmental Microbiology 72:686-694.

32. Lack J, Chaudhuri S, Chakraborty R, Achenbach L, Coates J. 2002. Anaerobic biooxidation of Fe(II) by Dechlorosoma suillum. Microbial Ecology 43:424-431.

33. Bray MS, Lenz TK, Haynes JW, Bowman JC, Petrov AS, Reddi AR, Hud NV, Williams LD, Glass JB. 2018. Multiple prebiotic metals mediate translation. Proceedings of the National Academy of Sciences 115:12164-12169.

34. Ramakrishnan V. 2002. Ribosome structure and the mechanism of translation. Cell 108:557-72.

35. Yonath A. 2002. The search and its outcome: high-resolution structures of ribosomal particles from mesophilic, thermophilic, and halophilic bacteria at various functional states. Annual Review of Biophysics and Biomolecular Structure 31:257-273.

36. Fox GE. 2010. Origin and evolution of the ribosome. Cold Spring Harbor Perspectives in Biology 2:a003483.

37. Bernier CR, Petrov AS, Kovacs NA, Penev PI, Williams LD. 2018. Translation: The universal structural core of life. Molecular Biology and Evolution 35:2065-2076.

38. Klein DJ, Moore PB, Steitz TA. 2004. The contribution of metal ions to the structural stability of the large ribosomal subunit. RNA 10:1366-1379.

39. Cusack S. 1997. Aminoacyl-tRNA synthetases. Current Opinion in Structural Biology 7:881-889.

40. Petrov AS, Bowman JC, Harvey SC, Williams LD. 2011. Bidentate RNA–magnesium clamps: On the origin of the special role of magnesium in RNA folding. RNA 17:291-297.

41. Hsiao C, Williams LD. 2009. A recurrent magnesium-binding motif provides a framework for the ribosomal peptidyl transferase center. Nucleic Acids Research 37:3134-3142.

42. Schuwirth BS, Borovinskaya MA, Hau CW, Zhang W, Vila-Sanjurjo A, Holton JM, Cate JHD. 2005. Structures of the Bacterial Ribosome at 3.5 Å Resolution. Science 310:827-834.

43. Demeshkina N, Jenner L, Westhof E, Yusupov M, Yusupova G. 2012. A new understanding of the decoding principle on the ribosome. Nature 484:256.

44. Selmer M, Dunham CM, Murphy FV, Weixlbaumer A, Petry S, Kelley AC, Weir JR, Ramakrishnan V. 2006. Structure of the 70S ribosome complexed with mRNA and tRNA. Science 313:1935-1942.

45. Petrov AS, Bernier CR, Hsiao C, Okafor CD, Tannenbaum E, Stern J, Gaucher E, Schneider D, Hud NV, Harvey SC. 2012. RNA–magnesium–protein interactions in large ribosomal subunit. The Journal of Physical Chemistry B 116:8113-8120.

46. Pyle A. 2002. Metal ions in the structure and function of RNA. Journal of Biological Inorganic Chemistry 7:679-690.

47. Pyle AM. 1993. Ribozymes: a distinct class of metalloenzymes. Science 261:709-714.

48. Ward WL, Plakos K, DeRose VJ. 2014. Nucleic acid catalysis: metals, nucleobases, and other cofactors. Chemical Reviews 114:4318-4342.

49. Okafor CD, Bowman JC, Hud NV, Glass JB, Williams LD. 2018. Folding and catalysis near life's origin: support for Fe2+ as a dominant divalent cation, p 227-243, Prebiotic Chemistry and Chemical Evolution of Nucleic Acids. Springer.

50. Lin S-Y, Wang Y-C, Hsiao C. 2019. Prebiotic iron originates the peptidyl transfer origin. Molecular Biology and Evolution.

51. Popović M, Fliss PS, Ditzler MA. 2015. In vitro evolution of distinct self-cleaving ribozymes in diverse environments. Nucleic Acids Research 43:7070-7082.

52. Okafor CD, Lanier KA, Petrov AS, Athavale SS, Bowman JC, Hud NV, Williams LD. 2017. Iron mediates catalysis of nucleic acid processing enzymes: support for Fe (II) as a cofactor before the great oxidation event. Nucleic Acids Research 45:3634-3642.

53. Tabor S, Richardson CC. 1989. Effect of manganese ions on the incorporation of dideoxynucleotides by bacteriophage T7 DNA polymerase and Escherichia coli DNA polymerase I. Proceedings of the National Academy of Sciences 86:4076-4080.

54. Litman RM. 1971. The differential effect of magnesium and manganese ions on the synthesis of poly (dGd· C) and *Micrococcus luteus* DNA by *Micrococcus luteus* DNA polymerase. J Mol Biol 61:1-23.

55. Kimura S, Sakai Y, Ishiguro K, Suzuki T. 2017. Biogenesis and iron-dependency of ribosomal RNA hydroxylation. Nucleic Acids Research 45:12974-12986.

56. Kigawa T, Yabuki T, Yoshida Y, Tsutsui M, Ito Y, Shibata T, Yokoyama S. 1999. Cell-free production and stable-isotope labeling of milligram quantities of proteins. FEBS Letters 442:15-19.

57. Dann III CE, Wakeman CA, Sieling CL, Baker SC, Irnov I, Winkler WC. 2007. Structure and mechanism of a metal-sensing regulatory RNA. Cell 130:878-892.

58. Keedy HE, Thomas EN, Zaher HS. 2018. Decoding on the ribosome depends on the structure of the mRNA phosphodiester backbone. Proceedings of the National Academy of Sciences 115:E6731-E6740.

59. Kjeldgaard M, Nissen P, Thirup S, Nyborg J. 1993. The crystal structure of elongation factor EF-Tu from Thermus aquaticus in the GTP conformation. Structure 1:35-50.

60. Campuzano S, Modolell J. 1981. Effects of antibiotics, N-Acetylaminoacyl-tRNA and other agents on the elongation-factor-Tu dependent and ribosome-dependent GTP hydrolysis promoted by 2′(3′)-O-l-Phenylalanyladenosine. European Journal of Biochemistry 117:27-31.

61. Chen Y, Feng S, Kumar V, Ero R, Gao Y-G. 2013. Structure of EF-G–ribosome complex in a pretranslocation state. Nature structural & molecular biology 20:1077-1084.

62. Lövgren T, Petersson A, Loftfield RB. 1978. The mechanism of aminoacylation of transfer ribonucleic acid. The role of magnesium and spermine in the synthesis of isoleucyl-tRNA. Journal of Biological Chemistry 253:6702-6710.

63. Thiebe R. 1975. Aminoacylation of tRNA. Magnesium requirement and spermidine effect. FEBS Letters 51:259-261.

64. Blanquet S, Dessen P, Kahn D. 1984. Properties and specificity of methionyl-tRNA f Met formyltransferase from Escherichia coli. Methods in enzymology 106:141-152.

65. Morin LG. 1977. Creatine kinase: re-examination of optimum reaction conditions. Clinical Chemistry 23:1569-1575.

66. Vasavada K, Kaplan J, Rao BN. 1984. Analysis of phosphorus-31 NMR spectra of enzyme-bound reactants and products of adenylate kinase using density matrix theory of chemical exchange. Biochemistry 23:961-968.

67. Ito Y, Tomasselli A, Noda L. 1980. ATP: AMP phosphotransferase from baker's yeast. Purification and properties. European Journal of Biochemistry 105:85.

68. Munoz-Dorado J, Inouye S, Inouye M. 1990. Nucleoside diphosphate kinase from Myxococcus xanthus. II. Biochemical characterization. Journal of Biological Chemistry 265:2707-2712.

69. Kankare J, Neal GS, Salminenlr T, Glumhoff T, Cooperman BS, Lahti R, Goldman A. 1994. The structure of E. coli soluble inorganic pyrophosphatase at 2.7 Å resolution. Protein Engineering, Design and Selection 7:823-830.

70. Bloch-Frankenthal L. 1954. The role of magnesium in the hydrolysis of sodium pyrophosphate by inorganic pyrophosphatase. Biochemical Journal 57:87.

71. Bernier CR, Petrov AS, Waterbury CC, Jett J, Li F, Freil LE, Xiong X, Wang L, Migliozzi BL, Hershkovits E, Xue Y, Hsiao C, Bowman J, Harvey S, Grover M, Wartell Z, Williams L. 2014. RiboVision suite for visualization and analysis of ribosomes. Faraday Disc 169:195-207.

72. Lenz TK, Norris AM, Hud NV, Williams LD. 2017. Protein-free ribosomal RNA folds to a near-native state in the presence of Mg^{2+}. RSC Advances 7:54674-54681.

73. Wilkinson KA, Merino EJ, Weeks KM. 2006. Selective 2′-hydroxyl acylation analyzed by primer extension (SHAPE): quantitative RNA structure analysis at single nucleotide resolution. Nature Protocols 1:1610.

74. Mortimer SA, Weeks KM. 2007. A fast-acting reagent for accurate analysis of RNA secondary and tertiary structure by SHAPE chemistry. Journal of the American Chemical Society 129:4144-4145.

75. Holmstrom E, Fiore J, Nesbitt D. 2012. Thermodynamic origins of monovalent facilitated RNA folding. Biochemistry 51:3732-3743.

76. Shimizu Y, Inoue A, Tomari Y, Suzuki T, Yokogawa T, Nishikawa K, Ueda T. 2001. Cell-free translation reconstituted with purified components. Nature Biotechnology 19:751.

77. Ban N, Nissen P, Hansen J, Moore PB, Steitz TA. 2000. The complete atomic structure of the large ribosomal subunit at 2.4 Å resolution. Science 289:905-920.

78. Becke AD. 1988. Density-functional exchange-energy approximation with correct asymptotic behavior. Physical Review A 38:3098.

79. Lee C, Yang W, Parr RG. 1988. Development of the Colle-Salvetti correlation-energy formula into a functional of the electron density. Phys Rev B 37:785.

80. Frisch M, Trucks G, Schlegel HB, Scuseria GE, Robb MA, Cheeseman JR, Scalmani G, Barone V, Mennucci B, Petersson G. 2009. Gaussian 09, Revision A.02. Gaussian Inc, Wallingford, CT 200.

81. Glendening ED, Streitwieser A. 1994. Natural energy decomposition analysis: An energy partitioning procedure for molecular interactions with application to weak hydrogen bonding, strong ionic, and moderate donor–acceptor interactions. The Journal of Chemical Physics 100:2900-2909.

82. Gordon MS, Schmidt MW. 2005. Advances in electronic structure theory: GAMESS a decade later, p 1167-1189, Theory and Applications of Computational Chemistry. Elsevier.

83. Athavale SS, Gossett JJ, Hsiao C, Bowman JC, O'Neill E, Hershkovitz E, Preeprem T, Hud NV, Wartell RM, Harvey SC, Williams L. 2012. Domain III of the *T. thermophilus* 23S rRNA folds independently to a near-native state. RNA 18:752-758.

84. Hsiao C, Lenz TK, Peters JK, Fang P-Y, Schneider DM, Anderson EJ, Preeprem T, Bowman JC, O'Neill EB, Lie L. 2013. Molecular paleontology: a biochemical model of the ancestral ribosome. Nucleic Acids Research:gkt023.

85. Lanier KA, Athavale SS, Petrov AS, Wartell R, Williams LD. 2016. Imprint of ancient evolution on rRNA folding. Biochemistry 55:4603-4613.

86. Goldberg A. 1966. Magnesium binding by *Escherichia coli* ribosomes. Journal of Molecular Biology 15:663-673.

87. Pronczuk A, Baliga B, Munro H. 1968. Effect of nucleoside triphosphate and magnesium ion concentration on the stability and function of rat liver polysomes in vitro. Biochemical Journal 110:783-788.

88. Brion P, Westhof E. 1997. Hierarchy and dynamics of RNA folding. Annual Review of Biophysics and Biomolecular Structure 26:113-137.

89. Tinoco I, Jr., Bustamante C. 1999. How RNA folds. Journal of Molecular Biology 293:271-81.

90. Bock CW, Katz AK, Markham GD, Glusker JP. 1999. Manganese as a replacement for magnesium and zinc: functional comparison of the divalent ions. Journal of the American Chemical Society 121:7360-7372.

91. Imlay JA. 2014. The mismetallation of enzymes during oxidative stress. Journal of Biological Chemistry 289:28121-28128.

92. Litman RM. 1971. The differential effect of magnesium and manganese ions on the synthesis of poly (dGd· C) and Micrococcus luteus DNA by Micrococcus luteus DNA polymerase. Journal of Molecular Biology 61:1-23.

93. Zheng H, Shabalin IG, Handing KB, Bujnicki JM, Minor W. 2015. Magnesium-binding architectures in RNA crystal structures: validation, binding preferences, classification and motif detection. Nucleic Acids Research 43:3789-3801.

94. Bowman JC, Lenz TK, Hud NV, Williams LD. 2012. Cations in charge: magnesium ions in RNA folding and catalysis. Current Opinion in Structural Biology 22:262-272.

95. Hensley MP, Tierney DL, Crowder MW. 2011. Zn (II) binding to Escherichia coli 70S ribosomes. Biochemistry 50:9937-9939.

96. Craine J, Peterkofsky A. 1976. Studies on arginyl-tRNA synthetase from Escherichia coli B. Dual role of metals in enzyme catalysis. Journal of Biological Chemistry 251:241-246.

97. Da Silva JF, Williams RJP. 2001. The Biological Chemistry of the Elements: the Inorganic Chemistry of Life, Second ed. Oxford University Press.

98. Daly MJ, Gaidamakova E, Matrosova V, Vasilenko A, Zhai M, Venkateswaran A, Hess M, Omelchenko M, Kostandarithes HM, Makarova K. 2004. Accumulation of Mn(II) in *Deinococcus radiodurans* facilitates gamma-radiation resistance. Science 306:1025-1028.

99. Outten CE, O'Halloran TV. 2001. Femtomolar sensitivity of metalloregulatory proteins controlling zinc homeostasis. Science 292:2488-2492.

100. Beauchene NA, Mettert EL, Moore LJ, Keleş S, Willey ER, Kiley PJ. 2017. O2 availability impacts iron homeostasis in Escherichia coli. Proceedings of the National Academy of Sciences doi:10.1073/pnas.1707189114.

101. Derry LA. 2015. Causes and consequences of mid-Proterozoic anoxia. Geophysical Research Letters 42:8538-8546.

102. Poulton SW, Canfield DE. 2011. Ferruginous conditions: a dominant feature of the ocean through Earth's history. Elements 7:107-112.

103. Johnson JE, Webb SM, Ma C, Fischer WW. 2016. Manganese mineralogy and diagenesis in the sedimentary rock record. Geochimica et Cosmochimica Acta 173:210-231.

104. Honda K, Smith MA, Zhu X, Baus D, Merrick WC, Tartakoff AM, Hattier T, Harris PL, Siedlak SL, Fujioka H, Liu Q, Moreira PI, Miller FP, Nunomura A, Shimohama S, Perry G. 2005. Ribosomal RNA in Alzheimer disease is oxidized by bound redox-active iron. Journal of Biological Chemistry 280:20978-20986.

105. Zinskie JA, Ghosh A, Trainor BM, Shedlovskiy D, Pestov DG, Shcherbik N. 2018. Iron-dependent cleavage of ribosomal RNA during oxidative stress in the yeast Saccharomyces cerevisiae. Journal of Biological Chemistry 293:14237-14248.

106. Woese CR. 2001. Translation: in retrospect and prospect. RNA 7:1055-67.

107. Noller HF, Kop J, Wheaton V, Brosius J, Gutell RR, Kopylov AM, Dohme F, Herr W, Stahl DA, Gupta R. 1981. Secondary structure model for 23S ribosomal RNA. Nucleic Acids Research 9:6167-6189.

108. Petrov AS, Bernier CR, Hsiao C, Norris AM, Kovacs NA, Waterbury CC, Stepanov VG, Harvey SC, Fox GE, Wartell RM. 2014. Evolution of the ribosome at atomic resolution. Proceedings of the National Academy of Sciences 111:10251-10256.

109. Hsiao C, Mohan S, Kalahar BK, Williams LD. 2009. Peeling the onion: ribosomes are ancient molecular fossils. Molecular biology and evolution 26:2415-2425.

110. Anbar AD. 2008. Elements and evolution. Science 322:1481-1483.

111. Hazen RM, Ferry JM. 2010. Mineral evolution: Mineralogy in the fourth dimension. Elements 6:9-12.

112. Holland HD. 2006. The oxygenation of the atmosphere and oceans. Philosophical Transactions of the Royal Society B: Biological Sciences 361:903-915.

113. Klein C. 2005. Some Precambrian banded iron-formations (BIFs) from around the world: Their age, geologic setting, mineralogy, metamorphism, geochemistry, and origins. American Mineralogist 90:1473-1499.

114. Holland HD. 1973. The oceans; a possible source of iron in iron-formations. Economic Geology 68:1169-1172.

115. Riemer J, Hoepken HH, Czerwinska H, Robinson SR, Dringen R. 2004. Colorimetric ferrozine-based assay for the quantitation of iron in cultured cells. Analytical biochemistry 331:370-375.

116. Maguire BA, Wondrack LM, Contillo LG, Xu Z. 2008. A novel chromatography system to isolate active ribosomes from pathogenic bacteria. RNA 14:188-195.

117. Rappsilber J, Mann M, Ishihama Y. 2007. Protocol for micro-purification, enrichment, pre-fractionation and storage of peptides for proteomics using StageTips. Nature Protocols 2:1896.

118. Cox J, Mann M. 2008. MaxQuant enables high peptide identification rates, individualized ppb-range mass accuracies and proteome-wide protein quantification. Nature Biotechnology 26:1367.

119. Cox J, Neuhauser N, Michalski A, Scheltema RA, Olsen JV, Mann M. 2011. Andromeda: a peptide search engine integrated into the MaxQuant environment. Journal of Proteome Research 10:1794-1805.

120. Kurylo CM, Alexander N, Dass RA, Parks MM, Altman RA, Vincent CT, Mason CE, Blanchard SC. 2016. Genome sequence and analysis of Escherichia coli MRE600, a colicinogenic, nonmotile strain that lacks RNase I and the type I methyltransferase, EcoKI. Genome Biology and Evolution 8:742-752.

121. Tyanova S, Temu T, Sinitcyn P, Carlson A, Hein MY, Geiger T, Mann M, Cox J. 2016. The Perseus computational platform for comprehensive analysis of (prote) omics data. Nature Methods 13:731.

122. Latham JA, Cech TR. 1989. Defining the inside and outside of a catalytic RNA molecule. Science 245:276-282.

123. Okafor CD. 2015. Metallobiochemistry of RNA: Mg (II) and Fe (II) in divalent binding sitesGeorgia Institute of Technology.

124. Zhang Y, Orner BP. 2011. Self-assembly in the ferritin nano-cage protein superfamily. International Journal of Molecular Sciences 12:5406-5421.

125. Helgeland L. 1968. The ferritin content of the free ribosome fraction isolated from adult male and female rat liver. FEBS Letters 1:308-310.

126. Massé E, Arguin M. 2005. Ironing out the problem: new mechanisms of iron homeostasis. Trends in Biochemical Sciences 30:462-468.

127. Nandal A, Huggins CCO, Woodhall MR, McHugh J, Rodríguez-Quiñones F, Quail MA, Guest JR, Andrews SC. 2010. Induction of the ferritin gene (ftnA) of Escherichia coli by Fe2+–Fur is mediated by reversal of H-NS silencing and is RyhB independent. Molecular Microbiology 75:637-657.

128. Wofford JD, Bolaji N, Dziuba N, Outten FW, Lindahl PA. 2019. Evidence that a respiratory shield in Escherichia coli protects a low-molecular-mass FeII pool from O2-dependent oxidation. Journal of Biological Chemistry 294:50-62.

129. Boyd PW, Watson AJ, Law CS, Abraham ER, Trull T, Murdoch R, Bakker DC, Bowie AR, Buesseler K, Chang H. 2000. A mesoscale phytoplankton bloom in the polar Southern Ocean stimulated by iron fertilization. Nature 407:695.

130. Keyer K, Imlay JA. 1996. Superoxide accelerates DNA damage by elevating free-iron levels. Proceedings of the National Academy of Sciences 93:13635-13640.

131. Braun V, Hantke K. 2011. Recent insights into iron import by bacteria. Current Opinion in Chemical Biology 15:328-334.

132. Hohle TH, O'brian MR. 2016. Metal-specific control of gene expression mediated by B radyrhizobium japonicum M ur and E scherichia coli F ur is determined by the cellular context. Molecular Microbiology 101:152-166.

133. Yang J, Suzuki M, McCarty DR. 2016. Essential role of conserved DUF177A protein in plastid 23S rRNA accumulation and plant embryogenesis. Journal of Experimental Botany 67:5447-5460.

134. Bray MS, Wu J, Reed BC, Kretz CB, Belli KM, Simister RL, Henny C, Stewart FJ, DiChristina TJ, Brandes JA, Fowle DA, Crowe SA, Glass JB. 2017. Shifting microbial communities sustain multiyear iron reduction and methanogenesis in ferruginous sediment incubations. Geobiology 15:678-689.

135. Pavlov AA, Kasting JF, Brown LL, Rages KA, Freedman R. 2000. Greenhouse warming by CH_4 in the atmosphere of early Earth. Journal of Geophysical Research: Planets 105:11981-11990.

136. Haqq-Misra JD, Domagal-Goldman SD, Kasting PJ, Kasting JF. 2008. A revised, hazy methane greenhouse for the Archean Earth. Astrobiology 8:1127-1137.

137. Kasting JF. 2005. Methane and climate during the Precambrian era. Precambrian Research 137:119-129.

138. Roberson AL, Roadt J, Halevy I, Kasting J. 2011. Greenhouse warming by nitrous oxide and methane in the Proterozoic Eon. Geobiology 9:313-320.

139. Ueno Y, Yamada K, Yoshida N, Maruyama S, Isozaki Y. 2006. Evidence from fluid inclusions for microbial methanogenesis in the early Archaean era. Nature 440:516-519.

140. Battistuzzi FU, Feijao A, Hedges SB. 2004. A genomic timescale of prokaryote evolution: insights into the origin of methanogenesis, phototrophy, and the colonization of land. BMC Evolutionary Biology 4:44.

141. Kappler A, Pasquero C, Konhauser KO, Newman DK. 2005. Deposition of banded iron formations by anoxygenic phototrophic Fe(II)-oxidizing bacteria. Geology 33:865-868.

142. Crowe SA, Jones C, Katsev S, Magen Cd, O'Neill AH, Sturm A, Canfield DE, Haffner GD, Mucci A, Sundby Br. 2008. Photoferrotrophs thrive in an Archean Ocean analogue. Proceedings of the National Academy of Sciences 105:15938-15943.

143. Craddock PR, Dauphas N. 2011. Iron and carbon isotope evidence for microbial iron respiration throughout the Archean. Earth and Planetary Science Letters 303:121-132.

144. Johnson CM, Beard BL, Roden EE. 2008. The iron isotope fingerprints of redox and biogeochemical cycling in modern and ancient Earth. Annual Reviews of Earth and Planetary Sciences 36:457-493.

145. Vargas M, Kashefi K, Blunt-Harris EL, Lovley DR. 1998. Microbiological evidence for Fe(III) reduction on early Earth. Nature 395:65-67.

146. Konhauser K, Newman D, Kappler A. 2005. The potential significance of microbial Fe(III) reduction during deposition of Precambrian banded iron formations. Geobiology 3:167-177.

147. Lovley DR, Phillips EJ. 1987. Competitive mechanisms for inhibition of sulfate reduction and methane production in the zone of ferric iron reduction in sediments. Applied and Environmental Microbiology 53:2636-2641.

148. Lovley DR, Goodwin S. 1988. Hydrogen concentrations as an indicator of the predominant terminal electron-accepting reactions in aquatic sediments. Geochimica et Cosmochimica Acta 52:2993-3003.

149. Zhou S, Xu J, Yang G, Zhuang L. 2014. Methanogenesis affected by the co-occurrence of iron (III) oxides and humic substances. FEMS Microbiology Ecology 88:107-120.

150. Lovley D, Phillips E. 1986. Organic matter mineralization with reduction of ferric iron in anaerobic sediments. Applied and Environmental Microbiology 51:683-689.

151. Fournier GP, Gogarten JP. 2008. Evolution of acetoclastic methanogenesis in *Methanosarcina* via horizontal gene transfer from cellulolytic *Clostridia*. Journal of Bacteriology 190:1124-1127.

152. Ettwig KF, Zhu B, Speth D, Keltjens JT, Jetten MSM, Kartal B. 2016. Archaea catalyze iron-dependent anaerobic oxidation of methane. Proceedings of the National Academy of Sciences 113:12792-12796.

153. Gal'chenko V. 2004. On the problem of anaerobic methane oxidation. Microbiology 73:599-608.

154. Sivan O, Antler G, Turchyn AV, Marlow JJ, Orphan VJ. 2014. Iron oxides stimulate sulfate-driven anaerobic methane oxidation in seeps. Proceedings of the National Academy of Sciences 111:4139-4147.

155. Caldwell SL, Laidler JR, Brewer EA, Eberly JO, Sandborgh SC, Colwell FS. 2008. Anaerobic oxidation of methane: mechanisms, bioenergetics, and the ecology of associated microorganisms. Environmental Science & Technology 42:6791-6799.

156. Zehnder AJ, Brock TD. 1980. Anaerobic methane oxidation: occurrence and ecology. Applied and Environmental Microbiology 39:194-204.

157. Sivan O, Adler M, Pearson A, Gelman F, Bar-Or I, John SG, Eckert W. 2011. Geochemical evidence for iron-mediated anaerobic oxidation of methane. Limnology and Oceanography 56:1536-1544.

158. Segarra KEA, Comerford C, Slaughter J, Joye SB. 2013. Impact of electron acceptor availability on the anaerobic oxidation of methane in coastal freshwater and brackish wetland sediments. Geochimica et Cosmochimica Acta 115:15-30.

159. Beal EJ, House CH, Orphan VJ. 2009. Manganese- and iron-dependent marine methane oxidation. Science 325:184-187.

160. Amos R, Bekins B, Cozzarelli I, Voytek M, Kirshtein J, Jones E, Blowes D. 2012. Evidence for iron-mediated anaerobic methane oxidation in a crude oil-contaminated aquifer. Geobiology 10:506-517.

161. Riedinger N, Formolo M, Lyons T, Henkel S, Beck A, Kasten S. 2014. An inorganic geochemical argument for coupled anaerobic oxidation of methane and iron reduction in marine sediments. Geobiology 12:172-181.

162. Noroi KA, Thamdrup B, Schubert CJ. 2013. Anaerobic oxidation of methane in an iron-rich Danish freshwater lake sediment. Limnology and Oceanography 58:546-554.

163. Crowe S, Katsev S, Leslie K, Sturm A, Magen C, Nomosatryo S, Pack M, Kessler J, Reeburgh W, Roberts J. 2011. The methane cycle in ferruginous Lake Matano. Geobiology 9:61-78.

164. Sturm A, Fowle DA, Jones C, Leslie KL, Nomosatryo S, Henny C, Canfield DE, Crowe S. 2015. Rates and pathways of methane oxidation in ferruginous Lake Matano, Indonesia. Biogeosciences Discussions 12:1-34.

165. Egger M, Rasigraf O, Sapart ClJ, Jilbert T, Jetten MS, Röckmann T, van der Veen C, Bândă N, Kartal B, Ettwig KF. 2015. Iron-mediated anaerobic oxidation of methane in brackish coastal sediments. Environmental Science & Technology 49:277-283.

166. Fu L, Li S-W, Ding Z-W, Ding J, Lu Y-Z, Zeng RJ. 2016. Iron reduction in the DAMO/*Shewanella oneidensis* MR-1 coculture system and the fate of Fe(II). Water Research 88:808-815.

167. Rooze J, Egger M, Tsandev I, Slomp CP. 2016. Iron-dependent anaerobic oxidation of methane in coastal surface sediments: Potential controls and impact. Limnology and Oceanography.

168. Cai C, Leu AO, Xie G-J, Guo J, Feng Y, Zhao J-X, Tyson GW, Yuan Z, Hu S. 2018. A methanotrophic archaeon couples anaerobic oxidation of methane to Fe (III) reduction. The ISME Journal:1.

169. Crowe SA, O'Neill AH, Katsev S, Hehanussa P, Haffner GD, Sundby B, Mucci A, Fowle DA. 2008. The biogeochemistry of tropical lakes: A case study from Lake Matano, Indonesia. Limnology Oceangraphy 53:319-331.

170. Crowe S, Roberts J, Weisener C, Fowle D. 2007. Alteration of iron-rich lacustrine sediments by dissimilatory iron-reducing bacteria. Geobiology 5:63-73.

171. Kuntz LB, Laakso TA, Schrag DP, Crowe SA. 2015. Modeling the carbon cycle in Lake Matano. Geobiology 13:454-461.

172. Hansen JW, Thamdrup B, Jørgensen BB. 2000. Anoxic incubation of sediment in gas-tight plastic bags: a method for biogeochemical process studies. Marine Ecology Progress Series 208:273-282.

173. Cornell R, Schwertmann U. 1996. The Iron Oxides: Structure, Properties, Reactions, Occurrence and Uses. VCH Verlagsgesellshaft GMBH Weinheim, Germany.

174. Stookey LL. 1970. Ferrozine---a new spectrophotometric reagent for iron. Analytical Chemistry 42:779-781.

175. Kostka JE, Luther GW. 1994. Partitioning and speciation of solid phase iron in saltmarsh sediments. Geochemica Cosmochimica Acta 58:1701-1710.

176. Brandes JA. 2009. Rapid and precise δ13C measurement of dissolved inorganic carbon in natural waters using liquid chromatography coupled to an isotope-ratio mass spectrometer. Limnology and Oceanography: Methods 7:730-739.

177. Scheller S, Yi H, Chadwick GL, McGlynn SE, Orphan VJ. 2016. Artificial electron acceptors decouple archaeal methane oxidation from sulfate reduction. Science 351:703-707.

178. Caporaso JG, Lauber CL, Walters WA, Berg-Lyons D, Lozupone CA, Turnbaugh PJ, Fierer N, Knight R. 2011. Global patterns of 16S rRNA diversity at a depth of millions of sequences per sample. Proceedings of the National Academy of Sciences 108:4516-4522.

179. Kozich JJ, Westcott SL, Baxter NT, Highlander SK, Schloss PD. 2013. Development of a dual-index sequencing strategy and curation pipeline for analyzing amplicon sequence data on the MiSeq Illumina sequencing platform. Applied and Environmental Microbiology 79:5112-5120.

180. Roden EE, Wetzel RG. 2002. Kinetics of microbial Fe (III) oxide reduction in freshwater wetland sediments. Limnology and Oceanography 47:198-211.

181. Jensen MM, Thamdrup B, Rysgaard S, Holmer M, Fossing H. 2003. Rates and regulation of microbial iron reduction in sediments of the Baltic-North Sea transition. Biogeochemistry 65:295-317.

182. Kostka JE, Roychoudhury A, Van Cappellen P. 2002. Rates and controls of anaerobic microbial respiration across spatial and temporal gradients in saltmarsh sediments. Biogeochemistry 60:49-76.

183. Hansel CM, Benner SG, Neiss J, Dohnalkova A, Kukkadapu RK, Fendorf S. 2003. Secondary mineralization pathways induced by dissimilatory iron reduction of ferrihydrite under advective flow. Geochimica et Cosmochimica Acta 67:2977-2992.

184. Poulton SW, Canfield DE. 2005. Development of a sequential extraction procedure for iron: implications for iron partitioning in continentally derived particulates. Chemical Geology 214:209-221.

185. Hori T, Müller A, Igarashi Y, Conrad R, Friedrich MW. 2010. Identification of iron-reducing microorganisms in anoxic rice paddy soil by 13C-acetate probing. The ISME journal 4:267-278.

186. Roden EE, Wetzel RG. 1996. Organic carbon oxidation and suppression of methane production by microbial Fe (III) oxide reduction in vegetated and unvegetated freshwater wetland sediments. Limnology and Oceanography 41:1733-1748.

187. Kashefi K, Holmes DE, Baross JA, Lovley DR. 2003. Thermophily in the Geobacteraceae: Geothermobacter ehrlichii gen. nov., sp. nov., a novel thermophilic member of the Geobacteraceae from the "Bag City" hydrothermal vent. Applied and Environmental Microbiology 69:2985-2993.

188. Rotaru A-E, Shrestha PM, Liu F, Shrestha M, Shrestha D, Embree M, Zengler K, Wardman C, Nevina KP, Lovley DR. 2014. A new model for electron flow during anaerobic digestion: direct interspecies electron transfer to Methanosaeta for the reduction of carbon dioxide to methane. Energy & Environmental Science 7:408-415.

189. Zehnder AJ, Brock TD. 1979. Methane formation and methane oxidation by methanogenic bacteria. Journal of Bacteriology 137:420-432.

190. Willems A. 2014. The family Comamonadaceae, p 777-851, The Prokaryotes. Springer.

191. Reinhold-Hurek B, Hurek T. 2015. Azospira. Bergey's Manual of Systematics of Archaea and Bacteria 1-3.

192. Converse BJ, McKinley JP, Resch CT, Roden EE. 2015. Microbial mineral colonization across a subsurface redox transition zone. Frontiers in Microbiology 6.

193. Niemann H, Steinle L, Blees J, Bussmann I, Treude T, Krause S, Elvert M, Lehmann MF. 2015. Toxic effects of lab-grade butyl rubber stoppers on aerobic methane oxidation. Limnology and Oceanography: Methods 13:40-52.

194. Zavarzina DG, Sokolova TG, Tourova TP, Chernyh NA, Kostrikina NA, Bonch-Osmolovskaya EA. 2007. Thermincola ferriacetica sp. nov., a new anaerobic, thermophilic, facultatively chemolithoautotrophic bacterium capable of dissimilatory Fe(III) reduction. Extremophiles 11:1-7.

195. Stolz JF, Ellis DJ, Blum JS, Ahmann D, Lovley DR, Oremland RS. 1999. *Sulfurospirillum barnesii* sp. nov. and *Sulfurospirillum arsenophilum* sp. nov., new members of the *Sulfurospirillum* clade of the ε-Proteobacteria. International Journal of Systematic and Evolutionary Microbiology 49:1177-1180.

196. Zegeye A, Bonneville S, Benning LG, Sturm A, Fowle DA, Jones C, Canfield DE, Ruby C, MacLean LC, Nomosatryo S. 2012. Green rust formation controls nutrient availability in a ferruginous water column. Geology 40:599-602.

197. Crowe SA, O'Neill AH, Kulczycki E, Weisener CG, Roberts JA, Fowle DA. 2007. Reductive dissolution of trace metals from sediments. Geomicrobiology Journal 24:157-165.

198. Hausrath EM, Liermann LJ, House CH, Ferry JG, Brantley SL. 2007. The effect of methanogen growth on mineral substrates: will Ni markers of methanogen based communities be detectable in the rock record? Geobiology 5:49-61.

199. Knoll AH, Bergmann KD, Strauss JV. 2016. Life: the first two billion years. Philosophical Transactions of the Royal Society B: Biological Sciences 371:20150493.

200. Konhauser KO, Pecoits E, Lalonde SV, Papineau D, Nisbet EG, Barley ME, Arndt NT, Zahnle K, Kamber BS. 2009. Oceanic nickel depletion and a methanogen famine before the Great Oxidation Event. Nature 458:750-753.

201. Eickhoff M, Obst M, Schröder C, Hitchcock AP, Tyliszczak T, Martinez RE, Robbins LJ, Konhauser KO, Kappler A. 2014. Nickel partitioning in biogenic and abiogenic ferrihydrite: the influence of silica and implications for ancient environments. Geochimica et Cosmochimica Acta 140:65-79.

202. Konhauser KO, Robbins LJ, Pecoits E, Peacock C, Kappler A, Lalonde SV. 2015. The Archean nickel famine revisited. Astrobiology 15:804-815.

203. Stüeken EE, Buick R, Anbar AD. 2015. Selenium isotopes support free O2 in the latest Archean. Geology 43:259-262.

204. Olson SL, Reinhard CT, Lyons TW. 2016. Limited role for methane in the mid-Proterozoic greenhouse. PNAS 113:11447-11452.

205. Sydow A, Krieg T, Mayer F, Schrader J, Holtmann D. 2014. Electroactive bacteria—molecular mechanisms and genetic tools. Applied microbiology and biotechnology 98:8481-8495.

206. Lovley DR. 2011. Live wires: direct extracellular electron exchange for bioenergy and the bioremediation of energy-related contamination. Energy & Environmental Science 4:4896-4906.

207. Lovley DR, Coates JD. 1997. Bioremediation of metal contamination. Current Opinion in Biotechnology 8:285-289.

208. Logan BE. 2009. Exoelectrogenic bacteria that power microbial fuel cells. Nature Reviews Microbiology 7:375-381.

209. Lovley DR. 1991. Dissimilatory Fe(III) and Mn(IV) reduction. Microbiological Reviews 55:259-287.

210. Ntarlagiannis D, Atekwana EA, Hill EA, Gorby Y. 2007. Microbial nanowires: Is the subsurface "hardwired"? Geophysical Research Letters 34.

211. Reguera G, McCarthy KD, Mehta T, Nicoll JS, Tuominen MT, Lovley DR. 2005. Extracellular electron transfer via microbial nanowires. Nature 435:1098-1101.

212. Reguera G, Nevin KP, Nicoll JS, Covalla SF, Woodard TL, Lovley DR. 2006. Biofilm and nanowire production leads to increased current in *Geobacter sulfurreducens* fuel cells. Applied and Environmental Microbiology 72:7345-7348.

213. Rotaru A-E, Shrestha PM, Liu F, Markovaite B, Chen S, Nevin KP, Lovley DR. 2014. Direct interspecies electron transfer between *Geobacter metallireducens* and *Methanosarcina barkeri*. Applied and environmental microbiology 80:4599-4605.

214. Giltner CL, Nguyen Y, Burrows LL. 2012. Type IV pilin proteins: Versatile molecular modules. Microbiology and Molecular Biology Reviews 76:740-772.

215. Cianciotto NP. 2009. Many substrates and functions of type II secretion: lessons learned from Legionella pneumophila. Future Microbiology 4:797-805.

216. Hobbs M, Mattick JS. 1993. Common components in the assembly of type 4 fimbriae, DNA transfer systems, filamentous phage and protein-secretion

apparatus: a general system for the formation of surface-associated protein complexes. Molecular Microbiology 10:233-243.

217. Ayers M, Howell PL, Burrows LL. 2010. Architecture of the type II secretion and type IV pilus machineries. Future Microbiology 5:1203-1218.

218. Vargas M, Malvankar NS, Tremblay P-L, Leang C, Smith JA, Patel P, Synoeyenbos-West O, Nevin KP, Lovley DR. 2013. Aromatic amino acids required for pili conductivity and long-range extracellular electron transport in *Geobacter sulfurreducens*. mBio 4.

219. Tan Y, Adhikari RY, Malvankar NS, Ward JE, Woodard TL, Nevin KP, Lovley DR. 2017. Expressing the *Geobacter metallireducens* PilA in *Geobacter sulfurreducens* yields pili with exceptional conductivity. mBio 8:e02203-16.

220. Tan Y, Adhikari RY, Malvankar NS, Ward JE, Nevin KP, Woodard TL, Smith JA, Snoeyenbos-West OL, Franks AE, Tuominen MT. 2016. The low conductivity of Geobacter uraniireducens pili suggests a diversity of extracellular electron transfer mechanisms in the genus Geobacter. Frontiers in microbiology 7:980.

221. Feliciano G, Steidl R, Reguera G. 2015. Structural and functional insights into the conductive pili of *Geobacter sulfurreducens* revealed in molecular dynamics simulations. Physical Chemistry Chemical Physics 17:22217-22226.

222. Malvankar NS, Vargas M, Nevin K, Tremblay P-L, Evans-Lutterodt K, Nykypanchuk D, Martz E, Tuominen MT, Lovley DR. 2015. Structural basis for metallic-like conductivity in microbial nanowires. MBio 6:e00084-15.

223. Kolappan S, Coureuil M, Yu X, Nassif X, Egelman EH, Craig L. 2016. Structure of the *Neisseria meningitidis* Type IV pilus. Nature Communications 7:13015.

224. Walker DJF, Adhikari RY, Holmes DE, Ward JE, Woodard TL, Nevin KP, Lovley DR. 2017. Electrically conductive pili from pilin genes of phylogenetically diverse microorganisms. The ISME Journal doi:10.1038/ismej.2017.141.

225. Walker DJF, Martz E, Holmes DE, Zhou Z, Nonnenmann SS, Lovley DR. 2019. The archaellum of *Methanospirillum hungatei* is electrically conductive. mBio 10:e00579-19.

226. Liu X, Tremblay P-L, Malvankar NS, Nevin KP, Lovley DR, Vargas M. 2014. A *Geobacter sulfurreducens* strain expressing *Pseudomonas aeruginosa* type IV pili localizes OmcS on pili but is deficient in Fe (III) oxide reduction and current production. Appl Environ Microbiol 80:1219-1224.

227. Castelle CJ, Brown CT, Thomas BC, Williams KH, Banfield JF. 2017. Unusual respiratory capacity and nitrogen metabolism in a Parcubacterium (OD1) of the Candidate Phyla Radiation. Scientific reports 7:40101.

228. Kantor RS, Wrighton KC, Handley KM, Sharon I, Hug LA, Castelle CJ, Thomas BC, Banfield JF. 2013. Small genomes and sparse metabolisms of sediment-associated bacteria from four candidate phyla. MBio 4:e00708-13.

229. Albertsen M, Hugenholtz P, Skarshewski A, Nielsen KL, Tyson GW, Nielsen PH. 2013. Genome sequences of rare, uncultured bacteria obtained by differential coverage binning of multiple metagenomes. Nature Biotechnology 31:533.

230. Brown CT, Hug LA, Thomas BC, Sharon I, Castelle CJ, Singh A, Wilkins MJ, Wrighton KC, Williams KH, Banfield JF. 2015. Unusual biology across a group comprising more than 15% of domain Bacteria. Nature 523:208-211.

231. Luef B, Frischkorn KR, Wrighton KC, Holman H-YN, Birarda G, Thomas BC, Singh A, Williams KH, Siegerist CE, Tringe SG, Downing KH, Comolli LR, Banfield JF. 2015. Diverse uncultivated ultra-small bacterial cells in groundwater. Nature Communications 6.

232. Nurk S, Bankevich A, Antipov D, Gurevich AA, Korobeynikov A, Lapidus A, Prjibelski AD, Pyshkin A, Sirotkin A, Sirotkin Y. 2013. Assembling single-cell genomes and mini-metagenomes from chimeric MDA products. Journal of Computational Biology 20:714-737.

233. Mikheenko A, Saveliev V, Gurevich A. 2015. MetaQUAST: evaluation of metagenome assemblies. Bioinformatics 32:1088-1090.

234. Wu Y-W, Simmons BA, Singer SW. 2015. MaxBin 2.0: an automated binning algorithm to recover genomes from multiple metagenomic datasets. Bioinformatics 32:605-607.

235. Parks DH, Imelfort M, Skennerton CT, Hugenholtz P, Tyson GW. 2015. CheckM: assessing the quality of microbial genomes recovered from isolates, single cells, and metagenomes. Genome Research:gr. 186072.114.

236. Aziz RK, Bartels D, Best AA, DeJongh M, Disz T, Edwards RA, Formsma K, Gerdes S, Glass EM, Kubal M. 2008. The RAST Server: rapid annotations using subsystems technology. BMC Genomics 9:75.

237. Hyatt D, Chen G-L, LoCascio PF, Land ML, Larimer FW, Hauser LJ. 2010. Prodigal: prokaryotic gene recognition and translation initiation site identification. BMC Bioinformatics 11:119.

238. Imam S, Chen Z, Roos DS, Pohlschröder M. 2011. Identification of surprisingly diverse type IV pili, across a broad range of gram-positive bacteria. PloS One 6:e28919.

239. Jones DT, Taylor WR, Thornton JM. 1992. The rapid generation of mutation data matrices from protein sequences. Bioinformatics 8:275-282.

240. Kumar S, Stecher G, Tamura K. 2016. MEGA7: molecular evolutionary genetics analysis version 7.0 for bigger datasets. Molecular Biology and Evolution 33:1870-1874.

241. Rodriguez-R LM, Konstantinidis KT. 2016. The enveomics collection: a toolbox for specialized analyses of microbial genomes and metagenomes. PeerJ Preprints.

242. Zhou L, Yu H, Ai G, Zhang B, Hu S, Dong X. 2015. Transcriptomic and Physiological Insights into the Robustness of Long Filamentous Cells of Methanosaeta harundinacea, Prevalent in Upflow Anaerobic Sludge Blanket Granules. Applied and Environmental Microbiology 81:831-839.

243. Goddard TD, Huang CC, Meng EC, Pettersen EF, Couch GS, Morris JH, Ferrin TE. 2017. UCSF chimerax: meeting modern challenges in visualization and analysis. Protein Science.

244. Reardon PN, Mueller KT. 2013. Structure of the type IVa major pilin from the electrically conductive bacterial nanowires of *Geobacter sulfurreducens*. Journal of Biological Chemistry 288:29260-29266.

245. Holmes DE, Dang Y, Walker DJ, Lovley DR. 2016. The electrically conductive pili of *Geobacter* species are a recently evolved feature for extracellular electron transfer. Microbial Genomics 2.

246. Mehta T, Childers SE, Glaven R, Lovley DR, Mester T. 2006. A putative multicopper protein secreted by an atypical type II secretion system involved in the reduction of insoluble electron acceptors in *Geobacter sulfurreducens*. Microbiology 152:2257-2264.

247. Han X, Kennan RM, Parker D, Davies JK, Rood JI. 2007. Type IV fimbrial biogenesis is required for protease secretion and natural transformation in *Dichelobacter nodosus*. Journal of Bacteriology 189:5022-5033.

248. Li Y, Hao G, Galvani CD, Meng Y, De La Fuente L, Hoch H, Burr TJ. 2007. Type I and type IV pili of *Xylella fastidiosa* affect twitching motility, biofilm formation and cell–cell aggregation. Microbiology 153:719-726.

249. Graupner S, Frey V, Hashemi R, Lorenz MG, Brandes G, Wackernagel W. 2000. Type IV pilus genes pilA and pilC of *Pseudomonas stutzeri* are required for natural genetic transformation, and pilA can be replaced by corresponding genes from nontransformable species. Journal of Bacteriology 182:2184-2190.

250. Böhm M, Hurek T, Reinhold-Hurek B. 2007. Twitching motility is essential for endophytic rice colonization by the N_2-fixing endophyte *Azoarcus sp.* strain BH72. Molecular Plant-Microbe Interactions 20:526-533.

251. Kang Y, Liu H, Genin S, Schell MA, Denny TP. 2002. *Ralstonia solanacearum* requires type 4 pili to adhere to multiple surfaces and for natural transformation and virulence. Molecular Microbiology 46:427-437.

252. Marrs CF, Schoolnik G, Koomey JM, Hardy J, Rothbard J, Falkow S. 1985. Cloning and sequencing of a *Moraxella bovis* pilin gene. Journal of Bacteriology 163:132-139.

253. Essex-Lopresti AE, Boddey JA, Thomas R, Smith MP, Hartley MG, Atkins T, Brown NF, Tsang CH, Peak IR, Hill J. 2005. A type IV pilin, PilA, contributes to adherence of *Burkholderia pseudomallei* and virulence *in vivo*. Infection and Immunity 73:1260-1264.

254. Doig P, Todd T, Sastry PA, Lee K, Hodges RS, Paranchych W, Irvin R. 1988. Role of pili in adhesion of *Pseudomonas aeruginosa* to human respiratory epithelial cells. Infection and Immunity 56:1641-1646.

255. Burrows LL. 2012. *Pseudomonas aeruginosa* twitching motility: type IV pili in action. Annual Review of Microbiology 66:493-520.

256. Thormann KM, Saville RM, Shukla S, Pelletier DA, Spormann AM. 2004. Initial phases of biofilm formation in *Shewanella oneidensis* MR-1. Journal of Bacteriology 186:8096-8104.

257. Kehl-Fie TE, Miller SE, Geme JWS. 2008. *Kingella kingae* expresses type IV pili that mediate adherence to respiratory epithelial and synovial cells. Journal of Bacteriology 190:7157-7163.

258. Rakotoarivonina H, Larson MA, Morrison M, Girardeau J-P, Gaillard-Martinie B, Forano E, Mosoni P. 2005. The *Ruminococcus albus* pilA1–pilA2 locus: expression and putative role of two adjacent pil genes in pilus formation and bacterial adhesion to cellulose. Microbiology 151:1291-1299.

259. Nien-Tai H, Wei-Ming L, Meng-Shiunn L, Avon C, Shu-Chung C, Yu-Ling S, Ling-Yun C. 2002. XpsG, the major pseudopilin in *Xanthomonas campestris* pv. *campestris*, forms a pilus-like structure between cytoplasmic and outer membranes. Biochemical Journal 365:205-211.

260. Bakaletz LO, Baker BD, Jurcisek JA, Harrison A, Novotny LA, Bookwalter JE, Mungur R, Munson RS. 2005. Demonstration of type IV pilus expression and a twitching phenotype by *Haemophilus influenzae*. Infection and Immunity 73:1635-1643.

261. Dougherty BA, Smith HO. 1999. Identification of *Haemophilus influenzae* Rd transformation genes using cassette mutagenesis. Microbiology 145:401-409.

262. Nassif X, Beretti J-L, Lowy J, Stenberg P, O'Gaora P, Pfeifer J, Normark S, So M. 1994. Roles of pilin and PilC in adhesion of *Neisseria meningitidis* to human

epithelial and endothelial cells. Proceedings of the National Academy of Sciences 91:3769-3773.

263. Tønjum T, Marrs CF, Rozsa F, Bøvre K. 1991. The type 4 pilin of *Moraxella nonliquefaciens* exhibits unique similarities with the pilins of *Neisseria gonorrhoeae* and *Dichelobacter* (*Bacteroides*) *nodosus*. Microbiology 137:2483-2490.

264. Paranjpye RN, Strom MS. 2005. A *Vibrio vulnificus* type IV pilin contributes to biofilm formation, adherence to epithelial cells, and virulence. Infection and Immunity 73:1411-1422.

265. Chen I, Provvedi R, Dubnau D. 2006. A macromolecular complex formed by a pilin-like protein in competent *Bacillus subtilis*. Journal of Biological Chemistry 281:21720-21727.

266. Laurenceau R, Péhau-Arnaudet G, Baconnais S, Gault J, Malosse C, Dujeancourt A, Campo N, Chamot-Rooke J, Le Cam E, Claverys J-P. 2013. A type IV pilus mediates DNA binding during natural transformation in *Streptococcus pneumoniae*. PLoS Pathogens 9:e1003473.

267. Bhaya D, Bianco NR, Bryant D, Grossman A. 2000. Type IV pilus biogenesis and motility in the cyanobacterium *Synechocystis* sp. PCC6803. Molecular Microbiology 37:941-951.

268. Villar MT, Hirschberg RL, Schaefer MR. 2001. Role of the *Eikenella corrodens* pilA locus in pilus function and phase variation. Journal of Bacteriology 183:55-62.

269. von Tils D, Blädel I, Schmidt MA, Heusipp G. 2012. Type II secretion in *Yersinia*—a secretion system for pathogenicity and environmental fitness. Frontiers in Cellular and Infection Microbiology 2:160.

270. Rudel T, van Putten JP, Gibbs CP, Haas R, Meyer TF. 1992. Interaction of two variable proteins (PilE and PilC) required for pilus-mediated adherence of *Neisseria gonorrhoeae* to human epithelial cells. Molecular Microbiology 6:3439-3450.

271. Pugsley AP. 1993. Processing and methylation of PulG, a pilin-like component of the general secretory pathway of *Klebsiella oxytoca*. Molecular Microbiology 9:295-308.

272. Rumszauer J, Schwarzenlander C, Averhoff B. 2006. Identification, subcellular localization and functional interactions of PilMNOWQ and PilA4 involved in transformation competency and pilus biogenesis in the thermophilic bacterium *Thermus thermophilus* HB27. The FEBS Journal 273:3261-3272.

273. Sandkvist M, Michel LO, Hough LP, Morales VM, Bagdasarian M, Koomey M, DiRita VJ. 1997. General secretion pathway (eps) genes required for toxin secretion and outer membrane biogenesis in *Vibrio cholerae*. Journal of Bacteriology 179:6994-7003.

274. Sauvonnet N, Vignon G, Pugsley AP, Gounon P. 2000. Pilus formation and protein secretion by the same machinery in Escherichia coli. The EMBO Journal 19:2221-2228.

275. Zhang Y, Tennent JM, Ingham A, Beddome G, Prideaux C, Michalski WP. 2000. Identification of type 4 fimbriae in *Actinobacillus pleuropneumoniae*. FEMS Microbiology Letters 189:15-18.

276. Howard SP, Critch J, Bedi A. 1993. Isolation and analysis of eight exe genes and their involvement in extracellular protein secretion and outer membrane assembly in *Aeromonas hydrophila*. Journal of Bacteriology 175:6695-6703.

277. Hahn HP. 1997. The type-4 pilus is the major virulence-associated adhesin of *Pseudomonas aeruginosa*–a review. Gene 192:99-108.

278. Arrieta JG, Sotolongo M, Menéndez C, Alfonso D, Trujillo LE, Soto M, Ramírez R, Hernández L. 2004. A type II protein secretory pathway required for levansucrase secretion by *Gluconacetobacter diazotrophicus*. Journal of Bacteriology 186:5031-5039.

279. Chanyi RM, Koval SF. 2014. Role of type IV pili in predation by *Bdellovibrio bacteriovorus*. PloS One 9:e113404.

280. Rossier O, Starkenburg SR, Cianciotto NP. 2004. *Legionella pneumophila* type II protein secretion promotes virulence in the A/J mouse model of Legionnaires' disease pneumonia. Infection and Immunity 72:310-321.

281. Stone BJ, Kwaik YA. 1998. Expression of multiple pili by *Legionella pneumophila*: identification and characterization of a type IV pilin gene and its role in adherence to mammalian and protozoan cells. Infection and Immunity 66:1768-1775.

282. Wu SS, Kaiser D. 1995. Genetic and functional evidence that type IV pili are required for social gliding motility in *Myxococcus xanthus*. Molecular Microbiology 18:547-558.

283. Craig L, Volkmann N, Arvai AS, Pique ME, Yeager M, Egelman EH, Tainer JA. 2006. Type IV pilus structure by cryo-electron microscopy and crystallography: implications for pilus assembly and functions. Molecular Cell 23:651-662.

284. Liu F, Rotaru A-E, Shrestha PM, Malvankar NS, Nevin KP, Lovley DR. 2015. Magnetite compensates for the lack of a pilin-associated c-type cytochrome in extracellular electron exchange. Environmental Microbiology 17:648-655.

285. Yang J, Yan R, Roy A, Xu D, Poisson J, Zhang Y. 2015. The I-TASSER Suite: protein structure and function prediction. Nature Methods 12:7.

286. Goddard TD, Huang CC, Meng EC, Pettersen EF, Couch GS, Morris JH, Ferrin TE. 2018. UCSF ChimeraX: Meeting modern challenges in visualization and analysis. Protein Science 27:14-25.

287. Vandecandelaere I, Nercessian O, Segaert E, Achouak W, Mollica A, Faimali M, De Vos P, Vandamme P. 2008. *Alteromonas genovensis* sp. nov., isolated from a marine electroactive biofilm and emended description of *Alteromonas macleodii* Baumann et al. 1972 (Approved Lists 1980). International journal of Systematic and Evolutionary Microbiology 58:2589-2596.

288. Hernsdorf AW, Amano Y, Miyakawa K, Ise K, Suzuki Y, Anantharaman K, Probst A, Burstein D, Thomas BC, Banfield JF. 2017. Potential for microbial H2 and metal transformations associated with novel bacteria and archaea in deep terrestrial subsurface sediments. ISME J 11:1915-1929.

289. Sharma S, Cavallaro G, Rosato A. 2010. A systematic investigation of multiheme c-type cytochromes in prokaryotes. JBIC Journal of Biological Inorganic Chemistry 15:559-571.

290. Zhong Y, Shi L. 2018. Genomic Analyses of the Quinol Oxidases and/or Quinone Reductases Involved in Bacterial Extracellular Electron Transfer. Frontiers in microbiology 9.

291. Hallberg KB, Hedrich S, Johnson DB. 2011. *Acidiferrobacter thiooxydans*, gen. nov. sp. nov.; an acidophilic, thermo-tolerant, facultatively anaerobic iron-and sulfur-oxidizer of the family *Ectothiorhodospiraceae*. Extremophiles 15:271-279.

292. Leguijt T, Engels P, Crielaard W, Albracht S, Hellingwerf K. 1993. Abundance, subunit composition, redox properties, and catalytic activity of the cytochrome bc1 complex from alkaliphilic and halophilic, photosynthetic members of the family Ectothiorhodospiraceae. Journal of bacteriology 175:1629-1636.

293. Harwani D. 2013. The great plate count anomaly and the unculturable bacteria. Microbiology 2:350-1.

294. Lok C. 2015. Mining the microbial dark matter. Nature News 522:270.

295. Audette GF, van Schaik EJ, Hazes B, Irvin RT. 2004. DNA-binding protein nanotubes: learning from nature's nanotech examples. Nano Letters 4:1897-1902.

296. Stadtman E, Levine R. 2003. Free radical-mediated oxidation of free amino acids and amino acid residues in proteins. Amino acids 25:207-218.

297. Baker CM, Grant GH. 2007. Role of aromatic amino acids in protein–nucleic acid recognition. Biopolymers: Original Research on Biomolecules 85:456-470.

298. Burley S, Petsko GA. 1985. Aromatic-aromatic interaction: a mechanism of protein structure stabilization. Science 229:23-28.

299. Kirchman DL. 2018. Processes in Microbial Ecology. Oxford University Press.

300. Cull SC, Arvidson RE, Catalano JG, Ming DW, Morris RV, Mellon MT, Lemmon M. 2010. Concentrated perchlorate at the Mars Phoenix landing site: Evidence for thin film liquid water on Mars. Geophysical Research Letters 37.

301. Luo Y-H, Chen R, Wen L-L, Meng F, Zhang Y, Lai C-Y, Rittmann BE, Zhao H-P, Zheng P. 2015. Complete perchlorate reduction using methane as the sole electron donor and carbon source. Environmental science & technology 49:2341-2349.

302. Lv P-L, Shi L-D, Wang Z, Rittmann B, Zhao H-P. 2019. Methane oxidation coupled to perchlorate reduction in a membrane biofilm batch reactor. Science of The Total Environment 667:9-15.

303. Ettwig KF, Butler MK, Le Paslier D, Pelletier E, Mangenot S, Kuypers MMM, Schreiber F, Dutilh BE, Zedelius J, de Beer D, Gloerich J, Wessels HJCT, van Alen T, Luesken F, Wu ML, van de Pas-Schoonen KT, Op den Camp HJM, Janssen-Megens EM, Francoijs K-J, Stunnenberg H, Weissenbach J, Jetten MSM, Strous M. 2010. Nitrite-driven anaerobic methane oxidation by oxygenic bacteria. Nature 464:543.

304. Sekar R, Shin HD, DiChristina TJ. 2016. Direct conversion of cellulose and hemicellulose to fermentable sugars by a microbially-driven Fenton reaction. Bioresource technology 218:1133-1139.

305. Balk M, Mehboob F, van Gelder AH, Rijpstra WIC, Damsté JSS, Stams AJ. 2010. (Per) chlorate reduction by an acetogenic bacterium, Sporomusa sp., isolated from an underground gas storage. Applied Microbiology and Biotechnology 88:595-603.

306. Gelwicks JT, Risatti JB, Hayes J. 1989. Carbon isotope effects associated with autotrophic acetogenesis. Organic Geochemistry 14:441-446.

307. Amann RI, Binder BJ, Olson RJ, Chisholm SW, Devereux R, Stahl DA. 1990. Combination of 16S rRNA-targeted oligonucleotide probes with flow cytometry for analyzing mixed microbial populations. Applied and Environmental Microbiology 56:1919-1925.

308. Wallner G, Amann R, Beisker W. 1993. Optimizing fluorescent in situ hybridization with rRNA-targeted oligonucleotide probes for flow cytometric identification of microorganisms. Cytometry: The Journal of the International Society for Analytical Cytology 14:136-143.

309. Manz W, Amann R, Ludwig W, Wagner M, Schleifer K-H. 1992. Phylogenetic oligodeoxynucleotide probes for the major subclasses of proteobacteria: problems and solutions. Systematic and Applied Microbiology 15:593-600.

310. Lücker S, Steger D, Kjeldsen KU, MacGregor BJ, Wagner M, Loy A. 2007. Improved 16S rRNA-targeted probe set for analysis of sulfate-reducing bacteria by fluorescence in situ hybridization. Journal of Microbiological Methods 69:523-528.

311. Richter H, Lanthier M, Nevin KP, Lovley DR. 2007. Lack of Electricity Production by Pelobacter carbinolicus Indicates that the Capacity for Fe(III) Oxide Reduction Does Not Necessarily Confer Electron Transfer Ability to Fuel Cell Anodes. Applied and Environmental Microbiology 73:5347-5353.